Minimum stress and pore fluid pressure in sedimentary basins

Adrian James White

Minimum Stress and Pore Fluid Pressure in Sedimentary Basins

By

Adrian James White

Department of Geological Sciences

This thesis has been submitted as partial fulfilment of the requirements of the University of Durham for the degree of Doctor of Philosophy.

December 2001

Abstract

Leak-off pressures (LOPs) recorded during leak-off tests (LOTs) conducted down boreholes are often used to estimate the magnitude of the minimum stress (usually assumed to be horizontal - S_h) in the subsurface. However, the reliability of these tests has previously been questioned in the literature and the accuracy of the data obtained from them has been in doubt. Using original LOT data from Mid-Norway, this study has shown that through stringent quality control, good LOT data can be used to accurately constrain the magnitude of S_h. Knowledge of the relationship between *in-situ* stress and pore pressures (P_p) in basins provides insights into their structure as well as having implications for well design and drilling safety.

Using stress-depth plots to display S_h measurements from Mid-Norway and six further basins from around the world reveals a variability in the magnitude of S_h at all depths. Analyses show that rock mechanical properties or differences in the way LOTs are performed cannot explain this variability. Separate analysis of extended leak-off test (XLOT) data from Mid-Norway shows that variability in the magnitude of the LOP (most often used to calculate S_h) is inherent in the testing procedure. This inherence suggests either the variations in S_h are real (they represent basin heterogeneities) or that they result from a combination or rock mechanical and/or pumping pressure test parameters. Further use of multiple cycle XLOTs shows that using LOPs and instantaneous shut-in pressures (ISIPs) to calculate S_h produces similar results. Considering re-opening cycles of tests and those tests from greater depths shows the difference between the magnitude of S_h calculated using the LOP and ISIP is reduced. These same high quality data have been used to calculate the magnitude of the three principal stress from Mid-Norway and show the contemporary stress situation to be $S_h<S_V<S_H$.

Compilations of S_h and P_p have also been used to calculate the lower bound to LOPs and the upper limit to P_p as means of predicting S_h. Results show that using the lower bound to estimate the maximum P_p (or the upper limit to estimate S_h) will lead to large errors within normally pressured zones but successful estimates at overpressured depths. Analyses also show that there is no systematic relationship between the magnitude of the lower bound to LOPs and the contemporary stress situation.

The S_h and P_p data were normalised to a "*hypothetical unconstrained basin*" and/or depth to investigate pore pressure *in-situ* stress coupling and quantify the change in S_h with overpressure. Results show that coupling can be inferred in three of the seven basins studied. Poro-elasticity or frictional limits to stress are the most likely coupling mechanisms because regional S_h magnitudes do not relate to tectonic regime. Coupling is not inferred for Mid-Norway. An explanation for the lack of coupling is the late timing of overpressure following normal compaction of the rocks. It is suggested that "inflationary mechanism" overpressures produce lower $\Delta S_h/\Delta P_p$ values than overpressures that developed synchronous with burial. Using the poro-elasticity equation to back-calculate the Poisson's ratio (ν) of the rocks reveals high values thus establishing a relationship between high ν and higher levels of compaction.

Acknowledgements

Woah...where do I begin eh? First of all a big thank you to my supervisor, Dick Swarbrick, for all his patience over the last three-and-a-bit years. I am pretty certain that without his enthusiasm mixed with those dire warnings I would not have got through this project intact. Dick provided me with a fantastic data set from the onset and was tireless in his striving to ply even more data from the *GeoPOP* sponsors as time progressed. Okay, so I moaned, but I'm not too proud to admit that doing a PhD. with Dick was worth a bit of trauma.

Thank you as well to the *GeoPOP* team (Daniel, Anthony, Gary, Des, Neville, Martin and Christine) for plenty of good ideas, listening to my whining and for reminding me that a job is only as good as the people you work with (and the junkets you can get out of the company...). Thanks must also go to the *GeoPOP* sponsors for handing over their valuable data to a fly-by-night postgraduate trying to make a name for himself. In particular, thanks to Linn Arnesen, Sven Hansen, Christian Zwach, Tørsten Jørgensen and Michael Erdmann at *Norsk Hydro* in Bergen for providing much-needed insights into data analyses (Tørsten), a seriously flashy flat (Linn), an introduction to ski-ing (Sven) and a top-notch house warming party (Michael). Thanks also to Lars Wensaas at *Statoil* and Ron Daniel at *Enterprise Oil.* I would especially like to show my gratitude to Dominique Grauls at *TotalFinaElf* not only for half of the data used in this study but also for his advise and guidance from the moment I started.

From within the department I'd like to thank a whole host of people. To start with: the postgraduates both past and present. In particular, a really big "ta" to Caroline, Hippy Sarah, Toby, Pauli, Matt, Gordon, Lee, Janine, Norwegian Fred, Abi, Sue, Helen, Rich, Dave, Kirstin, Sophie, Jimmy, Shaz, Woody, Nic, Graham and all the Usual Suspects who made Friday night *beer o'clock* what it was - a department tradition that should never be allowed to die. A special "cheers" to Lisa for the dodgy conversations in the *Muppet Collective* office and her realisation of what constitutes good music. To all the staff, both academic and technical, who made me feel a part of the place and helped me through the Second Year Blues. Thanks also to those staff who allowed me to tag along on fieldtrips as a demonstrator, thus partially fulfilling my desire in life to be a *geo-tourist.*

A big thank you must also go to Dougal Jerram and two of the fattest and hairiest moggies I've ever had the misfortune to share a sofa with. Mucho appreciation for the seriously cheap accommodation, *soccer a.m.* and DVDs projected on the wall of the living room. Thanks to the *New Inn* for three years worth of *Yellow Cards*, *The Times* for the *Concise Crossword* online and *Dunelm Stores* for flapjacks – the true food of the Gods.

To Terry Engelder, Don Fisher and the grad-students at Penn State University (especially Amy, Kelly, Christie and Redescal): thanks for all your guidance and help, your acceptance of a *limey* and an introduction to filter coffee drunk from buckets. To Richard Hillis and the raucous oiks at Adelaide (Stinger, Van Goof, Jerry, Scotty, Max, "Badgirl" Aaron, Nej and Rosalie): thanks for making a *pommie* feel welcome, all the help on *in-situ* stress prediction and my work in general. On a less serious note, I suppose I should be grateful for the introduction to Cooper's Pale, enlightening me as to the intricacies of a bonzer Aussie barbie and all the e-mails I've creased myself over this last eighteen months.

Finally thank you to those people from outside of Durham and the world of *in-situ* stress. Cheers to the Los Angeles babes, Alex and Sheila, for a great time out there. Especially to Alex for somewhere to doss, an ace afternoon frazzling on the beach and a reason to finish. Thanks to Pete for the early-morning training sessions; The Fanoir and Ron for the smutty, three-way e-mail conversations; and to Neil and Ange just for being great really.

Oh, nearly forgot. The **biggest thank you of all** to my family: Mum, Dad, Jon and Nick. You folks have supported me in just about every way for the last twenty-five years and I hope this goes some way to repaying your trust in me. I couldn't and probably wouldn't have made it without you.

To anyone else I may have missed out: consider yerself acknowledged if you think you deserve it.

Declaration

The content of this thesis is entirely the work of the named author. Any work by other people is acknowledged by reference. None of this work has previously been submitted for a degree at this or any other university.

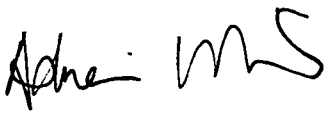

Adrian James White

University of Durham

December 2001.

Table of Contents

Figures

Tables

Chapter ONE: Introduction

1 Introduction

1.1 Objectives

The primary aim of this study is to **use leak-off test measurements recorded in boreholes to determine the magnitude of minimum *in-situ* stress (S_h)** in a range of sedimentary basins.

The main objectives can be listed as:

- **To assess data reliability and quality from original leak-off test records to ensure that only those of the highest quality are used for S_h determination.**
- **To use extended leak-off test (XLOT) data to constrain the relationship between the leak-off pressure and the instantaneous shut-in pressure.**
- **To understand the causes of scatter in the magnitude of S_h at a given depth.**
- **To create lower bounds to leak-off pressures and upper limits to pore pressures as alternative means of predicting the regional S_h.**
- **To test the relationship between the magnitude of overpressure and the magnitude of S_h by quantifying the change in S_h with overpressure.**
- **To analyse overpressure and S_h magnitudes in relationship to the overpressure generating mechanism (using data from Mid-Norway).**
- **To use XLOT data and the Kirsch equations to calculate S_H and make inferences about the contemporary stress situation (using data from Mid-Norway).**

While the magnitude of S_h is calculated for each individual leak-off test, compilations of data from entire regions allow the change in S_h with depth on a regional scale to be predicted. Investigations were conducted on S_h and pore pressure data from Mid-Norway, the Central North Sea, Brunei, the Gulf of Mexico, Onshore Nigeria, Offshore West Africa and the Barents Sea.

The importance and relevance of this study comes from the insights it provides into the structural evolution of a basin and knowledge of the contemporary stress and pore pressure situation. There are also important applications of this work that can be used in the petroleum industry relating to hydrocarbon production.

Knowledge of the stress situation and the magnitude and effects of overpressure on stress has implications for:

- **Better S_h and P_p prediction.**

- **Well design and planning and hence the cost of hydrocarbon extraction.**
- **Safe and efficient extraction of hydrocarbons.**

1.2 Sources and format of the data

The following section lists the companies and organisations that provided the data and explains the formats that the data arrived in.

1.2.1 Sources of the data

The data used were provided by a number of different oil companies who sponsor the *GeoPOP 2* project and came from several data bases:

- **Mid-Norway** *Norsk Hydro* (*PI Erico*) and *Statoil*;
- **The Central North Sea** *GeoPOP* and *PI Erico*;
- **Brunei** *TotalFinaElf*;
- **The Gulf of Mexico** *GeoPOP*;
- **Onshore Nigeria** *TotalFinaElf*;
- **Offshore West Africa** *TotalFinaElf*;
- **The Barents Sea** *Enterprise Oil*.

1.2.2 Format of the data

The format of the data used is listed below for each region:

Region	Format of the data
Mid-Norway	Original graphical record Computer spreadsheet On-rig computer data compilation
Central North Sea	*PressureView* data base
Brunei	Computer spreadsheet
Gulf of Mexico	*PressureView* data base
Onshore Nigeria	Computer spreadsheet
Offshore West Africa	Computer spreadsheet
The Barents Sea	*PressureView* data base

Table 1.1: Summary table of the format of the data used for each region.

The terms used to describe the format of the data can be explained as:

Format of the data	Description
Original graphical record	Paper graph of pumping pressure versus time drawn up during the test.
Computer spreadsheet	Spreadsheet listing interpretations of S_h from the paper graphs together with information on lithology, wellbore diameter, pumping rate, mud weight, formation etc.
On-rig computer data compilation	Digitalised records of pumping pressure and time.
***PressureView* data base**	Previous interpretations of S_h together with lithology, wellbore diameter, pumping rate, mud weight, formation etc. information.

Table 1.2: Explanation of terms used in **Table 1.1** for the format of the data.

1.3 Thesis synopsis

This thesis has been divided into seven chapters:

Chapter 1 introduces the objectives of this study and lists the format of the data used as well as the sources of these data.

Chapter 2 is the literature review. It provides the reader with background information on this work and some historical methods of minimum *in-situ* stress prediction. An introduction to fracture mechanics and the hydraulic fracturing of rocks is given. The terminology used in the performance of pumping pressure tests are explained as well as explanations of "*fracture gradient*" prediction. A review of the components that contribute to stresses in the Earth, the origins of overpressure and the relationship between overpressure and stress completes the chapter.

Chapter 3 introduces Mid-Norway - the main case study region. Details of the location of Mid-Norway and the importance of the region as a petroleum producer are given. Also included are summaries of the geology, the contemporary stress situation and the presence, timing and development of overpressure. There is a description of the compilation of the Mid-Norway data set and the quality control procedure undertaken to constrain the accuracy of the leak-off test data. Finally, the determination of the Mid-Norway lithostat is explained.

Chapter 4 presents results from Mid-Norway. These include quantification of the variability in S_h at specific depths on stress-depth plots and the use of rock mechanical and pumping pressure test parameters as means of understanding S_h variability. Stress-depth plots are also used to determine the lower bound to LOPs and upper limit to P_p. Investigations have been performed into the presence of pore pressure *in-situ* stress coupling. A smaller investigation into the difference between the leak-off pressure (LOP) and the instantaneous shut-in pressure (ISIP) when used to determine minimum stress is also presented.

Chapter 5 introduces case studies from the Central North Sea, Brunei, the Gulf of Mexico, Onshore Nigeria, Offshore West Africa and the Barents Sea. These studies follow the same approaches as were used for Mid-Norway.

Chapter 6 starts with a summary section comparing the results from **chapters 4** and **5**. Following the summary are discussions about the results and the implications that come out of the studies.

Chapter 7 completes this thesis by listing the main conclusions and suggesting future work on pore pressures and *in-situ* stress.

Chapter TWO: Theory

2 Theory

2.1 Introduction

The purpose of this chapter is to provide an introduction to the topics and ideas in this thesis. **Section 2.2** provides the reader with a literature review of both empirical and measured techniques for determining minimum *in-situ* stress and why knowledge of this stress is important. Whilst it is not intended to be an exhaustive summary, **section 2.2** shows how techniques have varied over time in terms of complexity and in the assumptions made.

Following this is an introduction (**section 2.3**) to the concepts behind fracture mechanics. Firstly an introduction to stress notation in rocks is given as well as how the stress situation can be described by three principal stresses. Also explained is the principle of stress superposition around boreholes and how this superposition can affect borehole stability. Leading on from this is an explanation of how rocks can hydraulically fracture and the conditions necessary for the process to initiate.

Leak-off tests are the source of data for minimum *in-situ* stress determination in this study. **Section 2.4** explains the terminology and the methodology behind the testing procedure. Also explained is how to calculate S_3 from pumping pressure magnitudes.

The derivation of fracture gradients and lower bounds to leak-off pressures (LOPs) by empirical methods and using leak-off tests is explained in **section 2.5**. Also explained is how lower bounds can be used to determine S_3 on a regional scale from large data sets of LOPs.

Finally, **section 2.6** explains the theoretical sub-surface stress situation and shows that such a situation is generally an oversimplification. Superimposed on this reference state of stress are the effects of different structures in the crust, the influence of tectonics and a contribution from overpressure. As all of these components add to the horizontal stresses, modelling them based on empirical relationships becomes more difficult. A summary of the effects of these parameters is hence given as an explanation for why good first-hand knowledge of S_3 is important.

2.2 Alternative approaches for minimum *in-situ* stress prediction

Accurate prediction of the minimum *in-situ* stress (S_3) is important in the petroleum industry. Firstly, it is worth noting that in many instances in sedimentary basins S_3 is

horizontal: $S_3 = S_h$. Knowledge of the minimum stress has implications for not only drilling safety and well design but also the costs of extraction of hydrocarbons. Because this stress is so important, it is felt that a historical review of some of the various ways of predicting S_3 is warranted. Despite not being a wholly exhaustive summary, it does reveal how ideas have evolved and how a greater number of parameters have been incorporated into models.

The literature documents many examples of workers using data from a variety of basins to derive empirical relationships for the magnitude of S_3, or in some cases, specifically S_h. In many situations, algorithms are produced to calculate the fracture pressure which is assumed equal to the minimum *in-situ* stress (Traugott, 1997). Many of the relationships rely on measured parameters such as vertical or overburden stress (the stress exerted by the weight of the overlying rocks and fluids), depth and pore pressure and combine them with mathematically derived functions such as Poisson's Ratio and the Biot coefficient. Initial, older relationships are more simplistic being based solely on the Poisson's Ratio and the ratio of effective stresses. Later relationships rely on data sets of LOPs (see Breckels & van Eekelen, 1982; Gaarenstroom *et al.*, 1993) to derive algorithms and also a greater number of measured parameters (see Miller, 1995). These relationships are reviewed in **section 2.2.1**.

Hillis (2000 & 2001b) provides useful summaries of how P_p can effect S_3 when it is horizontal; namely S_h. These summaries follow on from the relationships proposed by Zoback and Healy (1984) and Engelder and Fischer (1994). A review of the two key methodologies that describe the contribution made by P_p to the magnitude of S_h is given in **section 2.2.2**.

2.2.1 Measured and empirical methods of stress determination

2.2.1.1 The uniaxial strain model

The uniaxial strain model is used to constrain changes in horizontal stress as a function of changing vertical stress, assuming the rocks develop fixed *elastic* properties at some stage following deposition. Horizontal stresses are created because the rock pile wants to spread out as it is squashed from above. The model requires no influence from outside tectonic stresses but does require the basin to be confined (**Figure 2.1** from Engelder, 1993) and therefore unable to laterally expand when a vertical load is applied (Engelder, 1993). The horizontal stresses will be isotropic and depend on the vertical stress and the Poisson's Ratio (Arnesen *et al.*, 1997). These horizontal stresses can be calculated from Hooke's Law and knowledge of the overburden stress:

$$S_H = S_h = \left[\frac{\nu}{1-\nu}\right] S_V \qquad \textit{(equation 2.1)}$$

Where: S_H = maximum horizontal stress;

S_h = minimum horizontal stress;

ν = Poisson's Ratio;

S_V = vertical stress.

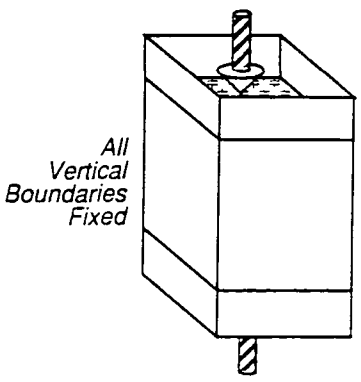

Figure 2.1: The model for uniaxial strain in the Earth's crust (from Engelder, 1993).

Poisson's Ratio defines the relationship between horizontal (ε_h) and vertical (ε_V) deformation, i.e. the amount of horizontal expansion/vertical contraction (Arnesen *et al.*, 1997):

$$\nu = -\frac{\varepsilon_h}{\varepsilon_V} \qquad \textit{(equation 2.2)}$$

In practice, uniaxiality is probably an over-simplification that is best suited to laboratory testing and possibly individual wells where the rheological properties of the rock and the temperature conditions etc. are well known. Tectonic stresses (namely components of the remote or far-field stress) usually occur in basins and when combined with intra-plate stresses, are superimposed onto the component of horizontal stress created by the overlying load of rocks and fluids. The result is that a triaxial stress situation is much more likely in nature (Hillis pers. comm., 2001).

2.2.1.2 The k notation

Empirical methods have been used in conjunction with real data to determine the minimum stress, again assumed to be S_h. Matthews and Kelly (1967) introduced the k notation as a way of expressing the ratio between minimum horizontal and vertical *effective* stresses. The effective stress (either σ_1, σ_2 or σ_3) is defined as the total stress (either S_1, S_2 or S_3) minus the pore pressure (P_p). Thus, the minimum horizontal effective stress (σ_h) is equal to S_h minus pore pressure and the vertical effective stress (σ_V) is S_V minus pore pressure. The parameter k is therefore defined as:

$$k = \frac{S_h - P_p}{S_V - P_p} = \frac{\sigma_h}{\sigma_V} \qquad \textit{(equation 2.3)}$$

Equation 2.3 can be re-arranged to give an equivalent of the standard fracture gradient relationship (Eaton, 1969; Traugott, 1997) used to calculate minimum horizontal stress from the pore pressure and vertical stress:

$$S_h = k\left(S_V - P_p\right) + P_p \qquad \textit{(equation 2.4)}$$

Because k is a calibration constant in *equation 2.4*, a number of methods have been documented as means of its determination. Where there is a poro-elastic response of rocks under the conditions of uniaxial strain, namely no lateral dimension change, k has been determined using the Poisson's Ratio, v, (see *equation 2.2*) such that:

$$k = \frac{\nu}{1-\nu} \qquad \textit{(equation 2.5)}$$

In a situation where rocks respond to strain in a plastic sense, k is unity (Traugott, 1997; Hillis, 2001b). The final situation assumes that rock stresses are in a state of equilibrium with those required to cause frictional failure, as described by Zoback and Healy (1984). This situation assumes that there are suitably orientated planes of no cohesion in a normal fault regime. If these conditions are satisfied then k can be described in terms of the coefficient of rock friction (μ):

$$k = \frac{1}{\left(\sqrt{\left(\mu^2 + 1\right)} + \mu\right)^2} \qquad \textit{(equation 2.6)}$$

2.2.1.3 Breckels and van Eekelen (1982)

Breckels and van Eekelen (1982) provide a good summary of the work of previous authors such as Matthews and Kelly (1967), Pennebaker (1968), Eaton (1969) and Pilkington (1978) on fracture gradients and lower bounds to LOPs for the US Gulf Coast. Each of these authors use the k value (ratio of horizontal to vertical effective stress – *equation 2.3*) to define their relationships of how stress changes with depth. Differences only really occur in the way they determine the minimum effective stress. For further information see Breckels and van Eekelen (1982).

Following this historical review, Breckels and van Eekelen (1982) derived a relationship between the minimum stress (S_h) and depth for the US Gulf Coast using fracture or "instantaneous shut-in" pressure data. Using a data set of over 300 points from the US Gulf Coast, they mathematically fitted a curve that described the lower bound to 93% of the data. The curve, a combination of a linear and power-law relationship, meant the magnitude of S_h could be determined solely from the depth (D):

$$S_h = 0.0197D^{1.145} \quad \text{for} \quad \text{D<7500 feet.} \qquad \textit{(equation 2.7)}$$

$$S_h = 1.167D - 4596 \quad \text{for} \quad \text{D>7500 feet.} \qquad \textit{(equation 2.8)}$$

More complex relationships were derived for S_h in abnormally pressured formations in the US Gulf Coast region using the depth and the magnitude of under/over-pressure (actual minus normal pore pressure). Data from Venezuela and Brunei were also used to derive power-law relationships for minimum stress determination using a combination of depth and under/over-pressure magnitude.

2.2.1.4 Gaarenstroom *et al.* (1993)

Gaarenstroom *et al.* (1993) observed that overpressures in pre-Cretaceous reservoirs in the Central North Sea graben follow a well-defined trend that increases with depth. Minimum stress (referred to solely as S_3 and therefore not allocated an orientation) derived from leak-off pressures also follow a similar trend that is related to the present day depth of

burial. Gaarenstroom *et al.* (1993) state that LOPs are generally equal to or higher than S_3 so fitting a *minimum LOP-line* to the data creates an approximation of S_3 as a function of depth.

Observations show that a difference of less than 1000 psi between P_p measurements and LOPs is enough to cause the breaching of a trap. They found that in wells where the difference between P_p and LOP was less than 1000 psi, the well is generally dry or has a "leaking seal". Essentially, they state that the LOP tends to over-estimate S_3 by around 1000 psi (or ~7 MPa). Therefore an empirical method based on measured data and observations has been developed to predict S_3 on a regional basis from LOP data.

2.2.1.5 Yassir and Bell (1994)

Yassir and Bell (1994) approached the pore pressure - stress relationship in terms of overpressure resulting in an increase in the minimum *in-situ* stress, S_h. Similarly, under-pressures result in anomalously low S_h values. Observations from the Scotian Shelf, offshore eastern Canada, show good relationships between stress magnitudes, stress orientations and pore pressures. In the region, the deep lying basal Jurasasic-age Argo salt acts as a detachment surface thus isolating the Mesozoic and Tertiary sediments overlying it from crustal *in-situ* stresses below. The salt body is around 2 km thick and overlies the horsts and grabens of the pre-Jurassic Scotian Basin.

Above the Argo salt, P_p in the area is hydrostatic down to about 4000 metres where top overpressure occurs. Just above top overpressure, S_h rapidly increases and approaches S_V. Paucity of borehole breakouts within the overpressured zone also indicates a lower horizontal stress anisotropy below this depth. Stress rotation is also observed in association with the top of overpressure. The stress orientations now parallel overpressure contours having rotated out of alignment with the older listric faults. Yassir and Bell (1994) state that neither tectonic shear nor disequilibrium compaction can account for the overpressure development. They believe it to be associated with the cracking of gas and hydrocarbon generation. It is believed that as hydrocarbons mature they change phase from a solid to a fluid, a consequence being an alteration of the Poisson's Ratio of the rock. Lateral constraints on the basin allow a poro-elastic (see Engelder & Fischer, 1994 below) response of stress to overpressuring and the increase in Poisson's Ratio due to oil and gas generation alters the rheology of the sediment. This rheological change induces an increase in the horizontal stresses relative to the vertical stress. The result would be that the triaxial stress situation heads towards being closer to isotropic.

2.2.1.6 Miller (1995)

Miller (1995) states that in a laterally constrained basin the magnitude of S_h is controlled by parameters other than just S_V, the Biot coefficient (α) and the pore pressure. The Biot coefficient is a parameter that is inversely proportional to the ratio of the stiffness of the framework of a particular rock and the bulk stiffness of all of the solid components that make up the rock (Engelder, 1993). Given a situation where horizontal strain is zero, the horizontal effective stress, σ_h, is also related to the vertical effective stress (σ_V), mass inflow and temperature:

$$\sigma_h = \frac{1}{1-\nu}\left[\nu\sigma_V - \omega\left(P_p - \alpha K_S T\right)\right] \qquad \textit{(equation 2.9)}$$

Where: ν = Poisson's Ratio;

ω = variable relating whole sediment modulus and sediment Poisson's Ratio;

K_S = bulk modulus of the rock grains;

T = temperature.

The effect of temperature in *equation 2.9* is to change the rock framework (assuming a certain stiffness and stress state) by changing the volume of rock grains when there is a change in temperature. The level of stress increase depends on the magnitude of the change in temperature and the thermal expansion coefficient of the solid grains. An illustration of the effect of temperature is what Miller (1995) calls "*hydraulic shrinkage fractures*" (see explanation below in **section 2.3.3**).

2.2.1.7 Grauls (1997 & 1998)

Work by Grauls (1997) uses LOP data to determine the evolution of S_3 as a function of depth for different geographical regions. Trends were determined using in-house data from Angola, Nigeria, Cameroon, Malaysia and Brunei as well as published data sets from eastern Canada (Bell, 1990), the UK Central North Sea (Gaarenstroom *et al.*, 1993) and the US Gulf Coast (Breckels & van Eekelen, 1982).

Moving on from the use of LOPs to produce a lower bound to LOPs proxy for S_3, Grauls (1998) tackles the prediction of S_3 from a different perspective. He points out that relationships between stress and overpressure resulting from causes other than disequilibrium compaction (e.g. tectonic stress, inflationary mechanisms etc.) are not

necessarily straightforward to quantify. He proposes a hydromechanical approach linking overpressure magnitude with the tectonic regime encountered at depth. Part of his argument is that the tectonic stress situation influences the overpressure increase as opposed to overpressure increasing stress (cf. Engelder & Fischer, 1994 in **section 2.2.2.3**).

Grauls (1998) used observed magnitudes of S_3 in different tectonic regimes to develop a power-law relationship for S_3 magnitude using depth and a power-law exponent, n, which is dependent on whether the tectonic regime is extensional, strike-slip or compressive:

$$S_3 = S_3^{sf} + 0.0055(Z - Z^{sf})^n \qquad \textit{(equation 2.10)}$$

Where: S_3 = minimum principal stress at depth Z (MPa);

S_3^{sf} = pressure of the overlying water column of height Z^{sf} (MPa);

Z = vertical depth referenced to sea level (m);

Z^{sf} = water depth (m);

n = exponent of the power-law function (dependent on tectonic regime).

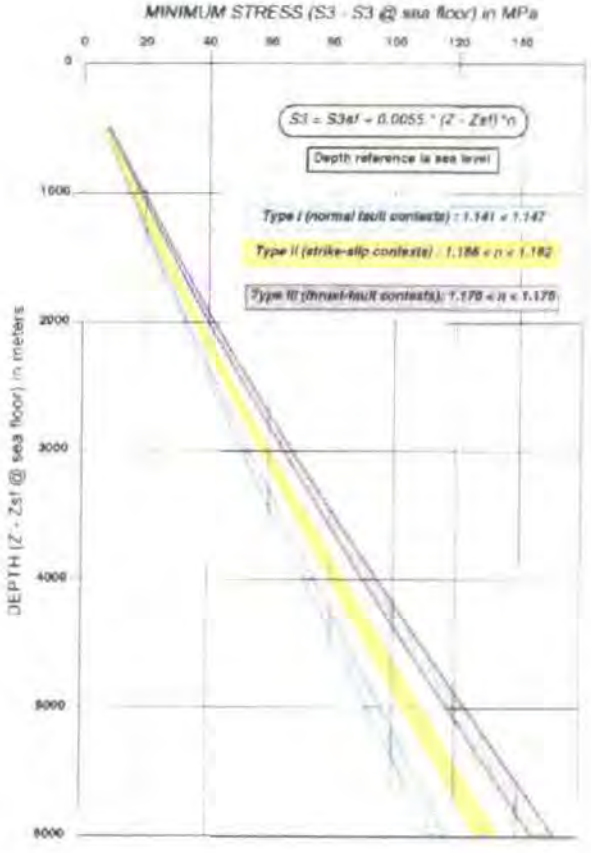

Figure 2.2: The evolution of the minimum principal stress as a function of depth and tectonic regime (from Grauls, 1998).

The results of applying *equation 2.10* can be seen in **Figure 2.2** (from Grauls, 1998) which shows how minimum stress evolves with depth for each tectonic setting. Because the method does not rely on knowledge of the P_p at depth, *equation 2.10* can be applied to "*different geological settings, for various facies and is particularly well suited to high pressure domains and confined settings*" (Grauls, 1998). The approach is tested on data from Offshore Brunei and the South China Sea (Grauls, 1997). Grauls (1998) also uses this theory to explain stress and P_p changes seen in the Central North Sea.

2.2.2 Methods assessing the contribution of pore pressure to stress

2.2.2.1 Hillis (2000 & 2001b)

Hillis (2000 & 2001b) describes the phenomenon of pore pressure *in-situ* stress (P_p-S_h) coupling and provides good summaries of the work of previous authors. For this reason it is felt that a review of Hillis' (2000 & 2001b) work is a good place to start this section.

Where overpressure exists, so the magnitude of *in-situ* stress is often observed to be greater at a given depth than would be expected if the fluids were normally pressured at that depth. Coupling is inferred to be occurring where an increase or decrease in P_p results in a change in the total minimum horizontal stress that is proportional to, but less than, the change in P_p magnitude. Hillis (1998a) quotes a number of examples including the Central North Sea, Scotian Shelf of Canada and the Australian Northwest Shelf to show that S_h increases by 60-80% of the rate of increase in P_p at the basin scale. Conversely, using the Ekofisk field data compiled by Teufel *et al.* (1991) he illustrates how S_h has decreased at approximately 80% of the rate of P_p depletion during the twenty-year production of the field (Hillis, 2001b). By calculating the change in S_h with a change in P_p ($\Delta S_h/\Delta P_p$) for an individual field or basin, the magnitude of S_h can be calculated when the P_p is known. Zoback and Healy (1984) and Engelder and Fischer (1994) describe examples of mechanisms of P_p-S_h coupling.

2.2.2.2 Zoback and Healy (1984)

Zoback and Healy (1984) explain that frictional sliding along a pre-existing fault plane can be expected to occur if the shear stress along the fault plane, τ_f, equals the frictional resistance to sliding, μS_n. For unfractured rock, the relationship linking these parameters is known as the *Coulomb-Navier failure criterion*:

$$\tau_f = C_O + \mu S_n \qquad \textit{(equation 2.11)}$$

Where: τ_f = failure stress;

C_o = cohesive strength (the strength of the rock in compression);

μ = coefficient of static friction;

S_n = normal stress.

Where a pre-existing fracture occurs, the cohesive strength component is removed, since $C_o = 0$, and μ becomes the coefficient of *sliding friction* (Sibson, 1985). Zoback and Healy (1984) claim to be able to predict S_3 given any tectonic regime or fault type as long as the coefficient of sliding friction is not too great as to inhibit motion and the fault plane is "favourably orientated" to allow slippage. For "favourably orientated" fault planes, the ratio of maximum to minimum effective stress (σ_1:σ_3) at which slipping will occur is a function of μ (Jaeger & Cook, 1979; Zoback & Healy, 1984):

$$\frac{\sigma_1}{\sigma_3} = \frac{S_1 - P_p}{S_3 - P_p} = \left(\sqrt{\left(\mu^2 + 1\right)} + \mu\right)^2 \qquad \textit{(equation 2.12)}$$

Where: S_1 = maximum principal *in-situ* stress;

S_3 = minimum principal *in-situ* stress.

If the σ_1 to σ_3 ratio is less than the function of μ then all faults should be stable and no slippage will occur. If the ratio is exactly this value, slip will only occur on "favourably orientated" fault planes; all other faults will be stable. Laboratory measuring of μ shows that it varies between 0.6 and 1.0 for the majority of rock types. Using a suitable value of μ and measurements of maximum stress (S_V for a normal fault regime) and P_p can give estimates of S_3 (S_h for a normal fault regime).

2.2.2.3 Engelder and Fischer (1994)

Engelder and Fischer (1994) explain that there are situations around the world where the minimum horizontal stress is greater in overpressured zones than in normally pressured zones at equivalent depths. They attribute this to a P_p-induced deformation of the grains called poro-elasticity. This behaviour explains how a lithified, porous rock (**Figure 2.3a** from Engelder, 1993) deforms when the pore space is filled with fluid and pressurised (**Figure 2.3b**

from Engelder, 1993). The mechanism relies on a basin being confined (unable to laterally expand) meaning the pressure of the pore fluid on the grains contributes solely to S_h. For a given increase in P_p (due to disequilibrium compaction) there is a proportional yet reduced increase in the magnitude of the S_h (**Figure 2.3b**). The approach does not rely on the action of friction or the addition of overburden.

According to poro-elastic theory, a dilation, ΔV, of the rock with initial volume V is induced by an increase in pore pressure, ΔP_p, as given by:

$$\frac{\Delta V}{V} = \alpha\beta\Delta P_p \qquad \textit{(equation 2.13)}$$

Where: α = the Biot coefficient of effective stress;

β = the compressibility of the rock.

Lateral confinement means the volume strain is zero so when the compressibility β is $(1/V)(\Delta V/\Delta P_c)$, *equation 2.13* may be re-written to describe the confining pressure, ΔP_c, as:

$$\Delta P_c = \alpha\Delta P_p \qquad \textit{(equation 2.14)}$$

It can be seen from *equation 2.14* that in a situation where $\alpha < 1$ a change in P_p will produce a smaller change in P_c. An exact equation for the rate of change of S_h with a change in P_p can be derived from equation for total S_h under uniaxial strain conditions:

$$S_h = \frac{\nu}{1-\nu} S_V + \alpha\frac{1-2\nu}{1-\nu} P_p \qquad \textit{(equation 2.15)}$$

Where: ν = the drained Poisson's Ratio.

Re-writing *equation 2.15* to account for a change in S_h with a change in P_p gives:

$$\frac{\Delta S_h}{\Delta P_p} = \alpha\frac{1-2\nu}{1-\nu} \qquad \textit{(equation 2.16)}$$

Engelder and Fischer (1994) used data from the Central North Sea Graben to support their theory.

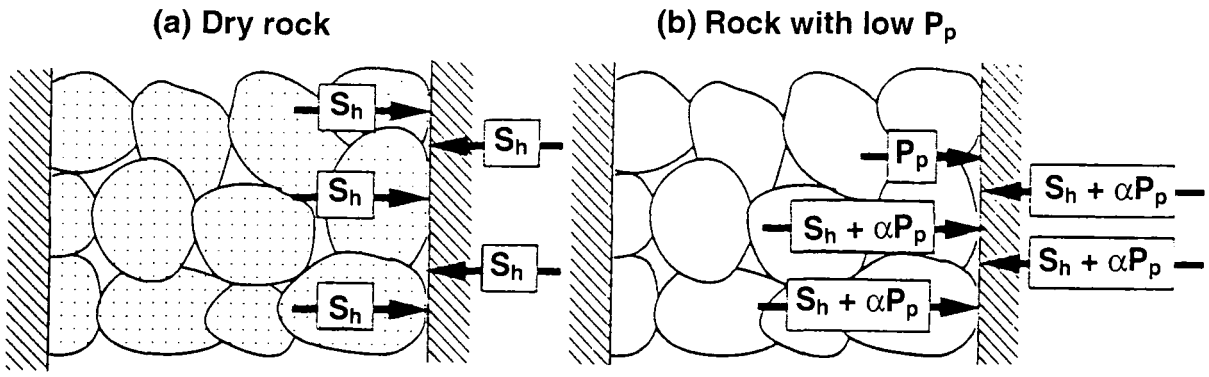

Figure 2.3: The effect of changing P_p on the total stress exerted by a rock against the rigid walls of a container: **(a)** dry rock; **(b)** rock with pore fluid at pressure = P_p (from Engelder, 1993).

2.2.3 Conclusion

Knowledge of regional and local stress magnitudes through knowledge of the lower bound to LOPs yields important information for different aspects of drilling, production and exploration in oil and gas areas. Stress influences amongst other things: borehole stability, sand production, reservoir performance, migration and accumulation and retention of hydrocarbons (Borgerud & Svare, 1995). Coupling is also important because where a relationship between pore pressure and minimum *in-situ* stress is established, knowledge of one parameter can be used to make assumptions about the other.

2.3 Fracture Mechanics: The theory behind rock hydraulic fracture

The development of hydraulic fractures has important implications for the petroleum industry. Hydraulic fractures can regulate the maximum fluid pressure through cyclic opening leading to pressure dissipation and closure which allows pressure build up. The presence of fractures will affect the distribution of oil and gas in sedimentary basins by influencing fluid flow. Linkage of hydraulic fractures means they can potentially act as migration pathways for these fluids.

2.3.1 Introduction to stress notation

Stresses can be represented in 2-dimensional space using Mohr diagrams (**Figure 2.4**). The stress ellipse indicates that the magnitudes of normal (S_n) and shear stresses (τ) experienced by a plane when it is subjected to compression change progressively with the orientation of the plane. Compressive stresses are more common in the Earth than tensile stresses due to the weight of the overlying rocks, the overburden.

Mohr diagrams show the relationship between the maximum (S_1) and minimum (S_3) of the three *principal stresses*. The principal stresses are stresses that act perpendicular to one another (**Figure 2.5**). Planes parallel and/or orthogonal to the principal stresses will have no shear stresses on them. Instead, such planes will have solely normal stress components and do not experience shearing. These planes are referred to as *principal planes*. For a given stress, the Mohr diagram shows the normal and shear stress components on planes of all possible orientations relative to a set co-ordinate system through a point plot on a circle called the *Mohr circle* (Twiss & Moores, 1992).

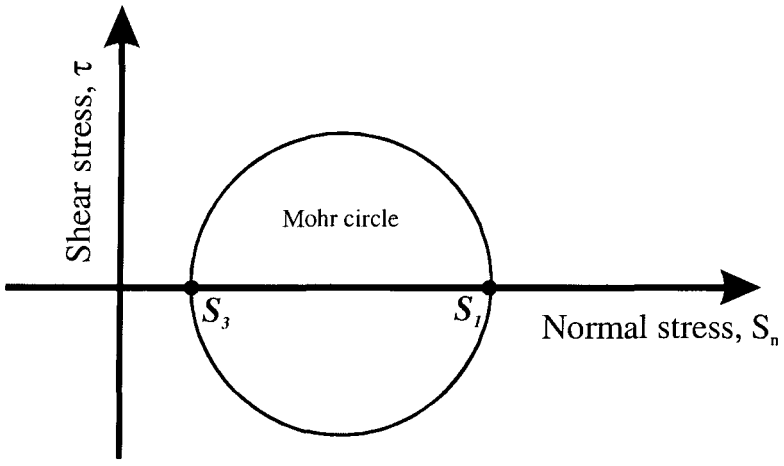

Figure 2.4: Mohr diagram showing the relationship between the maximum and minimum principal stresses.

The Mohr diagram shows more than just the relationship between S_1 and S_3. Of more importance to this work is the magnitude of the *differential stress at failure*, S_d, of the rock. This is also referred to as the *ultimate strength*. The magnitude of the ultimate strength can be calculated from the magnitudes of S_1 and S_3 in a situation where the Mohr circle touches the failure envelope (see **Figure 2.6**):

$$S_d = S_1 - S_3 \qquad \textit{(equation 2.17)}$$

In terms of the most common stress-state in the Earth, namely an extensional system, the ultimate strength is defined by the difference between the vertical S_1 and the horizontal S_3:

$$S_d = S_V - S_h \qquad \textit{(equation 2.18)}$$

Where: S_V = overburden (vertical) stress;

S_h = minimum horizontal stress.

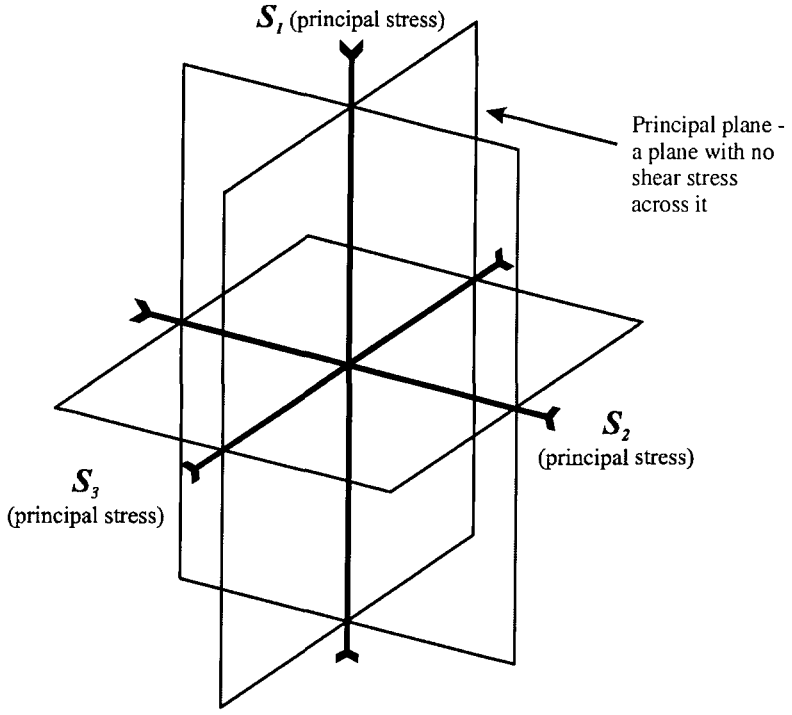

Figure 2.5: The principal stresses and the principal planes.

The magnitude of the vertical stress is generally constrained by the weight of the overlying rocks and fluids. Minimum horizontal stress (S_h) is constrained by the ultimate strength of the rock to remain within definite limits of S_V (Engelder, 1993). A rock subjected to a large differential stress will not be able to sustain this "awkward" stress-state (where S_h is so much less than S_V) and responds by deforming or failing (Engelder, 1993). The ultimate strength is thus a governing factor in keeping S_h within certain bounds. In an extensional or strike slip system, because S_h is the minimum of the principal stresses, it is this stress that is overcome when a rock fails. An extensional system is the most straightforward to understand ($S_V = S_1$ and $S_h = S_3$) so we shall use this as the example situation. Failure in this situation occurs when S_h is exceeded during, for example, the performance of a leak-off test.

As **Figure 2.6** illustrates, if the confining pressure increases (the Mohr circle shifts to the right), so the differential stress is able become larger before S_d is reached. In terms of a laboratory compression test, the confining pressure is the pressure of the fluid surrounding the sample. This fluid produces a pressure magnitude that is described in Mohr terms as being that of S_3. Increasing the magnitude of the differential stress will increase the size of the Mohr circle. As long as the circle remains below a certain size, the differential stress is *less than* S_d, the rock will be stable and it will not fail in shear. However, if the boundary of the circle crosses the *envelope of shear failure* then shear failure occurs. For unfractured rock, the envelope of shear failure is defined in terms of the cohesive strength (C_o) and the coefficient of friction (μ). The intersection of the envelope with the τ-axis occurs at the value equal to C_o in the Coulomb-Navier failure criterion (*equation 2.11*) and the gradient of the envelope, ϕ, is equal to $\tan^{-1} \mu$. Every lithology has its own envelope of shear failure because different lithologies have different coefficients of friction and cohesive strengths.

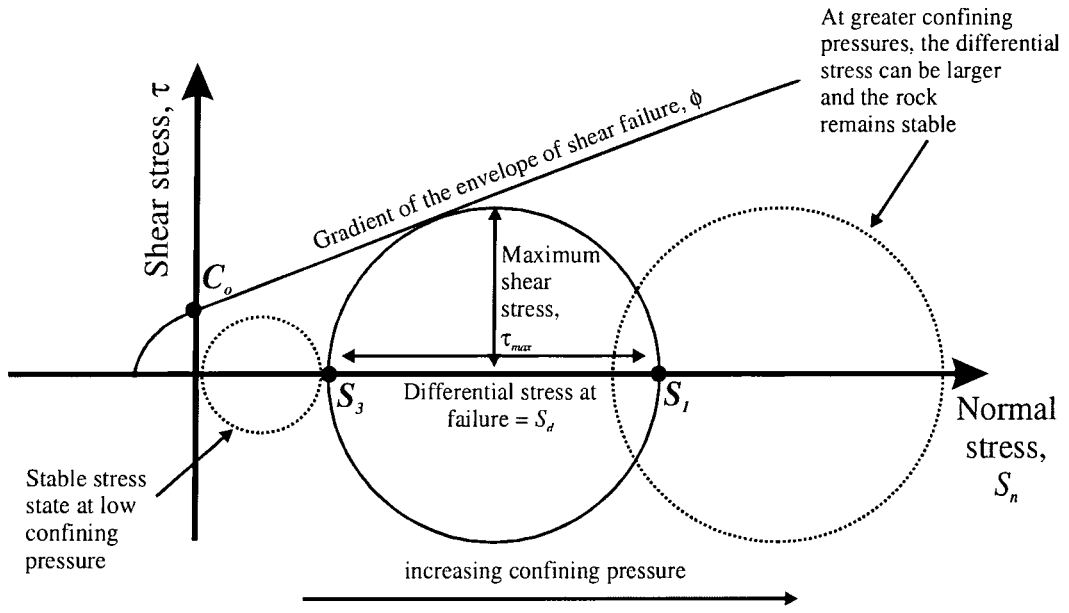

Figure 2.6: Mohr diagram showing the envelope of shear failure and stable and unstable stress situations.

Shear stresses will occur across a plane that is inclined at an angle to the principal stresses, in other words across all planes bar the three principal planes shown in **Figure 2.5**. Within the principal planes, because there is no shear stress development, the rock will not develop shear fractures along these planes. This is shown on a Mohr diagram where the intersection of the Mohr circle and the S_n-axis occurs at $\tau = 0$. Converse to this, shear stress reaches its maximum (τ_{max}) at a certain value of S_n such that:

$$\tau_{max} = \frac{S_1 - S_3}{2} \qquad \textit{(equation 2.19)}$$

From *equation 2.19*, τ_{max} is equal in magnitude to the radius of the Mohr circle and is half the value of the ultimate strength, S_d.

Most of the work relating to the Mohr diagram involves the failure of rocks by shearing when compressive stresses are applied to them. However, the field to the left of the τ-axis is the region of hybrid and tensile failure (**Figure 2.7**). If the envelope of shear failure is extrapolated back to the left of the τ-axis (dashed line) to where $\tau = 0$ then it appears that purely tensile failure only occurs when the differential stress is zero, i.e. when the Mohr circle is a point. Real failure in pure tension occurs at a point on the S_n-axis before the linear shear envelope touches the S_n-axis. This is because the failure envelope is drawn for *shear* failure and is thus not really applicable in the tensile failure field.

Fracturing experiments have shown that a more realistic scenario involves the use of a parabolic (curved) failure envelope (solid line in **Figure 2.7**) in the tensile field (Murrell, 1971). A curved failure envelope is believed to be more realistic because rocks contain microscopic flaws called *Griffith cracks*. The presence of these Griffith cracks weakens the rock meaning it is not as strong in tension as a linear failure envelope would predict it to be (Phillips, 1972). The curved failure envelope means the Mohr circle can be drawn with a finite size and a differential stress *does* exist for purely tensile fractures. Natural hydraulic fractures in sedimentary basins tend to be of the hybrid or tensile variety for the simple reason that the differential stress ($S_1 - S_3$) in basins is *low*. If the differential stress was not low then it would not be possible to use leak-off tests (where tensile fractures are developed) to predict S_3.

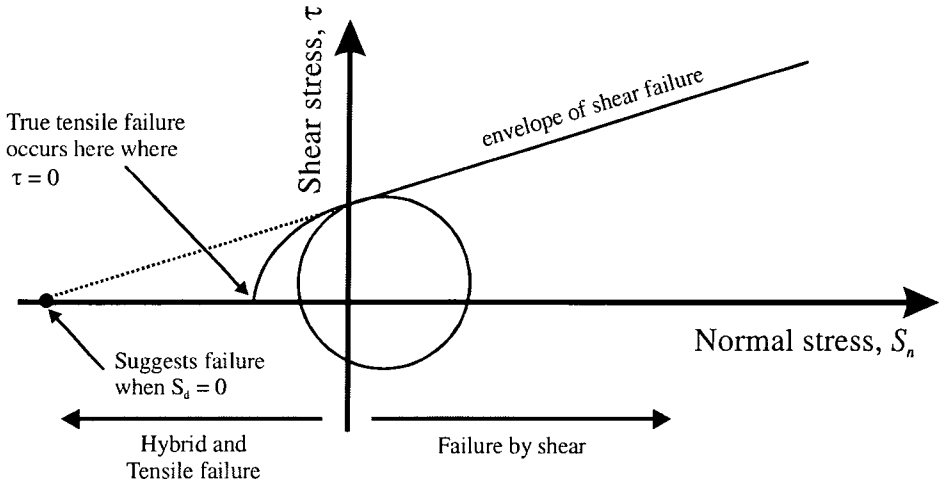

Figure 2.7: Mohr circle showing the regions of tensile and shear failure.

2.3.2 The stress around a borehole

2.3.2.1 Tangential (or hoop) stress

Assuming a 3-dimensional block of rock with elastic properties whose thickness is unity, applying a remote stress, S_r, will mean that all planes within the block orthogonal to S_r will experience the same amount of stress (**Figure 2.8**). For simplicity it is also assumed that the block is homogeneous and isotropic, the boundaries of the block are infinite distances apart and it is in equilibrium. If the assumptions are upheld, the response of all parts of the block in the direction of the compressive force, the applied S_r, should be the same.

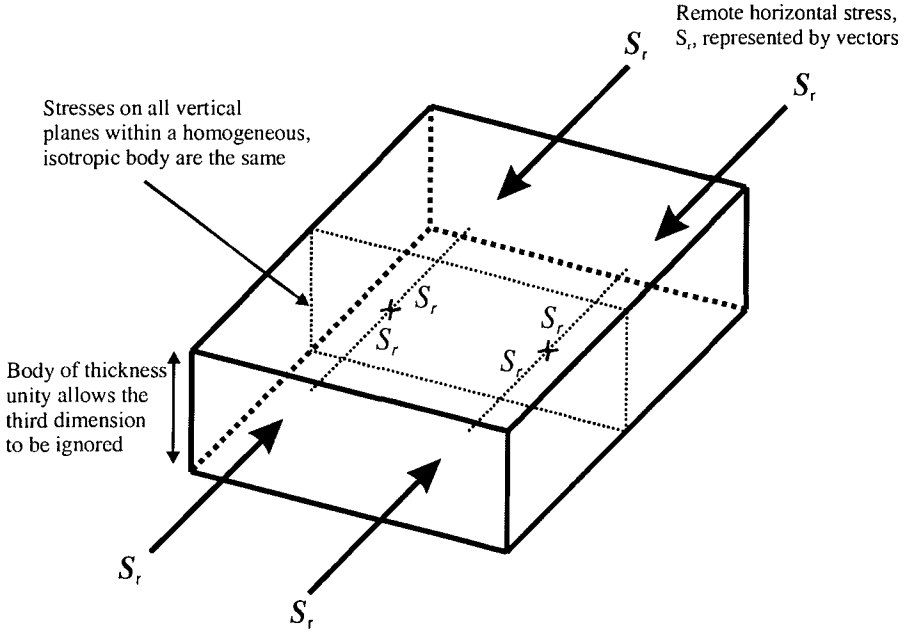

Figure 2.8: The effects of applying a remote stress to a homogeneous, isotropic, elastic block.

In a situation where there is a hole in the block (i.e. a borehole - **Figure 2.9**) then the *local* stress situation becomes more complicated due to a phenomenon called the *tangential* (or *hoop*) *stress*. Only the local stress, S_L, is affected by the presence of the borehole. The far field (remote stress) originates too far away for it to be effected. The first analysis of the hoop stress phenomenon was done by Kirsch (1898). Inglis (1913) modified Kirsch's original equations and was able to show that stress concentrations around a hole depend on its shape. Concentrations depend on the ratio of the borehole long axis (the c-axis) and short axis (the b-axis) when viewed in cross-section. Inglis (1913) showed that when S_r, is directed parallel to the b-axis, maximum stress concentrations occur at the tips of the c-axis:

$$S_L = S_r(\frac{2c}{b} + 1) \qquad \textit{(equation 2.20)}$$

Where: S_L = local stress concentration (hoop stress);

S_r = remote stress.

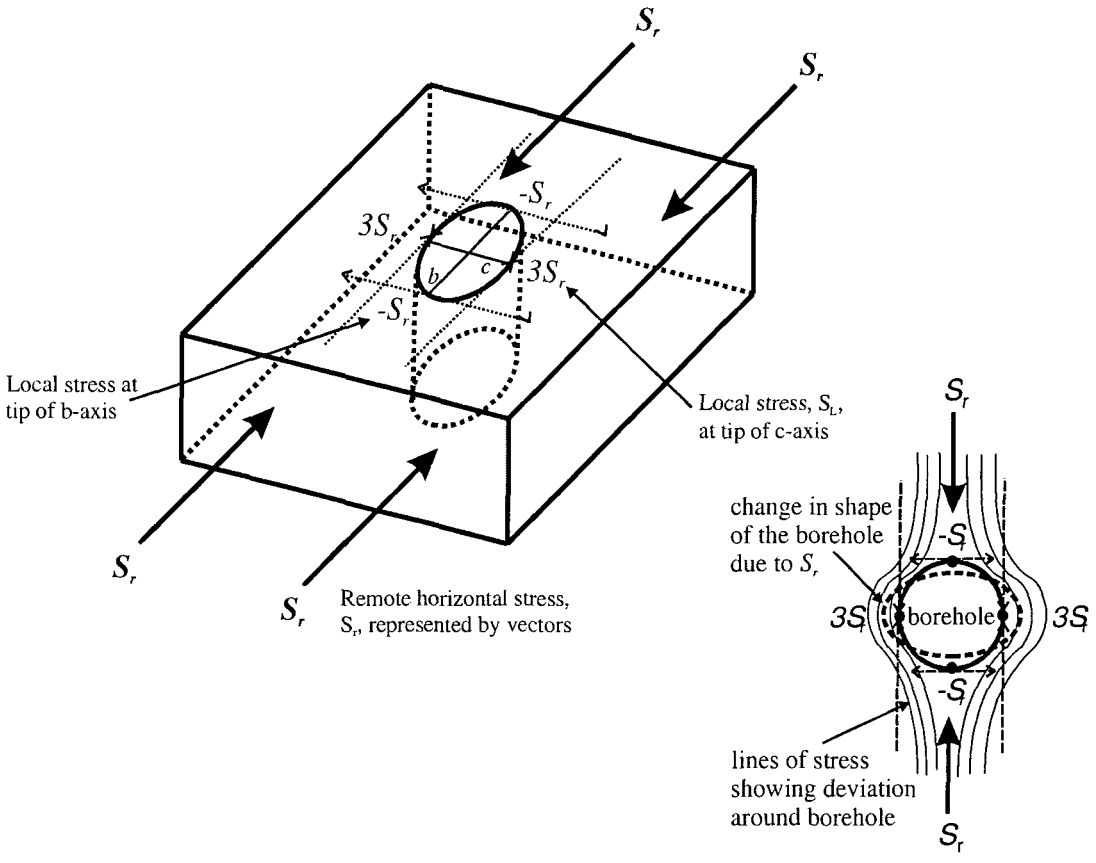

Figure 2.9: The effects of a wellbore on stress. Dashed arrows represent hoop stresses in the direction of, and orthogonal to, the remote stress at the tips of the b- and c-axis. Also shown is a representation of how S_r deviates around a borehole (from Jaeger & Cook, 1979).

No increase in S_L magnitude occurs at the tips of the b-axis because the borehole acts to deflect S_r around itself. The remote stress hits the tip of the b-axis orthogonal to the borehole wall. As the borehole acts as a *half space*, there is no hoop stress developed in the direction of the b-axis. **Figure 2.9** (from Jaeger & Cook, 1979) shows the stress at the tips of the b-axis has a magnitude of $-S_r$. This reflects the effective tension that occurs where S_r is "bent" around the hole and where the hole compresses in the b-axis direction as S_r is applied. The borehole also extends parallel to the c-axis as a consequence of the applied $-S_r$. The minus sign indicates a convention where tension is considered negative and compression is positive. **Figure 2.10** shows the decay of the local stress away from the borehole wall. The

graph plots the stress concentration along the line of the c-axis and shows that within the borehole itself, stress is zero because the borehole acts as a half space. At the edge of the borehole, S_L has a maximum value of $3S_r$ whilst at a distance of infinity away from the hole, S_L approximates the value of the remote stress. Inglis (1913) also discovered that the decay of the local stress with distance away from the borehole is proportional to the diameter of the borehole. For larger holes, the distance that is required for S_L to decay back to the magnitude of S_r is greater (Jørgensen & Fejerskov, 1998).

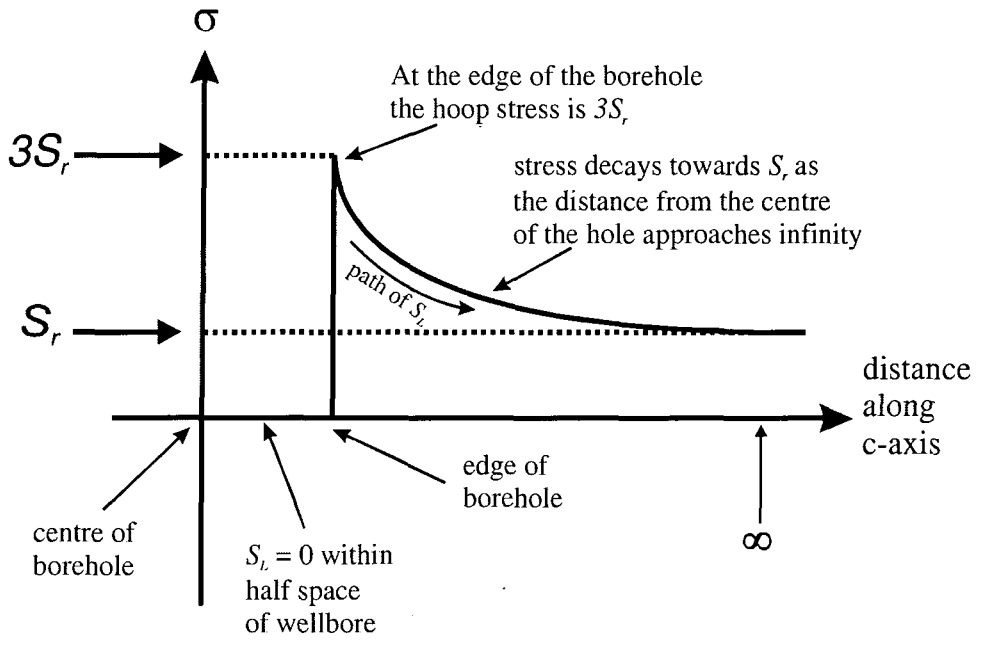

Figure 2.10: Schematic representation of the decay of hoop stress away from the centre of a wellbore in an elastic body. The rate of decay of S_L depends on the diameter of the wellbore.

Inglis (1913) also applied his work to cracks whose shapes can be approximated by ellipses with a b- and c-axis. He showed that cracks can have dimensional ratios of c:b in the region of 5000:1 and hence the hoop stress (S_L) at the tips of the c-axis can reach ten thousand times the magnitude of S_r. Hoop stresses of this size show that rocks are immensely strong in compression orthogonal to cracks and huge concentrations of stress are required at the tips of these cracks before propagation occurs.

2.3.2.2 Borehole stability

In a uniaxial compression experiment S_3 is zero; the rock is unconfined. From this situation the *uniaxial compression strength* of the rock can be determined. In Mohr terms, this is the maximum S_1 value the rock can sustain before the Mohr circle touches the envelope of

failure and shear failure occurs. However, as shown by the Inglis (1913) equation, drilling a borehole in a rock leads to hoop stress concentrations around its wall. The result is that the stress concentrations at the tip of the c-axis of the hole can exceed the uniaxial strength of the rock and induce fractures. This means that a rock with a borehole in it subjected to a uniaxial stress *lower* than the uniaxial compression strength of the rock can still fail by shear. Failure leads to a change in shape of the hole that is known by drillers as a *borehole breakout*. Borehole breakouts lead to elongation of the hole parallel to the minimum horizontal stress and orthogonal to the maximum horizontal stress. Thus, it is the stress concentration around the borehole that causes a breakout not the outright stress magnitude in the rock.

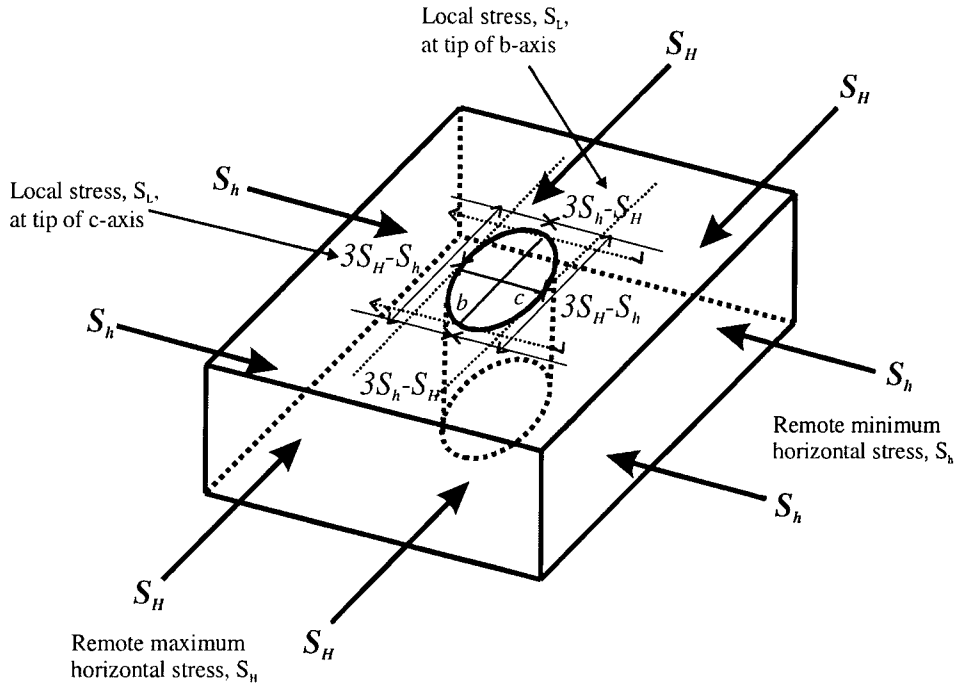

Figure 2.11: Superposition of the maximum and minimum horizontal stresses around a wellbore in an elastic body. Dashed arrows represent the magnitude of the local hoop stress.

Of course uniaxiality is not a realistic stress state in the Earth as there are always three resolvable orthogonal stresses acting on buried rock so S_3 is never zero. This means the *principle of stress superposition* needs to be adopted. Superposition considers the affects of the two horizontal stresses, S_H and S_h, on the borehole and resolves the stress magnitude at the tips of the b- and c-axis accordingly. **Figure 2.11** shows an example where the two horizontal stresses, S_H and S_h, act on the borehole. In the direction of the b- and c-axis the local stress concentrations, S_L, have been resolved. The net effect of having two orthogonal compressive stresses acting on a borehole is that the magnitude of S_L at the tips of the b- and c-axis is *lower* than the S_L value for only one stress. In other words smaller horizontal stress anisotropies mean borehole breakouts are less likely to occur.

2.3.3 Hydraulic fracturing of rocks

2.3.3.1 Introduction to fracturing

Fractures (from the Latin *fractus* meaning "broken") are surfaces along which rocks have broken. They are surfaces along which the material has lost cohesion. The relative motion that has occurred across the fracture surface during formation distinguishes the type of fracture in a rock (Twiss & Moores, 1992). Fractures may propagate by any one of three modes of displacement. Extensional mode (mode I) fractures form by separation of the crack walls without shear, under the action of tensile stresses (**Figure 2.12** redrawn from Engelder, 1993). Sliding mode (mode II) fractures propagate upon mutual shearing of the crack walls with the shear couple oriented in the direction normal to the crack front (**Figure 2.12** redrawn from Engelder, 1993). Tearing mode (mode III) fractures advance when the crack walls are subject to a shear couple aligned parallel to the crack front, as illustrated by **Figure 2.12** (redrawn from Engelder, 1993). A fracture that has components of displacement both parallel and normal to the fracture surface is an oblique extension fracture or mixed/hybrid mode fracture (Twiss & Moores, 1992).

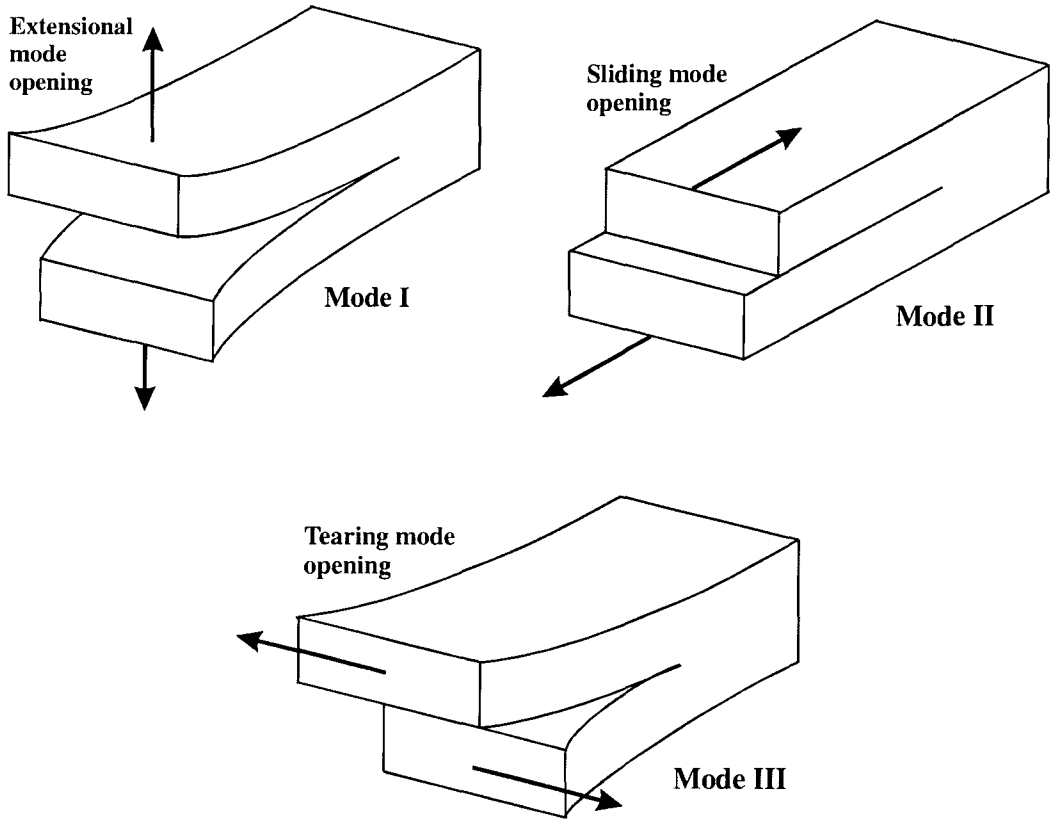

Figure 2.12: The three modes of rock fracture (redrawn from Engelder, 1993).

2.3.3.2 The orientation of fractures

The orientation of fractures is controlled by the orientation of the principal stresses. Purely tensional (mode I) fractures have orientations that are the most straightforward to predict. Tensional fractures open in the direction of the minimum principal stress (S_3) and propagate, or grow, parallel to the intermediate principal stress (S_2). Shear fractures (mode II and III) and those with a component of shearing and tensile opening (hybrid fractures) open at an angle to the principal stresses. Andersonian theory predicts that the optimum angle for shear fracture orientation is at 30° to the maximum principal stress (Anderson, 1905). More details on the orientation of faults and fractures relative to the orientation of the principal stresses are given in **section 2.6.1**.

2.3.3.3 Development of hydraulic fractures

Constraining the stress and P_p distribution in relation to depth and structural setting is of great importance in the petroleum industry. It is important to understand both the fluid retention capacity of a formation and the retention capability of faults. Knowledge of the P_p *in-situ* stress condition, with respect to depth and fault orientation, provides a valuable contribution to the evaluation of both natural and induced fluid migration and pressure distribution in faulted sedimentary basins (Arnesen *et al.*, 1997; Hillis, 1998b). Fluid pressure-related dynamic transfers (fluid expulsion) in overpressured sedimentary basins could be linked with brittle fault reactivation or shear fracture dilatancy and possibly hydraulic fracturing (Grauls, 1994 & 1998; Hillis, 1998a; Wang & Xie, 1998). These types of fracturing processes can effect the rheology and hydrology of the rock by altering fluid permeability (Simpson, 1998). Linking up of these networks of fractures enhances the permeability of the rock (Sibson, 1981). Sibson (1996) and Hillis (1998b) refer to these networks of fractures as "*structural permeability*" networks. The presence of these interconnecting networks provides a passage for primary migration of hydrocarbons from their source rocks (Miller, 1995). Secor (1965) was the first to suggest that excessive pore fluid pressures may be the cause of tensional fractures that form in a compressive regime. Many papers followed which, until recently, assumed that hydraulic fracturing occurred only at depths in excess of 3-4km (Miller, 1995). However, direct examination of sub-vertical, mineralised, tensional fractures in cemented cores from the Lower Cretaceous Travis Peak sandstone from east Texas by Laubach (1988) reveals evidence of intermittent fracturing and re-sealing. The evidence suggests an occurrence of episodic increases in P_p and fluid flow in the opened fractures. Based on $\delta^{18}O$ studies of the quartz cement, Laubach (1988) showed that these fractures formed at depths of only 900-1500 metres below the sea floor. Shallow fracturing can have

the effect of mobilising fluids throughout the entire basin with implications for hydrocarbon exploration assuming that fractures link up rather than remaining as distinct individuals.

Hydraulic fracturing occurs due to excess pore pressures. The process may occur on an autocyclic or episodic basis (Grauls, 1994 & 1997; Holm, 1998; Nashaat, 1998; Wang & Xie, 1998). This is similar to the cycling of stress build-up and release in relation to earthquake activity. Exceeding S_3 leads to a loss of fluid volume through fractures, a reduction of P_p and possible closure of the fractures. As reported by Bredehoeft *et al.* (1994), the process of pressure build-up is slow in comparison to the sudden pressure decline when hydraulic fractures are created and fluid expulsion takes place. Modelling overpressures created by oil generation in the Uinta Basin, Utah, Bredehoeft *et al.* (1994) show how pore pressure can build up to approximately 80% lithostatic levels in about 10,000 years. At that point fractures are created in the reservoir resulting in an abrupt decline in pressures. Following this, sufficient fracture permeability is established and the magnitude of overpressure stabilises at a level of approximately S_3.

Rock mechanical properties such as cohesion and tensile strength as well as the differential stress influence the occurrence of hydraulic fracturing (Grauls, 1998). If, as proposed, the minimum *in-situ* stress (S_3) regulates the development of hydraulic fractures, it also provides an indication of the maximum P_p to be encountered at the top of compartmentalised structures (permeability barrier isolated volumes of rock containing pore pressures of similar magnitude). Knowledge of S_3 is therefore important in the prediction of abnormal pressures, in hydro-mechanical modelling of the control of P_p by *in-situ* stress conditions (Grauls, 1997 & 1998) as well as predicting lost circulation zones and optimising drilling plans (Singh & Emery, 1998).

Miller (1995) proposes an alternative mechanism for P_p-induced fracturing. These fractures occur in any tectonic setting and depend only on a uniform P_p that developed in response to geological processes. Hence they will remain open on the same geological time scale that governs these processes. Other than governing their orientation, they do not require stress differentials to prop them open. Miller (1995) calls these fractures "*hydraulic shrinkage fractures*" because they form to accommodate the strain caused by P_p-induced compression (shrinkage) of the host rock grains. As an analogy, these types of fractures are formed in the same way as fractures that occur upon cooling (Miller, 1995). As the fluid pressure becomes overpressured, the vertical inter-granular stress is reduced because the pore fluid carries more of the total overburden load, which remains constant. The horizontal inter-granular stress decreases because both the vertical inter-granular stress and the grain size decrease, where as the overall horizontal strain is zero. If the P_p increases enough, tensile inter-granular stresses develop and shrinkage fractures will form (Miller, 1995). The process is mechanically stable in the sense that grain shrinkage does not depend on P_p gradients from the open fracture to the host rocks pores and provides space for fractures to

open even when overall lateral deformations are constrained. Vertical fractures tend to be more commonly formed and can occur at lower magnitudes of P_p in less compressible rocks buried in basins with lower geothermal gradients (Miller, 1995). Vertical fractures are more common simply because S_3 is most often S_h.

The Mohr diagram can be used to illustrate the effects of increasing the P_p of a rock. For this to be illustrated, the x-axis displays the *effective* normal stress, σ_n, which is total stress minus P_p (cf. the *total* normal stress, S_n, in **Figure 2.6**). When an increase in P_p occurs, the Mohr circles shifts to the left along the x-axis. Assuming the most simplistic situation (that of a non-coupled system), increasing the P_p does not affect the radius of the Mohr circle. In other words, a pore pressure increase produces the same decrease in effective stress in all directions. In order for shear failure to occur the failure envelope (as defined by the Coulomb-Navier failure criterion) must become tangential to the Mohr circle. For dilational failure to occur, then the circle must cross the shear stress axis (τ or y-axis) and intersect the failure envelope where effective normal stresses are negative or tensional and shear stress is zero (Hillis, 1998a). Whether shearing or dilational failure occurs depends to a certain extent on the magnitude of the differential stress. At large differential stresses the circle tends to fail in shear before it fails in dilation. For dilational failure to occur, very small differential stresses are required and the Mohr circle must first intersect the failure envelope to the left of the τ-axis. It is therefore clear that for dilational failure due to overpressure to occur, there has to be a limit on the magnitude of differential stress (Hillis, 1998a).

Zoback and Healy (1984) consider hydraulic fractures to develop in a different way (see **section 2.2.2.2**). The mechanism considers rocks to be in a state of frictional equilibrium and imminent failure by shear. Fracturing occurs due to frictional slip on pre-existing planes of no cohesion so the progressive development of overpressure will always lead to frictional slip failure rather than dilational failure (Zoback & Healy, 1984). Hence if there are suitably orientated pre-existing faults of no cohesion, overpressure will lead to the development of frictional slip on these planes, and dilational failure is unlikely to occur. Therefore, following the Zoback and Healy (1984) model, hydraulically induced fractures are more likely to be created by shearing than by dilation. The suitable orientation of these pre-existing structures is controlled by the slope of the failure envelope – i.e. the coefficient of sliding friction, μ (Hillis, 1998a).

2.4 Pumping pressure tests ("leak-off tests")

2.4.1 Pumping pressure test terminology

Pumping pressure test theory and interpretation comes with a large number of often confusing abbreviations and acronyms. The most accurate determinations of minimum *in-situ* stress come from infrequently performed **MINI-FRAC TESTS**. These are mainly performed in the Gulf of Mexico region (Breckels and van Eekelen, 1982, used many of these data to determine their US Gulf Coast curve) yet are scarcely conducted in European regions. Most commonly performed are **LEAK-OFF TESTS (LOTs)** and these are frequently used by industry to estimate minimum *in-situ* stress despite their reliability being questionable due to the effects of stress perturbation around wellbores (Breckels & van Eekelen, 1982; Jørgensen & Fejerskov, 1998). More accurate are **EXTENDED LEAK-OFF TESTS (XLOTs)** where the performance is similar to the LOT but pumping continues after leak-off. XLOTs are often run as several cycles so tensile strength and frictional components are removed (Bredehoeft *et al.*, 1976). More detailed explanations of the testing procedure can be found below. **FORMATION INTEGRITY TESTS (FITs)** have little or no use in determining *in-situ* stress magnitudes as the test is halted prior to formation leak-off being achieved (Jørgensen & Fejerskov, 1998).

XLOT, LOT and FIT output graphs often display a collection of confusing terminology. **Figure 2.13** shows an idealised multiple cycle XLOT graph with the relevant acronyms:

LOP = The **leak-off pressure** and is described as the pressure where there is a break from linearity in the increase in down hole pressure with time or volume of mud pumped. This occurs because fractures are induced (during initial pumping cycles) or re-opened (during subsequent cycles) in the formation and mud escapes down these enhanced permeability conduits. This pressure may also be referred to as the **wellbore failure pressure (P_{wf})** during initial pumping cycles where fractures are created.

FBP = **Formation breakdown pressure**. It describes a breakdown in the formation accompanied by a sudden decrease in down hole pressure and stable fracture propagation.

Stable fracture propagation = All extra mud pumped into the wellbore is lost down the fracture. Allowing stable fracture propagation ensures the fracture extends beyond the zone of damage created by the drilling of the wellbore and stress perturbation effects into the undisturbed formation where the stress situation is that of the remote or far-field stress, S_r.

ISIP = The **instantaneous shut-in pressure** is measured after the pumps are stopped once the FBP is achieved. Following cessation of pumping, a sudden decrease in pressure occurs before the decline becomes more gradual. The change from sudden to

gradual decline is referred to as the ISIP and represents the situation where asperities in the fracture walls first touch. This value is considered a good estimation of the minimum *in-situ* stress, S_3 (Breckels & van Eekelen, 1982). In other instances, the engineer may choose to continue pumping beyond the formation breakdown allowing stable propagation of the fracture beyond the zone of damage. Pumping is halted when the engineer is satisfied that the fracture has propagated far enough from the wellbore to give a good estimate of S_r. This latter situation occurs during the performing of an XLOT (Jørgensen & Fejerskov, 1998). Both pressures are described as the being the ISIP.

FCP = The **fracture closure pressure**. This is picked using the double tangent method (**Figure 2.13**) and represents the pressure where fractures fully close and the permeability is no greater than that of the surrounding formation. Where this value can be picked, it is considered the best estimate of S_3. However, in many records, the difference between ISIP and FCP is small and the two values can be difficult to distinguish.

P_r = The **fracture re-opening pressure**. This pressure is analogous to the LOP but is only relevant in re-opening (second, third etc. runnings for XLOTs) cycles. It is picked in the same way as the LOP yet better approximates S_3 because the re-opening of fractures means the tensile strength component of the rock has been removed (Bredehoeft *et al.*, 1976; Engelder, 1993) as have frictional components and stress perturbations (Hillis pers. comm., 2001).

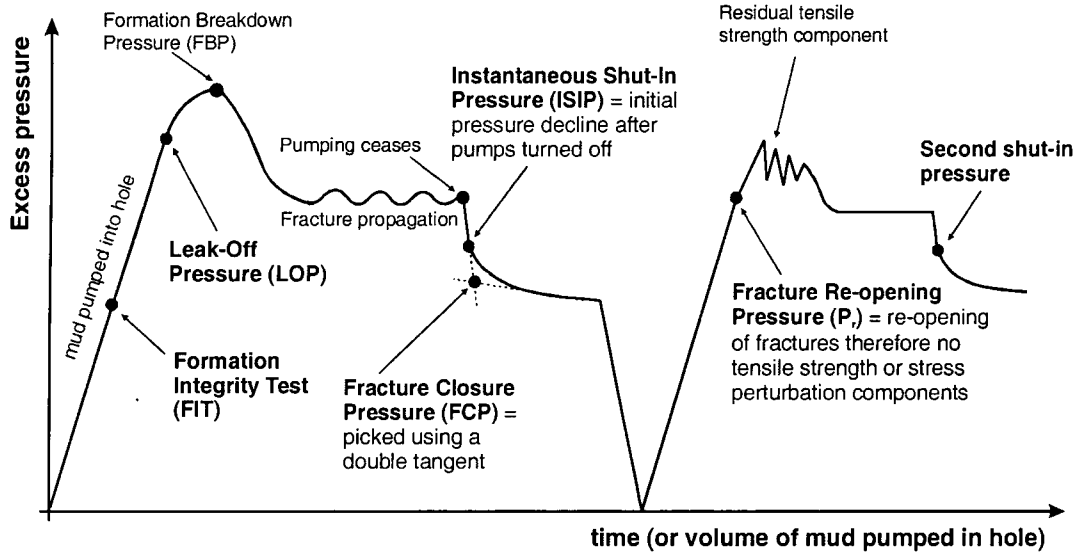

Figure 2.13: Idealised two-cycle XLOT showing FIT, LOP, ISIP and FCP.

2.4.2 The conducting of pumping pressure tests

The ideal way of determining stress is the **mini-frac test**. These tests are usually performed in the reservoir section of the well (Arnesen *et al.*, 1997). Stress measurements gained during these tests come from the fracturing of one to several metres of borehole using small volumes of drilling mud (Engelder, 1993). Mini-frac tests involve the isolation of an interval of wellbore so that drilling mud pumped in cannot migrate up or down the wellbore. For mini-fracs conducted over an interval of a couple of metres, two "*packers*" are tied together in an assembly called a "*straddle packer*". "*Packers*" themselves are rubber bladders inflated by pumping them full of water. A precise record of the mud pressure pumped into the injection interval is required during all phases of the mini-frac test. The most up-to-date technique uses wireline stress testing. Here, a pressure gauge actually in the injection interval transmits pressure-time data up the wireline direct to the surface in real time (Engelder, 1993). The apparatus used to perform a mini-frac is shown in **Figure 2.14** (from Engelder, 1993). Offshore mini-frac systems would consist of a drilling platform instead of the tripod and a drill-stem would replace the wireline and hydraulic hose.

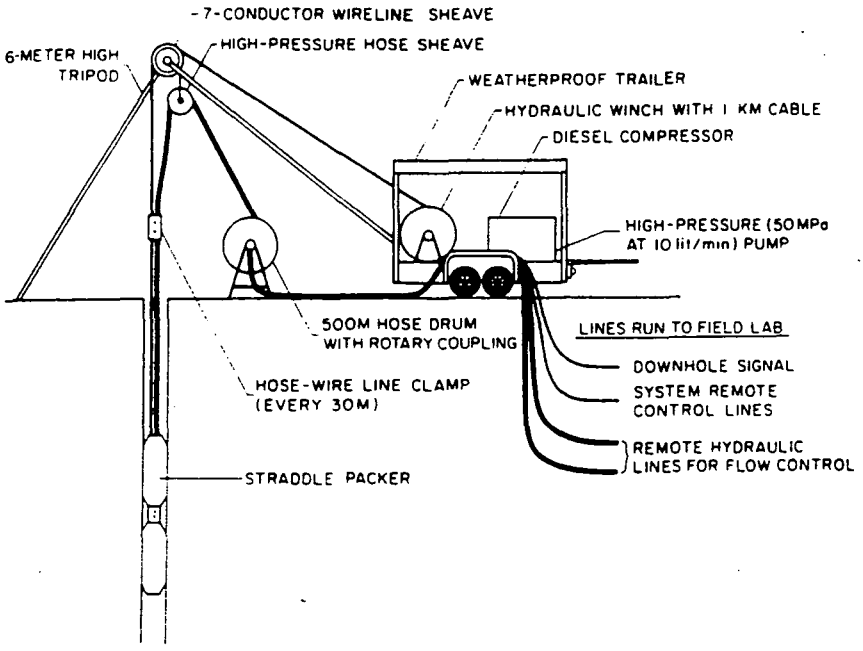

Figure 2.14: Diagram of a wireline hydraulic fracturing system. A "conventional" hydraulic fracturing system would consist of a drilling platform in place of the tripod and a drill rod in place of the wireline (from Engelder, 1993).

Unfortunately, mini-frac tests are rarely conducted, especially in Europe (Jørgensen pers. comm., 1999), so leak-off tests are used as methods of determining the S_3 magnitude.

The term *leak-off test* is collectively applied to all pumping pressure tests where the aim is to assess the fracture strength of the rock unit immediately underneath a newly set casing in a well (Bell, 1990). Such tests are conducted because drilling engineers need to know the maximum permissible mud weight that can be used without risk of damaging a well. Despite being designed to assess fracture strength, because they have many similarities to hydraulic fracturing (mini-frac) tests, pumping pressure tests are routinely used to predict magnitude (and orientation) of S_h at that particular depth (Jørgensen & Fejerskov, 1998). In many basin settings, S_h is the same as S_3 (as discussed above). Strictly speaking, pumping pressure tests are subdivided into **Formation Integrity Tests** (FIT), **Leak-Off Tests** (LOT) and **Extended Leak-Off Tests** (XLOT). Each of the three types of test is conducted in a similar fashion, the differences being the point at which pumping ceases and the number of pumping cycles. The basic technique involves drilling several metres beneath the base of a cement casing set in the bottom of the borehole and pumping in extra drilling mud while monitoring surface pump pressures for indications of formation breakdown. Pumping drilling mud into the borehole drives the pressure beyond that of the static mud column, resulting in elastic expansion of the hole. The increase in pressure with time continues in a sub-linear fashion until the rock passes its elastic limit and the leak-off pressure (LOP) is reached (**Figure 2.13**). At this point, the gradient of the pressure-time graph decreases as mud is able to escape into the formation in the open interval below the casing along pressure-induced "hydraulic" fractures (Engelder, 1993). Once leak-off has occurred, pumping is halted and the borehole fluid pressures are allowed to decay back to that of the static mud column (Bell, 1990). During XLOTs, pumping continues beyond the leak-off pressure and past the formation breakdown pressure (FBP) where the pressure in the borehole rapidly declines. Pumping continues beyond the FBP, usually for several minutes, to ensure stable hydraulic fracture propagation (**Figure 2.13**) into the undisturbed formation before the pressure is allowed to decay (Arnesen *et al.*, 1997). During this period of stable fracture propagation, the rate of flow of mud out of the borehole and into the fractures is equal to the rate of mud pumped. The wavy horizontal line in **Figure 2.13** indicates this. Pumps are then switched off and the mud drains into the fractures leading to a decrease in mud pressure in the hole. This continues until the instantaneous shut-in pressure (ISIP) is reached. At a pressure slightly lower than this is the fracture closure pressure (FCP). The main difference is that XLOTs are typically run as multiple cycle tests to ensure all effects of rock tensile strength are removed and the minimum *in-situ* stress (S_3) measurement gained is as accurate as possible (Fejerskov *et al.*, 1996; Hillis pers. comm., 2001). FITs (**Figure 2.13**) have little use in determining stress magnitude but instead are meant to test whether the wellbore can sustain the stresses expected during drilling and production (Jørgensen pers. comm., 1999). Therefore, the term leak-off test should really only be applied to tests where leak-off is evident (Jørgensen & Fejerskov, 1998).

The shortage of XLOT data (due to costs and the drilling engineers' reluctance to potentially damage the well) means LOP values from standard LOTs are commonly used for

calculations of the magnitude of S_3. LOP values themselves are useful indicators of the pressure required to create fractures, but better approximations are ISIPs and FCPs. LOPs usually only approximate S_3 because of the stress perturbation that occurs around the wellbore (Inglis, 1913; Engelder, 1993). During the first run of a pumping pressure test, if no pre-existing fractures are present, the pressure of wellbore failure is assumed to be:

$$P_{wf} = 3S_h - S_H - P_p + T \qquad \textit{(equation 2.21)}$$

Where: P_{wf} = wellbore failure pressure (the LOP);

S_h = minimum horizontal *in-situ* stress;

S_H = maximum horizontal *in-situ* stress;

P_p = pore pressure;

T = tensile strength of the rock.

For subsequent cycles run during an XLOT, Bredehoeft *et al.* (1976) amongst others suggest the Kirsch equation (*equation 2.21*) becomes:

$$P_r = 3S_h - S_H - P_p \qquad \textit{(equation 2.22)}$$

Where: P_r = fracture re-opening pressure;

S_h = minimum horizontal *in-situ* stress;

S_H = maximum horizontal *in-situ* stress;

P_p = pore pressure.

During fracture re-opening, the tensile strength component has been removed because initial formation rupture will not recur (Bell, 1990). Both *equation 2.21* and *equation 2.22* follow from the Kirsch equations (Kirsch, 1898) from rock mechanics. Both assume that the rock obeys Hooke's Law (it behaves elastically), that the borehole is circular without major breakouts and that there is no plastic zone surrounding the borehole (Goodman, 1980).

Once leak-off has been measured, pumping halts and the pressure is allowed to decay. This time is when the ISIP and FCP are determined (**Figure 2.13**). The ISIP corresponds to the inflection point on the pressure decay slope of the pressure-time graph (**Figure 2.13**). At a pressure slightly lower than this is the FCP when the fracture becomes impermeable to the mud. ISIP magnitudes are often chosen over FCPs because in many cases the inflection after pumping ceased is easier to pick than the FCP (**Figure 2.13**).

Because the ISIP and FCP are better estimates of S_3 than the LOP (Jørgensen & Fejerskov, 1998), combining them with the static mud pressure gives the best estimate of the minimum *in-situ* stress (Fejerskov *et al.*, 1996).

2.4.3 Stress determination from pumping pressure tests

The pressure decline following leak-off is not universally monitored as full LOTs and XLOTs are rarely conducted (Enever *et al.*, 1996). Therefore most determinations of S_3 rely on addition of the LOP value to the pressure exerted by the static mud column. Rock mechanical theory (see **section 2.4.2**) states that in order to create a new fracture, the tensile strength of the rock plus the stress perturbation must be overcome and this pressure is reflected in the magnitude of the LOP. Where full XLOTs are conducted, a pressure more analogous to S_3 comes from the ISIP or FCP that are ideally gained from later cycles in an XLOT. As stated above in **section 2.4.2**, when interpreting an XLOT graph the ISIP is easier to pick then the FCP and is therefore the choice approximation for S_3 of many authors (Breckels & van Eekelen, 1982; Arnesen *et al.*, 1997). The magnitude of minimum *in-situ* stress is calculated using:

$$S_3 = \left[pressure_{excess} + \left(weight_{mud} \times TVDKB \times 0.0981\right)\right] \qquad \textit{(equation 2.23)}$$

Where: S_3 = minimum *in-situ* stress (bar);

$pressure_{excess}$ = either LOP, ISIP or FCP (bar);

$weight_{mud}$ = weight [pressure] of static mud column (s.g.);

TVDKB = vertical depth relative to kelly bushing (m);

0.0981 = constant for converting to bars.

It is probable that uncertainties in the $weight_{mud}$ value used in *equation 2.23* arise as the pressure exerted at the depth of testing is surface derived. Errors in this pressure calculation could arise due to a number of factors. Rock spalling from the formation walls being included in the mud would alter the density if the mud were not circulated to remove these fragments. Fluid loss into the surrounding formations would increase the mud density and where tests are conducted without the use of a pressurised mud cap, the effect of air pressure adds to the mud pressure (Fejerskov *et al.*, 1996).

As well as the magnitude of S_h, the orientation of S_h can be determined from the hydraulic fractures created during LOTs. Hydraulic fractures open in the direction of S_h as this

is the easiest stress to overcome for it has the lowest magnitude at shallow depths and in laterally unconfined basins. Therefore hydraulic fractures propagate perpendicular to S_h and in the direction of S_H, the maximum horizontal stress.

2.5 Fracture gradients and lower bounds to leak-off pressures (LOPs)

A key requirement of drilling is the selection of a suitable mud weight. To prevent kicks during drilling operations it is necessary to maintain a mud weight that is slightly higher than the formation pressure. Using an appropriate mud weight can also stop the wellbore collapsing (Mouchet & Mitchell, 1989). It is, however, important to ensure that the drilling mud is not too dense that it exceeds the fracturing resistance of the rock by overcoming local *in-situ* stresses (Alberty & McLean, 2001). It is this latter eventuality which must be avoided by restricting the mud weight to a value below the fracture pressure at the level in question. Mud weight must be kept below the "*fracture gradient*" (Mouchet & Mitchell, 1989).

Accurate information on the fracture gradient is essential for a number of reasons:

1) To establish the drilling programme and casing depths. The scheduled mud densities in any one stage should not exceed the lowest expected fracture gradient in the open hole;

2) To determine the maximum annular pressure that can be tolerated when controlling kicks in order to avoid internal blowouts;

3) To estimate the pressures required for possible stimulation by hydraulic fracturing (Mouchet & Mitchell, 1989).

As Hubbert and Willis (1957) argue, from a theoretical and experimental examination of the mechanics of the hydraulic fracturing of rock, *in-situ* stresses are characterised by three unequal principal stresses (see **section 2.3.1**). Hydraulic pumping pressures must be approximately equal to the least of these main compressive stresses (Mouchet & Mitchell, 1989). Because of this, the terms "*fracture gradient*" and "*lower bound to leak-off pressures*" have been used interchangeably. There are a number of reasons why LOPs do not precisely give the magnitude of S_3 (see **sections 2.3.2** and **2.4.3** above) so it is important to note the difference between the two. As noted by Gaarenstroom *et al.* (1993) and Breckels and van Eekelen (1982) amongst others, lower bounds to LOPs tend to over-estimate S_3.

As explained in **section 2.2** there are essentially two approaches for predicting how the minimum principal stress changes with depth by predicting the fracture pressure, fracture gradient or lower bound to LOPs. Predictions are based on empirical methods and those that

rely on the use of LOPs plotted on pressure-depth plots. **Section 2.2** provides a good summary of some of the historically used methods so it is not necessary to repeat them here.

2.5.1 Empirical derivations

Empirically derived methods have been used to predict "*fracture gradients*" and produce good results but, as **Figure 2.15** (from Mouchet & Mitchell, 1989) shows, there can be large discrepancies in the outcome. **Figure 2.15** shows a situation where different empirical methods have been applied to wells with overpressure. Also shown for comparison are P_p measurements, LOPs and overburden measurements. As can be seen, using empirically-derived stress prediction methods leads to widely varying results. It therefore seems appropriate to heed the warning that empirical methods should be used with caution (Mouchet & Mitchell, 1989).

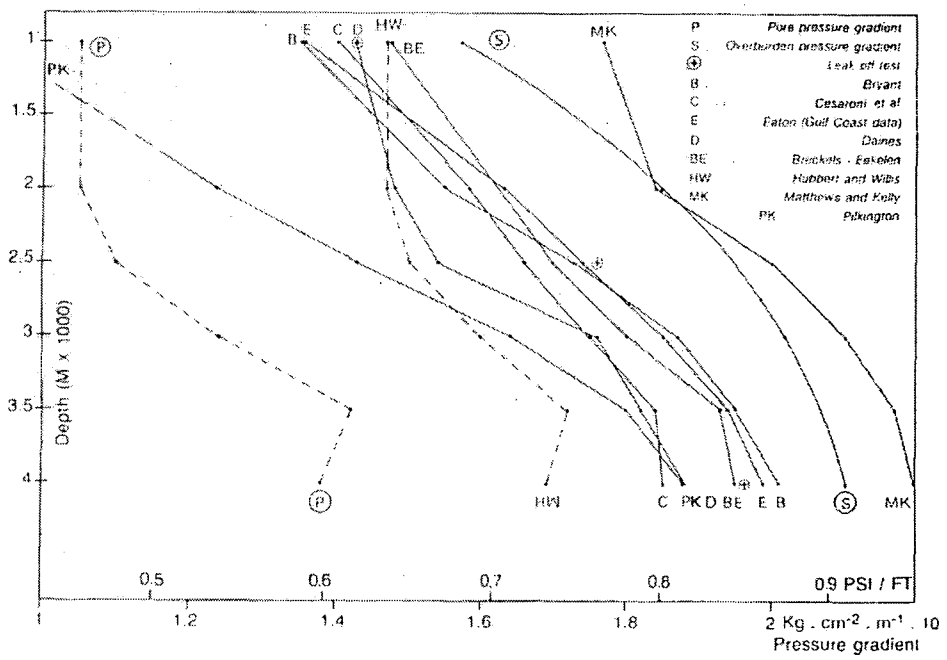

Figure 2.15: Comparison between different methods of predicting the fracture gradient (from Mouchet & Mitchell, 1989).

2.5.2 Using leak-off test data

Numerous authors have used large numbers of leak-off test data to determine the lower bound to leak-off pressures. The trends have been used to produce estimates of the

minimum *in-situ* stress in a region. Fitting an envelope to the lower extreme of the data ensures that the influences of stress perturbation around the wellbore are minimal (Breckels & van Eekelen, 1982; Gaarenstroom *et al.*, 1993; Hillis pers. comm., 2001). In ideal circumstances, the lower bound corresponds to the pressure required to re-open pre-existing fractures (see *equation 2.22* above) and is therefore derived from ISIPs or FCPs from multi-cycle XLOTs. An important point concerning the lower bound to LOPs is illustrated by **Figure 2.16** (from Gaarenstroom *et al.*, 1993). This plot provides visual evidence that the present-day fluid pressures are limited by the magnitude of the local minimum *in-situ* stress. Use of the lower bound to LOP for predicting S_3 was undertaken in this study.

The lower bound to LOPs approach can provide a good approximation of the evolution of minimum stress with depth (Breckels & van Eekelen, 1982). This statement is true as long as the quality of the data can be verified and the assumption that during a leak-off test it is S_3 that is overcome holds true.

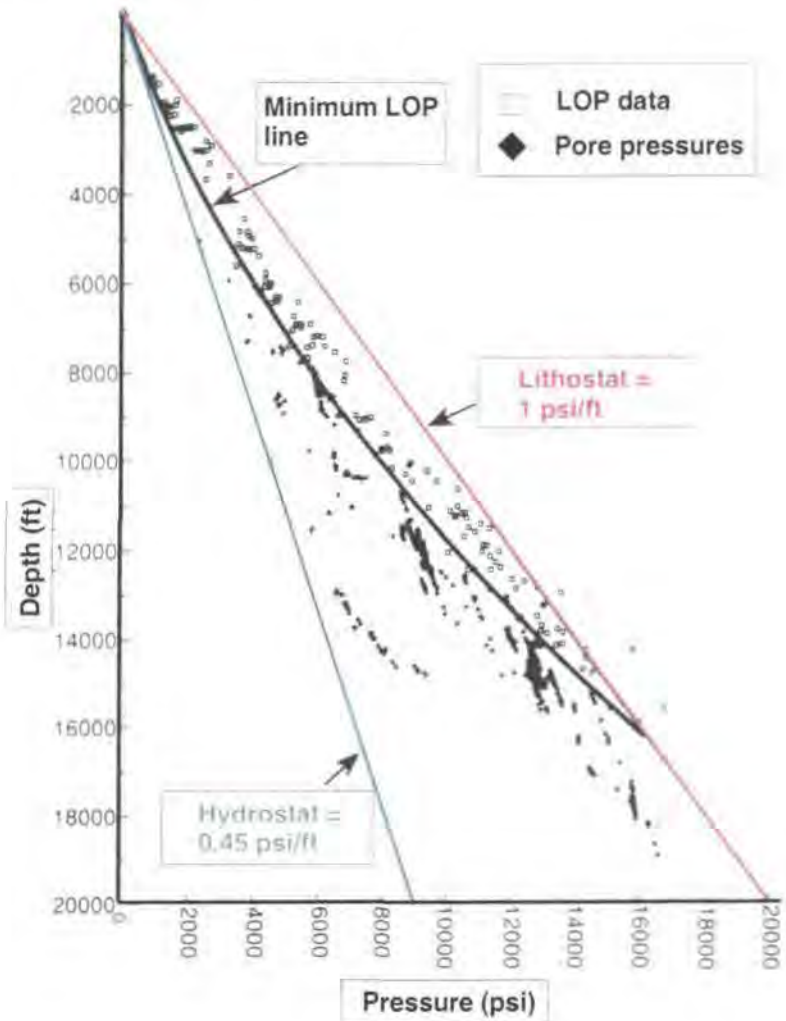

Figure 2.16: Plot of P_p and LOP data for the Central North Sea graben, also showing the lower bound to LOPs (from Gaarenstroom *et al.*, 1993).

2.6 The effects of tectonics and overpressure on horizontal stress

2.6.1 Theoretical sub-surface stresses

2.6.1.1 The "standard state" of stress

One school of thought regarding the state of stress in the Earth's crust is that it is "*hydrostatic*" – the three principal stresses are equal. This hypothesis is known as *Heim's Rule* (Anderson, 1942; Daines, 1982) and was later described as the "*standard state*". The theory states that stresses in rocks tend to become equal because of the ability of rocks to creep. Creep means that any stress difference will eventually be alleviated (Daines, 1982). Standard state theory is proved to be invalid by the large number of structures and deformations in the crust that require a stress differential to be formed and maintained. The occurrence of large-scale structures such as grabens, folds, faults and dyke swarms suggests that not only did large stress anisotropies exist in the past but that stresses are still in a state of flux, as testified by the occurrence of earthquakes (Daines, 1982; Holm, 1998). Because some external or tectonic stresses are required to create these structures, a "standard state" of stress is unrealistic for bulk Earth.

2.6.1.2 The "reference state of stress"

When we consider the state of stress in the crust we first need to adopt a "*reference state of stress*"; namely the particular situation that would occur in the absence of plate tectonics and crustal anisotropies which we accept exist. The reference state of stress can be thought of as the situation that would occur if the Earth was modelled as a static body of rock with a radially symmetrical density distribution. Additional stresses from plate motions, flexure etc. would be superimposed on top of this reference state of stress (Hillis, 2001a).

It is universally accepted that even in a basin environment devoid of any structural and tectonic influences and overpressures, lithostatic stress can increase solely as a consequence of the increase in depth. If rocks in the sub-surface are laterally constrained, horizontal compression occurs in response to vertical loading. Assuming that the rock deforms in an elastic manner and the horizontal strain is zero, then the magnitude of the two horizontal stresses are equal and related to the magnitude of S_V by Poisson's Ratio, ν (see *equation 2.1* above). This is known as the uniaxial strain state because it does not require lateral strain. Such a model is an oversimplification but it does provide the basis for fracture gradient relationships widely applied by drilling engineers (Hillis, 2001a).

2.6.1.3 The Andersonian fault model

The Mohr-Coulomb failure criterion provides a useful three-fold theoretical classification scheme for faults (Twiss & Moores, 1992). This explanation was first proposed by E. M. Anderson (1905) who described the model based on the assumption that the surface of the Earth is a free surface, i.e. it cannot support shear stress. It must therefore be a principal plane of stress (see **section 2.3.1** and **Figure 2.5**) and at the surface the principal stresses must be normal and parallel to the surface. The vertical stress in this classification is due to the overburden load and is invariant unless depth changes (Hillis, 2001a). The type of fault that develops in a situation with a vertical and two horizontal stresses depends on which of the three principal stresses is the largest. Andersonian theory predicts that the optimum orientation for a fault plane is at an angle of 30° to the maximum principal stress. If, for example, the maximum compressive stress is vertical ($S_1 = S_V$) then faults should form that have a dip of 60° to the horizontal and the sense of shear should be hanging wall down. These faults are known as normal faults and an example is shown in **Figure 2.17a** (redrawn from Twiss & Moores, 1992). Anderson (1905) proposed the relationship in *equation 2.24* for a normal fault regime (Twiss & Moores, 1992). Such a relationship provides a useful analogy for an extensional basin:

$$S_V \geq S_H \geq S_h \qquad \textit{(equation 2.24)}$$

Andersonian theory also determines models for the stress orientations in two further situations. These are strike-slip systems (**Figure 2.17b** redrawn from Twiss & Moores, 1992) and reverse, or compressive, systems (**Figure 2.17c** redrawn from Twiss & Moores, 1992). Assuming a lack of influence from overpressure, the stress situation for a strike-slip regime would place the maximum *in-situ* stress (S_1) as a horizontal stress such that:

$$S_H \geq S_V \geq S_h \qquad \textit{(equation 2.25)}$$

In a reverse or thrust fault regime (a compressive basin) both the maximum and intermediate principal stresses would be horizontal with the lithostat being the least principal stress (Anderson, 1905):

$$S_H \geq S_h \geq S_V \qquad \textit{(equation 2.26)}$$

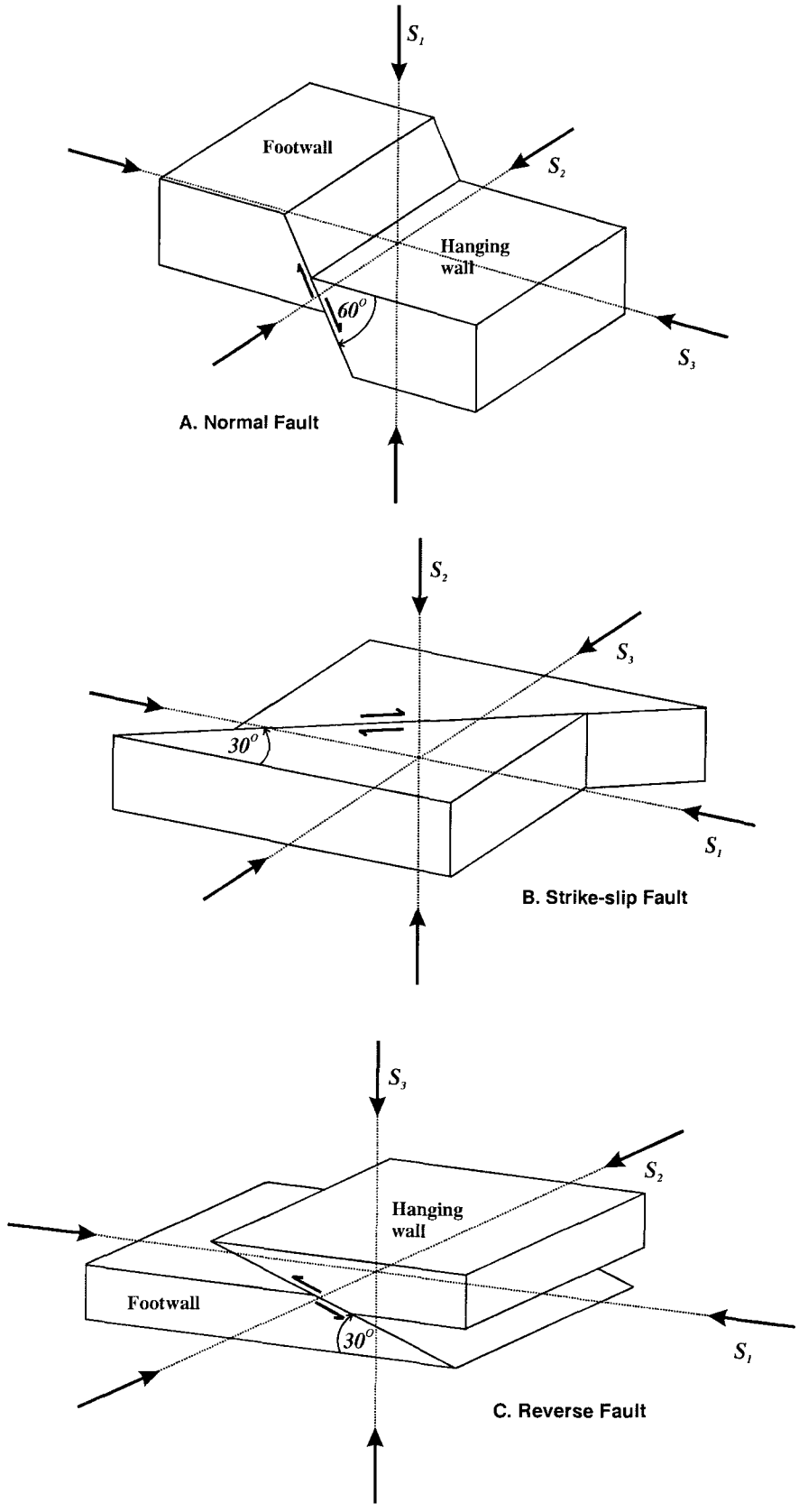

Figure 2.17: Andersonian fault models for: **(a)** normal fault; **(b)** strike-slip fault; **(c)** reverse fault (redrawn from Twiss & Moores, 1992).

The assumption that the ratio between the three stresses remains fixed with depth is generally regarded as an over-simplification (e. g. Grauls, 1997; Hillis pers. comm., 2001). The Poisson's Ratio changes with depth and varies with rock properties (Daines, 1982; Engelder, 1993). Overpressure also effects the magnitude of the horizontal stresses (Biot, 1941; Engelder & Fischer, 1994) and so does the friction between grains and on fault planes (Jaeger & Cook, 1979; Zoback & Healy, 1984). Tectonic components such as ridge push, slab pull and flexure also add to intraplate stresses (Hillis pers. comm., 2001). Structures, such as faults and salt diapirs, within a basin can perturb and re-orientate stress and can alter the apparent structural regime (Yassir & Zerwer, 1997). Discussed briefly below are some of the tectonic, structural and fluid pressure-derived components of the horizontal stresses.

2.6.2 The relationship between tectonics and S_h

2.6.2.1 Tectonics, structures and S_h

From the alignment of geological structures in provinces such as extensional basins and fold and thrust belts, it is clear that additional stresses are superimposed on top of the reference state of stress (Daines, 1982). These additional stresses contribute to the commonly observed anisotropic stress situation. Tectonic stresses are not only those associated with plate tectonic forces but also forces associated with regional and local phenomena such as lithospheric flexure and local density variations (Hillis, 2001a). In the Andersonian classification, because S_V is invariant, the normal, strike-slip and thrust regimes reflect changes in S_H and S_h brought about by tectonic stresses being superimposed on the reference state of stress.

Mapping of the Earth's contemporary stress field was carried out by the World Stress Map Project (Zoback, 1992; Mueller *et al.*, 2000). Results showed that there are large intraplate areas where the orientations of the horizontal stresses are uniform. As these orientations coincide with absolute plate motions, it has been inferred that forces driving and resisting plate motions are responsible for regional stress orientations within the crust. Forsyth and Uyeda (1975) carried out a comprehensive study of the forces acting on a plate. They concluded that forces such as ridge push, slab pull, plate friction during subduction, slab negative buoyancy and trench suction amongst others contribute to the first-order regional stress orientations (Forsyth & Uyeda, 1975; Hillis, 2001a). Regional horizontal stress orientations in Western Europe, mid-plate North America and South America are all consistent with absolute plate motion directions (Hillis, 2001a). Lindholm *et al.* (1995) show how stress directions extracted from earthquake focal mechanisms have been calculated for south-eastern and south-western Norway, the Norwegian Sea and the Barents-Finnmark

region. The principal stress directions show an anticlockwise rotation from north to south through the region. This rotation matches the stress trajectories expected to be generated by ridge push on the mid-Atlantic spreading axis (Lindholm *et al.*, 1995).

As well as plate motion forces, other components contribute to horizontal stress anisotropy, orientation and magnitude. Flexural stresses associated with bending of the lithosphere due to loading or unloading can be important. For example, in the area of Baffin Bay and the Labrador Sea, earthquakes occur whose origin and focal mechanisms are consistent with a stress field altered by glacial unloading (Stein *et al.*, 1979; Engelder, 1993).

The addition and subsequent collapse of the large mass of the Tibetan Plateau to the Asian Plate is a good example of how gravitational spreading can perturb the local stress field. Collision of the Indian and Asian Plates produce the background stress field (England, 1992). Earthquake focal mechanisms show that orogenic collapse re-orientates the stress field (**Figure 2.18** from England, 1992). Around the edges of the plateau there is thrust faulting with horizontal shortening roughly perpendicular to the contours of surface height. The interior of the plateau is deformed by a mixture of strike-slip and normal faulting.

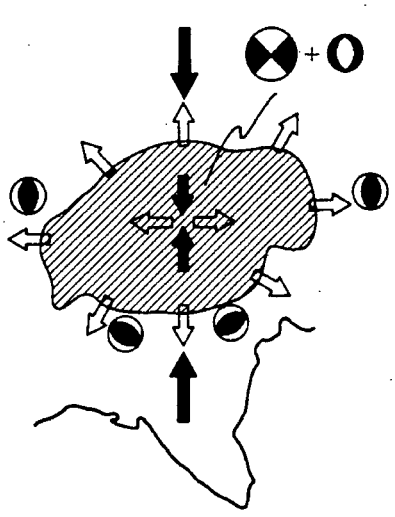

Figure 2.18: Schematic representation of the horizontal stress components in the India-Asia collision zone (from England, 1992).

Faults and fractures have a large effect on the stress field. In the Oseberg Field (North Sea), S_H is rotated parallel to the strike of faults (Aleksandrowski *et al.*, 1992). Within the Scott Field of the North Sea, stress partitioning within fault blocks leads to variations in horizontal stress orientations (Yale *et al.*, 1994). The Tertiary of the Mid-Norwegian margin also shows re-orientations of the stress directions. These re-orientations are believed to be caused by deeper lying faults in combination with a stress field less influenced by plate tectonics (Borgerud & Svare, 1995).

Stresses developed due to changes in the density structure of the lithosphere are also observed (Artyushkov, 1973; Engelder, 1993). These tend to occur especially at passive margins where oceanic crust is juxtaposed against continental crust and differing depth-density distributions arise (Bott & Dean, 1972). Bott and Dean (1972) explain how the body forces associated with low-density continental crust and the presence of juxtaposed oceanic crust give rise to a laterally varying stress system across the margin. Large margin-normal compressive stresses are created in the oceanic crust and normal faulting orientated parallel to the margin occurs in the continental crust. Examples of such a situation can be found all around the Atlantic seaboard (Bott & Dean, 1972).

Thinning of the lithosphere by thermally activated creep redistributes the load so that stress in the lithosphere is amplified (Engelder, 1993). Kusznir (1982) quotes the example of the Basin and Range Province where stress amplification due to lithosphere thinning has taken place. In this province, Kusznir (1982) shows that lithosphere has thinned from an initial thickness of 150 km to around 20 km in 10^8 years. The result is a seven-and-a-half times stress amplification factor in the upper lithosphere. The result of the increase is upper lithosphere fracturing and faulting (Kusznir, 1982; Engelder, 1993).

In the Offshore Louisiana region of the US Gulf Coast, Yassir and Zerwer (1997) report that the stress situation is affected by a number of phenomena such as the geometry of the clastic sedimentary wedge, local faults and salt structures. The upwardly convex geometry of the prograding clastic wedge promotes an extensional stress regime on the continental slope. This manifests itself as a highly anisotropic regime where S_h is aligned down the slope and S_H is parallel to the slope and the strike of the listric normal faults. This follows the Andersonian theory for normal faulting. The faults themselves are unlikely to alter the stress regime and trajectories in Offshore Louisiana because they are not prevented from moving in a seaward direction (Yassir & Zerwer, 1997). This contrasts with instances such as the San Andreas Fault and the Jeanne d'Arc Basin, offshore eastern Canada (Bell, 1990). Regional stress trajectories are deflected close to the San Andreas Fault. In the Jeanne d'Arc Basin, block compression due to fault hanging wall movement towards a confined surface can reduce the anisotropy and even re-orientate the S_H and S_h trajectories (Bell, 1990). In the Offshore Louisiana region, an effect similar to that in the Jeanne d'Arc Basin only appears close to the toe of the sedimentary wedge, where a lateral constraint to movement results in a locally compressive regime (Yassir & Zerwer, 1997).

The strongest control on anomalous local stress patterns in the US Gulf Coast region is exerted by salt structures. The reason is possibly because the salt is stiffer than the surrounding sediments and therefore "attracts" S_H trajectories because of its ability to withstand higher stresses. Also, the compressional stresses radiating from salt diapirs result in very high radial stresses and low extensional tangential stresses. This means that a borehole breakout recorded in the vicinity of a salt diapir will give S_H orientations

perpendicular, and S_h orientations tangential, to the structure, thus modifying the local stress field (Yassir & Zerwer, 1997).

To conclude this section, it is important to note that simply assuming that either a "standard state" of stress occurs or that the minimum horizontal stress evolves purely as a result of an increase in depth will lead to mis-estimates of its magnitude. The large number of contributors to S_h shows why direct measurements of S_h are the best ways of determining the true magnitude. It is also important to note that in different tectonic regimes the magnitude of the horizontal stresses relative to the vertical stress will vary. These variations are discussed below.

2.6.2.2 Tectonic regime and S_h

Profiles of the evolution of the principal stresses as functions of depth seem to be dependent on present day tectonic regimes (Grauls, 1997). Grauls (1997) applied the evolutionary trend approach to sedimentary basins. Extensional regimes, e.g. passive margins, are characterised by low S_3 evolutionary trends with depth and low S_3/S_V ratios of between 0.7 and 0.83 through the 500 m to 6 km depth interval. Examples include the US Gulf Coast, Offshore Angola and the Niger Delta (Grauls, 1994 & 1997). The S_3/S_V ratio for strike-slip regimes approaches unity and minimum stress values are characterised by a more rapid evolution with depth. Examples include Venezuela and the active margin of Northern Borneo (Grauls, 1994). In thrust environments, namely compressive basins, S_V is the minimum stress. Examples include Onshore Pakistan and the Bavarian Alps (Grauls, 1997) where the stress orientation can lead to overthrust faulting along basal décollements. Fluid pressure to S_V ratios equivalent to or slightly exceeding 1.0 contribute to the mechanics of this overthrust faulting (Grauls, 1997). **Figure 2.2** (from Grauls, 1998) shows how the evolutionary trends vary for different regimes.

Grauls (1994) proposes that in basins where there are lateral constraints restricting expansion, horizontal stresses created by the overburden and developing following elastic theory cannot dissipate. A consequence would be horizontal stress build up. The Central North Sea is an example of what Grauls (1997) believes is a stress evolutionary trend through the different tectonic regimes with depth. In the upper interval, the geological context is S_V dominated but becomes more lateral stress dominated below the Palaeocene unconformity at a depth in excess of 3000m (Grauls, 1994 & 1997). The reason for this evolution in regime with an increase in depth is likely to be an increase in compressional horizontal stress (Grauls, 1994). A similar situation is proposed for Offshore Louisiana, US Gulf Coast, where listric faults show the rotation of S_1 from vertical to horizontal with depth (Yassir & Zerwer, 1997). Katahara (1996) proposes that there may even be situations where the stress regime varies systematically from normal (S_V maximum) to strike-slip (S_V intermediate) to thrust (S_V

minimum) with increasing depth. An example is the Sable Basin, offshore eastern Canada (Bell, 1990) where the stress regime in the basin was established from borehole breakout directions.

A good knowledge of S_3/depth evolution together with its significance in terms of tectonic stress regime has implications for abnormal pressure prediction and overpressure-related geodynamic processes (Grauls, 1997). It is believed (Grauls, 1998) that strike-slip and compressive regimes can support greater fluid pressures due to elevated fracture gradients or lower bounds to LOPs. Therefore knowledge of the pore pressure to S_3 ratio with depth in a known tectonic setting can be applied to a poorly explored area where knowledge of the stress regime will allow the pressure regime to be predicted (Grauls, 1997). Caution must be exercised though. When applying an approach developed in one basin to another, differences in geology, stress system, stress history and overpressure mechanisms must be taken into consideration (Yassir *et al.*, 1998).

If in some basins, as Grauls (1997) claims, the stress regime evolves towards more compressive contexts, then this provides a means of increasing S_3 at given depth and also the P_p. It can explain why pressure values are 25% and 40% higher in strike-slip and thrust settings than in a normally faulted setting (Grauls, 1997). Yassir *et al.* (1998) state that in a tectonically active basin setting (a basin with active compression), the maximum horizontal stress, S_H, is potentially greater than S_V which causes an increase in shear stresses, possibly up to failure. P_p therefore increases in response to the change in shear stress, not just due to the change in the vertical stress. The tectonic component of the horizontal stress is superimposed on to the uniaxial component. The horizontal stress - P_p relationship for both normal and thrust faulted settings shows that the ratio of horizontal stresses becomes more isotropic with increasing P_p until $P_p = S_V$. In these highly overpressured situations, all stresses become isotropic (Yassir *et al.*, 1998).

2.6.3 The origins of overpressure

Osborne and Swarbrick (1997) give a detailed re-evaluation of the mechanisms that lead to the generation of overpressure. Overpressure itself is defined as the amount of P_p exceeding the hydrostatic, or normal, pressure (Dickinson, 1953; Gaarenstroom *et al.*, 1993; Osborne & Swarbrick, 1997). The following processes can produce overpressure:

1) Increases in the compressive stress (*mechanical approaches*);

2) Changes in volume of the pore fluid or rock matrix (also known as *inflationary mechanisms*);

3) Fluid movement or buoyancy.

Mechanical overpressure generating mechanisms rely on the effects of stresses to increase pore pressures. The addition of sediments during burial loads the underlying rock and increases the total vertical stress, S_V. If this rock is unable to lose its pore fluids either because it has sufficiently low permeability or because the rate of sedimentation is too rapid then overpressure can be generated. This is because the pore fluid takes up the load totally and the change in P_p is equivalent to the change in S_V. The process has been termed "disequilibrium compaction" (Osborne & Swarbrick, 1997). An underestimated effect of stress on P_p is the contribution from lateral stress in strike-slip and compressive regimes. In these domains, where strain does occur, lateral stresses can lead to an increase in P_p as fluids take up some component of the horizontal "load". Despite considerations made by Hubbert and Rubey (1959) in thrust fault contexts and by Grauls and Baleix (1993) in strike-slip contexts, the contribution of lateral stresses to overpressure remains rarely considered (Grauls, 1998).

Inflationary mechanisms approach the P_p-stress relationship from a different angle. Instead of pressure being generated by stress, the pressure increase itself causes a change in the total stress. Overpressure mechanisms involving a change in volume of either fluid or pore space require the rock to be "well sealed" to prevent fluid loss and pressure dissipation. Pressure solution along load bearing contacts of grains can bring about porosity reduction in a rock. Hermanrud *et al.* (1998) state that this process can create overpressures up to lithostatic magnitudes even when porosity is reduced by only a couple of tens of one percent. A necessary requirement for this process to be effective is the need for very low permeabilities or, idealIly, impermeable rocks.

Fluid volume increases associated with aquathermal expansion and clay mineral dehydration are considered too small to generate significant overpressure unless perfect sealing occurs. Hydrocarbon generation and cracking to gas could produce high overpressures as long as the necessary temperatures, kerogen types and rock permeabilities are met. However, these processes could be self-limiting in a sealed system because build up of pressure could inhibit further organic metamorphism (Osborne & Swarbrick, 1997).

Fluid movement due to a hydraulic head can potentially generate high overpressures in a "well plumbed, shallowly buried" basin (Osborne & Swarbrick, 1997). However, many examples of petroleum bearing basins do not fit these specific criteria. Calculations indicate that hydrocarbon buoyancy and an osmotic gradient are only capable of generating small amounts of overpressure. To date, it seems that mechanical processes (e.g. disequilibrium compaction) are the most likely causes of overpressure with a contribution from inflationary mechanisms such as hydrocarbon generation (Osborne & Swarbrick, 1997).

2.6.4 The relationship between overpressure and S_h

It is important to gain accurate pore fluid pressure (P_p) predictions to avoid the need to abort drilling operations when circumstances mean it would be dangerous to continue. The key parameter that can affect drilling constraints is overpressure (see descriptions above in **section 2.6.3**).

There is a great deal of evidence to suggest that overpressured rock is associated with an increase in the minimum principal horizontal stress, S_h (Biot, 1941; Engelder & Fischer, 1994; Yassir *et al.*, 1998). Excess P_p can increase the horizontal stress values above that of S_V (Miller *et al.*, 1998). However, if strain is allowed in all directions a change in P_p causes a change in the effective stress without affecting the total stress (Yassir *et al.*, 1998). Previous work in a number of regions, specifically the US Gulf Coast (Breckels & van Eekelen, 1982) and the Central North Sea (Teufel *et al.*, 1991; Gaarenstroom *et al.*, 1993; Engelder & Fischer, 1994) suggests that S_h increases more rapidly with depth in overpressured rocks than in normally pressured rocks. Many authors believe this rapid increase in stress to be a consequence rather than a cause of overpressure (Burrus, 1998). Grauls (1997) uses the example of the Central North Sea to argue that a change in tectonic regime with depth leads to an increase in the magnitude of the fracture gradient. This increase in S_3 allows high overpressures to be maintained.

2.6.4.1 Pore pressure *in-situ* stress coupling

In a situation where pore pressures affect the magnitude of the horizontal stresses and vertical stress in the same way (non-coupled situations), it is assumed that on a Mohr diagram the radius of the Mohr circle does not change with an increase or decrease in pore pressure. This is because the differential effective stress, σ_d, does not change (**Figure 2.19a** redrawn from Hillis, 2001b). In this situation, overpressure shifts the Mohr circle to the left while a P_p reduction moves the Mohr circle to the right (Secor, 1965; Davis & Reynolds, 1996). However, following elasticity theory, it is possible for a change in pore pressure to alter the minimum horizontal stress such that σ_d does change. Elastic theory shows that the elevation in pore pressure causes a corresponding increase in S_h. The result would be that both the vertical (σ_V) and minimum horizontal (σ_h) effective stresses decrease but σ_h decreases by a smaller amount (**Figure 2.19b** redrawn from Hillis, 2001b). Therefore, it is potentially difficult for the pore pressure to reach the fracture pressure. Coupling thus allows rocks to support very high overpressure magnitudes (Engelder, 1993; Arnesen *et al.*, 1997; Yassir *et al.*, 1998). Conversely, a decrease in P_p creates an increase in σ_d (**Figure 2.19c**

redrawn from Hillis, 2001b). The diameter of the Mohr circle (the magnitude of σ_d) changes in accordance to the nature of the pore pressure *in-situ* stress coupling.

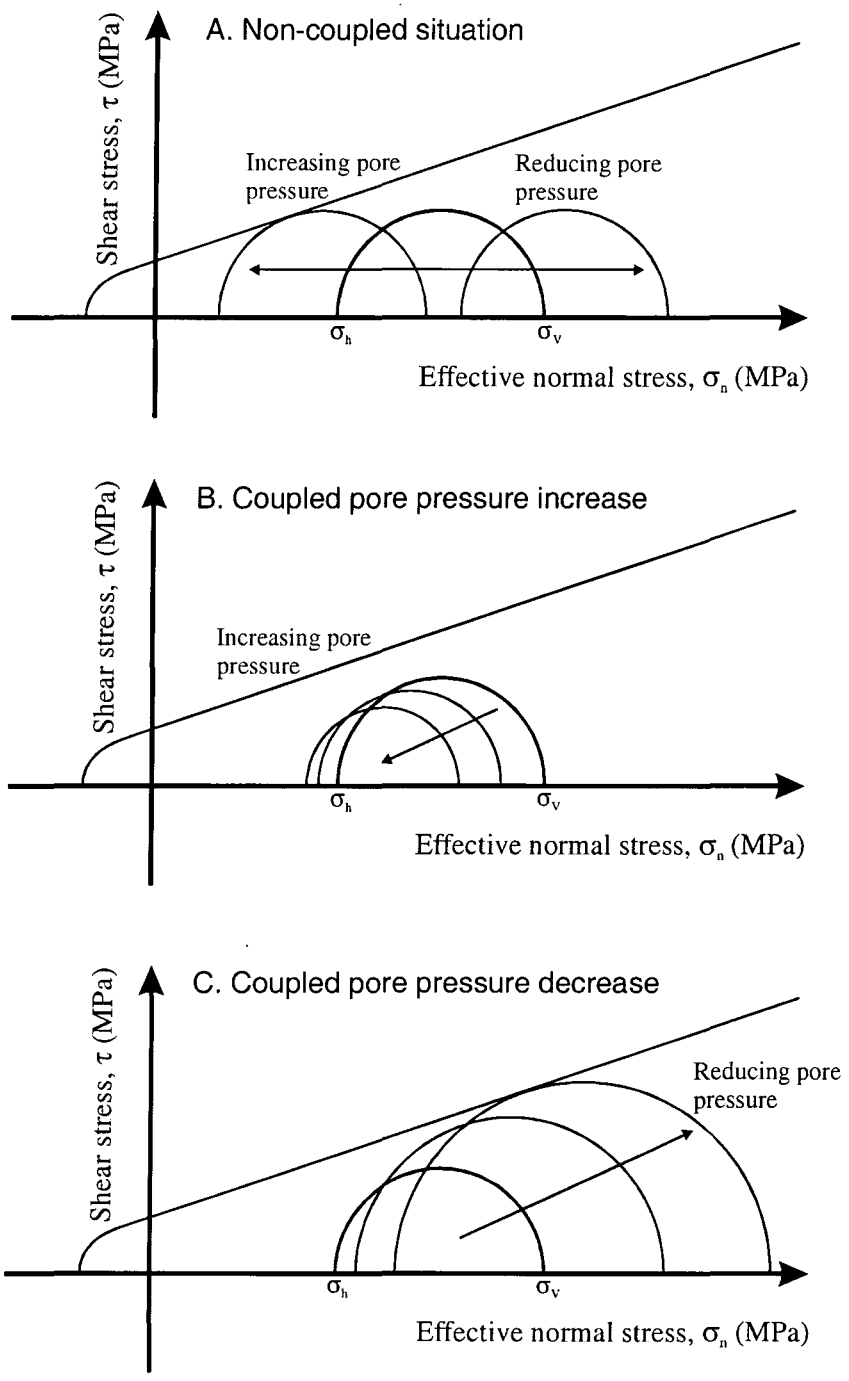

Figure 2.19: Mohr circles showing **(a)** the non-coupled situation; **(b)** coupled pore pressure increase; **(c)** coupled pore pressure decrease (redrawn from Hillis, 2001b).

Changes in pore pressure and minimum horizontal stress are coupled to one another over a range of spatial and temporal scales. Stress measurements have shown S_h to decline

during the production life of a field at the same time that the P_p is reduced. Likewise, repeat formation tester (see **section 3.7.3**) measurements of virgin pore pressures in basins have shown that stress increases through the depth interval in accordance with the magnitude of overpressure. On the scale of an individual field, pore pressure *in-situ* stress coupling develops over the life of the field, namely 10 to 20 years. At the scale of a basin, the coupling manifests over the geological time-scale of overpressure development (Hillis, 2001a). As stated by Hillis (2001a), there are very few direct measurements of the maximum horizontal stress, S_H. Therefore it is not possible to assess the way that it varies with overpressure. It is most commonly assumed to vary in the same way as S_h though.

Pore pressure *in-situ* stress coupling is seen on many single well stress-depth plots. The example of a SE Asia well (**Figure 2.20** from Harrold *et al.*, 1999) shows that below 1.8 km depth, pore fluids become overpressured. As well as this, the magnitude of the LOP measurements increases towards the lithostat. This response of stress to P_p reveals the presence of coupling. Another example comes from the Flamboyant Field, Offshore Trinidad where an increase in P_p is matched by a proportional increase in shale hydraulic fracture gradient (**Figure 2.21** from Heppard *et al.*, 1998). However, at 3.7 km depth there is a step-back in P_p and a coincident decrease in fracture gradient magnitude. Such a display of coupling implies that there is some control on the magnitude of minimum stress by the P_p.

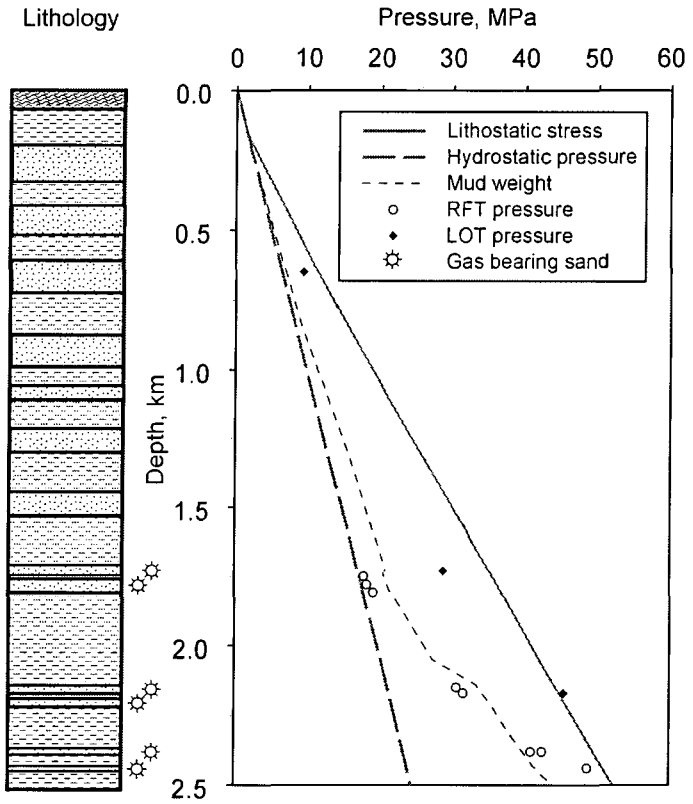

Figure 2.20: Example of a SE Asia well showing pore pressure *in-situ* stress coupling where as overpressures develop LOPs increase (from Harrold *et al.*, 1999).

Many data from sedimentary basins on continental margins – US Gulf Coast, Brunei, Venezuela (Breckels & van Eekelen, 1982) and The North Sea (Gaarenstroom *et al.*, 1993) – show pore pressure *in-situ* stress coupling. An example of basin-scale P_p-S_h coupling comes from Gaarenstroom *et al.*'s (1993) data from the UK Central North Sea graben (**Figure 2.16**). These data show that moving into the zone of high overpressure at 8000 feet, leak-off pressure magnitudes also increase. As the *minimum LOP line* shows, LOPs approach lithostatic values coincident with P_p approaching 80-90% lithostatic. A similar relationship is also shown in the Sable sub-basin of the Scotian Shelf, Canada where S_3 (in this case S_h) increases at a rate proportional to, but less than, the rate of increase of P_p. In all cases $\Delta S_h < \Delta P_p$. As Hillis (2001b) points out, the reduction in S_h accompanying a reduction in P_p due to reservoir depletion has been demonstrated in a number of situations. These include the Oligocene Vicksburg Formation of south Texas (Salz, 1977), the Eocene C4 and C5 sands of the Lake Maracaibo region of Venezuela (Breckels & van Eekelen, 1982) and the Ekofisk Field of the North Sea (Teufel *et al.*, 1991). These phenomena are consistent with *poro-elasticity* (see **section 2.2.2.3** above). Poro-elastic behaviour is also seen when the pressure within a hydrocarbon reservoir is drawn down (Engelder & Fischer, 1994; Hillis, 2001b). Data from the Ekofisk Field in the Norwegian North Sea (Teufel *et al.*, 1991; Hillis, 2001b) show that $\Delta S_h/\Delta P_p$ is as high as 0.8. The point is that because of the poro-elastic effect, a drawn down in fluid pressure leads to a corresponding decrease in the magnitude of S_h due to "poro-elastic relaxation". This creates an increase in the differential stress even without the need for the effects of friction or the addition of a greater overburden (Engelder & Fischer, 1994).

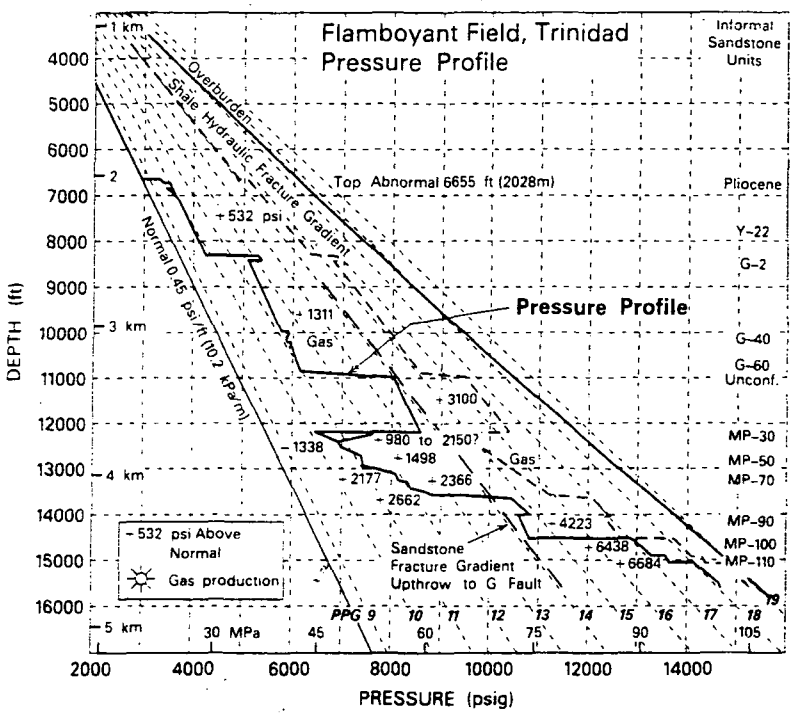

Figure 2.21: Pore pressure *in-situ* stress coupling from the Flamboyant Field, Offshore Trinidad (from Heppard *et al.*, 1998).

Coupling appears to be a phenomenon that is present regardless of the pore pressure evolution profile. The example of the Scotian Shelf, offshore eastern Canada (**Figure 2.22** from Hillis, 2001a), shows large overpressures developing at about 4 km depth and this is matched by a rapid increase in LOP values towards lithostatic values. The high magnitudes of LOP and P_p are maintained down to 6 km depth. A similar situation is shown in **Figure 2.23** (from Harrold, 2000), a single well plot from the Mahakam Delta. Here, the mud weight used for drilling shows that P_p are approximately hydrostatic down to 2.5 km. There is then a rapid increase of around 40 MPa as RFT and drill-stem test recorded P_p leap to sub-lithostatic. LOP measurements show an increase in S_3 coincident with the overpressure development. Excessively high P_p and LOP values continue down the depth interval. A different situation occurs for the Gulf of Mexico. Here, as well MC 755/2 (courtesy of GeoPOP) in **Figure 2.24** illustrates, the overpressure initiates at shallow depths and the pore pressure profile runs sub-lithostat parallel for the remainder of the depth interval. The LOP magnitudes are also consistently high throughout the succession, falling between the pore pressure profile and the lithostat.

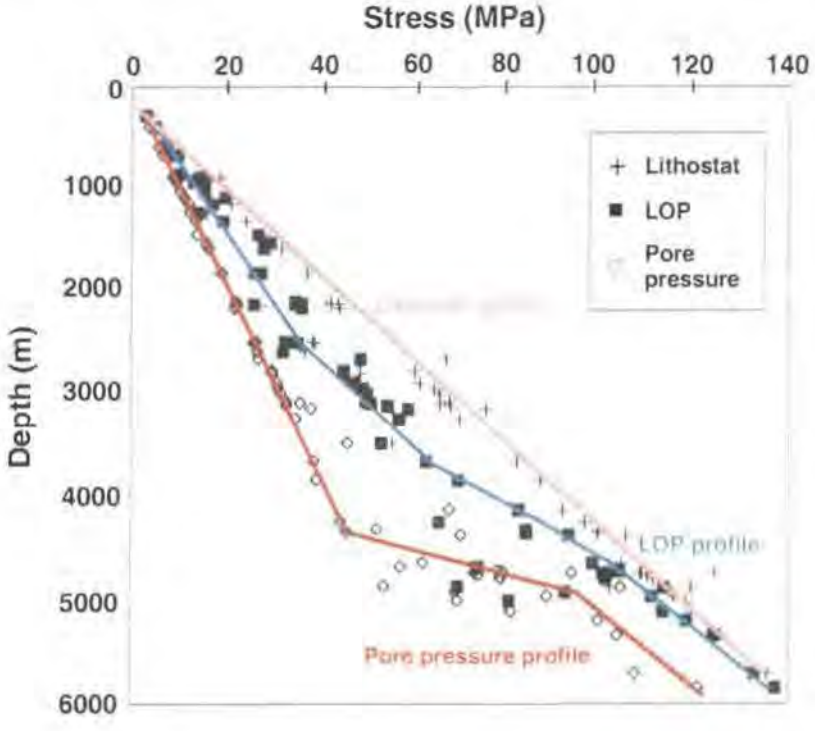

Figure 2.22: The Scotian Shelf, offshore eastern Canada, showing hard overpressure developing at 4 km depth (from Hillis, 2001a).

Just as stress can have an effect on P_p, so fluid flow through fractures can have a profound influence on the state of stress in a naturally fractured reservoir (Teufel *et al.*, 1991). For example, in the Ekofisk field in the Norwegian North Sea, production of petroleum has led

to a decrease in P_p with a subsequent increase in the amount of overburden stress (due to an increase in effective vertical stress, σ_V) which has to be supported by the chalk matrix. The consequence is that the chalk compacts and at the same time undergoes shear failure that occurs as the pore pressure is drawn down. This shear failure can lead to an increase in fracture density and a reduction in matrix block dimensions thereby maintaining reservoir permeability that would otherwise be decreased by the compaction (Teufel *et al.*, 1991). Interestingly, the total minimum horizontal stress, S_h, appears to decrease in a linear fashion with P_p drawdown. The change in S_h is about 80% of the net change in P_p; therefore an increase in the effective minimum horizontal stress, σ_h, will occur with any decrease in P_p (Teufel *et al.*, 1991).

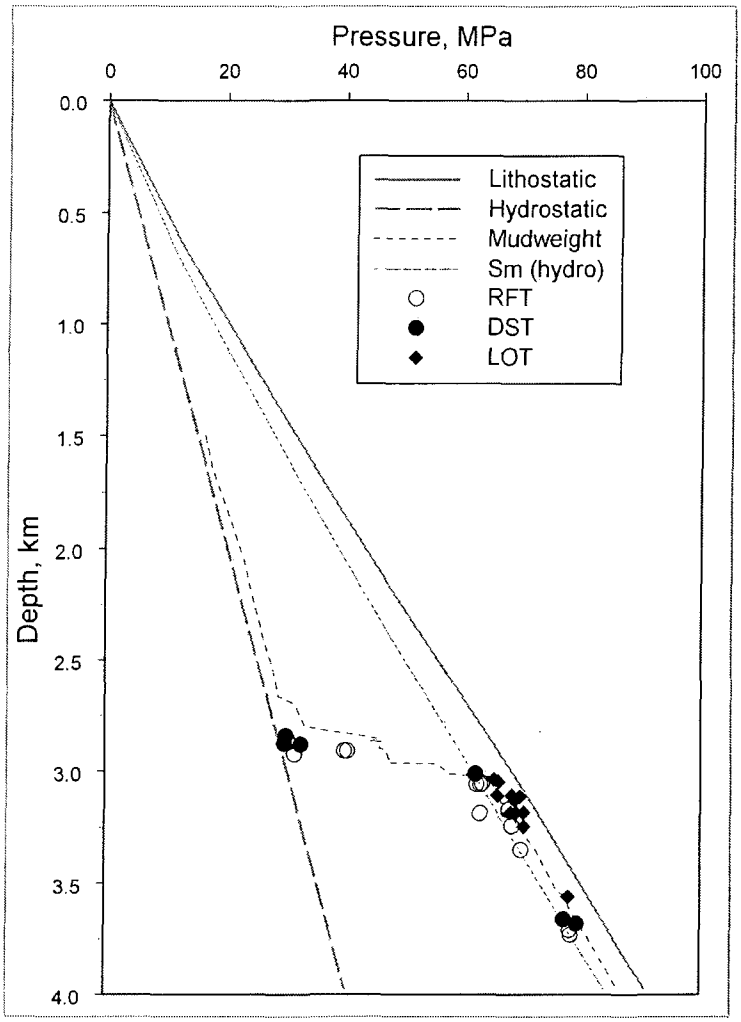

Figure 2.23: Single well plot from the Mahakam Delta showing rapid development of overpressure up to sub-lithostatic magnitudes (from Harrold, 2000).

Coupling is critical to both oil field development and sedimentary basin tectonics. The nature of stress changes can effect the stability of open (uncased) wellbores throughout the life of the field. On a basin scale, the nature of coupling can limit the magnitude of

overpressure by dictating whether tensional or shear failure occurs (Hillis, 2001a). Essentially the nature of the coupling influences the diameter of the Mohr circle which will determine where the Mohr insects the failure envelope when overpressuring occurs (see above and **section 2.3.1**). It is because of this importance that coupling comprises a large part of the investigations in the thesis.

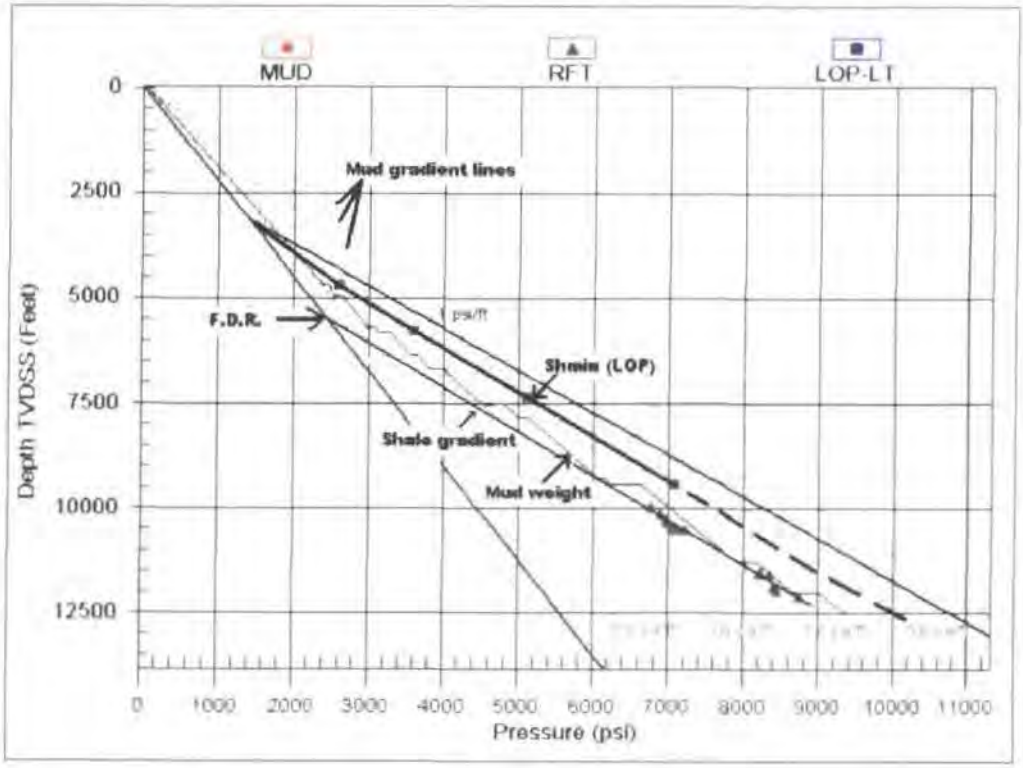

Figure 2.24: Well MC 755/2 from the Gulf of Mexico showing overpressure initiating as shallow as 3000 feet with pore pressure then running sub-parallel to the lithostat. Leak-off tests also show a profile that is lithostat sub-parallel (courtesy of *GeoPOP*).

Chapter THREE: Mid-Norway Introduction

3 Mid-Norway Introduction

3.1 Introduction

The purpose of this chapter is to introduce the Mid-Norway region. The aim is to arm the reader with background information on the area so that the data analyses in **Chapter 4** have more of a context. Given in the initial subsections are details on the geographical location of Mid-Norway (**section 3.2**) followed by information on the importance of the region as a producer of petroleum and the companies operating there (**section 3.3**).

Section 3.4 summarises the geological history of Mid-Norway in terms of the sediments that overlie the Caledonian metamorphic basement and also the complex structural deformations and tectonic evolution that has occurred. The burial history from the Triassic through to the present day is also summarised.

As an introduction to the stress situation in the region a summary of previous work on the determination of the contemporary stresses is given in **section 3.5**. The overpressure in Mid-Norway is described in **section 3.6**. This section reveals the location of the major overpressures and outlines previous work on the origins and timing of development.

A description of the sources and types of data analysed is given in **section 3.7**. As well as explaining the form of the data an explanation of the quality control procedure that was undertaken is given and the results that came out of this quality control. Also explained is the compilation of the "*comparable depth*" data set used to investigate pore pressure *in-situ* stress coupling.

Finally, **section 3.8** describes and shows the creation of the lithostat from the density log from well 6506/12-1 and the contribution by the water column and atmosphere.

3.2 The geographical location of Mid-Norway

The Norwegian Sea region of the Norwegian continental shelf comprises most of the continental margin (in the geological sense) between 62^{O}N and 69^{O}30'N (**Figure 3.1** from the *Philip's Atlas of the World*) between the western coastal towns of Kristiansund in Romsdal, and Harstad on Hinnøya (Blystad *et al.*, 1995). In petroleum licensing terms, the Møre-Trøndelag-Magnus-West Shetlands Spine Fault Complex is considered the delineation that separates the Mid-Norway region from the North Sea Province (Swiecicki *et al.*, 1998).

Figure 3.1: The location of Mid-Norway (from the *Philip's Atlas of the World*).

3.3 The importance of Mid-Norway as a petroleum producing region

Mid-Norway is important due to the large number of oil and gas fields both formerly and currently in production. These fields are operated by a multi-national collection of companies. **Figure 3.2** (from the *Norwegian Petroleum Directorate*) shows the principal fields and their operators. The first licences on the Norwegian continental shelf were allocated in the Halten Terrace (see **Figure 3.3** from Jensen & Doré, 1993) region in 1980. Since then, the Halten Terrace has produced 80% of the hydrocarbons found to date in Mid-Norway (Swiecicki *et al.*, 1998). Of the fields in operation in Mid-Norway, amongst the more important and famous are Åsgard and Smørbukk on the Halten Terrace.

Licences were granted as a consequence of the acquisition of seismic data that began as early as 1969. As an indication of the rate of growth of Mid-Norway as a petroleum producer, by the end of 1994, 108 exploration wells had been drilled and around 600,000 kilometres of seismic data acquired (Blystad *et al.*, 1995). The first well was drilled on the Trøndelag Platform and was found to be dry. Subsequent drilling activity has mainly concentrated on the Halten Terrace (**Figure 3.3**). Exploration has been steadily expanding since then into new areas and in 1994 the whole of the Møre and Vøring Basins were opened for exploration drilling (Blystad *et al.*, 1995). In terms of hydrocarbon potential, its extreme

depth of burial discounts the Devonian and Triassic interval across the whole of Mid-Norway. Jurassic and Cretaceous rocks have proved to be the most promising to date (Swiecicki *et al.*, 1998). Gas, gas-condensate and oil sourced from the Jurassic Spekk Formation and trapped within Early and Middle Jurassic clastics in tilted fault blocks provide the principal type of play on the Halten Terrace. Examples of these types of field include Smørbukk, Midgard, Njord, Norne and Heidrun (**Figure 3.2**). The Draugen field provides the only notable exception with shallow marine sand bars of Late Jurassic age forming the reservoirs (Swiecicki *et al.*, 1998).

3.4 The geology of the Mid-Norway region

3.4.1 Summarising the sedimentary history of Mid-Norway

The sedimentary succession overlies a basement consisting of metamorphic rocks and intrusives of Caledonian age (Grigo *et al.*, 1993) mainly exposed in northern Scotland and Norway.

Between the Devonian and the Triassic, a succession of mainly extensional tectonic episodes took place in a continental depositional environment. This was followed by the deposition of a thick (probably greater than 2 km) package of continental clastics capped by the Late Triassic to Early Jurassic Åre Formation (Jensen & Doré, 1993). This brackish marine, coaly unit is regarded as an important source of gas, condensate and some oil. A continuous transgressive regime resulting in the deposition of the coarse deltaic and shallow-marine clastics of the Tilje Formation, part of the Fangst Group (**Figure 3.4** from Hermanrud *et al.*, 1998a), dominated the Jurassic. These units produce the principal reservoirs of the Halten Terrace province (Jensen & Doré, 1993). The Trøndelag Platform (see **Figure 3.3**) was not heavily affected by rifting but underwent stable subsidence resulting in uniform thicknesses of Jurassic sediments (Bøen *et al.*, 1984). Widespread mudstone deposition towards the end of the Jurassic signified the end of the transgression. The muddy shale sequence is capped by the principal oil-prone source rock, the Spekk Formation. The Spekk Formation is of Late Jurassic to Early Cretaceous age (**Figure 3.4**) and was probably deposited in a restricted basin experiencing anoxic conditions (Vik & Hermanrud, 1993). Extensional movement in the Late Jurassic created the block-faulted terrain of the area with thermal subsidence following in the Late Cretaceous as a consequence of the extension.

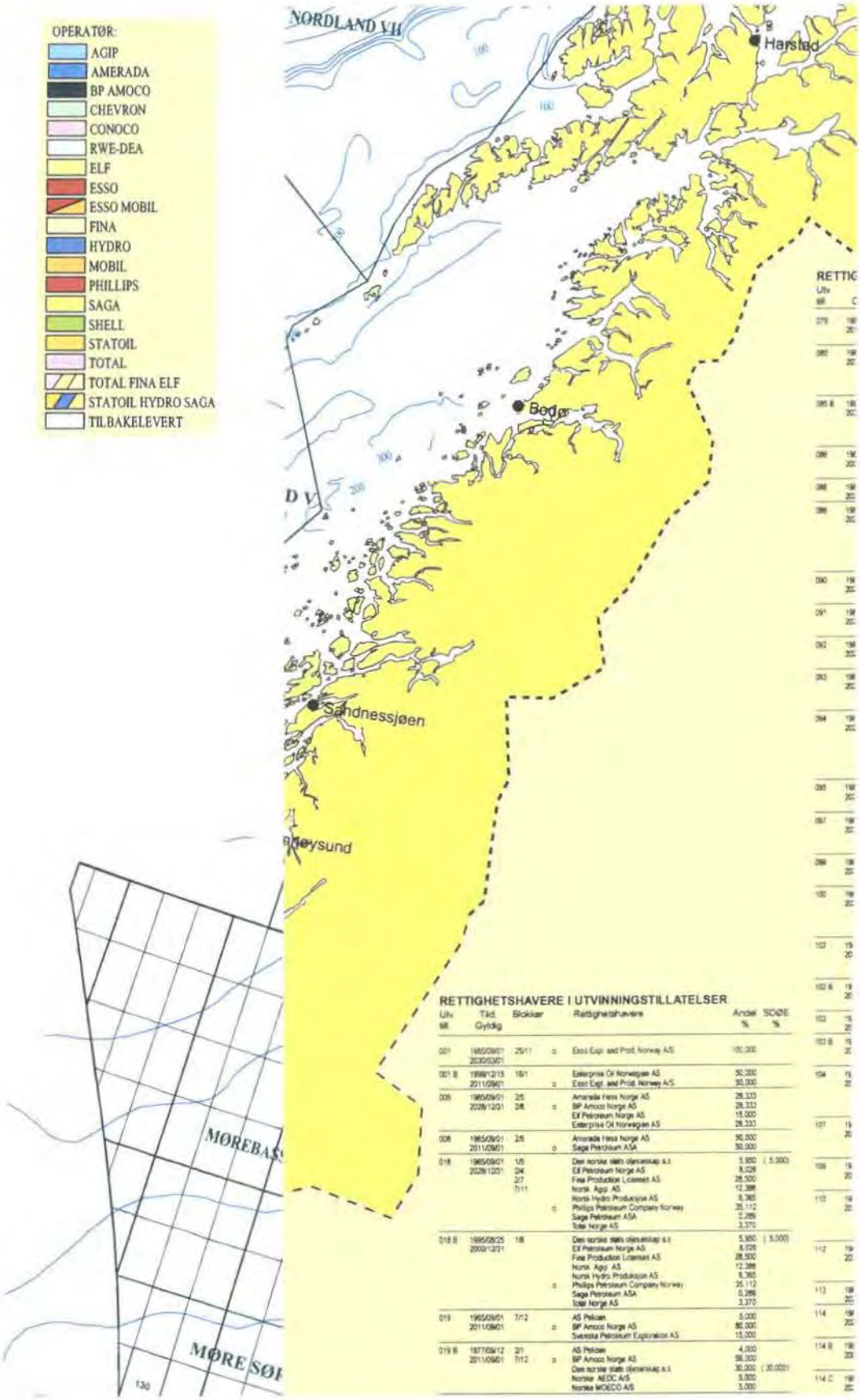

Figure 3.2: Petroleum fields and operators in Mid-Norway (from the *NPD*).

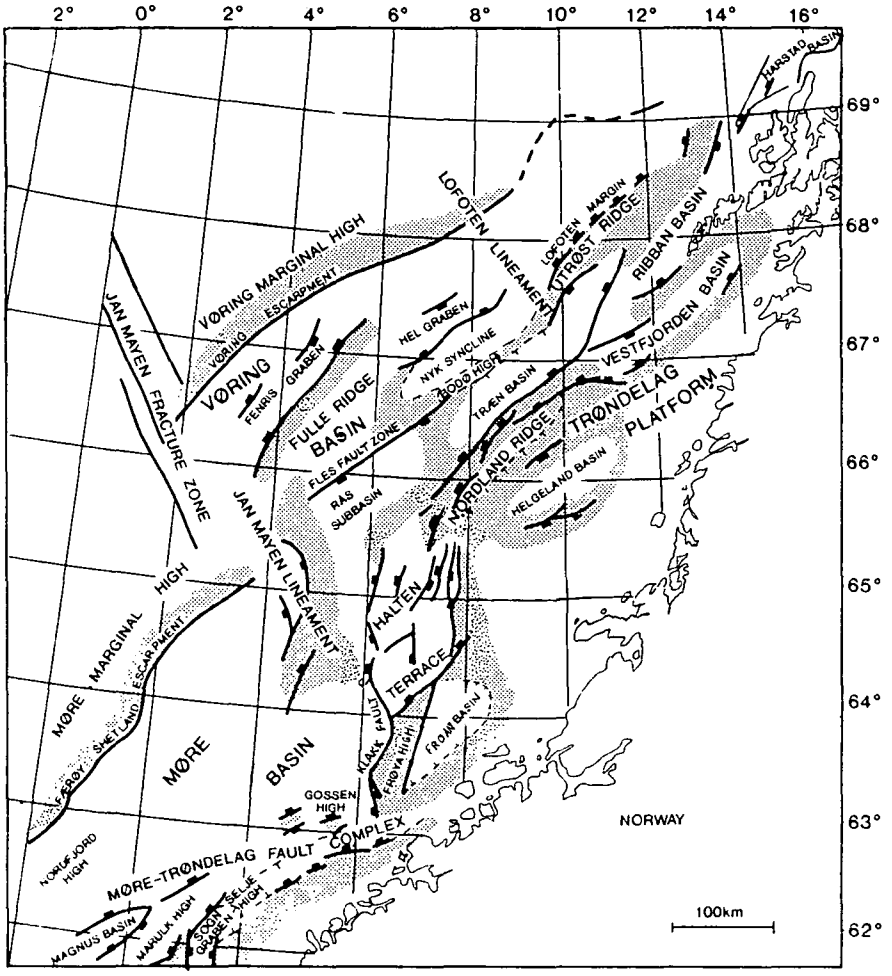

Figure 3.3: Location map showing the major structural features of Mid-Norway (from Jensen & Doré, 1993).

The Lower Cretaceous Cromer Knoll Group (**Figure 3.4**) deposited in this basin is characterised by marls that pass laterally and upwards into claystones which are locally silty near the top. The Lower Cretaceous succession suggests a eustatic high-stand during the deposition of the Cromer Knoll Group (Grigo *et al.*, 1993). Background deposition of claystones continued due to ongoing subsidence throughout the remainder of the Cretaceous to produce the Shetland Group (**Figure 3.4**).

The tectonic and sedimentary history of the Cenozoic Era is of particular importance since the principal source rocks are believed to have reached maturation and generation thresholds during this time interval. With the opening of the Atlantic Ocean, volcanic activity led to the deposition of tuffs between the end of the Palaeocene and the start of the Eocene. These tuffs comprise the Tare Formation (Jensen & Doré, 1993) and cap the Rogaland Group (**Figure 3.5** from Jensen & Doré, 1993). In the Halten Terrace area, gentle subsidence during

the Eocene to Early Oligocene meant the accumulation of the predominantly argillaceous Hordaland Group.

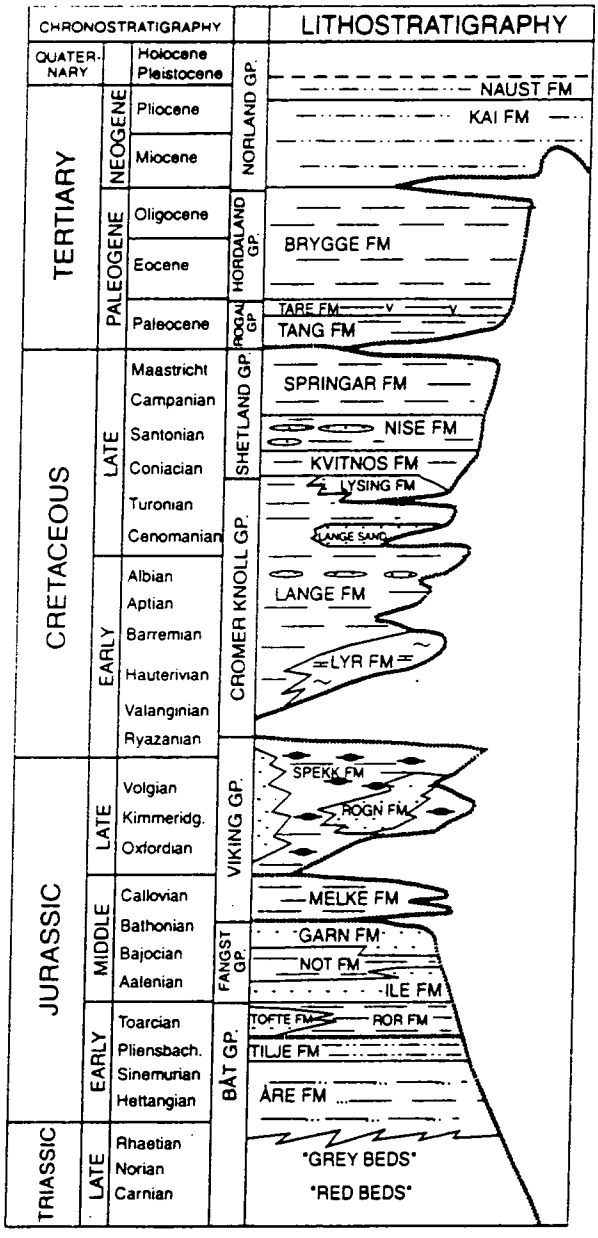

Figure 3.4: Generalised lithostratigraphy of the Halten Terrace (from Hermanrud *et al.*, 1998a).

Throughout the Cenozoic, erosion of the Fennoscandian Shield produced a significant amount of sediment that was deposited in the basins to the west. Uplift and erosion of the Shield was episodic in nature. The most important events took place during the Late Oligocene to Pliocene times (Jensen & Doré, 1993). The Nordland Group in the Halten Terrace area is a 1000-metre thick westward prograding clastic wedge. Differential amounts of uplift of parts of inner Mid-Norway (e.g. the Trøndelag Platform) resulted in widely varying lateral thicknesses of the Nordland Group (Jensen & Doré, 1993). The Nordland Group is

comprised of coarser sediments than the Hordaland Group. Throughout the Miocene and Lower Pliocene, deposition of the lower member of the Nordland Group, the Kai Formation (**Figure 3.5**), in an open marine environment produced a succession of shales with interbedded sandstones (Grigo *et al.*, 1993).

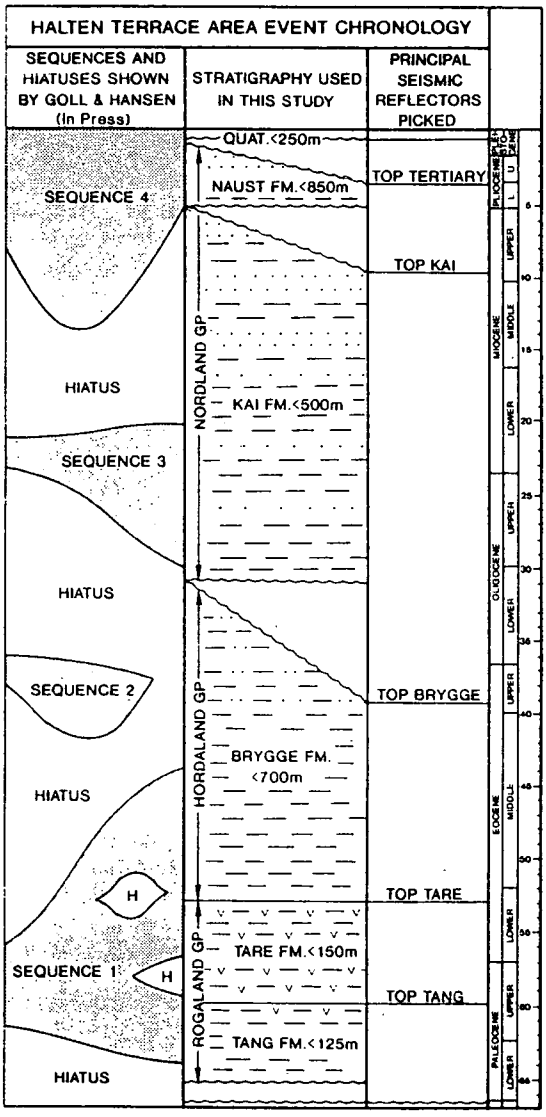

Figure 3.5: Cenozoic Halten Terrace stratigraphy (from Jensen & Doré, 1993).

Rapid subsidence and sedimentation took place during the Late Pliocene to Early Pleistocene (Hollander, 1984). Up to one kilometre of alternating fine sand and claystone was deposited during this period of only 1-1½ Ma to produce the Naust Formation (Jensen & Doré, 1993). Features of the Upper Pliocene succession permit the identification of a high-stand systems tract (Grigo *et al.*, 1993). Vik and Hermanrud (1993) believe that the deposition was again related to the uplift of the Fennoscandian Shield. 200-500 metres of glacio-marine sediments deposited in the later Quaternary cap the Pleistocene sediments (Vik & Hermanrud, 1993).

3.4.2 Tectonic evolution

The structural framework of the Mid-Norway continental margin is highly complex (cf. **Figure 3.3**). The evolution was compression-dominated prior to the Late Devonian when Iapetus closure took place and rift-dominated from the Late Carboniferous to the Late Palaeocene (Bukovics *et al.*, 1984). Only after crustal separation between Fennoscandia and Greenland during the Early Eocene did the area enter a true post-rift, passive margin setting (Bukovics *et al.*, 1984; Blystad *et al.*, 1995; Mjelde *et al.*, 1998).

The break-up and formation of the North Atlantic during the Tertiary more heavily influenced the tectonic development of the Norwegian Sea region than any other part of the Norwegian continental shelf. Two major plate tectonic episodes, the Caledonian Orogeny and the break-up of the North Atlantic, divide the tectonic history into three distinct epochs (Blystad *et al.*, 1995):

(A) The ***pre-Late Devonian*** epoch ending in the final closure of the Iapetus Ocean (the Proto-Atlantic) during the Caledonian Orogeny in Late Silurian and Early Devonian times.

(B) The ***Late Devonian to Palaeocene***: a period of episodic extensional deformation culminating in the continental separation of Eurasia and Greenland at the Palaeocene-Eocene boundary.

(C) The ***earliest Eocene to Present***: a period of active sea floor spreading between Eurasia and Greenland.

Both the Caledonian Orogeny and the continental break-up constituted important changes in the regional stress regimes. Prior to the Late Devonian, the plates were in a state of compression. This compression reverted to extension from the Late Devonian until continental separation during the Eocene. Following on from the Early Eocene, during sea floor spreading, the plates were, and are still believed to be, in a mildly compressive stress regime (Blystad *et al.*, 1995).

Following the Caledonian Orogeny, a period of orogenic collapse during the Middle to Late Devonian led to the development of intramontane extensional basins. Also associated with this orogenic collapse were regional scale strike-slip fault motions. During the 350 Ma that preceded the early Tertiary continental break-up, several other major rifting episodes effected the region. These most probably occurred in the Late Carboniferous, in the Early Permian, between the Late Jurassic and Early Cretaceous (Bøen *et al.*, 1984) and in the Late Cretaceous to Early Tertiary. Coupled with these major rifting events, several smaller scale extensional tectonic phases (Triassic, Early Jurassic, Aptian/Albian, post-Cenomanian, Late Cretaceous and Palaeocene) also affected the region. It is these 350 Ma between the end of

the Devonian and the early Tertiary that holds most interest to the petroleum industry (Blystad *et al.*, 1995).

Large amounts of tectonic activity affected the Norwegian Sea area during the Late Carboniferous to Early Permian. A block-faulted terrain probably generated during the later Early Permian rifting episode can be mapped beneath the Trøndelag Platform and the Halten Terrace. This block faulting appears to have effected most of the area and manifests itself as planar normal faults with a predominant NNE trend. The large Froan Basin was formed during this period as were many of the basins with the characteristic NNE strike. Further block faulting took place during the Middle to Late Triassic adding to the phase of basin development to the east of the Nordland Ridge and Frøya High (Blystad *et al.*, 1995).

The latest Bathonian (Middle Jurassic) was a time of transition into a strong late Middle Jurassic to Early Cretaceous rifting episode. This particular rifting episode is considered the most important tectonic period. Fault orientations associated with this event are most commonly N-S and NE-SW. These particular fault zones provide the major structural framework of the Mid-Norway region (Swiecicki *et al.*, 1998). Such faults now bound the Halten Terrace from the stable Trøndelag Platform to the east and the basins to the west (**Figure 3.3**). The rifting episode can be divided into three phases (Blystad *et al.*, 1995):

1) ***Bathonian*** to ***Callovian***;

2) ***Kimmeridgian***;

3) ***Neocomian.***

During phases one and two, the Halten Terrace formed the western, and tectonically most active, part of the Trøndelag Platform with pronounced flexuring and faulting taking place along the eastern edge of the Møre Basin. During the third phase, in the Neocomian (Early Cretaceous), the separation of the platform and adjacent terraces became progressively more accentuated (Blystad *et al.*, 1995).

The large-scale faulting and flexuring involved the basement, whereas the smaller scale tectonics on the Trøndelag Platform and the Halten Terrace involved listric faults which penetrated to more shallow depths. A characteristic feature of the second rifting phase (the Kimmeridgian) was the uplift and erosion of the western edges of the Trøndelag Platform which included the Halten Terrace, the Frøya High and Nordland Ridge (**Figure 3.3**).

Between the Neocomian rifting phase and the end of the Cenomanian (Mid-Cretaceous), the large Vøring and Møre Basins experienced thermal subsidence. There is evidence of probable faulting along boundary faults in the area as displayed by a pronounced expansion of the Lower Cretaceous strata. This faulting is believed to have taken place during the Aptian/Albian although there is a lack of well information to provide substantial evidence. Onlapping of post Cenomanian sediment on to the eastward sloping margins of the Gjallar Ridge and the westward side of the Trøndelag Platform produces a "steerhead structure".

This structure provides evidence for the onset of tectonic activity at the end of the Cenomanian (Blystad *et al.*, 1995).

The final intra-continental rifting episode initiated during Maastrictian to Palaeocene times. The result was continental separation between Eurasia and Greenland at the Palaeocene-Eocene boundary. Although rifting was centred west of the Møre and Vøring Highs it caused reactivation of fault zones such as the Jan Mayen Fracture Zone leading to local folding in the Vøring Basin (**Figure 3.3**). The late syn-rift period of the Maastrictian-Palaeocene episode involved central rift uplift that effected western parts of Mid-Norway and the north of the Jan Mayen Fracture Zone resulting in erosion of the Møre and Vøring Highs (Blystad *et al.*, 1995).

Following break-up, extensional deformation by normal faulting, Cenozoic subsidence and igneous activity in the Vøring Basin shows the spatial link between separation and melt generation due to crustal thinning. The rifting episode is characterised by massive emplacement of sill-like intrusives within the Vøring Basin sediments and basaltic lava flows (Mjelde *et al.*, 1998). The Møre Basin was "apparently tectonically quiet" and experienced continual subsidence during the Tertiary although lavas may hide the structural signature of the Early Tertiary tectonics (Blystad *et al.*, 1995).

Active spreading during the Earliest Eocene changed the stress field from extensional to weakly compressive. It is suggested that this stress field re-orientation created anticlines in Mid-Norway as a result of tectonic reactivation (in the reverse sense) along major mobile fault zones like the Jan Mayen Fracture Zone (Blystad *et al.*, 1995). These anticlines are believed to result from regional tectonic phases in the Late Eocene-Early Oligocene and the Late Miocene.

The last important tectonic period started in the Mio-Pliocene with a strong differential westward tilt and uplift of mainland Norway. Uplifting and tilting led to erosion of the sedimentary cover over Scandinavia creating the Plio-Pleistocene sequence that blankets the shelf (Borgerud & Svare, 1995). The increased Pliocene sedimentation rate is attributed to uplift as a consequence of the glacial rebound of Fennoscandia (Blystad *et al.*, 1995).

3.4.3 The burial history

Within the Halten Terrace, sedimentation took place in a uniform fashion across the whole region during Late Triassic to Early Jurassic times where the rate of burial averaged around 200 metres per Ma. During the Mid-Jurassic burial was progressively reduced down to less than 5 m/Ma. Within the Mid-Cretaceous period small amounts of erosion took place interspersed with hiatuses (Hollander, 1984).

Most is known about the burial history of the Halten Terrace during the Late Cretaceous and Tertiary. The subsidence history of the region over the last 50 Ma is shown in **Figure 3.6** (from Dahl & Augustson, 1993). The Halten Terrace subsided steadily at a rate of around 25 m/Ma between the Mid-Eocene and 25 Ma. More rapid subsidence occurred at a rate of ~80 m/Ma from the Late Oligocene to Early Miocene at 21 Ma. Throughout the Mid-Miocene subsidence was zero resulting in a hiatus lasting 8 Ma. The Miocene hiatus came to an end at 13 Ma with rapid uplift and erosion of up to 300 metres of sediment. These erosional magnitudes vary across the basin. From 11 Ma and into the Early Pliocene was another period of hiatus that was broken by the very rapid subsidence of the Plio-Pleistocene (**Figure 3.6**). The greatest burial rates seen and a significant proportion of the total subsidence of the region took place in this last 5 Ma. Deposition of in excess of 1000 metres of interbedded clay, silt and sand took place in 2-3 Ma producing a burial rate of over 300 m/Ma. Subsidence rates being consistent across the whole area during this period show the Halten Terrace to have subsided as one basin (Hollander, 1984). The rapid Plio-Pleistocene subsidence is the likely timing of oil generation in the Halten Terrace. Between 1 and 2 Ma the depositional system was peneplaned, either due to sea-level change or uplift, and there was up to 500 metres of erosion (Dahl & Augustson, 1993).

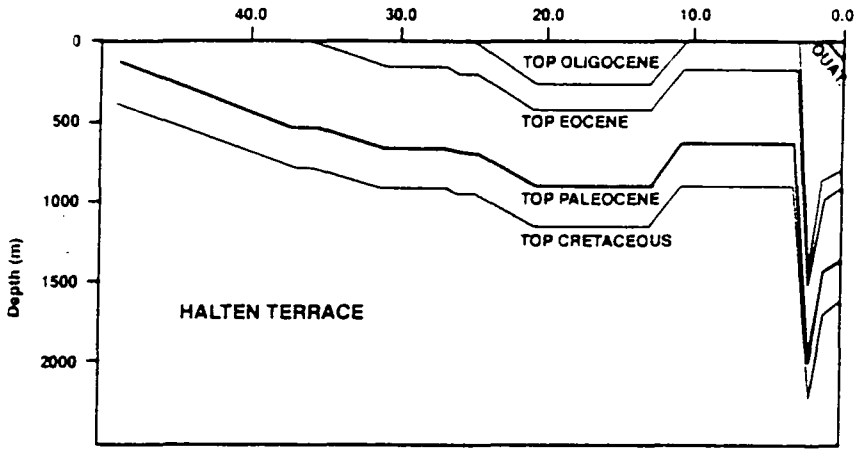

Figure 3.6: Subsidence curve for the Halten Terrace over the last 50 Ma (from Dahl & Augustson, 1993).

3.5 Previous studies of the Mid-Norway contemporary stress field

The contemporary stress field is the stress field that we measure at the present day. Previous studies of the contemporary stress field have used a number of different data forms to determine its type. Using 9 earthquake focal mechanisms mainly on the continental margin and with hypocentres ranging in depth from 10 to 30 km, Lindholm *et al.* (1995) were able to

determine the Mid-Norway stress situation. The dominant faulting situations are interpreted as strike-slip and reverse with ridge push assumed to be the major stress-generating mechanism. An observed maximum horizontal stress (S_H) trajectory of ~N135^{O}E is consistent with a spreading pole at 47.3^{O}N and 123.0^{O}E for the Mid-Atlantic spreading axis (Lindholm *et al.*, 1995). They admit that there is "considerable uncertainty in the individual focal mechanisms used but the extracted principal stress directions are remarkably consistent". The E-W S_H direction found from earthquakes in northern Sweden suggests that there is also a contribution to the Mid-Norway stress field from the Fennoscandian uplift centre in the inner Bothnian Sea (Lindholm *et al.*, 1995).

Van Balen and Skar (2000) report that earthquake focal mechanisms give NW-SE S_H directions with a dominance of strike-slip (mainly) and reverse fault motions. These authors also agree with ridge push being the dominant stress-generating mechanism.

Fejerskov *et al.* (1995) used a data set of 10 earthquake focal mechanisms, 17 borehole breakouts from 15 wells and 19 overcoring data, all from the Fennoscandian Rock Stress Database. The focal mechanisms from depths of between 5 and 30 km indicate compressive reverse faulting and a S_H direction of NW-SE. Borehole breakouts from between 1100 and 4800 metres also give a consistent S_H direction of NW-SE (Fejerskov *et al.*, 1995). The overcoring data indicate "very high stresses close to the surface" and whilst also giving a NW-SE orientation for S_H they show more scatter about the trend than the other types of data. Fejerskov *et al.* (1995) state that the consistency between different techniques increases confidence in the overall results especially since they come from widely varying depth intervals.

Milne *et al.* (2001) used global positioning system (GPS) data from permanent monitoring stations to demonstrate that 3-dimensional crustal deformation in Fennoscandia is dominated by glacial isostatic adjustment. The uplift is centred on the northern Bothnian Sea and surface movements in a NW-SE direction in eastern Sweden suggest a S_H direction orientated NW-SE producing a "mildly compressive stress regime" (Milne pers. comm., 2001) for offshore Norway.

Bukovics *et al.* (1984) report that at shallow levels in the sediment pile on the Mid-Norway continental margin, the structural style is characterised by a uniform seaward prograding clastic wedge of post-Eocene age. The wedge is little affected by faulting but there is "local evidence of mild compression". No direct line of evidence is stated to support this remark.

The descriptions above rely on data from depths greater than 5 km (earthquake focal mechanisms) to determine the relative magnitudes of the horizontal stresses. Data, such as borehole breakouts and overcoring, from less than 5 km depth, are used to determine the orientation of the horizontal stresses rather than the outright magnitude. GPS-derived movement directions of the crust confirm the S_H orientation to be NW-SE. By referring the

results to the known tectonic forces in the area, inferences about the driving mechanism behind the contemporary stresses are made. This study differs in the use of direct measurements of leak-off pressures to determine a magnitude for S_h. From knowledge of the magnitude of S_h relative to the magnitude of the other accurately and readily determined principal stress, S_V, inferences about Mid-Norway's contemporary stress situation are made.

3.6 Overpressure in Mid-Norway

The sections below review previous work on the overpressure in Mid-Norway. **Section 3.6.1** summarises the current knowledge on the presence and location of the overpressures in the region and explains how pore pressure magnitudes vary both throughout the depth interval and laterally. **Section 3.6.2** reviews work concerning the origin and timing of the overpressure and explains how different authors view its generation. Some authors adopt a disequilibrium compaction approach with others adopting late-stage fluid migration and "inflationary" approaches. A review of the causes of overpressure is given in **section 2.6.3** and also in Osborne and Swarbrick (1997).

3.6.1 The presence and location of the overpressure

Overpressured rocks are encountered at a range of depths and in different lateral positions throughout Mid-Norway. Hermanrud *et al.* (1998a) use "indirect methods" (i.e. interpretation of drilling parameters and wireline logs) to infer that fluids are hydrostatic from the seabed down to the Palaeocene shales of the Rogaland Group (**Figure 3.4**). Hermanrud *et al.* (1998b) do state that these methods produce results that are "highly uncertain". RFT measurements from sandstones of the Lysing and Lange Formations (**Figure 3.4**) show that overpressures develop in the middle of the Upper Cretaceous rocks (Hermanrud *et al.*, 1998). They state that P_p above the Jurassic appear to be laterally uniform across the whole region. Van Balen and Skar (2000) in their figure 2 show P_p to be hydrostatic from the surface to the top of the Miocene at 1.8 km depth. Overpressures then increase across the whole region throughout the Upper Cretaceous reaching a maximum of 30 MPa at the top of the Lower Cretaceous.

RFT measurements made in reservoirs adjacent to shales of the Jurassic Not and Ror Formations (**Figure 3.4**) are assumed indicative of pressures within the shales themselves (Hermanrud *et al.*, 1998). These measurements show that the Jurassic shales occur in two distinctly different pressure regimes (see **Figure 3.7** from Hermanrud *et al.*,

1998a). In the east, on the Trøndelag Platform, hydrostatic conditions and overpressures (< 7½ MPa) occur. This situation requires a step-back from the overpressures at the base of the Cretaceous (Van Balen & Skar, 2000). Between 20 and 35 MPa of overpressure are seen in the west on what is referred to as Halten West (Teige *et al.*, 1999; Skar *et al.*, 1999). The north-south trending Smørbukk Fault complex separates east and west Jurassic reservoirs. The major difference in fluid pressures provides evidence for different present day hydrodynamic systems in the area (Skar *et al.*, 1999).

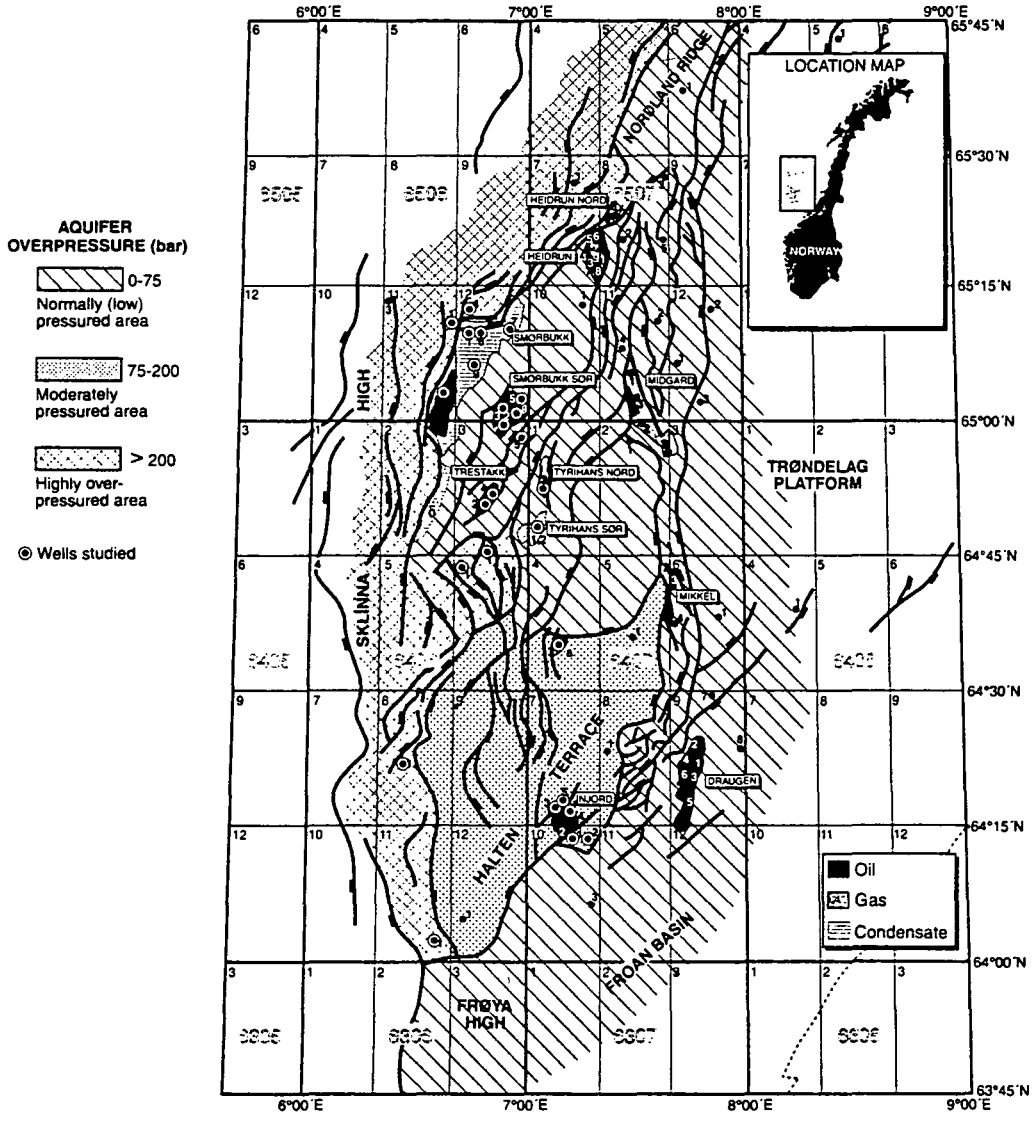

Figure 3.7: Halten Terrace map showing structures and pressure cells for the Jurassic (from Hermanrud *et al.*, 1998a).

Immediately to the east of the fault complex, but only in the south of the Halten Terrace, there is a moderately overpressured transition zone. This is shown in **Figure 3.7** (Hermanrud *et al.*, 1998a). Moving across the Smørbukk Fault complex, P_p increase in a stepwise fashion from east to west in a distribution best described by fault-bounded pressure cells (Koch & Heum, 1995; Van Balen & Skar, 2000). A schematic cross-section through the Halten Terrace from west to east is shown in **Figure 3.8** (from Van Balen & Skar, 2000) indicating where overpressures occur relative to normal pressures.

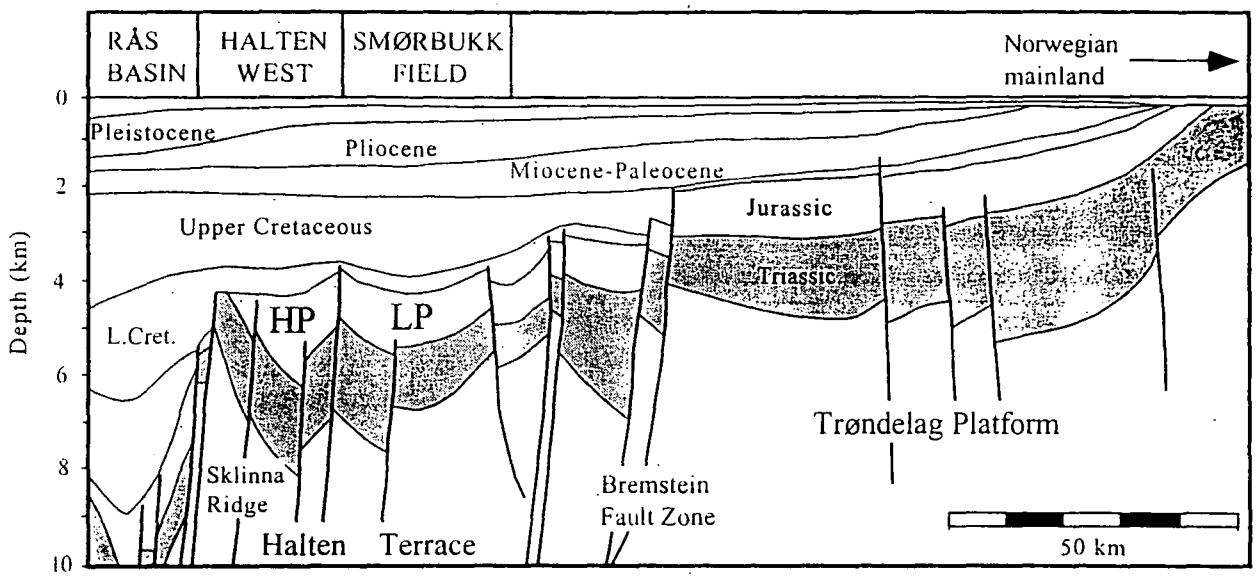

Figure 3.8: Schematic cross-section through the Halten Terrace from west (left) to east (from Van Balen & Skar, 2000).

3.6.2 The origin and timing of overpressure

The origin and timing of the overpressure in Mid-Norway is somewhat controversial. Of the mechanisms proposed by Osborne and Swarbrick (1997) as being potential generators of overpressure, three (disequilibrium compaction, fluid migration and quartz precipitation) are considered in the literature to be viable for Mid-Norway. Koch and Heum (1995) and Hermanrud *et al.* (1998a) suggest that the overpressures west of the Smørbukk Fault result from a combination of disequilibrium compaction and fluid migration. Hermanrud *et al.* (1998b) later backtrack by saying "undercompaction is not observed in shales [from] offshore Norway". By stating this they disregard any contribution to the overpressure by disequilibrium compaction. However, they state the importance of overpressure development by quartz precipitation reducing pore volume and explain that temperature, rather than effective stress, controls the porosity reduction and P_p increase.

Hermanrud *et al.* (1998a & 1998b) use porosity data to explain why the overpressures in Mid-Norway must be "late stage" as opposed to forming by disequilibrium

compaction at the time of sediment deposition. Sonic and resistivity logs indicate that different shale porosities occur in overpressured and normally pressured shales, yet the neutron and density logs do not show these differences. The porosity of Halten Terrace intra-reservoir shales determined from neutron and density logs does not vary significantly between highly overpressured and normally pressured areas, yet higher *apparent* porosities in overpressured units are shown by sonic and resistivity logs. They believe this is because sonic and resistivity logs respond to texture changes, such as microfracturing, brought about by overpressure. Hermanrud *et al.* (1998a) believe that the low porosities seen in overpressured rocks reveal a late stage generation of overpressure in normally compacted rocks.

Hermanrud *et al.* (1998b) state that a modest porosity reduction in an impermeable rock from 10% to 9.7% will lead to a P_p increase from hydrostatic to lithostatic pressures. The porosity reduction would be brought about by thermally controlled diagenesis assuming dissolution takes place along load bearing contacts. They believe this to partially be the cause of the Mid-Norway overpressures especially since neither neutron nor density logs show the elevated porosities usually associated with disequilibrium compaction. In Offshore Norway, Hermanrud *et al.* (1998b) note that the observed porosity correlates better with temperature than the effective stress for both shales and sandstones. Bjørkum (1996) also states that chemical processes, namely dissolution and re-precipitation of quartz, can produce the necessary excess P_p by reducing pore volumes. Bjørkum (1996) states that the occurrence of mica grains penetrating into quartz grains without being significantly deformed is evidence for the dissolution and reprecipitation of the quartz at low pressures.

Following on from the work of Hermanrud *et al.* (1998a), Teige *et al.* (1999) state that the sonic and resistivity logs differ between normally pressured and overpressured regimes in the Not and Ror Formations (**Figure 3.4**) while density and neutron logs do not show the same differences. They dismiss disequilibrium compaction as being the overpressure generating mechanism for the Jurassic and instead argue that sonic and resistivity logs respond to superimposed changes in the rock brought about by overpressure itself. If high porosity had been preserved then surely the density log would show this, yet it does not they argue. Teige *et al.* (1999) believe formations have individually compacted during burial.

Van Balen and Skar (2000) believe that the high Jurassic overpressures are caused by fluid flow from the 9 km deep Rås Sub-basin to the west of the Halten Terrace through fractures in the Mesozoic, deep seated Klakk Fault Complex (**Figure 3.8**). These authors believe that the rate and amount of sedimentation during the Plio-Pleistocene (see **section 3.4.3**) was not great enough on its own to create upwards of 30 MPa overpressures. Conversely, fractures contribute to the lack of overpressure around the Smørbukk Field by allowing lateral drainage out of the system to the north-east (Van Balen & Skar, 2000).

Skar *et al.* (1998) believe that lower overpressures within the Cretaceous shales of the Halten Terrace are consistent with disequilibrium compaction. The bulk density data and

the results of forward modelling of mechanical compaction indicate this. Density logs from Cretaceous shales occurring between 2 and 3 km depth show suitably elevated porosities consistent with undercompaction. They suggest diagenetic processes may have contributed to a partial reduction in porosity and possibly increased the fluid pressure below ~ 2.7 km depth. Skar *et al.* (1998) do not quote a precise mechanism for the deeper buried Jurassic shales overpressure (suffice to say thermally activated and lateral migration processes are important) which is in excess of that in the Cretaceous.

To close this section, many authors believe overpressures within the Cretaceous shales have come about due to disequilibrium compaction. There is a suggestion that high Plio-Pleistocene sedimentation rates (Hermanrud *et al.*, 1998a) contributed to the disequilibrium compaction generated overpressure. Further contributions at greater depths (around 2.7-2.9 km) from chemical compaction mechanisms (quartz precipitation) and lateral migration of fluids (Skar *et al.* (1998) have occurred.

The deeper Jurassic shales do not show the necessary high porosities for disequilibrium compaction to be the sole cause of the overpressure (Skar *et al.*, 1999). Instead lateral transfer of fluids through the Klakk Fault Complex from the Rås Sub-basin of the Møre Basin (in sub-Recent times – Skar *et al.*, 1998) combined with quartz precipitation are heralded as the main causes (Hermanrud *et al.*, 1998a). Discussions on the effects of overpressure on stress in Mid-Norway and the consequences of the late-stage generation can be found in **Chapter 6**.

3.7 Compilation and quality control of the Mid-Norway data

3.7.1 Source, form and type of data

The source, form and type of data has been summarised below in **Table 3.1**:

Company	Data set	Form	Record type
Norsk Hydro	*PI Erico*	Graphical record	Paper LOT graph
Norsk Hydro	*PI Erico*	Computer database	Numerical and statistical
Statoil		Computer database	Computerised LOT and XLOT graphs

Table 3.1: Summary table listing the company that provided the Mid-Norway data, the source of the data set, the form of the data and the type of record provided.

The computerised *PI Erico* database numerically lists well numbers, pumping pressure test types, depth of testing and pressure measurements in spreadsheet format. The *Norsk Hydro* graphical records provided a record of pumping pressure versus time for each test. *Statoil* further extended the database by providing computerised records of leak-off (LOTs) and extended leak-off tests (XLOTs) conducted in the last ten years.

3.7.1.1 Data provided by *Norsk Hydro*

Original LOT graphs provided by *Norsk Hydro* made it possible to directly pick values of LOP, ISIP or FCP. This stringent quality control exercise was applied to the data to ensure that the magnitudes of stress used in the rest of the study were as accurate as possible. The process of hand picking data from the graphs reduced the data set from 287 tests to only 145. This was because those test data used were either from LOTs or XLOTs. Formation integrity tests (FITs) were ignored. Also excluded were tests where the graph was of too poor quality to be properly, or conclusively, interpreted. Examples of the type of graphical record provided by *Norsk Hydro* are shown in **Figures 3.9** and **3.10**. **Figure 3.9** is an example of a good quality record where it is straightforward to pick the LOP and ISIP. A record where there is no clear LOP or ISIP is shown in **Figure 3.10**. This type poor quality record was considered unreliable and therefore discarded. It is the type of LOT response expected within a tightly interbedded clay-sand succession (Grauls pers. comm., 2001).

3.7.1.2 Data provided by *Statoil*

The digital *Statoil* data listed interpretations of LOP and ISIP and other information such as drilling mud weight used, depth of testing, drill bit diameter and lithological information. Using the large amounts of data from these records, pressure magnitudes were cross-plotted against time to create a "mock ups" of the original graphs (**Figure 3.11**). Following this, magnitudes of LOP, ISIP or FCP were noted and used to calculate S_h.

3.7.2 Quality control of the *Norsk Hydro* data

3.7.2.1 Purpose of the quality control

The majority of the *Norsk Hydro* data were computerised records listing interpreted values of pumping pressure read directly from records drawn up on-site by the drilling engineer and the test records stored by on-rig computers (Jørgensen pers. comm., 1999).

FORMASJONSSTYRKETEST

BRØNN NR.: 6406/12-2 Dato: 11.09.95

FORING:	2308 mTVD				FARTØY:	Deepsea Bergen			
DIAMETER	9 5/8	tommer	TYNGDE:	53,5 lbs/ft	HØYDE til RKB:				
MAKS TRYKK:	480	bar	GRAD:	P-110	Over vannflaten	23	m	Over sjøbunn	357 m

BORESLAM:					PUMPE:				
TETTHET:	1,55	g/cm³	VISC.	62 sec	TYPE:	Sement		KAPASITET:	1.200 l/m
P.V.	27	mPas	Y.P.	16,5 Pa	VOL./TIDSENH.	100	l/min	TILB. STR.:	210 l/m
FILTERTAP:	2,8	ml/min	GELEST.:	4 - 8 mPa					

FORMASJONSSTYRKE:

UNTATT STYRKE: 1,99 g/cm³ | OBSERVERT SPREKKE TRYKK: 108 bar | EKV. FORMASJ. STYRKE: 2,02 g/c

Volum/tid	Trykk	Volum/tid	Trykk	Volum/tid	Trykk	Anmerkninger
30	8	250	35	0	40	Tap til formasjonen er 200 liter.
70	22	270	85	1	92	Konklusjon LOT OK.
90	28	290	92	2	81	
110	32	310	98	3	76	
130	38	330	105	4	74	
150	45	350	110	5	72	
170	52	370	114	6	72	
190	59	390	116			
210	65	410	117			SIGN.: D. Sundfjord
230	72					

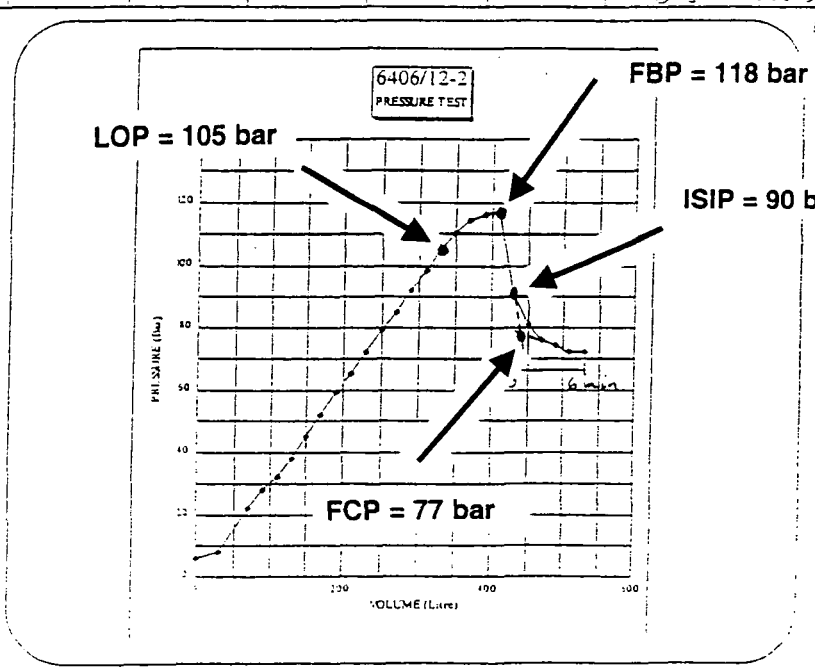

Figure 3.9: Good quality leak-off test record.

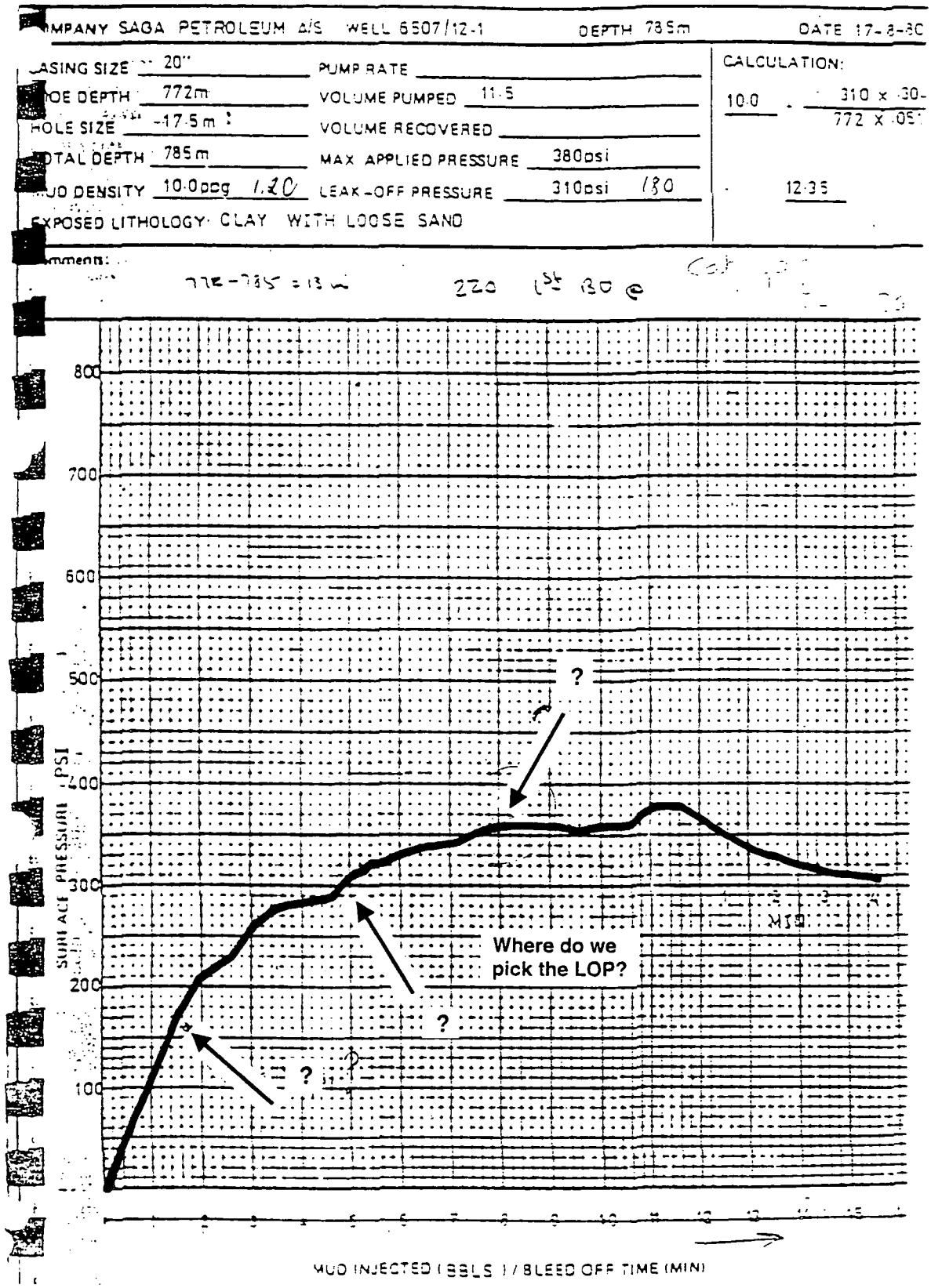

Figure 3.10: Poor quality leak-off test record typical of an interbedded clay-sand succession where mud is periodically lost into the sand.

Part of the quality control exercise was to compare the values in the *Norsk Hydro* database with those shown by the paper LOT records of each test. Where it was felt that neither the value quoted on the original record (see **Figures 3.9** and **3.10**) or the *Norsk Hydro* interpretation matched the true value of pumping pressure, a re-interpretation was made. As well as compiling a database of pumping pressure values felt to be the most accurate achievable, the graphs were assessed for quality. Poor quality graphs are difficult to analyse and the results they depict can mis-represent the S_h value. Inaccurate values of pumping pressure will have repercussions for results in the remainder of the study. The purpose of the quality control was to increase confidence in the accuracy of company interpreted pumping pressures used for S_h prediction. This was felt necessary because the majority of data from the other regions studied (the Central North Sea, the Gulf of Mexico, Brunei, Offshore West Africa, Onshore Nigeria and the Barents Sea) do not have the original records.

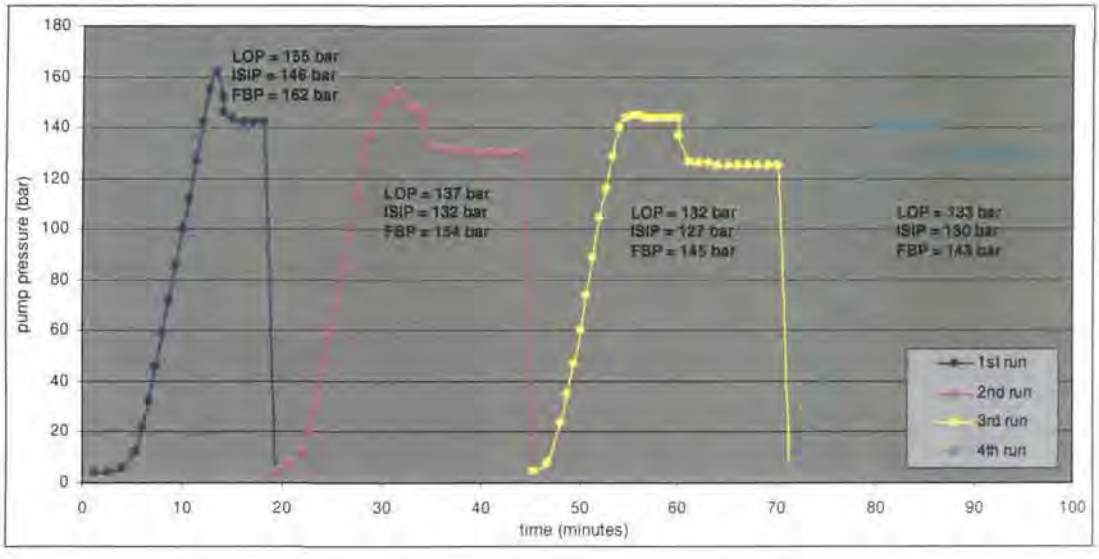

Figure 3.11: "Mock up" of an original extended leak-off test graph.

3.7.2.2 Technique adopted

The majority of the graphs provided by *Norsk Hydro* were incomplete leak-off tests because pumping rarely continued beyond the formation breakdown pressure value (see **Figure 2.13**). This meant that very few graphs showed true ISIPs or FCPs. The result was that in the majority of cases the leak-off pressure (see explanation in **section 2.4**) had to be chosen from the graph. A direct comparison between the *PI Erico* graphs and the *Norsk Hydro* database was made. Pumping pressure in the majority of cases reflected either the FIT or LOP. Thus, by assessing the extent to which the *Norsk Hydro* interpretations correlated with the *PI Erico* records, it is hoped that the same level of confidence can be applied to other

regional data sets lacking original data. Where good quality graphs existed new values for formation integrity value (FIT), LOP, ISIP or FCP were picked.

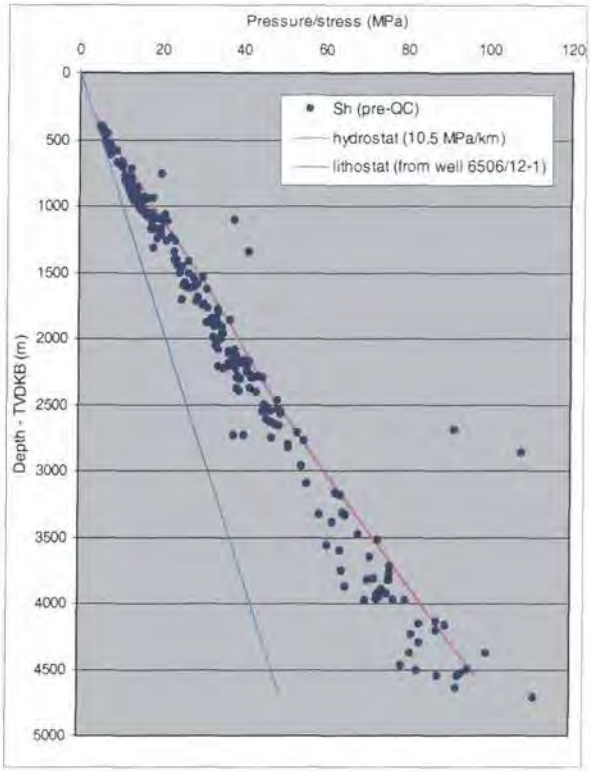

Figure 3.12: All *Norsk Hydro* pumping pressure data prior to the quality control.

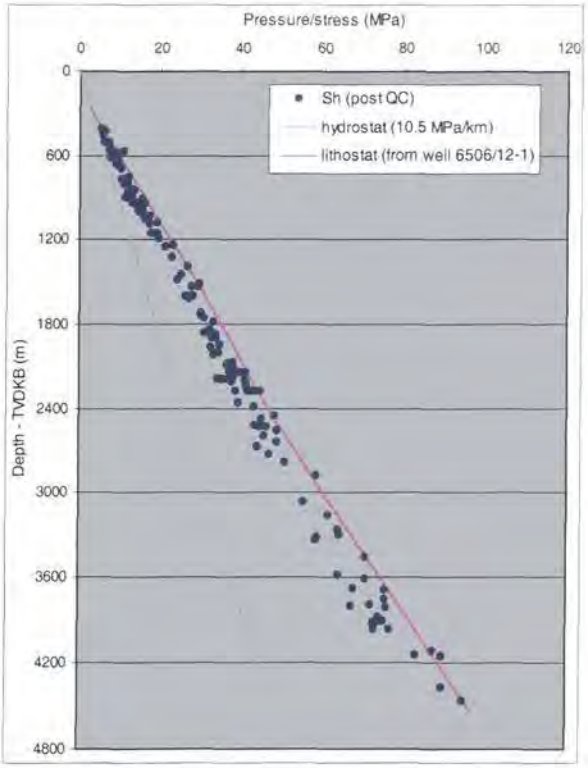

Figure 3.13: S_h measurements gained following the quality control.

3.7.2.3 Results and interpretations

287 leak-off tests had either a *PI Erico* graphical record or *Norsk Hydro* value for pumping pressure. **Figure 3.12** shows these S_h values calculated from the *Norsk Hydro*-provided data prior to quality checking. Out of these, 177 had graphs of suitable clarity that a re-interpretation could be made. The following types of pressure were chosen to calculate S_h:

Fracture closure pressure (FCP)	**5**
Instantaneous shut-in pressure (ISIP)	**21**
Leak-off pressure (LOP)	**119**
Formation integrity value (FIT)	**32**

Table 3.2: Pressure measurement used and the number of such occurrences.

Because FIT values do not give reliable estimates of stress they were discarded from the database. **Figure 3.13** shows the resulting measurements gained from the quality test. These 145 good quality pumping pressure measurements were used in the remainder of the Mid-Norway study.

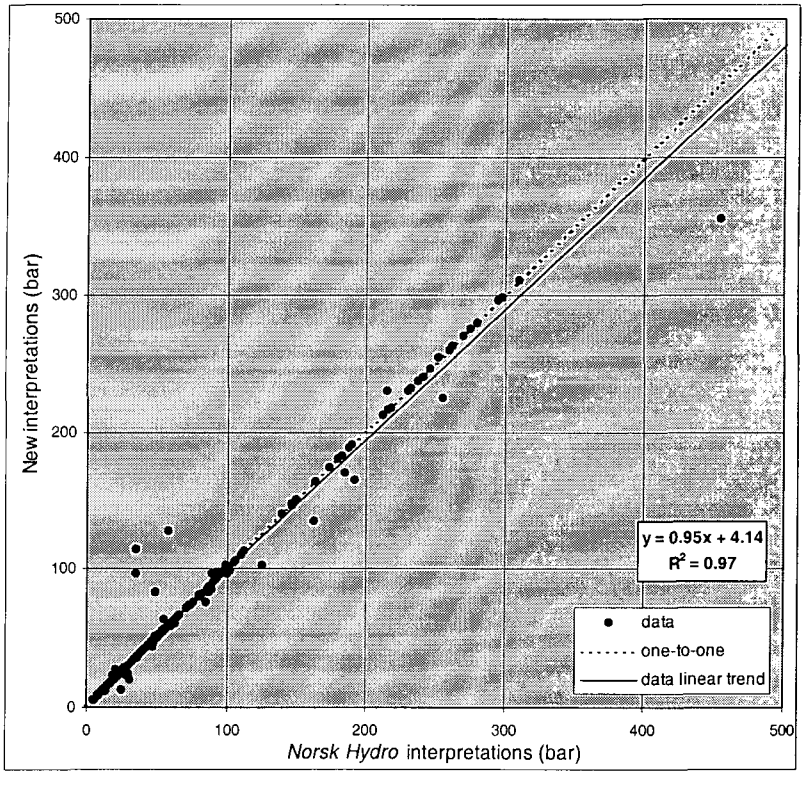

Figure 3.14: A comparison between the *Norsk Hydro* interpretations and the new interpretations for pumping pressure from the *PI Erico* graphs.

A direct comparison between the pumping pressure values noted by *PI Erico* and the *Norsk Hydro* interpretations showed that the *Norsk Hydro* interpretations of pumping pressure are below those stated on the *PI Erico* graphs. Results show that there is a 5 to 10% over-estimation in the pumping pressure value quoted on the *PI Erico* records compared to the interpretation by *Norsk Hydro*.

Following the re-interpretation of the paper LOT graphs, it can be stated that the *Norsk Hydro* interpretations very closely represent the values for pumping pressure that are quoted in the statistics table on the *PI Erico* graphs. A comparison between the *Norsk Hydro* database values and the new interpretations from the original *PI Erico* graphs is shown in **Figure 3.14** The one-to-one correlation line shows that the match is very good with the exception of a small number of points.

3.7.2.4 Conclusions

In conclusion, it seems that those pumping pressure data within the *Norsk Hydro* database are of good quality and reflect the true values ascertained from the tests. The S_h values should therefore be sound enough to produce valid results. From this quality checking procedure of the *Norsk Hydro* data set, it is felt that confidence in the quality of other data sets from other sources and regions has been gained, assuming they were compiled in the same fashion.

3.7.3 Mid-Norway pore pressure (P_p) data

In order to investigate the effects of overpressure on stress, good quality, direct measurements of pore pressures (P_p) in the wells are needed. P_p data come from a variety of different measurement techniques and are variable in their quality. The P_p data used in this study were restricted to those measured using either repeat formation tester (RFT) tools or formation multi-tester (FMT) tools. Of these types of measurements only those data described as "good" or "fair" were used.

Both RFT and FMT tools operate in a very similar way. Both isolate a small section of formation from the fluid within the wellbore and allow formation fluids to flow into chambers in the tool. A pressure gauge records the subsequent pressure build-up during inflow into the chambers. During any particular "run" these tools can make an unlimited number of measurements.

3.7.4 Mid-Norway "*comparable depth*" data

In order to analyse the effects of overpressure on the magnitude of minimum stress calculated from the pumping pressure measurement (be it LOP, ISIP, FCP etc.) a certain constraint has to be applied to the data. To determine whether pore pressure *in-situ* stress coupling is occurring within a region, it is necessary to create a data set of "appropriate" S_h and P_p measurements. This section explains how such a data set of S_h and P_p was created. Firstly, **Figure 3.15** shows the entire quality-checked Mid-Norway S_h data set with P_p measurements.

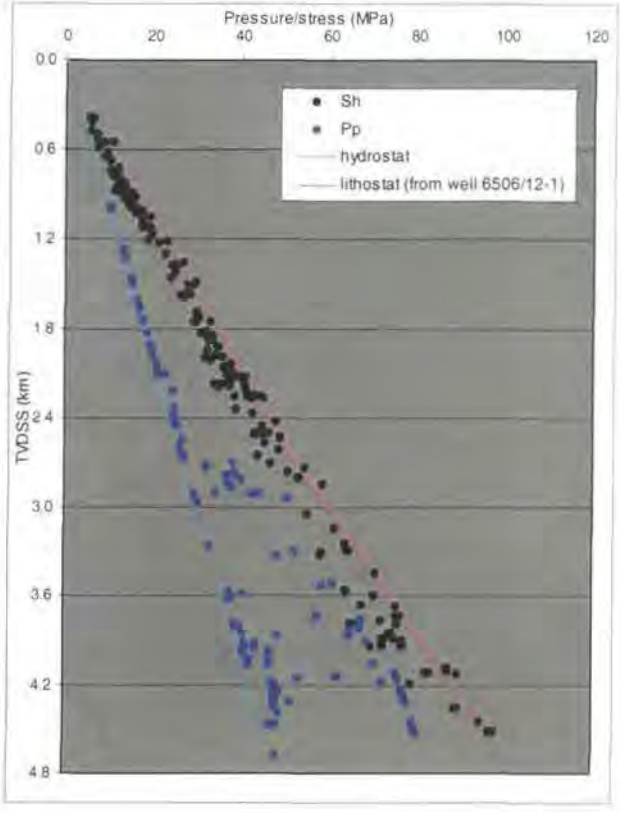

Figure 3.15: All quality checked Mid-Norway S_h and P_p data (from RFT measurements).

Whilst such a stress-depth plot (**Figure 3.15**) shows the evolution of S_h and P_p with depth on a broad, regional scale, it does not intrinsically show if and how P_p is effecting the stress magnitude. **Figure 3.16** again shows the entire data set but superimposed on top are the five S_h (red) and three P_p (yellow) measurements provided by *Norsk Hydro* for a single well. The well chosen as an example is 6406/3-2. It can be seen that within this single well there are P_p and S_h measurements that appear to be recorded at very similar depths.

Because these P_p and S_h come from an individual vertical well, it is safe to assume that there is not a huge amount of lateral discrepancy between the measurements. Closer inspection reveals that two-out-of-five S_h measurements have a P_p measurement recorded within one hundred vertical metres. These particular data are referred to as "*comparable depth*" data for this research and the 100 vertical metres constraint is an important one. The formal definition of the "*comparable depth*" data can be stated as:

"Data where a minimum stress measurement is paired with a pore pressure measurement recorded in the SAME WELL at a distance of LESS THAN ONE HUNDRED VERTICAL METRES from the depth of leak-off test."

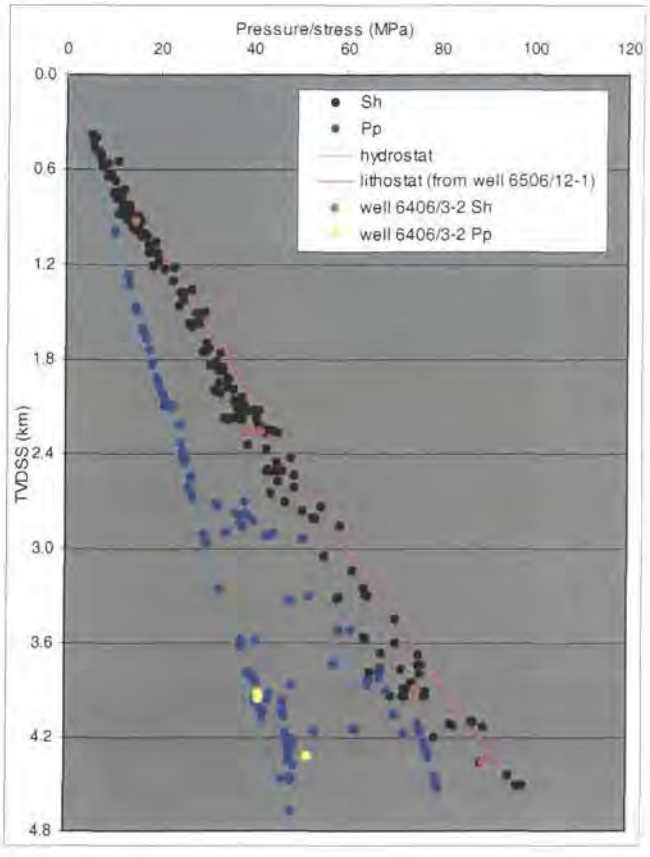

Figure 3.16: All quality checked Mid-Norway S_h and P_p data with data from well 6406/3-2 superimposed over the top.

It is believed that these data are the best to use for analyses into the degree of coupling that occurs. By using these data, we can be as sure as it is possible that any affect of pore pressure on stress magnitude is revealed in the pumping pressure magnitude. Using a P_p measurement taken as close as possible to the LOT improves the likelihood that the measurement represents the true P_p within the formation where fractures are being induced or re-opened during the test. Applying this depth constraint reduced the Mid-Norway data set

of 227 *Norsk Hydro* and *Statoil* S_h measurements to only 60. This data subset is shown on a stress-depth plot in **Figure 3.17**.

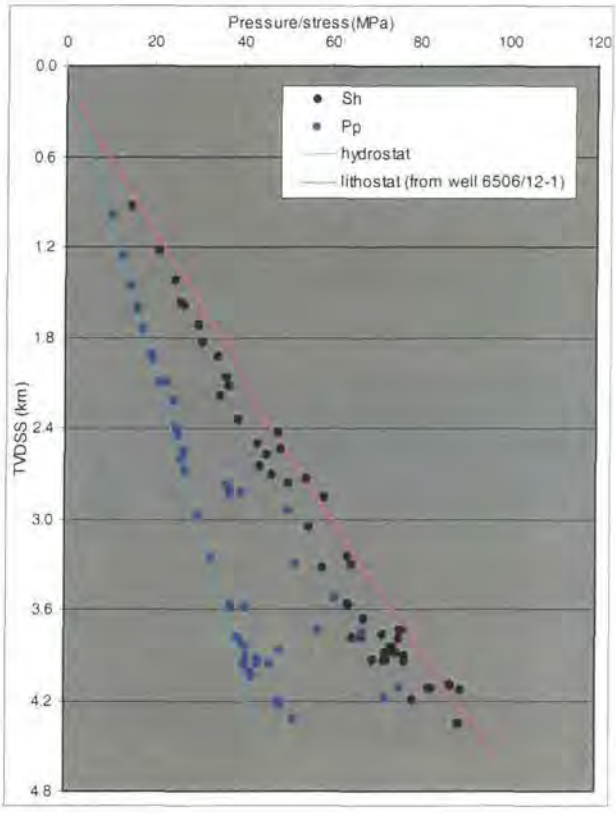

Figure 3.17: Mid-Norway "*comparable depth*" data subset.

3.8 Determination of the Mid-Norway lithostat

As well as constraining the magnitude of minimum *in-situ* stress as accurately as possible it is also important to constrain the lithostatic or overburden stress, S_V. This is the stress exerted by the combined weight of all overlying sediments, fluids and the atmosphere at a specified depth. A common assumption used by many authors (i.e. Matthews & Kelly, 1967; Gaarenstroom *et al.*, 1993) is that the lithostat increases with depth at a rate of 1psi/ft or 22.6MPa/km. While this approximately holds true there are many documented circumstances (cf. Hillis *et al.*, 1998) where it is shown that the lithostat ranges from 0.8psi/ft at shallow depth intervals to over 1.1psi/ft in deeper, well-compacted sections. This variation occurs because sediments generally become more compacted with depth and hence their

density increases. Following on from this, the true vertical stress (S_V) exerted at a particular depth can be expressed mathematically as:

$$S_V = Z\rho_b g \qquad \textit{(equation 3.1)}$$

Where: Z = vertical depth from the reference surface;

ρ_b = average bulk density of overlying sediments and fluids;

g = gravity.

Density logs sample sediment densities at set intervals down the wellbore. For Mid-Norway the density log for well 6506/12-1 was used because it provided the most complete record for the whole depth interval of almost 5 km. Readings were recording every 6 inches (15 cm) and for each of these sampling increments, the vertical stress (S_{Vi}) was calculated using:

$$S_{Vi} = \Delta Z \rho_{bi} g \qquad \textit{(equation 3.2)}$$

Where: ΔZ = the sampling increment;

ρ_{bi} = the bulk density of the depth increment.

To calculate the total vertical stress at depth $n\Delta Z$, each of the individual vertical stress increments needs to be summed together using (adapted from Sadler & Thorning, 1987):

$$S_V = \sum_{i=1}^{n} S_{Vi} \qquad \textit{(equation 3.3)}$$

Where: n = number of depth increments.

Problems arose, however, because the density log for well 6506/12-1, like many others, was not conducted at shallow depths. The log starts at 330 metres below the seafloor. Within the upper 300 or so metres, the sediment is most likely to be unconsolidated (Eaton & Eaton, 1997). The contribution of the top 330 metres of the sediment to S_V was calculated using an estimated bulk density for unconsolidated sediment. This estimate was added to the "real" density log data.

Within the Mid-Norway region, the water depth ranges from 220 metres to about 500 metres. However, the majority of the wells are drilled in a water depth of around 300 metres. To increase the accuracy of the Mid-Norway lithostat further, the pressure exerted by a 300 m water column was added to the contribution made to S_V by the sediments. Also taken into account was the small contribution of the atmosphere to the total vertical stress.

As shown by Eaton and Eaton (1997), bulk densities for air, sea water and unconsolidated sediment can be fairly easily estimated:

Depth interval (m)	Bulk density, ρ_b (g/cc)	Description
To sea level	0.001	Air
Sea level to sea bed (~300 metres)	1.06	Sea water
Sea bed to 330 metres depth	1.6	Clay, unconsolidated sediment

Table 3.3: Average bulk densities for air, sea water and unconsolidated sediment (from Eaton & Eaton, 1997).

Using the bulk densities in **Table 3.3**, it was possible to calculate the components of S_V produced by the weight of the atmosphere, the overlying sea water and the unconsolidated sediment interval where density log measurements were not recorded. These calculations used the appropriate depth, thickness or height increment for each component fed into *equation 3.2*. The resulting calculations were then summed with the stress increments from the density log measurements to produce an accurate representation of the way that the lithostat changes with depth. The final lithostat for Mid-Norway is shown in **Figure 3.18** with the S_h and P_p data removed for the sake of clarity.

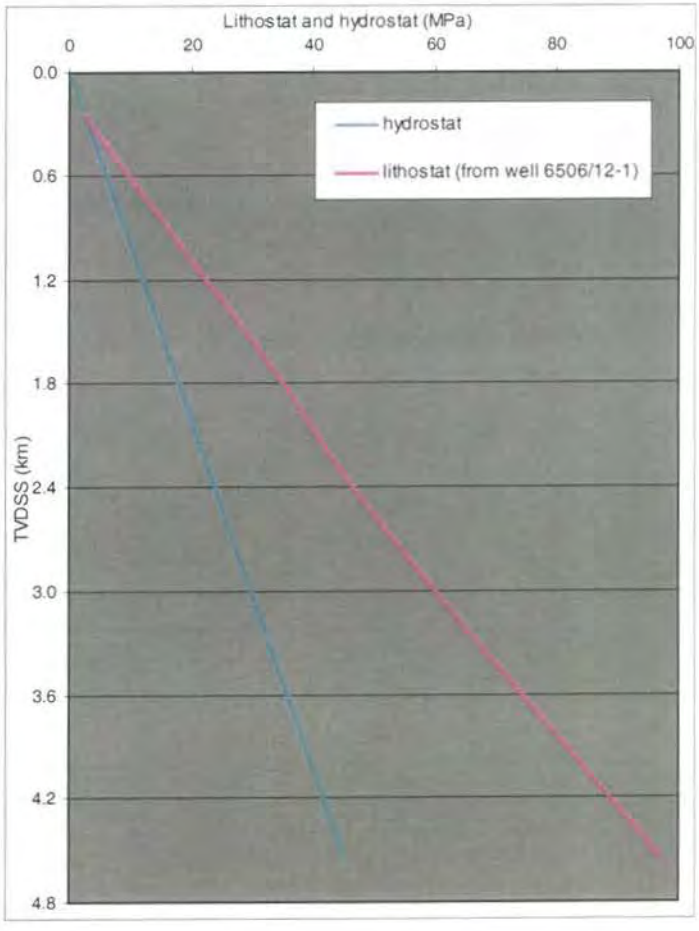

Figure 3.18: The calculated lithostat for Mid-Norway (from well 6506/12-1).

Chapter FOUR: Analysing the Mid-Norway Data

4 Analysing the Mid-Norway Data

4.1 Introduction

This chapter concentrates solely on Mid-Norway. Because of the good quality of the data, a large proportion of study time was spent on these investigations and analyses. For this reason it is felt that the results warrant a separate chapter.

Initial analyses in **section 4.2** show stress and pore pressure data plotted on stress/pressure-depth plots. The objective is to investigate the relationship between S_h derived from LOTs and S_V and the relationship between P_p and hydrostatic pressure. By looking at S_h and P_p data from the "*comparable depth*" data set (see **section 3.7.4**), the effects of overpressure on minimum stress magnitude could be investigated. Plotting the stress data by a number of different parameters (lithology, wellbore diameter, pumping rate etc.) in **section 4.3** investigated whether differences in the testing procedure and in the rock properties were responsible for variabilities in stress magnitude.

The minimum *in-situ* stress data are used to create lower bounds to leak-off pressures (**section 4.4**). Lower bounds were created initially from all S_h data and then from the 60 "*comparable depth*" data to see if differences in the derived trends occurred as a result of the number of data used. P_p data are used to create an upper limit to P_p as another means of estimating minimum stress. Finally the "*comparable depth*" data are used to investigate the presence of pore pressure *in-situ* stress coupling in Mid-Norway (**section 4.5**).

Section 4.6 reviews a separate investigation into the use leak-off pressures (LOPs) and instantaneous shut-in pressures (ISIPs) to calculate minimum stress. The *Statoil* multi-cycle extended leak-off test (XLOT) data have been used for this purpose. Results can provide insights into the contemporary stress situation. They also have important implications for the calculation of S_h in Mid-Norway. The results of all the Mid-Norway analyses are summarised in **Section 4.7**.

4.2 Stress-depth plots

The Mid-Norway data set of 227 S_h measurements derived from LOTs has been plotted wholesale on a stress-depth plot (**Figure 4.1**) to look for basin wide patterns in pore pressure and *in-situ* stress data. The investigations in **section 4.2** can be summarised as:

- Quantifying the amount of variability in the magnitude of S_h at depth;
- Quantifying the magnitude of overpressure variation at depth;
- Looking at the effects of overpressure on the magnitude of S_h and the variation in S_h.

On the stress-depth plots, as means of reference, is the lithostat as created from the density log of well 6506/12-1 (see **section 3.8**) and the hydrostat. The hydrostat was created assuming a water density of 1.01 g/cc, i.e. a pressure gradient of 0.45 psi/ft or approximately 10 MPa/km. The red, brown and darker blue lines are gradient lines referenced to the lithostatic gradient. The red line represents 70% of the lithostat (S_V), the brown line is 80% S_V and the darker blue line is 90% S_V (or an approximate gradient of 20.3 MPa/km).

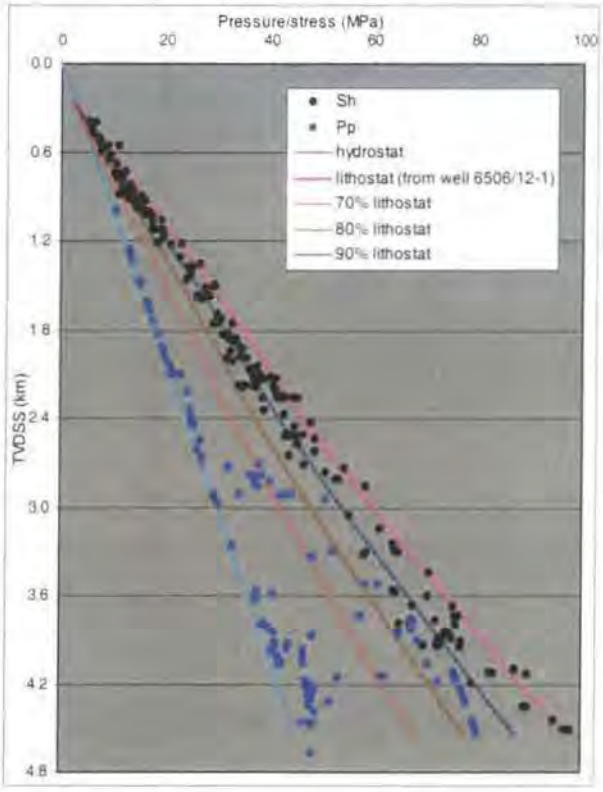

Figure 4.1: All S_h and P_p data for Mid-Norway.

Considering all the S_h data (**Figure 4.1**), at a given depth, scatter in their magnitude is limited. The maximum scatter occurs at 3.75 km depth where a variability of 13 MPa occurs. Statistically this is a 20% variation of the outright magnitudes of in excess of 60 MPa. Considering the shallow depths (<2 km) where the bulk of the S_h data fall, scatter is less than 5 MPa. Depths >2 km show more scatter in S_h despite there being fewer data at these depths. **Figure 4.2** shows the S_h data with envelopes fitted to the left and right edges of the swarm. The difference between left and right envelopes (quantification of the S_h scatter) is given every 250 metres in **Table 4.1.**

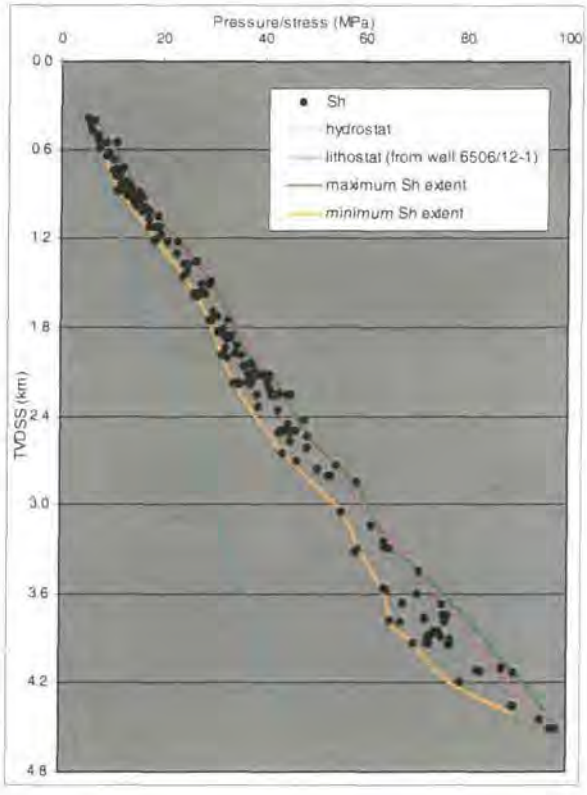

Figure 4.2: S_h data with envelopes showing the maximum and minimum extent of S_h with depth.

Of note is the close proximity many S_h measurements have to the lithostat at all depths. All data are in excess of the red 70% S_V line and the majority are greater than 80% S_V (brown line in **Figure 4.1**). As the darker blue line shows, at depths >3 km, a significant proportion of S_h measurements are greater than 90% of the lithostat. When looking at the swarm of S_h data in **Figure 4.1** it can be seen that the left-hand edge progressively moves in the direction of S_V with an increase in depth. The left edge is close to 70% S_V up to 1 km depth, crosses 80% S_V at 1.2 km and is between 85% and 90% S_V up to 4.2 km. Below 4.2 km all data are in excess of 90% S_V. To examine how S_h measurements evolve relative to the lithostat with depth, S_h was normalised to S_V at the depth of testing to create the S_h/S_V value shown in **Figure 4.3**. The greatest amount of scatter in the ratio occurs in the upper 1 km interval where S_h varies widely between 72% and 108% of S_V. There are also two points in excess of 120% S_V. However, below 1.2 km the data start to cluster together to produce a more linear form centred just in excess of 90% of the lithostat. The average ratio for depths >1.2 km is 0.93.

Depth (kilometres)	Variability in S_h (MPa)
0.5	2
0.75	3
1.0	3
1.25	4.5
1.5	5
1.75	4.5
2.0	5.5
2.25	9
2.5	7.75
2.75	8.5
3.0	6
3.25	6
3.5	10
3.75	13
4.0	13
4.25	12.75

Table 4.1: Variability in the magnitude of S_h at 250 metre intervals.

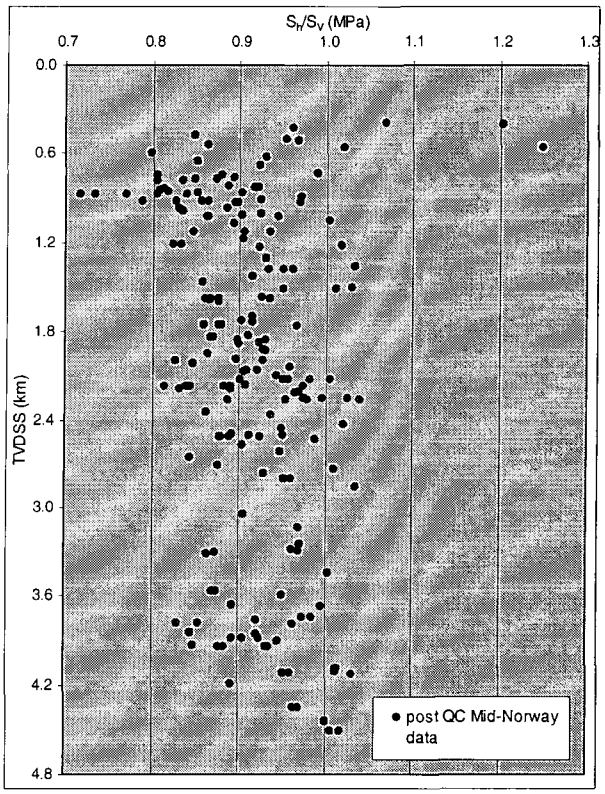

Figure 4.3: S_h normalised to S_v.

The P_p data in **Figure 4.1** display more scatter than the S_h data. At 3.8 km depth where S_h data show a 13 MPa variation, P_p data range from hydrostatic (~40 MPa) to 70 MPa. A pore pressure of 70 MPa at 3.8 km depth represents 30 MPa of overpressure or a pressure equal to 85% S_V. Up to 2¾ km, P_p are approximately hydrostatic. Below 2¾ km some overpressures appear. However, within the depth interval of overpressured fluids there are measurements that remain hydrostatic and the magnitude of overpressure is variable.

Considering P_p and S_h data together (**Figure 4.1**) shows that in the upper 2¾ km where normal pressures exist, S_h measurements are in excess of 80% lithostatic and show up to 8½ MPa of variability (**Figure 4.2** and **Table 4.1**). Below 2¾ km where greater overpressures occur, the S_h values display up to 13 MPa scatter. They also increase their magnitude towards the 90% S_V line (confirmed by **Figure 4.3**).

In order to investigate whether the increase in S_h towards the lithostat (see **Figure 4.1**) and amount of S_h variability is a consequence of overpressure, the "*comparable depth*" data subset was used (see **Figure 3.14**). These 60 data pairs were separated into those that had a hydrostatically pressured P_p (**Figure 4.4**) and those with an overpressured P_p measurement (**Figure 4.5**). The criterion used to define hydrostatically pressured data was that a data pair with a P_p less than 105% of the hydrostat at the depth of measurement was classified as being normally pressured. This 5% flexibility was felt necessary to account for water density differences (e.g. salinity variations) throughout the depth interval and across the region that would alter the magnitude of the hydrostat.

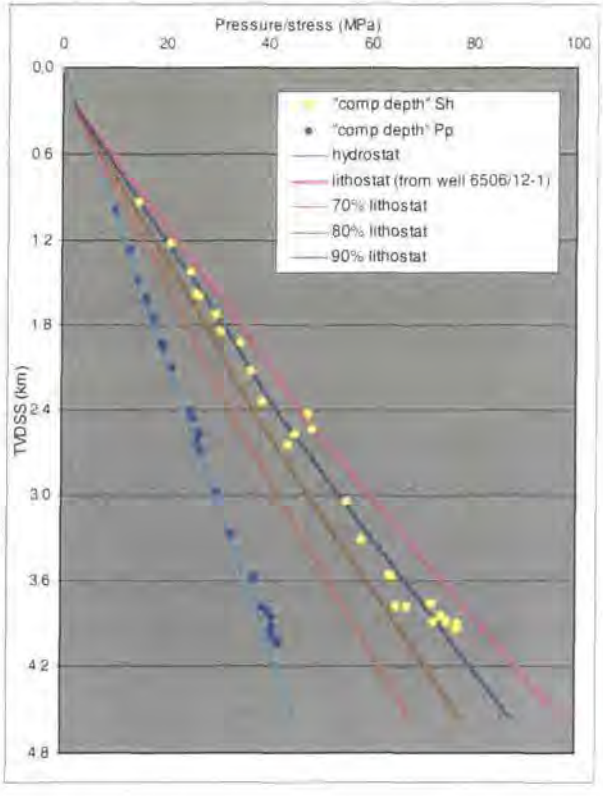

Figure 4.4: Normally pressured "*comparable depth*" data.

Figure 4.4 shows that there is a tightly constrained trend in S_h measurements for hydrostatically pressured fluids. Significant scatter (**Table 4.2**) only occurs where there are "outliers" at 2½ km and 4 km. The S_h measurements are consistently high and range between 80% and 100% S_V. Three-quarters of the data sit on or within 2 MPa of the 90% S_V gradient.

For the S_h measurements associated with overpressured fluids (**Figure 4.5**) the data produce more scatter and reach greater magnitudes than the normally pressured S_h measurements. S_h measurements in **Figure 4.5** have magnitudes that are mostly greater than 90% S_V. P_p measurements show more variation at a given depth than the S_h data. Below 2¾ km, overpressures are all > 6 MPa above the hydrostat but at 4.2 km the variation in P_p is 30 MPa. A quantitative comparison between the amount of scatter in S_h by 500-metre increments for normally pressured and overpressured data is given in **Table 4.2.**

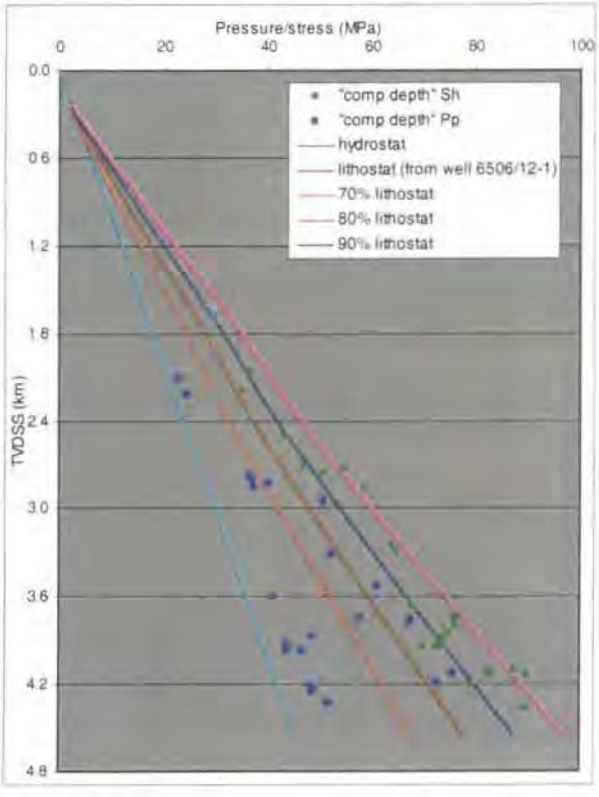

Figure 4.5: Overpressured "*comparable depth*" data.

Depth interval (km)	Variability in normally pressured S_h (MPa)	Variability in overpressured S_h (MPa)
1 – 1½	1	-
1½ - 2	2	2
2 – 2½	8	2
2½ - 3	7	10
3 – 3½	3	1
3½ - 4	10	13
4 – 4½	-	13

Table 4.2: Variability in S_h magnitude for normally and overpressured data.

By comparing the S_h magnitudes in **Figures 4.4** and **4.5**, a quantitative link between the magnitude of S_h and the amount of overpressure cannot be stated. The "*comparable depth*" data set shows importantly that S_h magnitudes are consistently high relative to the lithostat (greater than 80% S_V) regardless of the P_p. In the upper 2½ km in **Figure 4.4** the S_h values produce a linear trend along the 80% S_V line. Comparing this relationship to the data from > 2½ km in **Figures 4.4** and **4.5** where P_p greatly varies, the scatter in S_h is much more noticeable (up to 13 MPa at 4.2 km in **Figure 4.5**). It can therefore be stated that P_p variations are seen together with S_h variations but it is not possible from **Figure 4.1** and **Figures 4.4** and **4.5** to precisely quantify the relationship.

4.3 Understanding the patterns in stress-depth plots

As well as comparing overpressure magnitude and S_h magnitude (**section 4.2**), S_h data have been plotted on stress-depth plots by a number of different parameters. This has been done to investigate whether the scatter seen in the data revealed by **Figures 4.1, 4.2, 4.4** and **4.5** can be explained by a parameter other than P_p variation. There are many accounts of different drilling and rock mechanical parameters affecting the magnitude of the pumping pressure at leak-off; thus the magnitude of S_h (Engelder pers. comm., 2000). These include lithological differences, variations in the diameter of the drill bit used to drill the well, pumping rate variations and variations in the age of the rock encountered (essentially rheological variations). Also taken into account is the position of the well relative to major structures. As described in **section 3.6**, fluid pressures to the west of the Halten Terrace are up to 30 MPa overpressured relative to fluids in rock at the same depth to the east (Teige *et*

al., 1999). It is hoped that analysing S_h and P_p based on structural location will explain S_h scatter and also provide insights into the relationship between S_h and P_p.

4.3.1 Lithology and S_h magnitude

Rock mechanical theory predicts that certain lithologies sustain greater stress magnitudes than others. For example, in sandstone stress magnitudes are often seen to be lower than in shale. The reason for this difference is considered rheological (Engelder, 1993). More detail can be found in **Chapter 6**.

Figure 4.6 shows the S_h data with a recorded lithology plotted to investigate whether the test lithology exerts a control on S_h. It is clear from **Figure 4.6** that there is no link between lithology and stress magnitude. No one lithology sustains a higher or lower stress magnitude. Shale is the most common lithology where a test has been performed with 47% of all the S_h measurements. S_h magnitudes recorded in shale scatter throughout the entire cloud of data in **Figure 4.6**.

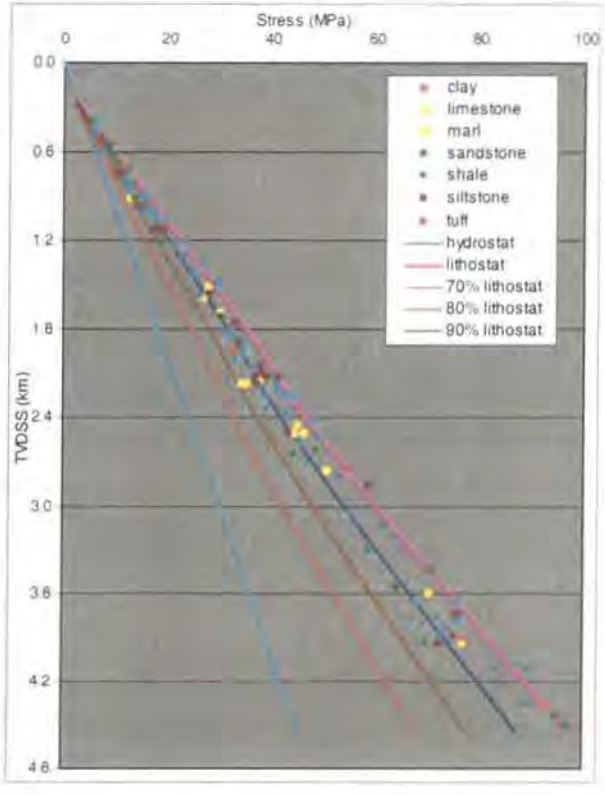

Figure 4.6: All S_h data plotted by the lithology in which the test was conducted.

4.3.2 Wellbore diameter and S_h magnitude

Rock mechanical theory predicts that sample strength scales with sampling area. The statistical reasoning is that larger samples are more likely to contain flaws or anisotropies capable of reducing material strength. Following this reasoning it would appear possible that larger wellbores (with greater surface areas) are more likely to contain weakness that result in a lower recorded magnitude for pumping pressure (Engelder pers. comm., 2000).

The entire Mid-Norway data set is plotted (**Figure 4.7**) by wellbore diameter where the LOT was performed and shows that wellbore diameter differences do not explain the scatter in S_h at a given depth. This result is revealed by the data from the wellbore with a diameter of 8½". Stress magnitudes within this small diameter hole range from 80% lithostatic to supra-lithostatic values.

Also of note is that the correlation (described above) between the magnitude of S_h and the wellbore diameter is not applicable here. In fact where data from the 12¼" wellbore overlap with the 8½" wellbore data at ~2½ km there is not a difference in recorded S_h between the two data clusters. Fitting linear regression lines through the data for the each of the wellbore diameters (**Figure 4.8**) suggests that the result is in fact the opposite of that predicted by rock mechanical theory. Between 1.3 and 2.5 km, the 8½" wellbore shows lower S_h magnitudes than the 12¼" wellbore and between 3.2 and 4.2 km, S_h magnitudes for the 6" wellbore are lower than those for the 8½" wellbore through the same depth interval.

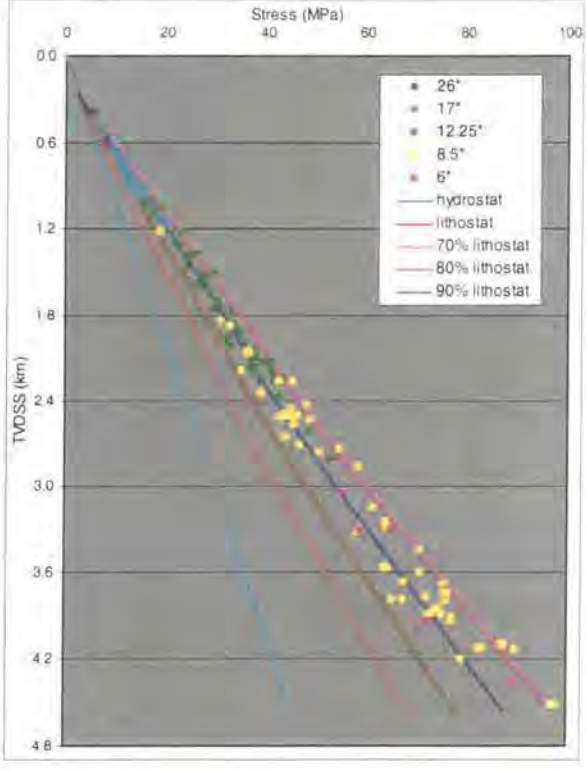

Figure 4.7: All S_h data plotted by wellbore diameter in which the test was conducted.

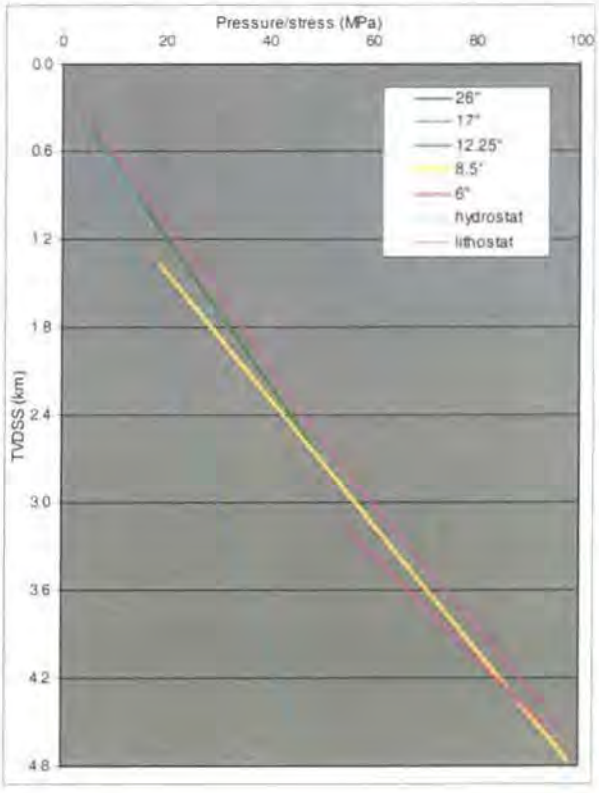

Figure 4.8: Linear regression lines fitted to the S_h data based on wellbore diameter.

4.3.3 Pumping rate and S_h magnitude

Variations in the pumping rate of mud into the wellbore during a LOT can also effect the magnitude of the derived S_h value. This is because faster pumping rates do not allow drilling mud to infiltrate the formation and should thus lead to higher recorded wellbore failure pressures (Jørgensen pers. comm., 1999). **Section 2.4.2** gives the mathematical expression (*equation 2.21*) of how infiltrating drilling mud raises the formation P_p and thus decreases the measured wellbore failure pressure (the LOP).

The data in **Figure 4.9** show pump rate variations of more than an order of magnitude. However, variations of between 10 and 400 litres per minute (l/min) do not produce variations in S_h magnitude. For example at 2 km depth in **Figure 4.9**, pumping rates vary between 40 and 140 l/min yet the data points do not show a systematic increase in S_h with an increase in pump rate. The data in **Figure 4.9** can be interpreted as not showing S_h variations as a consequence of pumping rate differences and pumping rate does not account for scatter.

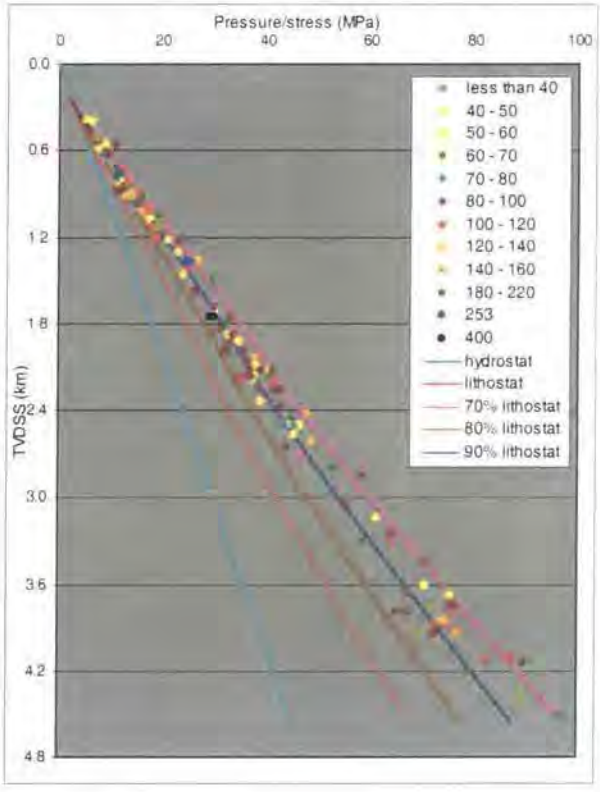

Figure 4.9: S_h data plotted by leak-off test pumping rate.

4.3.4 Age of the rock and S_h magnitude

The age of a particular rock type can also have an effect on the magnitude of S_h derived from leak-off tests. This would be a consequence of the amount of burial and compaction a rock has undergone thereby effecting the density and rheological properties.

Plotting the S_h data by age, as derived from the Formation or the Group (**Figure 4.10**), does not reveal a link between S_h magnitude and age. Considering data from between 1.8 and 2.4 km depth where old and young rocks occur at the present, older formations (i.e. Triassic and Lower Jurassic ages) do not show greater stress magnitudes than younger, presumably less well-compacted, sediments (i.e. Miocene to Recent ages). This is interpreted as evidence for the age of the rock not controlling the magnitude of the contemporary S_h.

Figure 4.10 reveals that rocks of Lower Cretaceous (darker orange) age vary in their current depth of burial (when considering the data available) between 2 km and 4½ km. There is an increase in S_h magnitude in the Lower Cretaceous rocks from 85-90% S_V to supra-lithostatic with an increase in the current depth of burial. Lower Jurassic (darker blue) rocks show a similar increase. The S_h magnitude is 45 MPa (85% S_V) at 2.6 km and lithostatic at their maximum occurrence of 4½ km depth. From these pieces of evidence it can be

interpreted that the depth of burial of a formation, rather than the actual age, has a greater control on the magnitude of S_h.

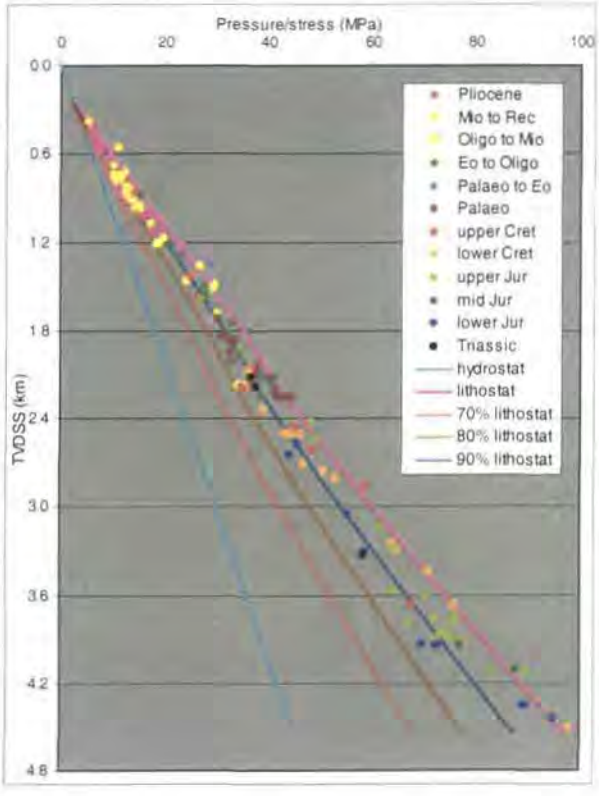

Figure 4.10: S_h data plotted by age of the rock that the test was conducted in.

4.3.5 Geographical position and S_h magnitude

Mid-Norway is a large geographical area and, as the list of names in **Figure 4.11** shows, there are a large number of structural elements in the region (named and defined by the *Norwegian Petroleum Directorate*) where wells are drilled. As a broad way of assessing geographical position versus S_h magnitude, the data have been plotted by the structure where the well occurs. It is clear that there is not an obvious relationship shown in **Figure 4.11** between the magnitude of S_h and location of the well. By solely considering the geographical position, variations in S_h at given depths are not explained.

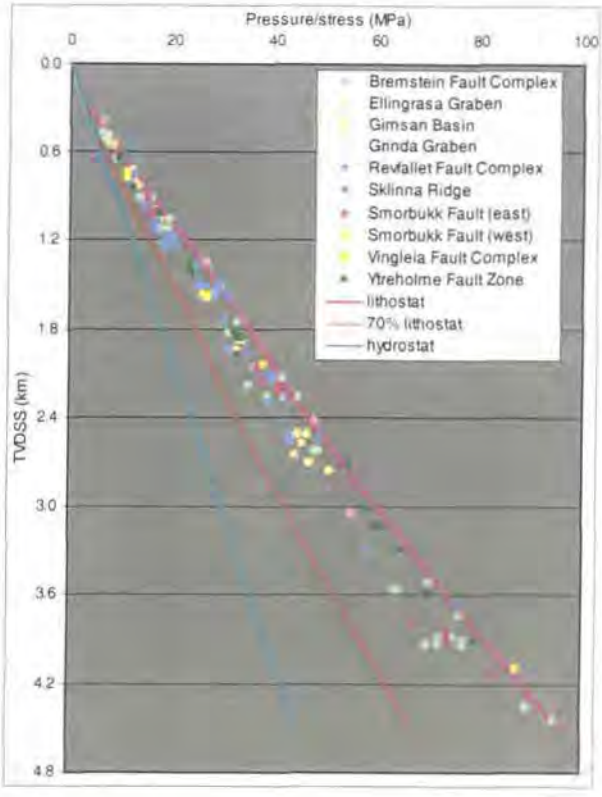

Figure 4.11: S_h data plotted by geographical position in Mid-Norway.

4.3.6 The Halten Terrace data and S_h variation

4.3.6.1 The significance of the Halten Terrace

The Halten Terrace is the largest and most important structural element within Mid-Norway and is where the majority of the wells are drilled and data originate. The Halten Terrace is also important because of the P_p situation that occurs across it (see **section 3.6** for further information). Because of the Terrace's importance, data are plotted by their geographical position on the Terrace (which also relates to the P_p situation – see Hermanrud *et al.*, 1998a) in **Figure 4.12**. Results show that 85% of the data come from the eastern Halten Terrace (where P_p are normally pressured to slightly overpressured) and the S_h data show all of the variation seen in **Figure 4.1**. E Halten Terrace S_h data provide no greater insight into S_h scatter than plotting all the data from the whole of Mid-Norway (**Figure 4.11**) by location. The remaining 15% of the data come from the south-west and western Halten Terrace. S_h magnitudes that fall within the centre of the data cluster (green) come from the SW Halten Terrace. Those data from the W Halten Terrace generally produce the greatest S_h magnitudes (maroon) of close to lithostatic. P_p data show a systematic increase from

hydrostatic to low overpressures (east) to moderate (70% S_V) overpressures in the south-west to high (85-90% S_V) overpressures in the west.

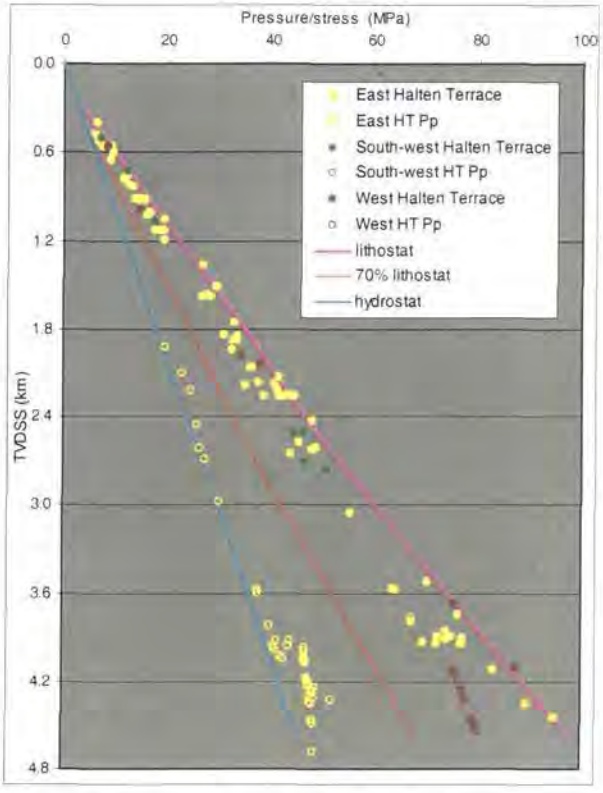

Figure 4.12: S_h and P_p data from the Halten Terrace plotted by relative position on the Terrace.

An inference is that part of the variation in S_h magnitude in the Halten Terrace can be attributed to the position of the well but as the data from the eastern province show, scatter is still present for individual provinces so position does not completely explain S_h variation.

4.3.6.2 East and west of the Smørbukk Fault

4.3.6.2.1 Why the Smørbukk Fault?

As explained in **section 3.6.1**, P_p in the west of the Halten Terrace are overpressured whilst those in the east are approximately hydrostatically pressured and those in the south-west form a transition between the two provinces. The lineament that separates the high P_p Halten West region from the normally pressured Smørbukk Field is the Smørbukk Fault. P_p and S_h data shown in **Figure 4.13** are from wells within the Smørbukk field to the east of the

Smørbukk Fault and well 6506/11-1 occurring immediately to the west of this fault. Data have been separated to see if differences in S_h manifest in the same way as P_p differences.

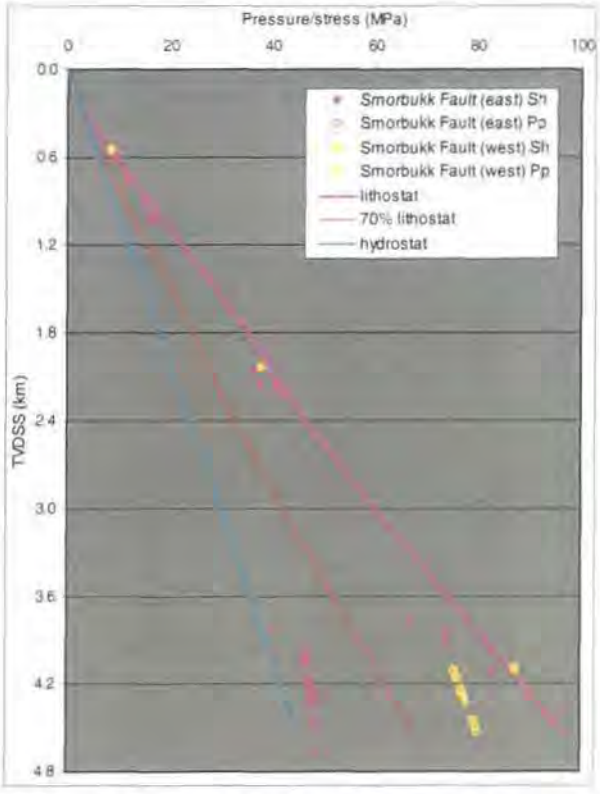

Figure 4.13: S_h and P_p data from wells east and west of the Smørbukk Fault.

4.3.6.2.2 Smørbukk Fault pressure and stress results

The results of plotting P_p and S_h data from immediately east and west of the Smørbukk Fault are shown in **Figure 4.13**. The P_p data reveal a clear distinction between east and west sides of the fault. Eastern P_p measurements are hydrostatic to 5 MPa overpressured whilst western P_p are between 30 and 33 MPa overpressured.

The S_h data show a less clear pattern. Considering S_h measurements from the same depth on either side of the Smørbukk Fault, there is no difference between magnitudes at ½ and 2 km (unfortunately P_p data are not available to compare how P_p varies at these depths). At 4 km however stresses show a small difference of 5 MPa between west and east.

When plotting the "*comparable depth*" data for either side of the Smørbukk Fault (**Figure 4.14**) it is clear that regardless of the P_p magnitude, S_h is high relative to S_v (>80% S_v). Inferences about how S_h varies with P_p cannot be made due to the scarcity of data and the small difference between normally pressured and overpressured S_h measurements. Overpressured S_h measurements are only 5 MPa greater than the highest normally pressured

S_h measurement. The scatter of 6 MPa in the normally pressured S_h measurements between 3.8 and 4.1 km shows the insignificance of this difference. At 4.2 km, the scatter shown by the entire data set in **Figure 4.1** is 13 MPa – over twice the difference between normally and overpressured S_h in **Figure 4.14**. Hence, position relative to the Smørbukk Fault does not explain the S_h scatter at depth.

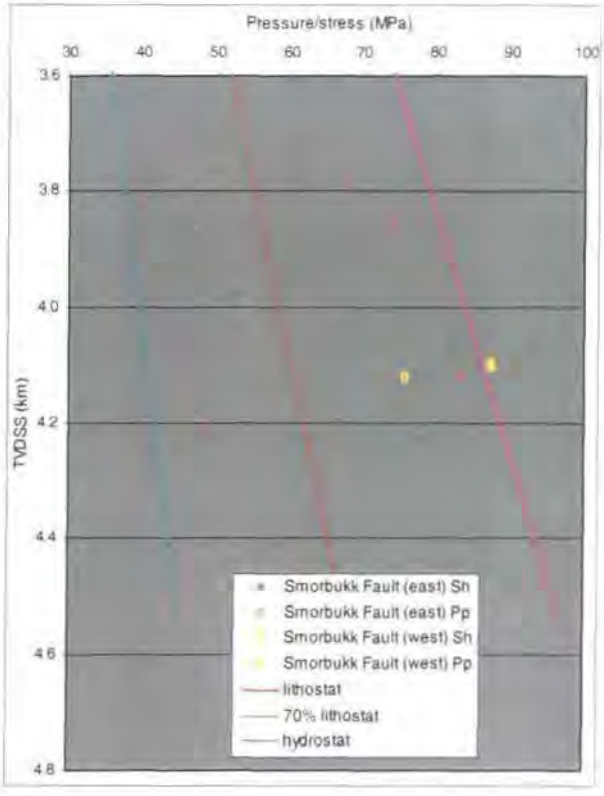

Figure 4.14: "*Comparable depth*" data from east and west of the Smørbukk Fault.

4.3.7 Summarising what the stress-depth plots reveal about S_h magnitude

The results of plotting the Mid-Norway S_h data by overpressure, lithology, wellbore diameter, pumping rate, age of the rock that the test was conducted in and position relative to major structural elements are summarised in **Table 4.3**.

The best explanations for the variability in the magnitude of S_h can be explained by P_p variations (**Figures 4.4** and **4.5**), and the position of the well on the Halten Terrace (**Figure 4.12**). **Figures 4.13** and **4.14**, where P_p and S_h data are plotted relative to their position east or west of the Smørbukk Fault, show how large P_p differences may be influencing S_h magnitude. Plotting the data by the age of the Formation (**Figure 4.10**) shows an increase in S_h with current depth of burial within a specific Formation (cf. the Lower Cretaceous). This piece of evidence suggests that the current burial depth rather than the age of the Formation influences the S_h magnitude.

Reason for S_h variability	Do we see variability?	Does this explain the variability?
Overpressure	Yes	Possibly
Lithology	Yes	No
Wellbore diameter	Yes	No
Pumping rate	Yes	No
Age of rock that test was conducted in	Yes	Possibly
Position relative to structure	Yes	No
Position on the Halten Terrace	Yes	Possibly

Table 4.3: Summary table of the results of plotting S_h by various parameters to determine the reasons for S_h variability at a given depth.

4.4 Using the data to estimate the regional minimum *in-situ* stress

4.4.1 Creating lower bound trends to LOPs and an upper limit to P_p

A second order polynomial (**Figure 4.15**) has been fitted to all 227 Mid-Norway S_h data shown in **Figure 4.1**. This line describes the lower bound trend (yellow) to the majority of S_h magnitudes calculated from LOP measurements (see **section 2.5.2**). The lower bound envelope to the data can be termed an approximation of the *regional fracture gradient* and shows how minimum *in-situ* stress changes with depth.

The "*comparable depth*" data subset was used to create a lower bound trend to "*comparable depth*" LOPs (green line in **Figure 4.16**). This data subset numbers only 60 so creating a trend from these data tests the need for large numbers of data to create an accurate lower bound. Seeing how the lower bounds differ shows the effect a reduction from 227 to 60 S_h measurements may have on Mid-Norway results (**Figure 4.17**).

An upper limit to pore pressures (black) was created using all the P_p data (**Figure 4.18**). The upper limit was then compared and contrasted to both lower bounds to LOPs. The aim is to see if there is a significant difference in the "*fracture gradient*" depending on whether P_p or S_h is used to create it.

4.4.2 Results

Figure 4.17 shows all 227 S_h data, all P_p data and both lower bound trends. It is clear that the number of data used to create the lower bound does not greatly influence the shape and equation of the trend. The lower bound trend for the entire Mid-Norway data set is described by *equation 4.1* whilst the "*comparable depth*" data lower bound is described by *equation 4.2*:

$$y = -0.000165x^2 + 0.065678x + 0.04152 \qquad \textit{(equation 4.1)}$$

$$y = -0.00018x^2 + 0.06905x - 0.07954 \qquad \textit{(equation 4.2)}$$

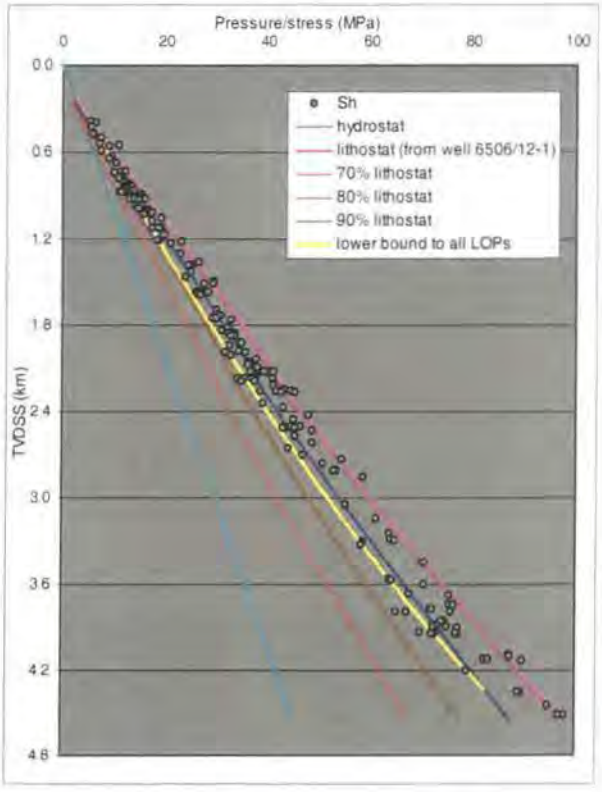

Figure 4.15: Lower bound to LOPs for the entire Mid-Norway data set.

The small amount of scatter in the Mid-Norway S_h data set (cf. **Figure 4.2**), especially at depths of <2 km, makes the lower bound to LOPs easy to define. Greater scatter occurring below 3½ km depth (**Figures 4.15** and **4.16**) means those S_h measurements plotting to the left of the main data swarm inevitably plot to the left of the lower bound. The same degree of scatter seen in the entire data set occurs in the "*comparable depth*" data subset. Therefore the smaller number of data does not effect the lower bound results.

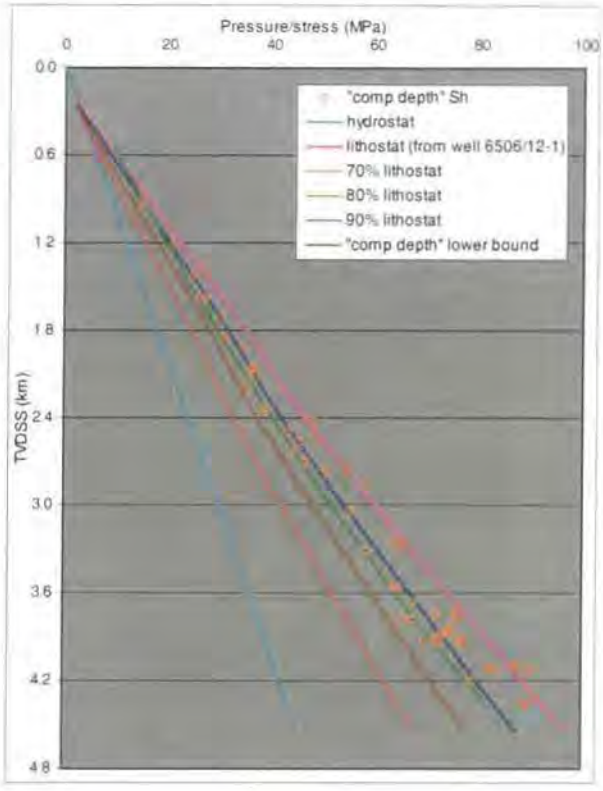

Figure 4.16: Lower bound to LOPs for the "*comparable depth*" data subset.

It is clear that regardless of the data set used, the lower bound trend for Mid-Norway does not follow the 70% S_V line. Instead, as **Figure 4.17** shows, both lower bounds range between 80 and 90% S_V with an average magnitude of 85% S_V. Curvature towards S_V is seen in both lower bounds at depths of >3½ km. This curvature reflects the increase in S_h:S_V ratio shown by **Figure 4.3**. All P_p data are constrained below both lower bounds (**Figure 4.17**).

Analysing **Figure 4.18** shows the upper limit line (black) produces a good estimate of the maximum P_p encountered in Mid-Norway for those data available. Over 95% of the pore pressure measurements fall to the left of the trend. The shape of the upper limit to P_p is more complex than the lower bounds and is described using the third order polynomial:

$$y = 0.000012x^3 - 0.0019x^2 + 0.1314x - 0.1768 \qquad \textit{(equation 4.3)}$$

Comparing both lower bounds and the upper limit (**Figure 4.19**) reveals a significant difference (up to 9 MPa at 1.8 km) between the magnitude of the upper limit and the lower bounds at <3 km depth. The S_h magnitudes are high in the upper 2½ km. As explained in **section 3.6**, P_p magnitudes in the upper 2½ km are "inferred from well logs as being hydrostatic" (Hermanrud *et al.*, 1998a). The P_p magnitudes may therefore be incorrect and the

mismatch not representative of the true difference between S_h and P_p. Below 3½ km, within the overpressured zone, the three trends converge and both lower bounds produce an accurate maximum for P_p magnitude.

The outcome of these results is that lower bounds produce a good estimate of the regional S_h. For Mid-Norway, the "tightness" of the data swarm, especially at depths of <2 km, means that the number of data used does not influence the magnitude of the lower bound. Consistently high S_h magnitudes at shallow depths mean the lower bounds overestimate the maximum P_p seen (although the measurements for P_p may not be representative) but within the overpressured zone they produce a reliable estimate (**Figure 4.19**).

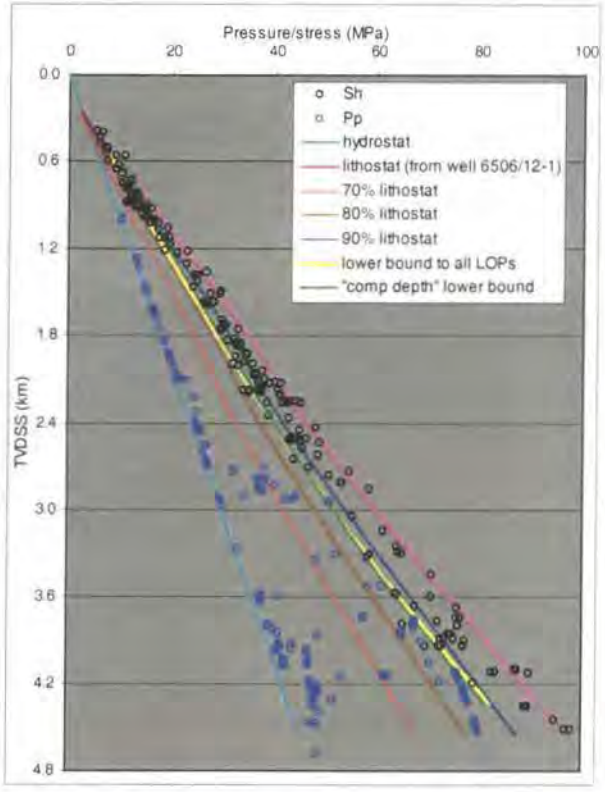

Figure 4.17: Lower bounds to all and "*comparable depth*" data.

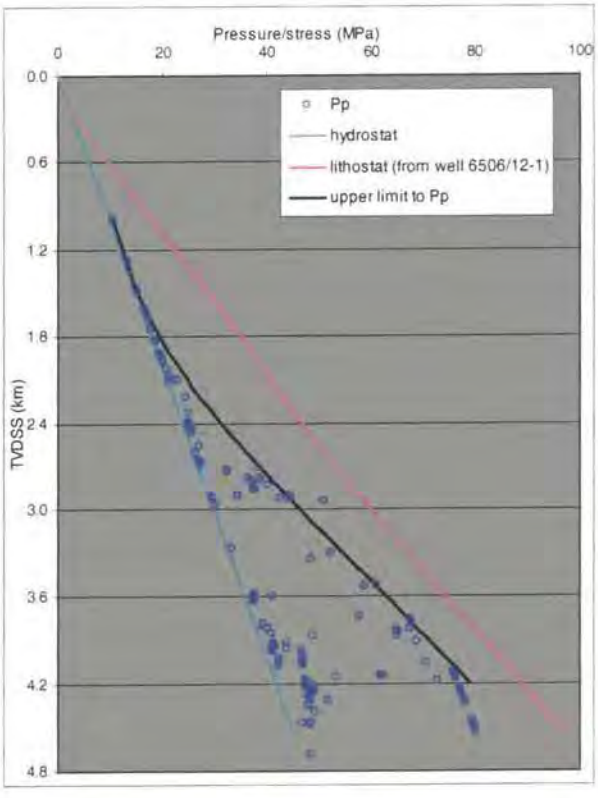

Figure 4.18: Upper limit to P_p data created from all Mid-Norway P_p data.

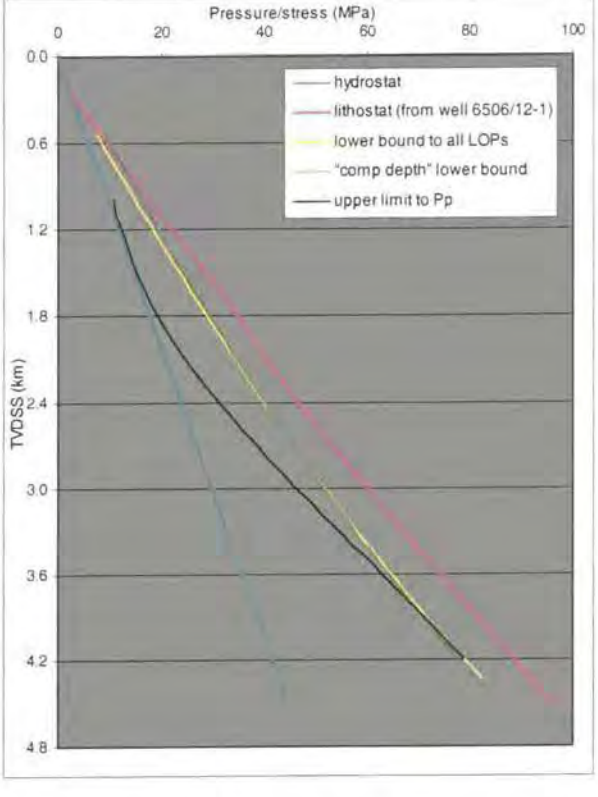

Figure 4.19: Comparative plot showing both lower bounds and the upper limit.

4.5 Pore pressure *in-situ* stress coupling

4.5.1 Looking for insights into coupling

Stress-depth plots (e.g. **Figures 4.4** and **4.5**) can show that where overpressures exist so S_h is higher than when P_p is hydrostatic. If P_p directly effects S_h then this is known as pore pressure *in-situ* stress coupling (see **section 2.6.4**). Basin-scale data are collected from a wide range of depths therefore plotting P_p versus S_h (**Figure 4.20**) inevitably produces a strong correlation as each parameter increases with depth. As a means of showing the relationship between P_p and S_h a control situation is also shown in **Figure 4.20**. The dashed line represents a hypothetical unconstrained basin where P_p increases following the hydrostat and S_h increases at a rate of 70% S_V with depth.

The approach shown in **Figure 4.20** does not quantify coupling. However, there are ways of revealing insights into the degree of coupling that occurs. Firstly, in order to assess the effects of P_p on stress, it is necessary to be as sure as possible that the P_p and S_h measurements can be meaningfully compared. For this reason the "*comparable depth*" data set was used (see **section 3.7.4**). The "*comparable depth*" data have been plotted by two techniques to investigate the level of coupling. **Figure 4.21** shows S_h and P_p data where:

- P_p is normalised to the hydrostat and then depth. The resulting graph plots **[(P_p-hydrostatic P)/depth]** on the x-axis.
- S_h data are firstly normalised to $S_h(T)$ – where $S_h(T)$ is taken as being 70% S_V assuming a normally pressured S_h/S_V of 0.7 – and then to depth. This produces **[(S_h-$S_h(T)$)/depth]** on the y-axis.

The hydrostatic pressure and $S_h(T)$ values were arbitrarily chosen as the "expected" magnitudes of P_p and S_h in a normally pressured situation. A basin where P_p is hydrostatic and $S_h = S_h(T)$ would plot at the origin on such a cross-plot.

Figure 4.22 shows the "*comparable depth*" data with the absolute magnitudes of S_h and P_p normalised to depth thus plotting:

- **P_p-gradient** on the x-axis;
- **S_h-gradient** on the y-axis.

On this plot, the square-cross symbol represents the relationship between P_p and S_h for a hypothetical basin where P_p increases hydrostatically and S_h increases following the $S_h(T)$ line. In this situation S_h-gradient = 15.75 MPa/km and P_p-gradient = 10 MPa/km.

Both approaches can reveal the presence of coupling and show the rate of increase of S_h with an increase in P_p (the $\Delta S_h/\Delta P_p$ value). Both techniques require the data to be depth-

normalised so they can be compared together without the large differences in magnitude brought about by differences in depth.

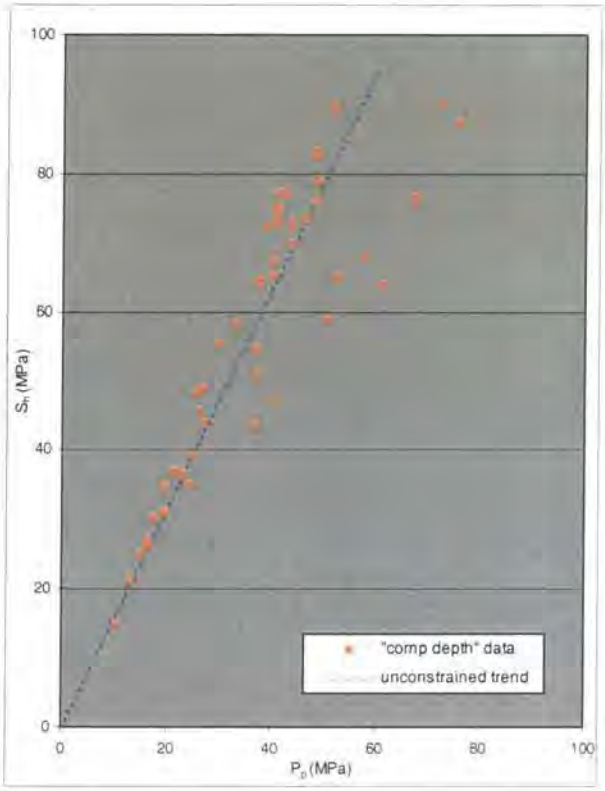

Figure 4.20: Absolute magnitude of S_h versus absolute magnitude of P_p.

The "*comparable depth*" data were separated (**Figures 4.23** and **4.24**) into normally pressured and overpressured data (as described in **section 4.2)** and plotted using the approaches described above. The objectives of the coupling investigations are to assess the rate of change of S_h with a change in P_p and determine whether coupling can be inferred.

4.5.2 Results

It is clear from **Figure 4.20** that the Mid-Norway data do not obey the hypothetical unconstrained basin relationship. There is a significant proportion of the data that plot to the right of the "*unconstrained trend*" indicating that P_p increases relative to S_h at a rate greater than in an unconstrained basin. Plotting the data by other means allows a quantification of any relationship and the significance to be tested.

All "*comparable depth*" data are shown normalised to a hypothetical unconstrained basin and depth (**Figure 4.21**) and plotted as gradients in **Figure 4.22**. Best of fit linear

regression lines are fitted to the data to determine the $\Delta S_h/\Delta P_p$ value. Data are separated into normally and overpressured groups in **Figures 4.23** and **4.24** and linear regression lines are fitted to the overpressured (green) data. Results are summarised in **Table 4.4** below:

Data statistics refer to	**Data plotted as gradients (e.g. *[S_h-gradient]*)**		**Data normalised to an "unconstrained basin" & depth (e.g. *[(S_h-S_h(T))/depth]*)**	
	$\Delta S_h/\Delta P_p$	**r^2**	**$\Delta S_h/\Delta P_p$**	**r^2**
All data	0.34	0.41	0.28	0.43
Overpressured	0.32	0.39	0.29	0.48

Table 4.4: Summary table showing the nature of pore pressure *in-situ* stress coupling ($\Delta S_h/\Delta P_p$) and correlation co-efficients (r^2) for Mid-Norway.

Table 4.4 shows that the $\Delta S_h/\Delta P_p$ value is low (~0.3) in Mid-Norway regardless of whether all data or only the overpressured data are analysed. Correlation co-efficients (r^2 values) of less than 0.5 for the linear regression lines show that these relationships are poor. **Figures 4.23** and **4.24** show that when P_p is hydrostatic there is a swarm of data (yellow) covering the whole range of values for "excessive" stress. Given the relationships shown in **Table 4.4** coupling cannot be inferred for Mid-Norway.

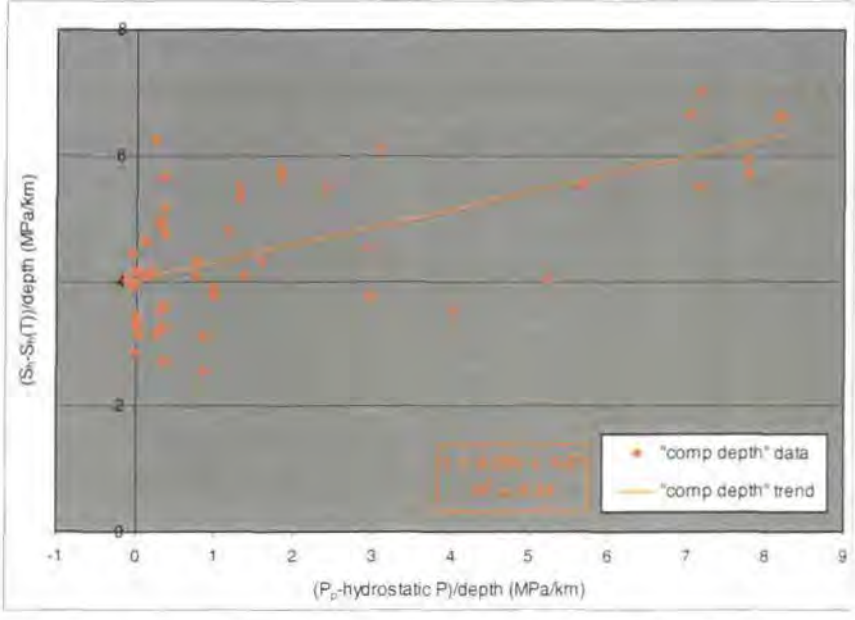

Figure 4.21: All "*comparable depth*" data normalised to a hypothetical unconstrained basin and depth.

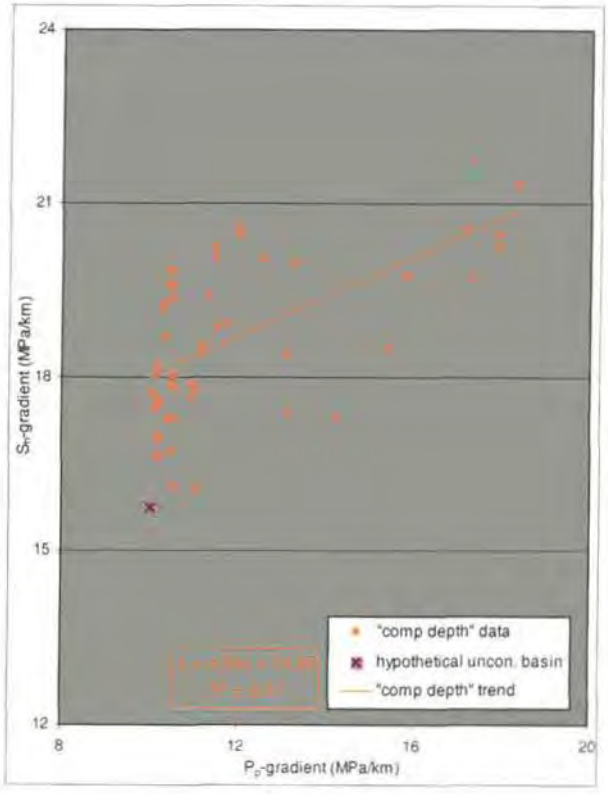

Figure 4.22: All "*comparable depth*" data normalised to depth (gradients).

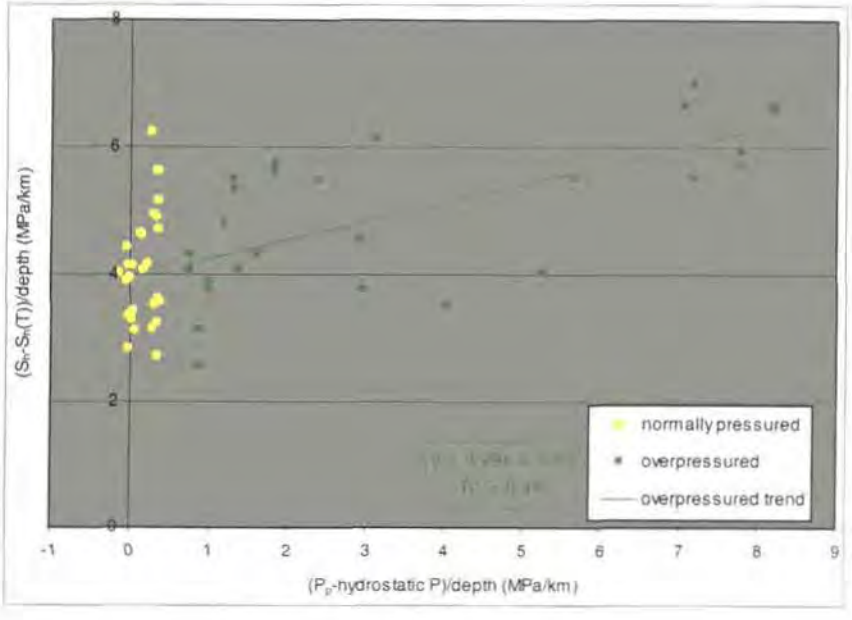

Figure 4.23: Normally pressured and overpressured "*comparable depth*" data normalised to a hypothetical unconstrained basin and depth.

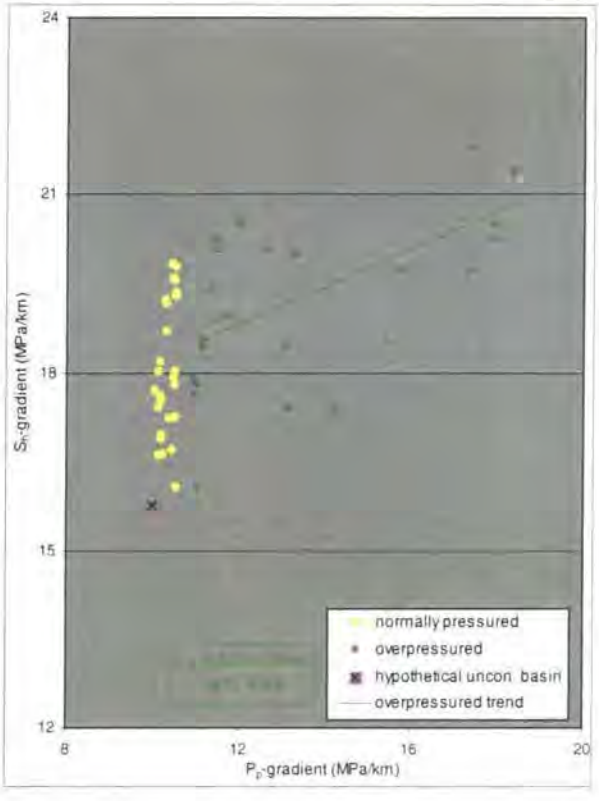

Figure 4.24: Normally pressured and overpressured "*comparable depth*" data normalised to depth (gradients).

To investigate whether the range of "excessive" stress magnitudes at normal P_p can be linked to depth differences, the data are plotted by kilometre increments in **Figures 4.25** and **4.26**. Overpressures occur at 2¾ km depth so this method will reveal any relationship between where the points plot in **Figures 4.21** to **4.24** and depth. **Figures 4.25** and **4.26** show that at depths of less than 2 km P_p remain hydrostatic and S_h remains less than 18 MPa/km. For data from 2-3 km depth more of a spread occurs in coincidence with the development of overpressure. **Figures 4.25** and **4.26** show that the greatest magnitudes of overpressure and "excessive" stress occur at greater depths although considerable scatter does occur. When analysing the range of "excessive" stress at normal pressures, the greatest S_h-gradients in **Figure 4.26** come from the greatest depths.

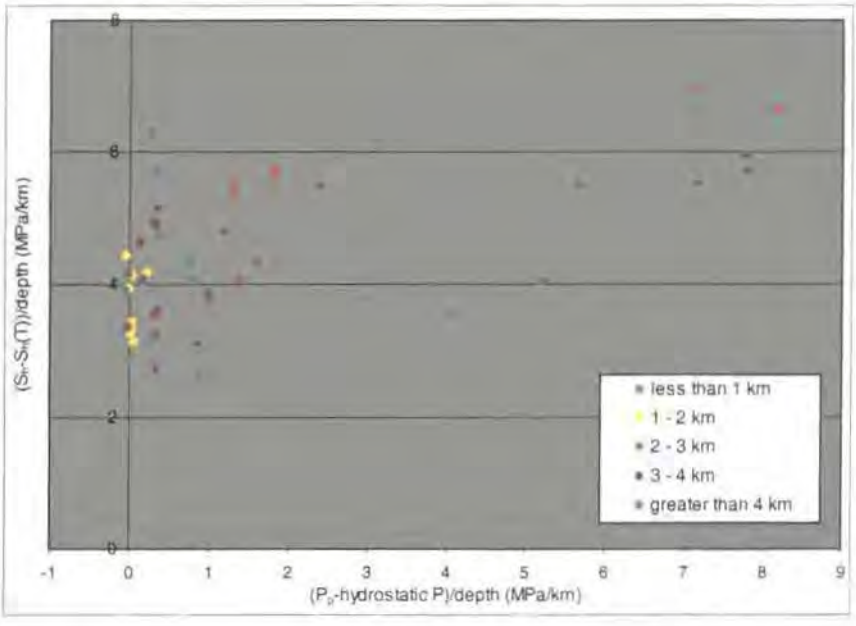

Figure 4.25: All "*comparable depth*" data normalised to a hypothetical unconstrained basin and depth and plotted by kilometre depth increments.

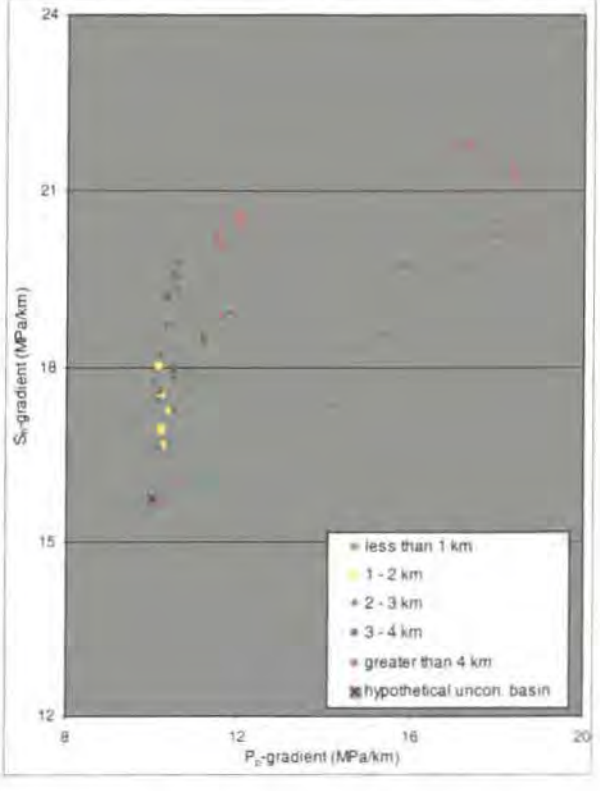

Figure 4.26: All "*comparable depth*" data normalised to depth (gradients) and plotted by kilometre depth increments.

4.6 Does it really matter whether we use the LOP or ISIP?

4.6.1 Introduction

It has long been considered a problem to calculate a reliable estimate for the minimum *in-situ* stress (S_h) from borehole data and hence determine a lower bound to leak-off pressures. Pumping pressure test graphs are widely used for this purpose despite uncertainties about which point on the graph is the better estimate of S_h (see **section 2.4.2**). Using the *Statoil* Mid-Norway data, an investigation was undertaken into whether it matters if the leak-off pressure (LOP) or instantaneous shut-in pressure (ISIP) is used to predict the magnitude of minimum *in-situ* stress.

4.6.2 Methodology: using LOT and XLOT graphs to calculate S_h

In order to investigate the difference between the magnitude of LOP and ISIP, full leak-off tests or extended leak-off tests were needed and here was the advantage of the *Statoil* data. As described in **section 3.7.1.2**, the original test graphs were recreated from the data. **Figure 3.11** is a good example of a four-cycle test record from the Norne field in Mid-Norway. Whilst easier to interpret than many of the graphs in this study the test is typical of the data used. For each cycle the LOP, ISIP and FBP is shown. The study had 57 XLOT cycles made available to it. For each cycle, both LOP and ISIP were hand picked from the graphs and used to calculate S_h. This subsection of the Mid-Norway study aims to assess whether there is a significant and meaningful difference in the calculated magnitude of S_h depending whether the LOP or ISIP is used and also if differences can explain the scatter in S_h shown in **Figure 4.1**.

4.6.3 Results

Plotting the LOP value versus the ISIP value (**Figure 4.27**) reveals how close the two are in many of the XLOT cycles. Despite some scatter about the one-to-one line, the statistics reveal the relationship to be good:

$$y = 0.973x - 0.34 \qquad \textit{(equation 4.4)}$$

$$r^2 = 0.979 \qquad \textit{(equation 4.5)}$$

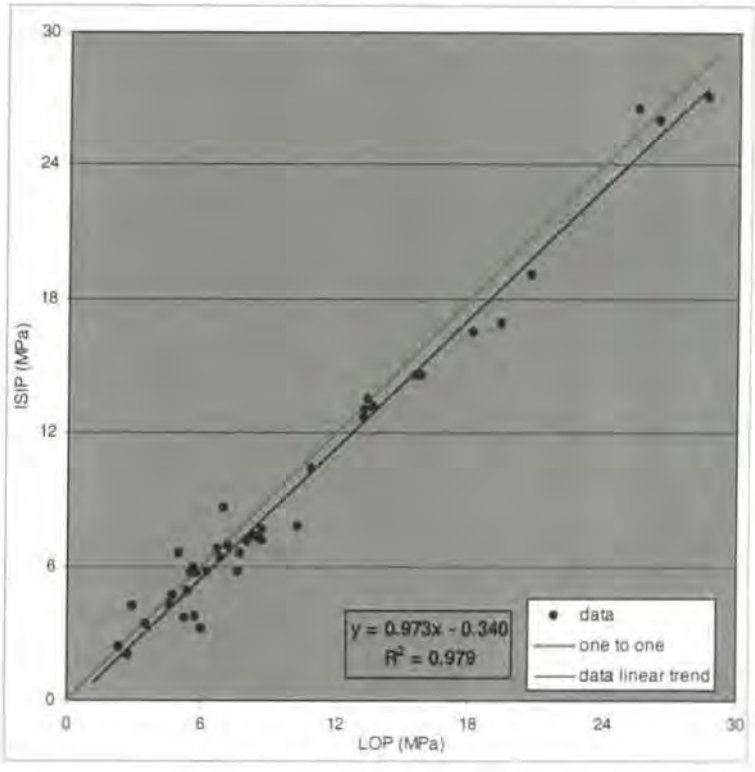

Figure 4.27: ISIP versus LOP for extended leak-off tests from Mid-Norway.

The same data are plotted in **Figure 4.28** by cycle number. The greatest amount of scatter either side of the one-to-one line occurs for first cycles. Fitting envelopes to the first cycle points shows a 5 MPa variation in the magnitude of the LOP relative to the ISIP. The variation is taken relative to the ISIP because it is generally accepted that the ISIP *equals* S_h (Hillis pers. comm., 2001). This variation in LOP for the first cycles has important repercussions for the magnitude of S_h. Since most data shown in **Figure 4.1** are calculated from first cycle LOPs, some of the scatter in S_h at a given depth can be attributed to variability in the LOP. Therefore a component of the scatter in S_h can be attributed to *data uncertainty* which will not be solved even by stringent quality control.

Subsequent cycles in XLOTs show the data points plotting closer to the one-to-one line implying LOP and ISIP magnitudes converge. The convergence is confirmed by **Figure 4.29**. Those XLOTs with 3 or 4 cycles show the difference between LOP and ISIP is reducing although the LOP does mainly remain in excess of ISIP. The inference is that within re-opening cycles components of friction, rock tensile strength and stress perturbations seen during the rock failure cycle have been removed (Engelder, 1993; Fejerskov *et al.*, 1995). The results for Mid-Norway suggest that LOP ≈ ISIP especially in later cycles.

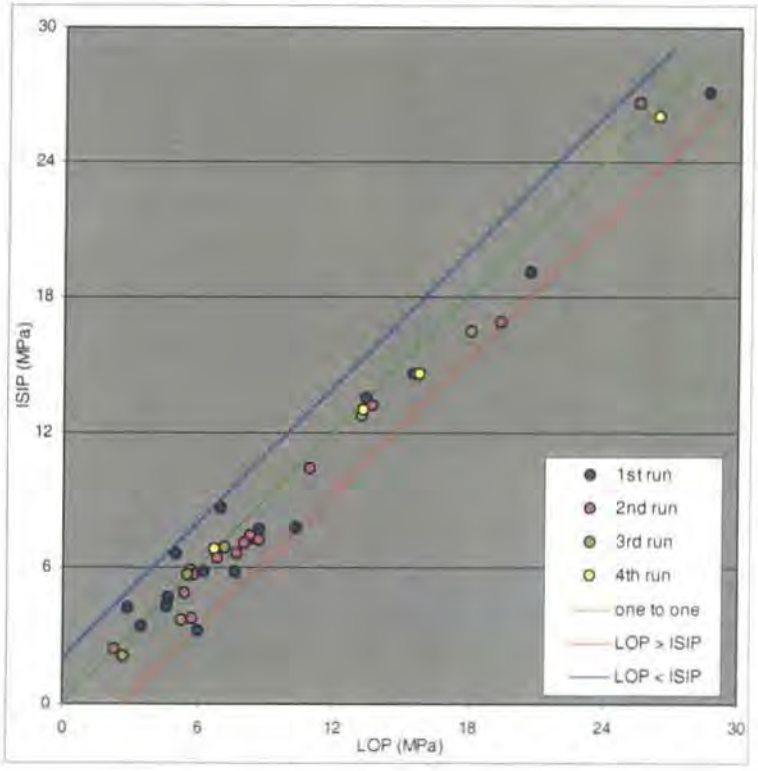

Figure 4.28: ISIP versus LOP plotted by cycle number.

Combining the pressure of the static mud column to the LOP and ISIP value allows a comparison between LOP-derived and ISIP-derived S_h magnitudes (**Figure 4.30**). Little difference in the S_h values is shown. The majority of data fall between the 5% error lines showing the difference to be less than 5%. The linear regression line in **Figure 4.30** has statistics:

$$y = 1.012x - 1.116 \qquad \textit{(equation 4.6)}$$

$$r^2 = 0.997 \qquad \textit{(equation 4.7)}$$

The negative intercept shows that LOPs produce a slight overestimate for S_h but only by 1.1 MPa or 11 bar. This overestimate is expected because the LOP value itself contains a component of rock tensile strength during initial wellbore failure and a stress perturbation around the wellbore component. Further explanations for these phenomena can be found in Inglis (1913) and Engelder (1993).

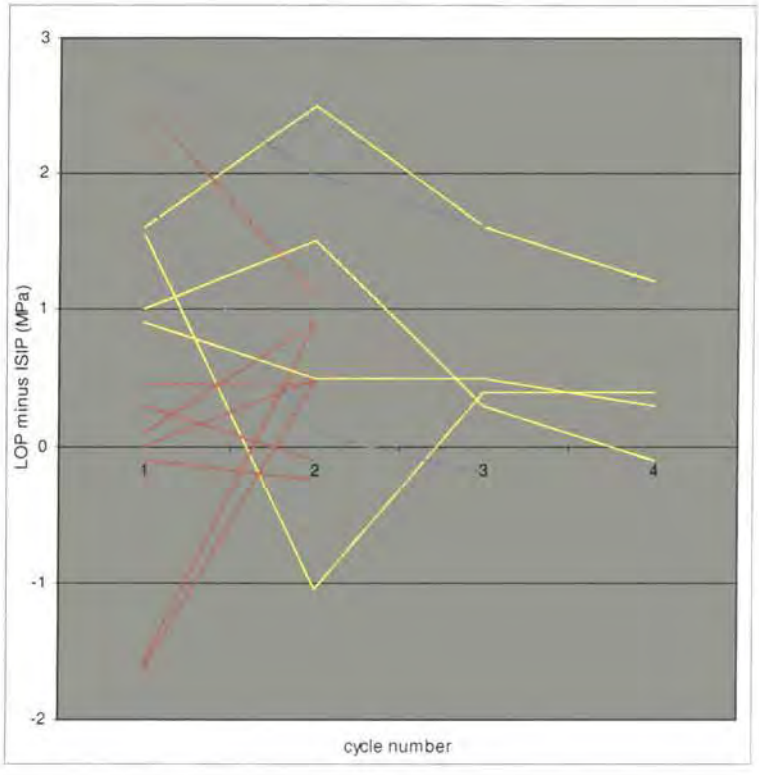

Figure 4.29: LOP minus ISIP for each cycle number from a particular test.

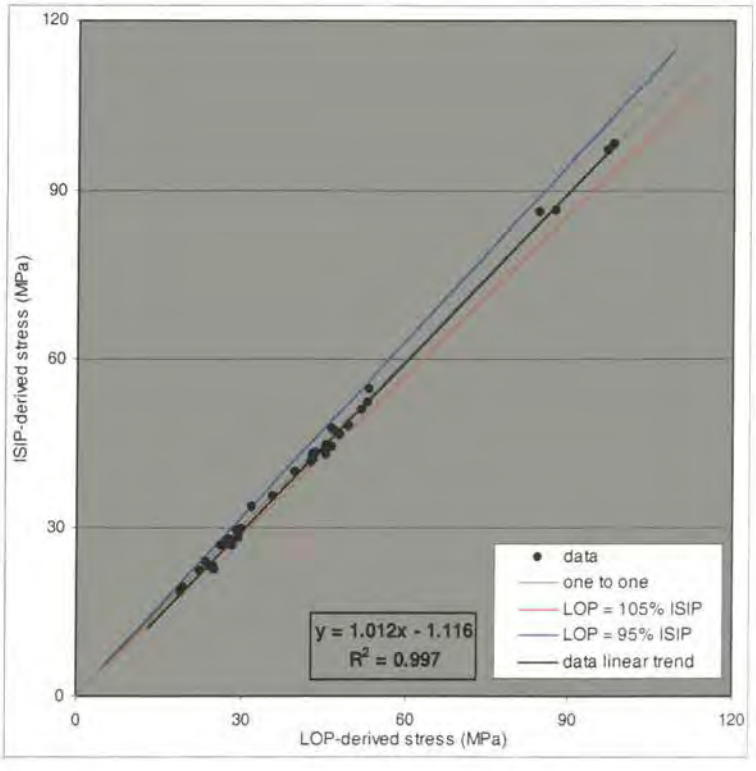

Figure 4.30: ISIP-derived minimum stress versus LOP-derived minimum stress.

Both sets of derived S_h magnitudes for Mid-Norway are plotted on a stress-depth plot in **Figure 4.31**. The LOP-derived and ISIP-derived values plot almost on top of one another. Results shown in **Figures 4.30** and **4.31** lead to the interpretation that whether LOP or ISIP is combined with the static mud column pressure, little difference is made to the derived S_h magnitude in Mid-Norway. Further discussions on the implications these results have for the magnitude of the maximum horizontal stress, S_H, can be found in **Chapter 6**.

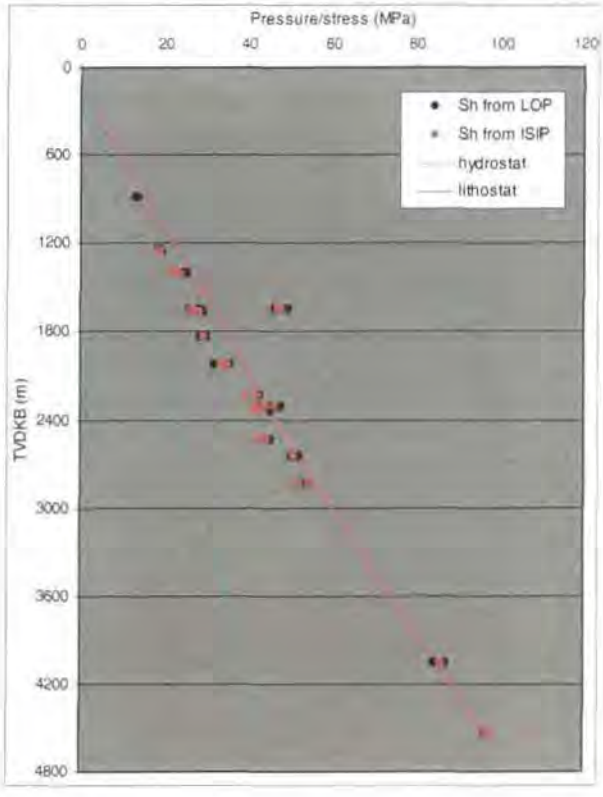

Figure 4.31: Stress-depth plot showing the difference between S_h as calculated from ISIP and LOP.

4.7 Summarising the results for Mid-Norway

A stringent quality control procedure led to the creation of the Mid-Norway data set. In the study described above, these data have been plotted on stress-depth plots, normalised to both a hypothetical unconstrained basin and depth, and plotted as gradients. The reasons were to investigate the variations in and controls on S_h magnitude and look for insights into P_p-S_h coupling. Also undertaken was a smaller investigation using XLOT data into the effects that using the LOP or ISIP has on the magnitude of S_h. The results are summarised below:

- Quantitatively, the scatter in S_h is less than 6 MPa in the upper 2 km and reaches a maximum of 13 MPa at 3.75 km.
- Stress-depth plots reveal S_h to be consistently high relative to S_V through the whole depth interval. The S_h:S_V ratio is >0.7 and below 1 km it is >0.8 with an average of 0.93.
- S_h is consistently high despite the variations in P_p of up to 36 MPa (at 4.1 km).
- Normally pressured "*comparable depth*" S_h data show a S_h variability of <3 MPa (except at 2½ and 4 km depth) and magnitudes between 80% and 100% S_V.
- Overpressured "*comparable depth*" S_h data show scatter of up to 13 MPa with magnitudes mostly >90% S_V especially where larger overpressures occur.
- From stress-depth plots, a conclusive link between S_h and P_p cannot be stated or quantified.
- P_p variations, the current depth of burial of a Formation of a particular age and the position on the Halten Terrace, especially in relation to the Smørbukk Fault, may partially account for the variation in S_h magnitude at specific depths.
- An important explanation for S_h variability comes from the variation/uncertainty in the magnitude of the LOP as picked from first order cycles of XLOTs.
- Lower bounds for all data and the "*comparable depth*" data are the same.
- Mid-Norway lower bounds average 85% S_V and curve towards S_V at depths >3½ km.
- A maximum difference of 9 MPa occurs between the lower bounds and upper limit to P_p at <3 km depth. Within the overpressured zone the trends converge.
- From the data available an interpretation is that lower bounds produce a good estimate of the regional S_h and a reliable maximum to P_p (especially where overpressure exists).
- The "*comparable depth*" data show that pore pressure *in-situ* stress coupling is not occurring in Mid-Norway. The $\Delta S_h/\Delta P_p$ values are ~0.3 and the r^2 values <0.5.
- Hydrostatically pressured data reveal a broad range of values of "excessive" S_h.
- Shallow depth data have lower P_p and S_h magnitudes – greater overpressures and "excessive" S_h magnitudes occur for data from deeper depths.
- For the normally pressured data, the greatest S_h-gradients occur at the greatest depths.

Chapter FIVE: Case Studies from Other Regions

5 Case Studies from Other Regions

5.1 Introduction

Following the analyses performed on the data from Mid-Norway, leak-off test and pore pressure data from six other regions around the world were analysed.

Results are described for the Central North Sea (**section 5.2**), Brunei (**section 5.3**), the Gulf of Mexico (**section 5.4**) Onshore Nigeria (**section 5.5**), Offshore West Africa (**section 5.6**), and the Barents Sea (**section 5.7**). The locations of these regions are shown on the world map in **Appendix 1**.

In contrast to the data from Mid-Norway, these regions did not have original pumping pressure test graphs so a quality check was not possible and data reliability had to be assumed. Analyses for each region follow the same formula as those for Mid-Norway.

Following an introduction to the region and an explanation of the compilation of the data, stress-depth plots show the entire data set and the "*comparable depth*" data subset (where it was necessary to create one). Plotting S_h and P_p data together shows the relationship between the two parameters with depth. The variability in the magnitude of S_h at specific depths is investigated and quantified and explanations are sought for its occurrence.

Lower bounds to LOPs for the entire data set and the "*comparable depth*" data and upper limits to P_p were determined as ways of estimating the regional minimum stress. Finally, the "*comparable depth*" data were used to investigate pore pressure *in-situ* stress coupling. Where coupling is seen the relationship between S_h and P_p is quantified.

5.2 The Central North Sea

5.2.1 Introduction to the Central North Sea

This introduction provides background information on the Central North Sea. Following the location of the region, the contemporary stress situation is reviewed. The burial history is summarised followed by the overpressure in terms of distribution, its link to specific lithologies and the likely causes of its generation.

- **Location**

The geographical definition of the Central North Sea Graben is the area of the UK continental shelf between 56° and 58° north and 0° and 3° east. It is the stretch of sea between the United Kingdom to the west and Denmark and southern Norway to the east.

- **The contemporary stress situation**

The *World Stress Map Project* (Mueller *et al.*, 2000) uses a compilation of borehole breakout data to determine a regional NW-SE orientation for the maximum horizontal stress (S_H). Therefore S_h is oriented NE-SW. Earthquake focal mechanisms have been used by Aadnoy *et al.* (1994) to invoke a present day regional NW-SE compressive trend at depth. This S_H direction is believed to be a consequence of plate tectonics. Borehole elongation measurements show local stress orientations to deviate from the regional trend probably due to the local fault patterns. Some borehole breakouts show a NE-SW S_H direction close to major faults (Gaarenstroom *et al.*, 1993; Mueller *et al.*, 2000).

Using the leak-off inversion technique, Aadnoy *et al.* (1994) show the horizontal to vertical stress ratios are low near the surface. Below the Palaeocene unconformity the stress regime becomes more lateral stress dominated (Grauls, 1997). At depths of less than 1200 metres the S_h:S_V and S_H:S_V ratios are ~0.8 which is are consistent with a relaxed depositional basin. A tectonic influence at depths of 1.5 to 2 km means greater horizontal stress anisotropy occurs and both S_H and S_h are greater relative to S_V. S_H is equal to or even in excess of S_V. This ratio suggests a transpressive tectonic regime. Depths >2 km show clear horizontal stress anisotropy with S_H again possibly exceeding S_V.

- **The burial history**

The burial history shows Early Mesozoic subsidence through to the end of the Jurassic was slow with an average of <7 m/Ma. This was followed by further gradual burial during the Early Cretaceous. More rapid burial into the Late Cretaceous and Early Tertiary took place with ~1 km of sediment deposited in the 60 Ma to the end of the Miocene. During the last 3 Ma (Pliocene to Recent) the burial rate increased to ~500 m/Ma. The continuous deposition (especially during the Pliocene) led to the accumulation of >2½ km of fine-grained sediments (Swarbrick *et al.*, 2000).

- **Overpressure**

The main overpressures in the Central North Sea can be found in the Triassic, the Upper Jurassic Fulmar Sandstone (>4 km depth) and the Upper Cretaceous Chalk Group (3 - 4½ km depth).

In the Central Graben, the distribution and magnitude of the overpressure in the pre-Cretaceous rocks follows the structural morphology. Upper Jurassic sandstones vary from normally pressured near the flanks to highly overpressured in the deeper buried, N-S trending

axial region where P_p can be >100 MPa (Holm, 1998). Overpressures in these pre-Cretaceous rocks are located within "pressure cells" bounded by permeability barriers. "Pressure cells" document the transition from the highly overpressured axial region to the lower pressures on the flanks (Gaarenstroom *et al.*, 1993). While permeability barriers are believed to mostly prevent the dissipation of overpressures at the graben margins, faults may act as conduits for fluid flow out of the deeper parts of the graben towards the flanks (Holm, 1998). The marl of the Lower Cretaceous Cromer Knoll Group seals the Jurassic sandstones.

The Palaeocene rocks are suggested to control the overpressure in the Upper Cretaceous Chalk Group. Where the Palaeocene consists of sheet sandstones, which form a normally pressured regional aquifer, the upper part of Chalk Group is similarly normally pressured. Overpressures do occur within the Chalk Group when overlain by Palaeocene sandstones. These regions are restricted to small porous lenses encased by impermeable chalk or marl and only occur where the Chalk Group overlies the Kimmeridge Clay. In southern parts of the graben, the Palaeocene consists of claystones that act as a seal to overpressures found throughout the Chalk Group (Holm, 1998).

Early studies considered overpressures in the Jurassic to result solely from disequilibrium compaction (Holm, 1998). However, the importance of hydrocarbon generation is now recognised to contribute to the extreme overpressures present in the Jurassic sandstones. These overpressures are considered to result from the cracking of oil to gas within the Late Jurassic Kimmeridge Clay Formation.

Recent work by Swarbrick *et al.* (2000) shows that overpressures up to 24 MPa in the Triassic reservoirs of the Judy Field can be attributed to disequilibrium compaction. They result from rapid burial in the last 1–3 Ma. This recent study considers the contribution from gas generation to be small.

Disequilibrium compaction is also considered to be the overpressure generating mechanism in the Chalk Group. Porosities of 30 – 40% at 3 km in clays within the Chalk Group are quoted as evidence for this (Hancock, 1990). Hydrocarbon generation from within the Kimmeridge Clay Formation is also believed to contribute small amounts to Chalk Group overpressures (Holm, 1998).

To summarise, disequilibrium compaction is now considered to be the main overpressure generating mechanism in the Central North Sea but there is also a contribution from gas generating mechanisms (Hancock, 1990; Holm, 1998; Swarbrick *et al.*, 2000).

5.2.2 Compiling the data

The Central North Sea data set was created from the *PI Erico* data set. Despite original records being unavailable, a data set of 369 S_h values was compiled by selecting values from *PressureView* (see **section 1.2**). The S_h data set comprises true leak-off values (LOP-LOs) and lost circulation values (LOP-LCs) which under-estimate the real leak-off pressure at the depth of the test. Because LOP-LC magnitudes are under-estimates of leak-off, the data were re-calculated to give the magnitude of leak-off at the previous casing depth. The reason for this re-calculation is that it is believed mud loss occurs at the previous casing shoe rather than actually at the depth recorded for lost circulation (Traugott pers. comm., 1998; Swarbrick pers. comm., 1999). For each LOP-LC, the "actual" leak-off pressure at the casing depth was calculated using:

$$LOP_{casing} = LOP - LC \times \left(\frac{depth_{casing}}{depth_{LOP-LC}} \right) \qquad \textit{(equation 5.1)}$$

Where: LOP_{casing} = the leak-off pressure at the casing depth;

$LOP\text{-}LC$ = the recorded lost circulation value;

$depth_{casing}$ = the depth below the sea surface of the last casing shoe;

$depth_{LOP\text{-}LC}$ = the recorded depth of lost circulation.

Out of the 369 S_h measurements only 35 had a P_p measurement recorded within 100 metres of the pumping pressure test. These 35 data points are the Central North Sea "*comparable depth*" data set (cf. **section 3.7.4**).

5.2.3 Stress-depth plots

Following compilation of the data (as described above), S_h and P_p have been plotted on stress-depth plots. It is aimed to:

- Investigate and quantify the change in the magnitude of S_h with depth;
- Quantify and investigate reasons for the S_h variation at a specific depth;
- Investigate the amount of overpressure variation with depth;
- Analyse the effects of overpressure on the magnitude of, and the variation in, S_h.

These objectives are also applicable to the other regions described in this chapter. The results of the Central North Sea investigations are described below.

5.2.3.1 Relationships shown by stress-depth plots

The 369 S_h measurements and the P_p data from the Central North Sea are plotted wholesale on a stress-depth plot in **Figure 5.1**. For reference are the lithostat (taken as 22.62 MPa/km), the hydrostat and 70% S_V (red), 80% S_V (brown) and 90% S_V (darker blue) gradients used to illustrate how S_h changes relative to the lithostat with depth.

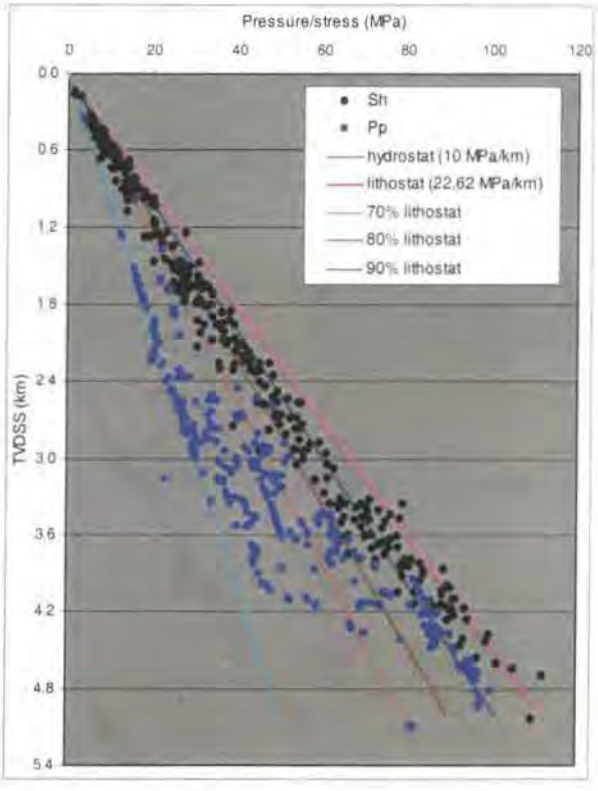

Figure 5.1: All S_h and P_p for the Central North Sea.

The S_h data in **Figure 5.1** show significant variability throughout the depth interval. This variability has been quantified at 250 metre intervals in **Table 5.1** (cf. **section 4.2**).

Table 5.1 and **Figure 5.1** show that the greatest scatter occurs between 2 and 3 km with a maximum of 17 MPa at 2¾ km. The greatest S_h magnitude at 2¾ km is 55 MPa so the variation is 31% of the highest S_h magnitudes. Depths where small amounts of scatter occur are those depths with the fewest data points.

Depth (kilometres)	Variability in S_h (MPa)
0.5	4.5
0.75	5.5
1.0	6.25
1.25	9
1.5	8
1.75	6.25
2.0	8.5
2.25	12
2.5	4
2.75	17
3.0	11
3.25	2.5
3.5	15
3.75	14
4.0	13
4.25	6
4.5	4

Table 5.1: Variability in the magnitude of S_h at 250 metre intervals.

S_h is normalised to S_V (**Figure 5.2**) to investigate the increase in S_h. There is a clear increase in the S_h:S_V ratio with depth. The ratio averages 0.7 at 1 km but the average increases to 0.95 at 4¼ km. **Figure 5.2** also illustrates the amount of scatter in S_h at a specific depth. The scatter in the S_h:S_V ratio is 0.6 - 0.95 at 1 km depth yet reduces to 0.85 - 1.05 below 4 km depth. The increase in S_h relative to S_V with depth is also clear in **Figure 5.1**. In the upper 2 km 21% of the S_h data in this interval are <70% S_V yet below 4 km depth all S_h measurements exceed 90% S_V. Some measurements are equal to or in excess of S_V below 4 km.

P_p measurements show greater variation than the S_h measurements (**Figure 5.1**). Despite most P_p being hydrostatic down to 2.3 km, overpressures up to 7 MPa occur from 1¼ km depth. Larger overpressures initiate at 2½ km with the transition from normally pressured to overpressured for the whole set of data occurring between 2½ and 3½ km depth. The greatest range in P_p occurs at 4 km depth where variation is 5 - 44 MPa of overpressure. P_p measurements reach their maximum values of 90% S_V (>45 MPa overpressure) at depths >4½ km.

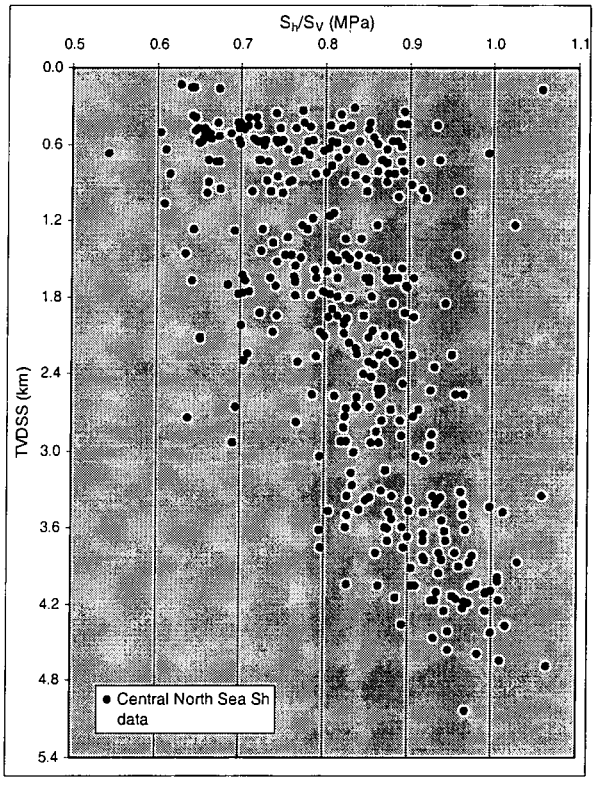

Figure 5.2: S_h normalised to S_V for the Central North Sea.

Figure 5.1 reveals greater overpressures coincide with greater S_h measurements. In the overpressure transition zone (2½ to 3½ km), S_h increases from 75% S_V to over 85% S_V. Where overpressure reaches its maximum extent of 50 MPa above the hydrostat (4½ km) S_h reaches its greatest magnitudes of 95 to 100 MPa.

The 35 "*comparable depth*" data are used to more precisely investigate the effects of overpressure on S_h (**Figure 5.3**). Considering all the data, S_h increases relative to S_V with depth from 0.75 at 1½ km to >0.9 below 4 km. P_p show an increase from hydrostatic magnitudes at <2 km depth to 90% S_V at 4½ km.

To clarify the relationship between P_p and S_h and investigate the scatter in S_h (of 17 MPa at the 2¾ km) normally pressured and overpressured "*comparable depth*" data are considered separately. **Figure 5.3** shows that lower values of S_h (<80% S_V) are associated with normally pressured fluids whilst overpressures are generally associated with higher values of S_h (those values >80% S_V). An interpretation would be that P_p exerts a control on S_h but stress-depth plots do not allow the relationship to be quantified. The scatter in S_h of up to 17 MPa in the overpressure transition zone (2½ to 3½ km) could be attributed to large P_p differences at these depths.

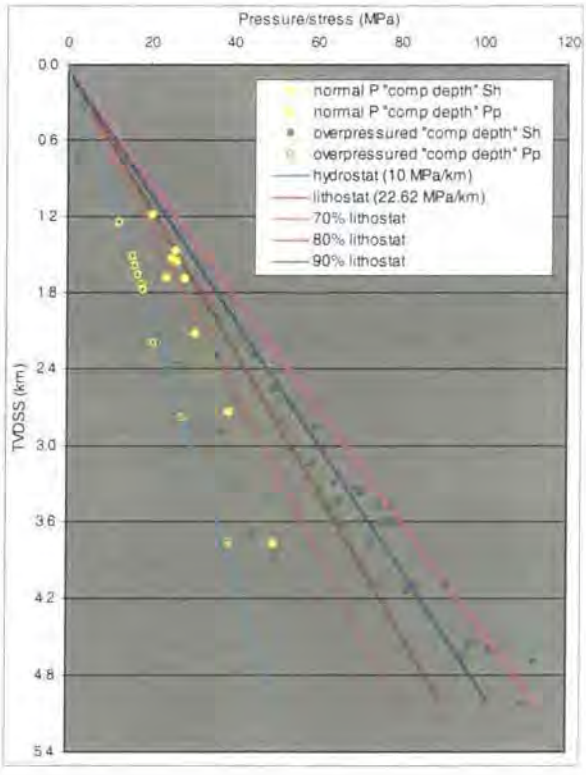

Figure 5.3: Normally and overpressured "*comparable depth*" data for the Central North Sea.

5.2.3.2 Understanding the patterns shown by stress-depth plots

The S_h data from the Central North Sea are plotted by different parameters in an attempt to further explain the S_h variation (see **section 4.3**). The whole S_h data set was plotted by lithology and wellbore diameter to assess their contribution to S_h variability.

- **Lithology and S_h magnitude**

It is clear from **Figure 5.4** that LOTs being conducted in different lithologies do not explain the variation in S_h. 68% of tests were conducted in fine-grained claystone/siltstone yet these lithologies show some of the lowest and highest magnitudes of S_h at a specific depth. Despite the difference in rheological properties, no systematic differences in S_h magnitude appear due to lithology.

- **Wellbore diameter and S_h magnitude**

The S_h data are shown plotted by wellbore diameter in **Figure 5.5**. Whilst there is clearly a progressive decrease in wellbore diameter with depth, where different diameters overlap (e.g. at ~0.7 km and from 1.8 - 2½ km), there is no clear distinction in S_h magnitude. As **Figure 5.6** shows, fitting linear regression lines to the data series based on diameter reveals that smaller diameter wellbores record both lower and higher S_h magnitudes than

larger wellbores. Wellbore diameter variations therefore do not explain S_h differences or contribute to an understanding of the S_h magnitude variation at a specific depth.

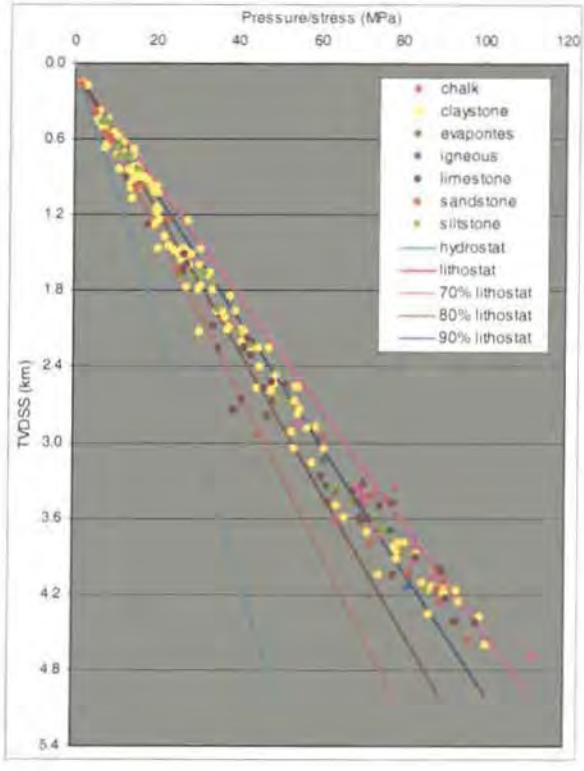

Figure 5.4: All S_h data plotted by lithology that the test was conducted in.

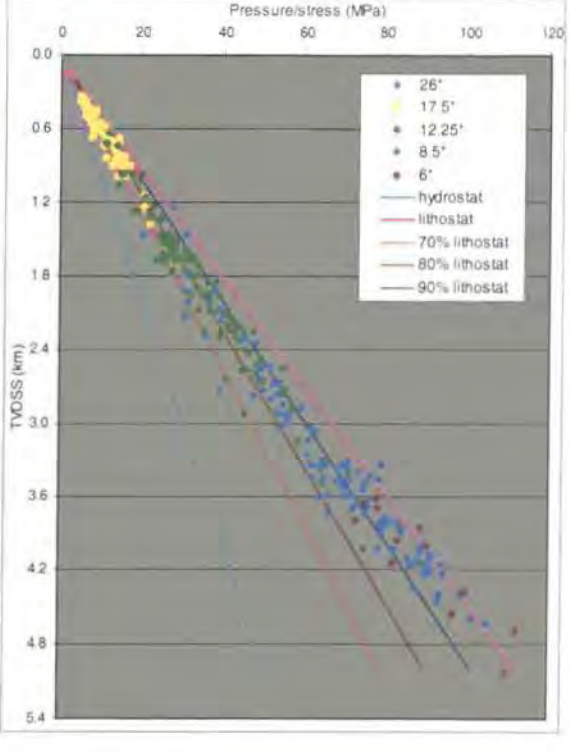

Figure 5.5: All S_h data plotted by wellbore diameter that the test was conducted in.

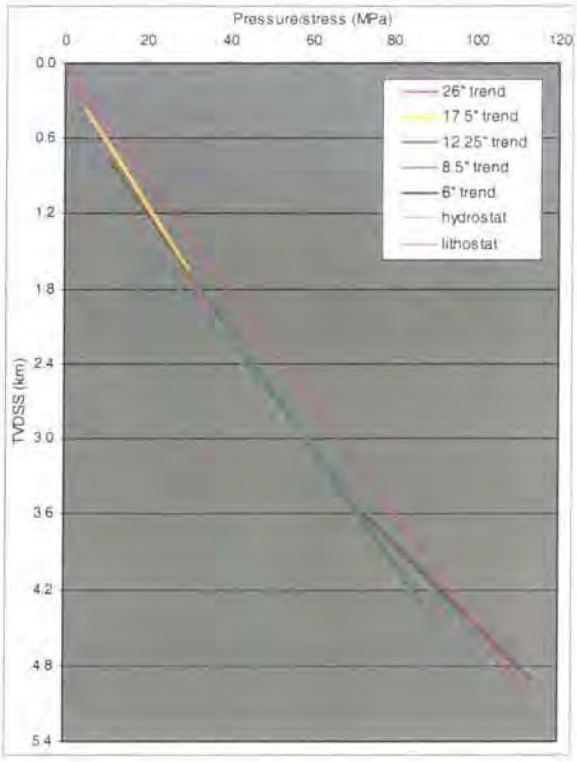

Figure 5.6: Linear regression lines fitted to the S_h data based on wellbore diameter.

5.2.3.3 Summarising what stress-depth plots reveal about S_h magnitude

Plotting the data by lithology (**Figure 5.4**) and wellbore diameter (**Figure 5.5**) does not account for the scatter seen in the S_h magnitudes. Considering **Figure 5.1**, P_p differences exert the greatest control on S_h magnitude in the Central North Sea. S_h magnitudes are 75% to 80% S_V in the shallow, predominantly normally pressured section yet increase to >90% S_V where overpressures are greatest below 4 km. The "*comparable depth*" data separated into normally pressured and overpressured groups reveals normal P_p to be paired with "low" S_h magnitudes and the highest overpressures to be paired with the greatest S_h magnitudes. The relationship is quantified in **section 5.2.5**.

5.2.4 Using the data to estimate regional minimum *in-situ* stress

The regional S_h has been estimated using two approaches. These are the creation of a lower bound to leak-off pressures and an upper limit to pore pressures. The lower bounds to LOPs were created using S_h measurements from the entire data set (**Figure 5.7**) and the "*comparable depth*" data (**Figure 5.8**). The minimum magnitude of S_h was considered for the majority of the data set so that lower bounds plot to the left of most data points while ignoring

rogue "outliers" that drastically under-estimate S_h. Following the creation of lower bounds, P_p data were used to create an upper limit to P_p (**Figure 5.9**). The trends are compared and contrasted and the results given below.

The lower bound to the entire Central North Sea data set is shown in **Figure 5.7**. The curve produces a lower bound to 95% of the S_h measurements. The magnitude of the lower bound increases with depth from 65% S_V at <1 km depth to 70% S_V at 2½ km. Below 2½ km there is a rapid increase up to a maximum of 95% S_V at 4½ km depth. Mathematically, the lower bound can be described as a 2nd order polynomial:

$$y = -0.00023x^2 + 0.06855x + 0.08192 \qquad \textit{(equation 5.2)}$$

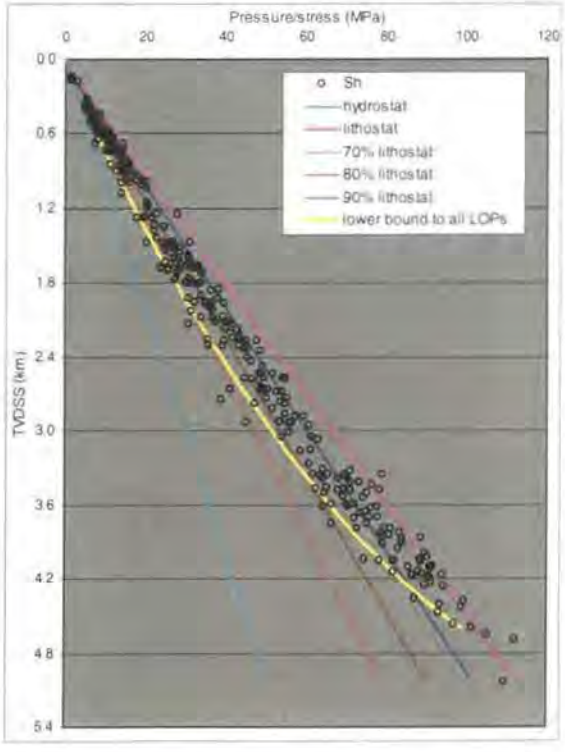

Figure 5.7: Lower bound to all LOPs for the Central North Sea.

The "*comparable depth*" data lower bound is shown in **Figure 5.8**. This lower bound is less well constrained than that for the entire data set but 80% of the S_h data still plot to the right of the curve. The curve shows a rapid increase in magnitude below 2 km depth from 70% to 90% S_V. Accurately constraining the curve at depths of >4 km is hindered by the lack of data. The lower bound to "*comparable depth*" data is described by:

$$y = -0.00022x^2 + 0.06884x - 0.04111 \qquad \textit{(equation 5.3)}$$

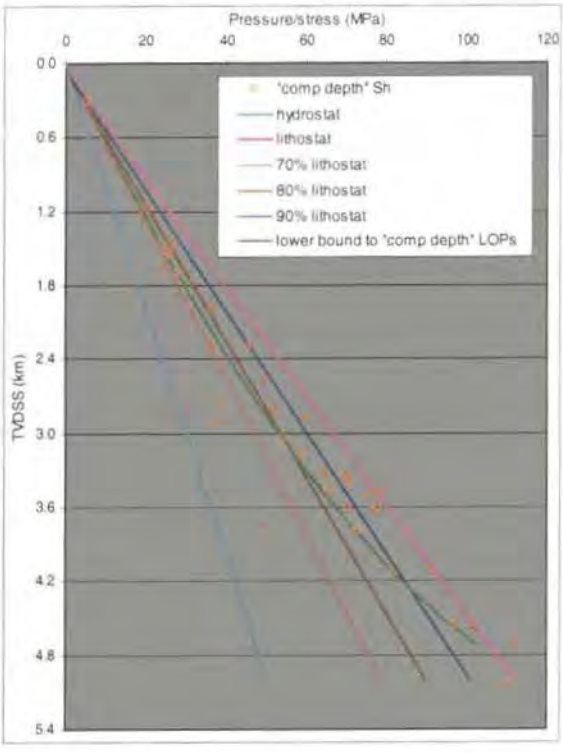

Figure 5.8: Lower bound to "*comparable depth*" LOPs for the Central North Sea.

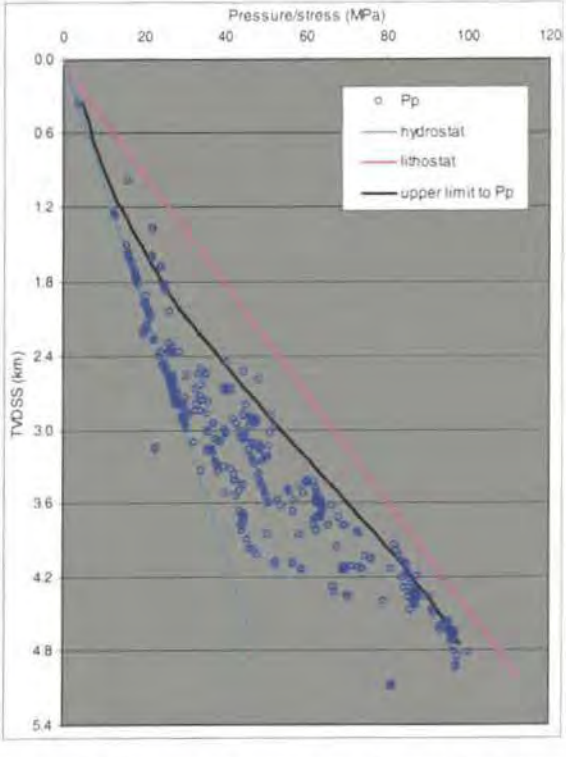

Figure 5.9: Upper limit to P_p for the Central North Sea.

Figure 5.9 shows the upper limit to P_p to be a good estimate of the maximum P_p encountered in the region. Over 90% of the data fall to the left of the trend. The increase in P_p from normally pressured to overpressured is clearly revealed hence the need for two inflexion points. The trend is a 3rd order polynomial:

$$y = (5.34E-06)x^3 - (1.01E-03)x^2 + 0.096x - 0.039 \qquad \textit{(equation 5.4)}$$

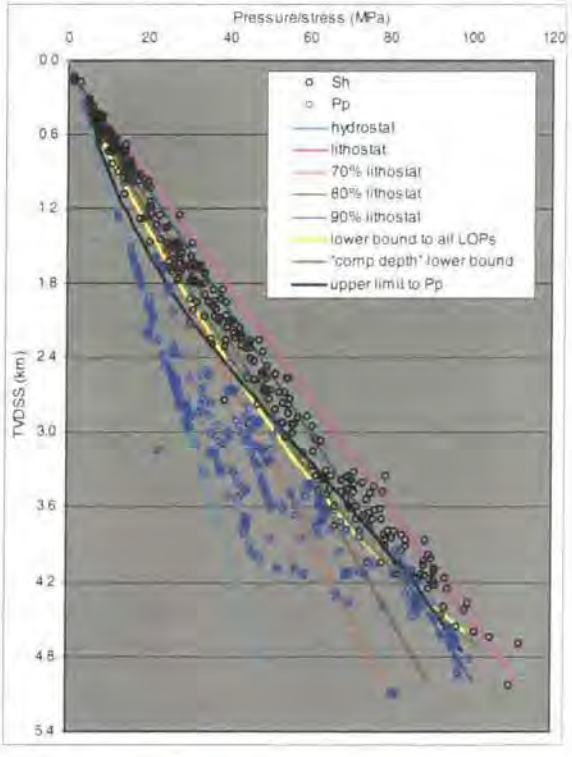

Figure 5.10: Comparative plot showing both lower bounds and the upper limit.

The similarity in both lower bounds shows that a ten-fold reduction in the number of data used to create the trends does not effect the shape or magnitude. The curvature towards S_V shown by both trends reflects the increase in the S_h:S_V ratio with depth shown by **Figure 5.2**. Comparing all three trends (**Figure 5.10**) shows a strong concurrence at all depths. The greatest mismatch occurs at depths of between 0.8 and 2 km where most P_p data are normally pressured and S_h is 70% S_V. In this shallow depth interval the lower bounds are up to 4 MPa in excess of the upper limit. Between 3 and 4 km some P_p are in excess of some S_h measurements and the upper limit to P_p exceeds both lower bounds. The maximum amount that the lower bounds are exceeded by the upper limit is 3½ MPa at 3½ km depth. The strongest concurrence between the three trends occurs in the top part of the transition from normal P_p to overpressures (2.4 to 3 km). The results above show that for the Central North Sea, lower bounds and upper limits can be used to accurately constrain maximum P_p and

minimum S_h magnitudes. This is especially true in the overpressure transition zone (2½ to 3½ km) where the greatest overpressure magnitudes match the lowest magnitudes of S_h (**Figure 5.1**).

5.2.5 Pore pressure *in-situ* stress coupling

This section describes the approaches used to investigate the relationship between the P_p and S_h data. Following on from this, the occurrence of and quantification of pore pressure *in-situ* stress coupling was investigated. The "*comparable depth*" data (see **section 3.7.4**) are used for these investigations.

5.2.5.1 Looking for insights into coupling in the Central North Sea

Initially, P_p data were cross-plotted with S_h data to see how each series increased relative to one another (**Figure 5.11**). The approaches used to look for coupling follow those explained in **section 4.5.1**. The "*comparable depth*" data were firstly plotted wholesale by each approach and then separated into normally pressured and overpressured groups (**Figures 5.12** and **5.13**) to determine the $\Delta S_h/\Delta P_p$ values.

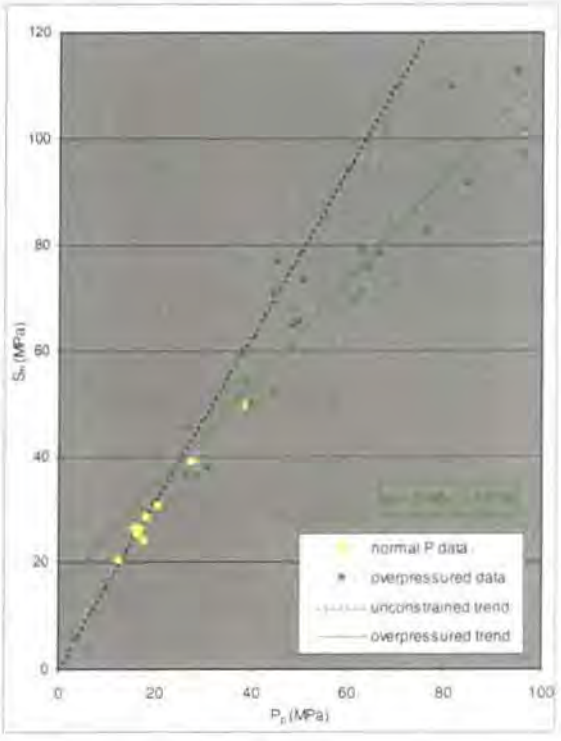

Figure 5.11: S_h versus P_p for the "*comparable depth*" data.

5.2.5.2 Results

A cross-plot of the normally pressured (yellow) and overpressured (green) data is shown in **Figure 5.11**. The dashed line represents a hypothetical unconstrained basin where P_p increases following the hydrostat and S_h increases at a rate of 70% S_V with depth. In this "control situation" P_p and S_h data plotting along the dashed line means their increase can be attributed to an increase in depth (Hillis pers comm., 2001). All bar one of the normally pressured data plot within 3 MPa of the "*unconstrained trend*" showing a hydrostatic increase in P_p and a S_h increase that is 70% lithostatic. Overpressured data plot along a trend with a gradient of 0.98 showing that P_p increases relative to S_h at a rate greater than in the hypothetical unconstrained basin (where the gradient is 1.58) with an increase in depth. Plotting the data by other means allows the $\Delta S_h/\Delta P_p$ value to be determined.

All "*comparable depth*" data were normalised to a hypothetical unconstrained basin and depth and plotted as gradients (depth-normalised). Linear regression lines fitted through the data give the $\Delta S_h/\Delta P_p$ value. These data are separated into normally pressured and overpressured groups in **Figures 5.12** and **5.13**. Regression lines are fitted to the overpressured data and the results summarised below:

Data statistics refer to	Data plotted as gradients (e.g. *[S_h-gradient]*)		Data normalised to an "unconstrained basin" & depth (e.g. *[(S_h-S_h(T))/depth]*)	
	$\Delta S_h/\Delta P_p$	r^2	$\Delta S_h/\Delta P_p$	r^2
All data	0.64	0.69	0.70	0.49
Overpressured	0.54	0.59	0.52	0.57

Table 5.2: Summary table showing the nature of pore pressure *in-situ* stress coupling ($\Delta S_h/\Delta P_p$) and correlation coefficients (r^2) for the Central North Sea.

Figures 5.12 and **5.13** show hydrostatically pressured data are associated with the lowest S_h values. Normal pressure S_h gradients range from 13.1 MPa/km (cf. hypothetical unconstrained gradient of 15.75 MPa/km) to 17.8 MPa/km giving a range of 4.7 MPa/km. This contrasts with the overpressured data where S_h gradients range between 15.7 MPa/km and 23.9 MPa/km (a range of 8.2 MPa/km). The greater range for the overpressured data reflects the large range in P_p gradients (between 10.6 and 20.7 MPa/km).

The $\Delta S_h/\Delta P_p$ values in **Table 5.2** are between 0.5 and 0.7 depending which data are analysed. Correlation coefficients (r^2 values) of between 0.5 and 0.7 show relationships to be

quite strong. Coupling is thus inferred for the Central North Sea with a 1 MPa increase in P_p producing a 0.55 MPa S_h increase. Coupling is also inferred to be the strongest control on S_h magnitude, aside from depth. It is felt to be the best explanation for why the largest scatter in S_h coincides with the greatest range of overpressure (**Figure 5.1**).

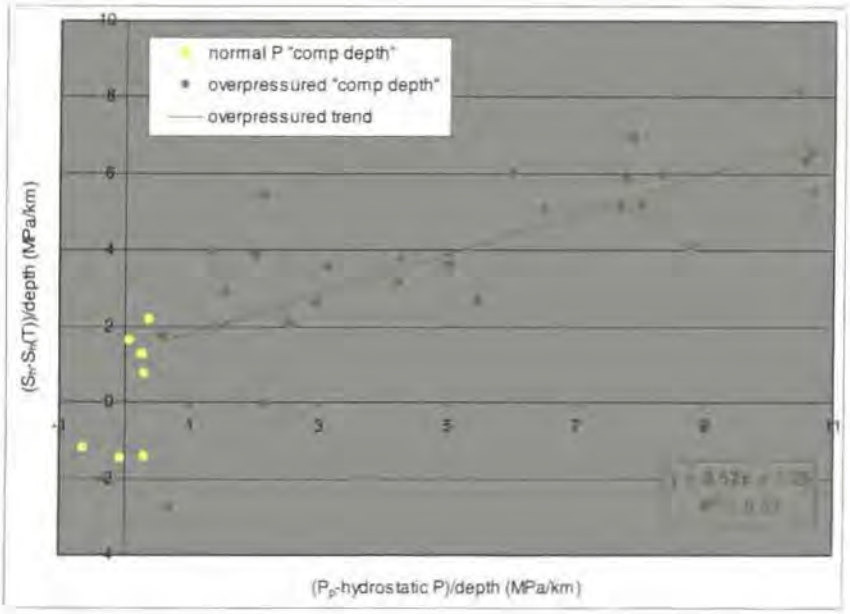

Figure 5.12: Normally pressured and overpressured "*comparable depth*" data normalised to a hypothetical unconstrained basin and depth.

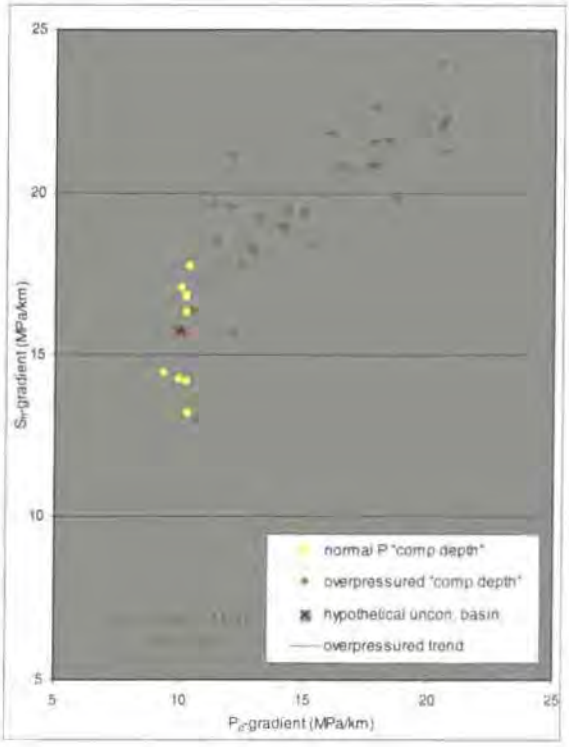

Figure 5.13: Normally and overpressured "*comparable depth*" data depth-normalised.

5.2.6 Summarising the results for the Central North Sea

In the above study, the Central North Sea S_h and P_p data (compiled from *PressureView*) have been plotted on stress-depth plots, normalised to both a hypothetical unconstrained basin and depth, and plotted as gradients. This was done to investigate the variations in, and controls on, S_h magnitude. Also undertaken were investigations that look for insights into P_p-S_h coupling. The results are summarised below:

- The scatter in the magnitude of S_h at a specific depth is large with a maximum of 17 MPa at 2¾ km (which can be quantified as being 30% of S_V at that depth).
- The transition from normal pressure to overpressure occurs from 2½ - 3½ km. The greatest range in P_p occurs at 4 km where overpressure variation is between 5 and 44 MPa.
- The average magnitude of S_h increases relative to S_V with depth from 0.7 at 1 km to 0.95 at 4¼ km. The greatest rate of increase is coincident with the onset of overpressure. Overpressure thus exerts a control on S_h magnitude.
- The "*comparable depth*" data show that higher values of S_h are associated with overpressures.
- Differences between individual tests (i.e. lithology and wellbore diameter differences) are not reflected in the S_h magnitude and do not explain S_h variation.
- Lower bounds to LOPs created for all the data and the "*comparable depth*" data show strong similarities. Both curve towards the lithostat at depths greater than 2½ km.
- The upper limit to P_p matches both lower bounds closely (the variation is <4 MPa).
- Lower bounds and upper limits can be used to accurately estimate the maximum P_p and the minimum magnitude of S_h (especially in overpressured zones).
- Pore pressure *in-situ* stress coupling is inferred for the Central North Sea. High S_h magnitudes are coincident with overpressuring. Where overpressures occur, the $\Delta S_h/\Delta P_p$ value is ~0.55 with a correlation coefficient of 0.6.

5.3 Brunei

5.3.1 Introduction to Brunei

This introduction provides background information on Brunei. The location of the region is given and the contemporary stress situation reviewed. The burial history is summarised followed by the overpressure in terms of distribution, its link to specific lithologies and the likely causes of its generation.

- **Location**

Brunei Darussalam sits 5^{O} N of the equator with a latitude of 115^{O} E. It occupies the northern portion of the island of Borneo in the South China Sea and shares the island with parts of Malaysia and Indonesia (Curiale *et al.*, 2000).

- **The contemporary stress situation**

The stress situation in Brunei is believed to be a transpressive regime and has the geological context of an active margin (Grauls & Baleix, 1994; Grauls, 1997). Grauls (1994) states that the magnitudes of S_h are up to 13% greater in Brunei compared to a passive margin regime. The region is believed to be influenced by the subduction of the South China Sea to the south of Borneo (Grauls, 1994 & pers. comm., 1999) which creates the transpressive context. Borehole breakout and earthquake focal mechanism data from the *World Stress Map Project* (Mueller *et al.*, 2000) show the maximum horizontal stress direction is NW-SE and the regime is compressive. These are confirmed (Tingay & Hillis pers. comm., 2001) by stress orientations deduced from drilling-induced tensile fractures (DITFs).

- **The burial history**

The Brunei region is composed of thick (up to 10 km) Mid-Miocene to Recent marine deltaic sediments (Van Rensbergen & Morley, 2000). Since the wells used in this study come from the upper 3 km of the sedimentary succession, the Neogene sediments are considered. To a depth of 3400 metres the succession can be divided into three intervals:

- The Upper Pliocene to Recent is up to 1800 metres thick and shows sedimentation rates of in excess of 700 m/Ma and up to 1000 m/Ma (Grauls, 1998). It is characterised by a high sand to shale ratio (Grauls & Cassignol, 1993).
- The Lower Pliocene section from 1800 to 2500 metres depth is mainly composed of shales and reflects a lower (but still a high 500 m/Ma) sedimentation rate connected with deltaic progradation.

- The Upper Miocene section extends to 3400 metres depth and is characterised by fissile shales with thin, low permeability silt layers (Grauls & Cassignol, 1993). Sedimentation rates were lower than later in the succession.

- **Overpressure**

The geographical locations of the wells are confidential and are not available to this study. Based on knowledge of the operational areas of *TotalFinaElf* the overpressure situation has been deduced for the NE of the Brunei region. Three main intervals exist:

- The high sand to shale ratio in the Upper Pliocene (as shown by the gamma ray log – Grauls & Cassignol, 1993) has resulted in normal compaction of the shales due to easy drainage through the sands (Grauls, 1998). No overpressures occur in this interval.
- The predominance of shales in the Lower Pliocene interval results in a region of high overpressure. The interval from 1800 to 2500 is undercompacted implying disequilibrium compaction and a constant build up of fluid pressures from hydrostatic at 1800 metres to 20 MPa overpressure at 2500 metres (Grauls & Cassignol, 1993).
- Despite a similar lithology to the Lower Pliocene, higher magnitudes of overpressure are found through the Upper Miocene section from 2500 to 3400 metres. Fluid pressures extend up to 60 MPa at 3000 metres (30 MPa of overpressure) and are locally in excess of the minimum stress. The overpressure through this interval is believed to be partially caused by compressive tectonics that existed during the Upper Miocene (Grauls, 1998). There is also believed to be a contribution from episodic transfer of deep fluids though the hydraulically-induced fracture network in existence at these depths (Grauls & Cassignol, 1993).

5.3.2 Compiling the data

TotalFinaElf provided the Brunei data set of 23 P_p and S_h measurements. As P_p were recorded at the same depth as S_h measurements were taken these data are also "*comparable depth*" data. Both P_p and S_h data were recorded in grammes per cubic centimetre (g/cc) so were converted to Mega Pascals (MPa). The conversion is straightforward and uses *equation 5.5*:

$$MPa = \left(\frac{g/cc \times 0.0981 \times TVDKB}{10} \right) \qquad \textit{(equation 5.5)}$$

Where: *TVDKB* = depth from the kelly-bushing (m).

The lithostat for Brunei was calculated using the algorithm for S_V in a sand-shale succession proposed by Traugott (1997). The equation used is:

$$S_V = \frac{8.5W + \rho_{ave.}(D - W - A)}{D} \qquad \textit{(equation 5.6)}$$

Where: W = water depth (ft);

D = TVDKB (ft);

A = Kelly-bushing elevation (ft);

$\rho_{ave.}$ = average density of the sediment (ppg).

The average density of the sediment is calculated using:

$$\rho_{ave.} = 16.3 + \left[\frac{D - W - A}{3125}\right]^{0.6} \qquad \textit{(equation 5.7)}$$

5.3.3 Stress-depth plots

Following the conversions of units from g/cc to MPa for the S_h and P_p data and the determination of the lithostat (see above) the data have been plotted on stress-depth plots. The objectives that apply to this section have been listed in **section 5.2.3**.

5.3.3.1 Relationships shown by stress-depth plots

The Brunei S_h and P_p data are shown separated into normally pressured and overpressured groups and plotted on a stress-depth plot in **Figure 5.14**. Also shown are the lithostat (see **section 5.3.2.**), hydrostat (10 MPa/km), 70% S_V (red), 80% S_V (brown) and 90% S_V (darker blue) gradients.

The small number of data in **Figure 5.14** makes quantifying the amount of scatter in S_h difficult. The only depth where significant (9 MPa) scatter occurs is 2.6 km. The amount of scatter is tabulated in **Table 5.3** following the technique described in **section 4.2**.

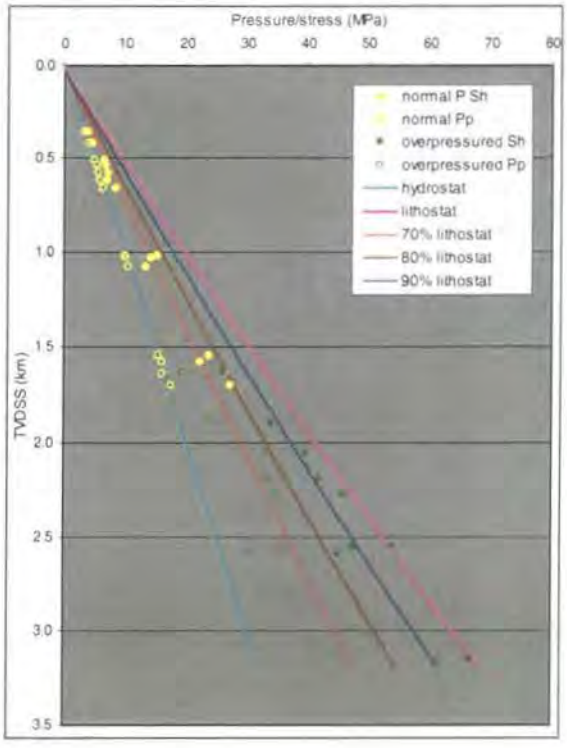

Figure 5.14: Normally and overpressured S_h and P_p data from Brunei.

Depth (kilometres)	Variability in S_h (MPa)
0.5	1.5
0.75	-
1.0	3
1.25	-
1.5	2
1.75	2
2.0	-
2.25	2
2.5	9
2.75	-
3.0	-
3.25	-

Table 5.3: Variability in the magnitude of S_h at 250 metre intervals.

Relative to the lithostat, S_h increases from 60% S_V at depths <1 km, to 70% S_V at 1½ km, 80% S_V at 1¾ km and 90% S_V below 2 km (**Figure 5.14**). The deepest measurement at 3.2 km, shows S_h to be lithostatic. The S_h:S_V ratio versus depth plot (**Figure 5.15**) shows an evolution from 0.57 – 0.67 at 0.3 to 0.5 km through to 0.83 - 1.01 at 2.6 km. Despite scatter, the increase in S_h with depth is greater than the increase in the lithostat with depth. From this evidence it can be interpreted that the S_h increase in Brunei is due to more than just the increase in depth.

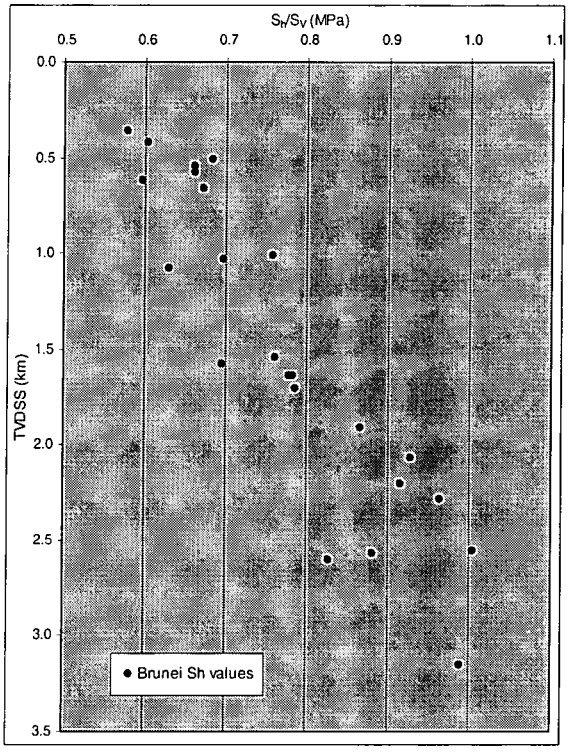

Figure 5.15: S_h normalised to S_V.

P_p magnitudes show that at less than 1.6 km depth, pressures are hydrostatic. Below 1.6 km overpressures range from 3 MPa at 1.6 km depth to 30 MPa of overpressure at the base of the section (3.1 km). This 30 MPa of overpressure at 3 km corresponds to 91% of S_V.

Separating the data into normally pressured (yellow) and overpressured (green) groups shows normal P_p are paired with S_h measurements from 60% - 80% S_V. Higher S_h magnitudes (80% to 101% S_V) are recorded in rocks with overpressures. The data show that high P_p are paired with higher S_h values (relative to S_V) although the relationship cannot be quantified from this plot (**Figure 5.14**). Overpressure variations can explain the scatter in S_h magnitude at specific depths. Where the 9 MPa S_h variation occurs at 2.6 km overpressures show their largest variation of 19 MPa.

5.3.3.2 Understanding the patterns shown by stress-depth plots

The only parameter available to plot the Brunei S_h data by is the wellbore diameter. The results are shown in **Figure 5.16** and described below:

- **Wellbore diameter and S_h magnitude**

The scarcity of data makes analysing for the effects of wellbore diameter differences on S_h difficult. Fitting linear regression lines to each data series shows that at 1 km depth there is an overlap between the 17½" wellbore and the 12¼" wellbore. At this depth the 12¼" wellbore supports a 3 MPa higher magnitude of S_h. This one instance does not provide conclusive evidence for a link between wellbore diameter and the recorded magnitude of S_h. It does not explain the remainder of the scatter between 1¾ and 2.6 km depth.

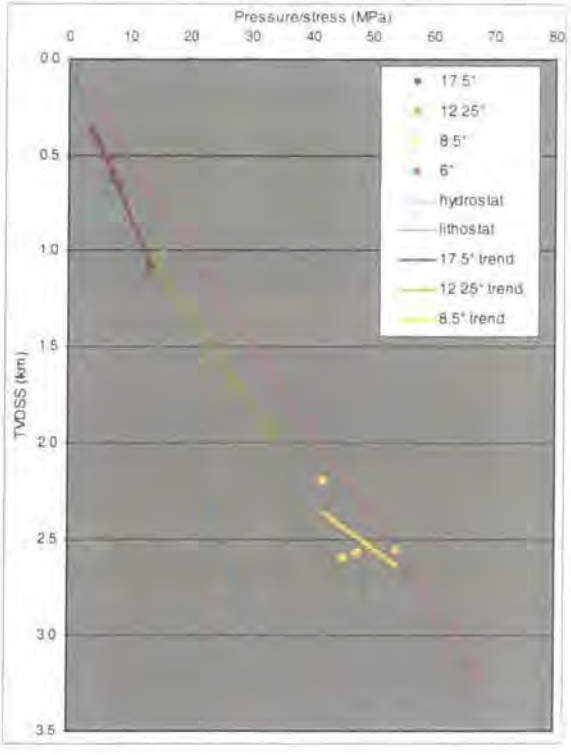

Figure 5.16: S_h data plotted by wellbore diameter for Brunei.

5.3.3.3 Summarising what stress-depth plots reveal about S_h magnitude

Analyses into explanations for the scatter seen in S_h are hindered by a lack of information associated with the data. Wellbore diameter is the only known parameter. **Figure 5.16** reveals the scatter in the magnitude of S_h at a given depth is not explained by differences in the wellbore diameter. The scatter can be attributed to the magnitude P_p especially at greater depths (**Figure 5.14**). Lower P_p are paired with lower values of S_h while overpressures

are paired with greater S_h magnitudes. Further analyses on the P_p-S_h relationship appear in **section 5.3.5.**

5.3.4 Using the data to estimate regional minimum *in-situ* stress

Two approaches were used to gain estimates of the regional minimum *in-situ* stress in Brunei. Firstly, a lower bound to LOPs (**Figure 5.17**) was created from the S_h measurements so that all S_h data plotted to the right of, or actually on, the trend. The paucity of data meant that accurately constraining the trend (especially >1¾ km depth) was difficult because there were no obvious under-estimates of S_h. Secondly, independent use of the P_p data created an upper limit to P_p (**Figure 5.18**). Both trends were then compared and contrasted (**Figure 5.19**). The results are described below.

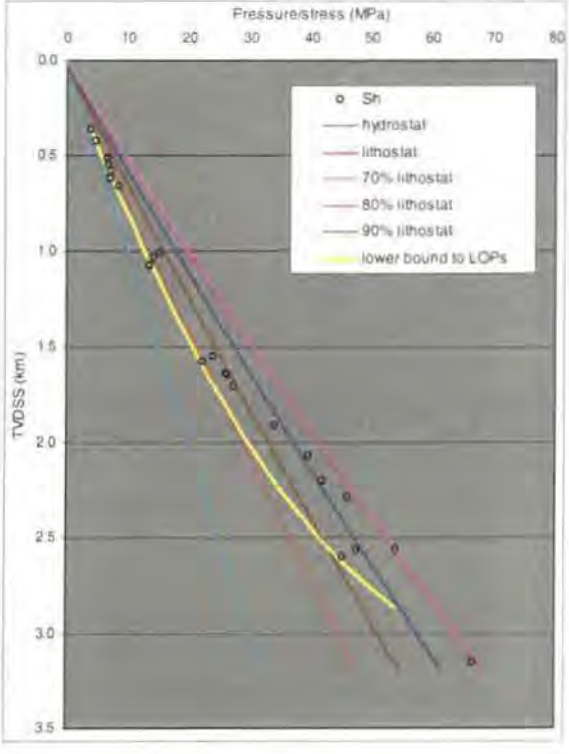

Figure 5.17: Lower bound to LOPs for Brunei.

The lower bound to LOPs for Brunei is shown in **Figure 5.17**. The curve produces a lower bound to all S_h measurements in the data set. The magnitude shows an increase from 60-65% S_V at depths of <1½ km to 70% S_V at 1.8 km. Below 1.8 km depth the trend noticeably swings towards the lithostat. The trend crosses 80% S_V at 2½ km and touches the 90% S_V gradient at 2.9 km. Mathematically, the lower bound can be described by:

$$y = -0.00055x^2 + 0.0819x + 0.04525 \qquad \textit{(equation 5.8)}$$

The upper limit to P_p (**Figure 5.18**) provides a good estimate for the maximum P_p encountered in the region (based on the data available) as all points fall on, or plot to the left of, the trend. The transition from normally pressured to overpressured fluids between 1½ and 2 km shows the need for two inflexion points meaning the curve is a 3rd order polynomial:

$$y = (1.537E-05)x^3 - (1.857E-03)x^2 + 0.107x - 0.0201 \qquad \textit{(equation 5.9)}$$

Comparing the lower bound and the upper limit (**Figure 5.19**) shows varying amounts of mismatch. The greatest mismatch occurs below 2 km where the upper limit exceeds the lower bound by up to 5 MPa. Between ½ and 1.4 km the lower bound is in excess of the upper limit by a maximum of 3 MPa. The only real concurrence occurs between 1.4 and 1.7 km (coincident with the onset of overpressure) and is where the upper limit switches from being less than to greater than the lower bound.

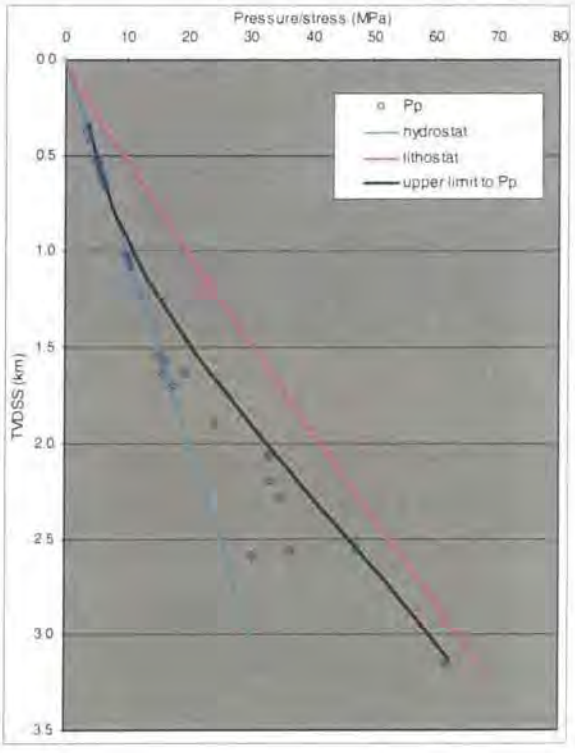

Figure 5.18: Upper limit to P_p for Brunei.

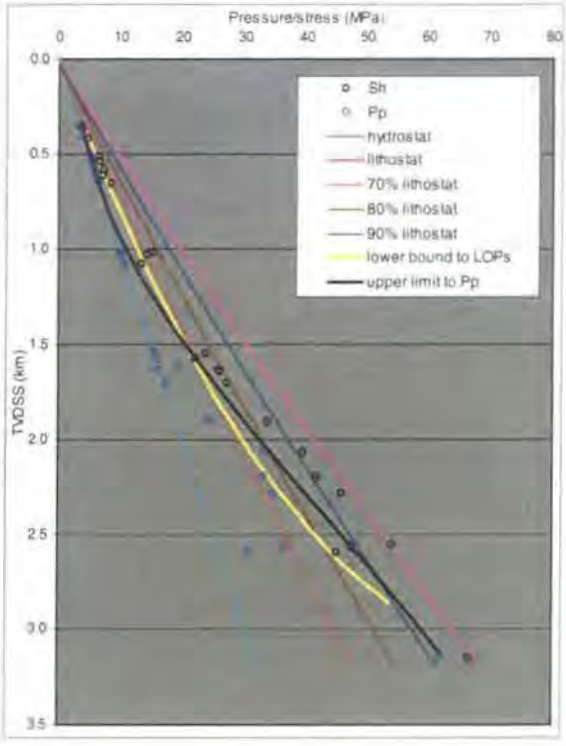

Figure 5.19: Comparative plot showing the lower bound and the upper limit.

Given the data available for Brunei, relying on the lower bound to LOPs to estimate the maximum P_p or the upper limit to P_p to determine S_h will leads to mis-estimates of up to 5 MPa. The reason for the mismatches is felt to be the lack (rather than quality) of data making highly accurate constraints of the trends difficult.

5.3.5 Pore pressure *in-situ* stress coupling

In the following section the relationship between P_p magnitude and S_h magnitude at the same depth is undertaken. This investigation leads to the examination of the presence of P_p-S_h coupling and a quantification of the way S_h changes with overpressure.

5.3.5.1 Looking for insights into coupling in Brunei

Figure 5.20 shows one way of comparing overpressure and S_h. P_p data are normalised to the hydrostat and S_h data are normalised to S_v and the data plotted versus depth to compare how each ratio changes at the same location. The hydrostat and lithostat were chosen as normalisation parameters because they can be accurately measured.

The data are separated into normally and overpressured pairs and absolute P_p and S_h magnitudes cross-plotted in **Figure 5.21**. This approach investigates the way both parameters increase relative to each other. To investigate the occurrence and level of P_p-S_h coupling (the $\Delta S_h/\Delta P_p$ value), all data were normalised to a hypothetical unconstrained basin and depth and plotted as gradients (depth-normalised). Normally pressured and overpressured groups are plotted using these techniques in **Figures 5.22** and **5.23**. The methodology is explained in **section 4.5.1**.

5.3.5.2 Results

In the upper 1½ km (**Figure 5.20**) P_p remain at a fixed 1:1 ratio with the hydrostat. S_h data show a spread in S_h:S_V ratio of 0.6 - 0.7 for the same depths. Below 1½ km, both P_p and S_h increase their respective ratios up to a maximum of 1.96 for P_p:hydrostat and 0.99 for S_h:S_V at 3.2 km. Results confirm the belief from **Figure 5.14** that greater S_h magnitudes are coincident with greater overpressures but they relationship cannot be quantified here.

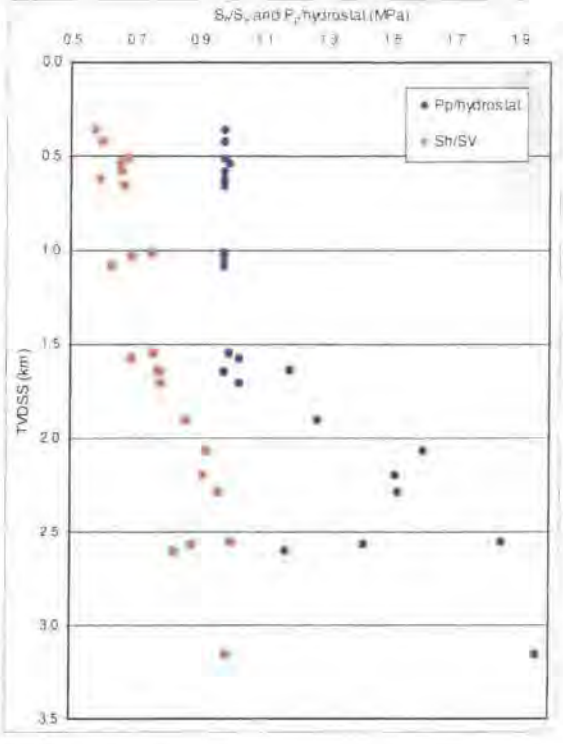

Figure 5.20: S_h:S_V and P_p:hydrostat versus depth for the Brunei data.

The data are shown separated into normally pressured (yellow) and overpressured (green) groups in **Figure 5.21** with S_h on the y-axis and P_p on the x-axis (cf. **section 5.2.5.2**). Normally pressured data follow the "*unconstrained trend*" showing P_p and S_h closely follow the

unconstrained model. Overpressured data depart to the right (gradient = 0.9 versus 1.58) of the "*unconstrained trend*" showing P_p are increasing at an above hydrostatic rate. The increase in the magnitude of the overpressured S_h and P_p data cannot be solely attributed to depth increases. Other approaches are used below to further explain the relationship between P_p and S_h.

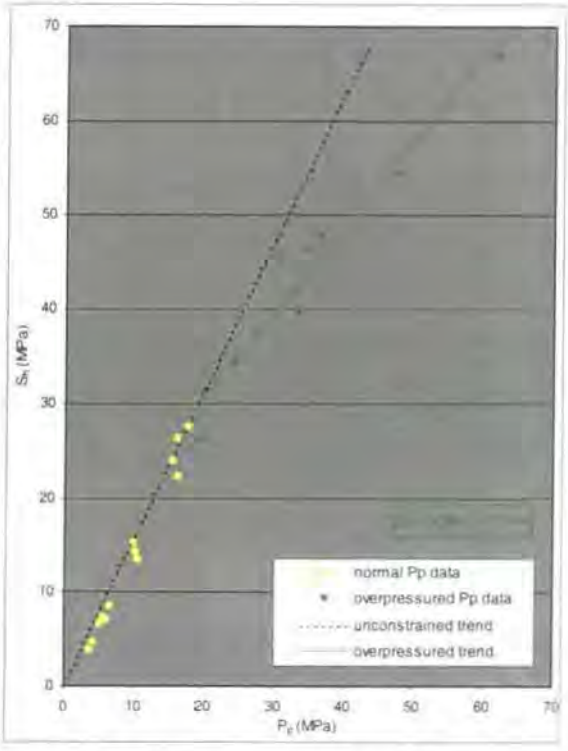

Figure 5.21: S_h versus P_p for the Brunei data.

Cross-plotting the Brunei data by the approaches described in **section 4.5.1** and fitting linear regression lines gives the $\Delta S_h/\Delta P_p$ value. The data are separated into normally pressured and overpressured groups in **Figures 5.22** and **5.23**. Regression lines are fitted to the overpressured data. **Table 5.4** summarises the relationships:

Data statistics refer to	**Data plotted as gradients (e.g. *[S_h-gradient]*)**		**Data normalised to an "unconstrained basin" & depth (e.g. *[(S_h-S_h(T))/depth]*)**	
	$\Delta S_h/\Delta P_p$	**r^2**	**$\Delta S_h/\Delta P_p$**	**r^2**
All data	0.94	0.78	0.80	0.82
Overpressured	0.59	0.87	0.54	0.87

Table 5.4: Summary table showing the nature of pore pressure *in-situ* stress coupling ($\Delta S_h/\Delta P_p$) and correlation coefficients (r^2) for Brunei.

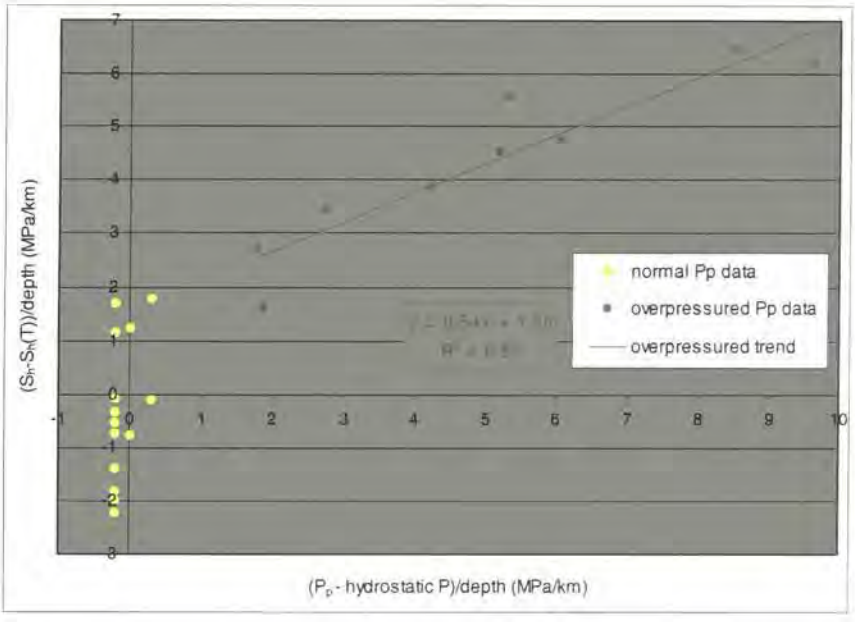

Figure 5.22: Normally pressured and overpressured data normalised to a hypothetical unconstrained basin and depth.

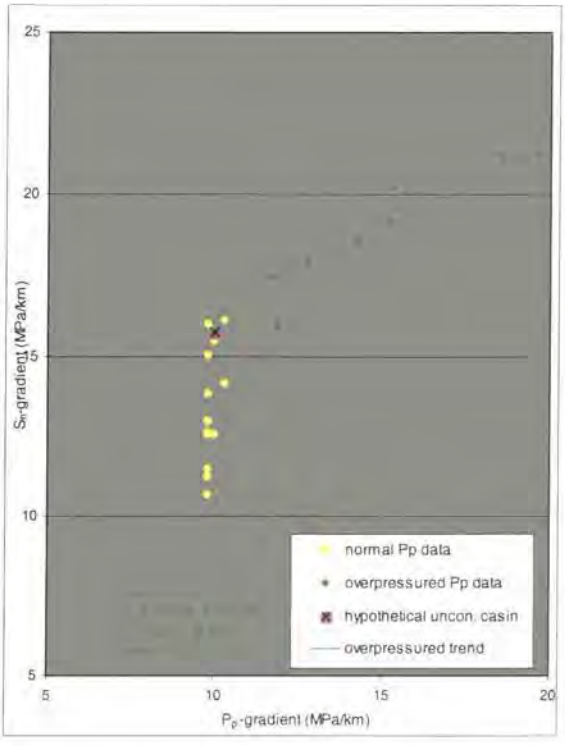

Figure 5.23: Normally and overpressured data depth-normalised.

Figures 5.22 and **5.23** show that overpressured data have associated with them the greatest S_h magnitudes. These can be expressed as gradients varying from 15.9 to 21.1 MPa/km. The highest S_h gradients are paired with the highest P_p gradients (up to 19.6

MPa/km). The normally pressured P_p data show that some S_h gradients are well below the hypothetical unconstrained basin gradient of 15.75 MPa/km. Gradients are as low as 11 MPa/km. These low gradients are paired with P_p gradients of 9.8 MPa/km.

The overpressured data in **Figures 5.22** and **5.23** show clear increases in S_h with P_p increases. Correlation coefficients (r^2 values) of 0.87 show P_p-S_h coupling to be occurring in Brunei with S_h increasing at ~60% of the P_p increase. Coupling best explains the high S_h magnitudes in overpressured zones and why larger S_h variations occur at depths where there are large overpressure ranges.

5.3.6 Summarising the results for Brunei

The sections above describe the results of plotting the Brunei data on stress-depth plots, normalising the data to both a hypothetical unconstrained basin and depth, and plotting the data as gradients. The reasons were to examine the scatter in, and controls on, S_h magnitude at depth, provide estimates for the regional minimum *in-situ* stress and look for insights into P_p-S_h coupling. The results are summarised below:

- A small number of data results in a smaller amount of scatter (compared to the Central North Sea). At 2.6 km the scatter in S_h is 9 MPa. At all other depths scatter is <3 MPa.
- The transition from normal P_p to overpressures at 1½ km is coincident with P_p data showing more variation. The maximum overpressure range of 4 - 23 MPa occurs at 2.6 km.
- The greatest increase in S_h relative to S_V is coincident with the onset of overpressure (below 1.6 km). Stress-depth plots show higher S_h magnitudes are paired with higher P_p measurements.
- The greatest S_h variation occurs at the same depth as the greatest overpressure range (namely at 2.6 km). This is further evidence for P_p influencing S_h magnitude.
- Wellbore diameter variations do not explain S_h magnitude variations.
- The lower bound to LOPs is curvi-linear in shape and shows strong curvature towards the lithostat below 1.8 km depth (coincident with overpressuring).
- The upper limit to P_p shows up to a 5 MPa mismatch with the lower bound. The reason for the mismatches is considered to be the lack (rather than quality) of data making accurate constraints of the both trends difficult.
- P_p-S_h coupling is the strongest explanation for why larger S_h magnitudes occur within the overpressured zone. For the overpressured data, S_h increases at ~60% the increase in P_p. A r^2 value of 0.87 shows the relationship to be statistically strong.

5.4 The Gulf of Mexico

5.4.1 Introduction to the Gulf of Mexico

Background information on the Gulf of Mexico is given in this introduction. The location of the region is given and the contemporary stress situation reviewed. The sedimentation is summarised followed by the overpressure in terms of distribution and the likely causes of its generation.

- **Location**

The Gulf of Mexico is the region between North America and Mexico to the west and Cuba to the east. These data in this study come from Offshore Louisiana on the Mississippi delta.

- **The contemporary stress situation**

The maximum *in-situ* stress has been shown by borehole breakout compilations from the *World Stress Map Project* (Mueller *et al.*, 2000) and Yassir and Zerwer (1997) to be NE-SW in the Offshore Louisiana region. This direction is parallel to the strike of the progradational clastic wedge indicating the minimum horizontal stress (S_h) direction to be normal to the shelf margin (down dip). However there are local perturbations in the region due to the presence of faults and salt structures (Yassir & Zerwer, 1997).

The correspondence between the orientation of fault trends, salt structures, S_H orientations from breakouts and the margin of the clastic wedge confirms the existence of a stress anisotropy. The stress anisotropy is caused by the geometry and orientation of the prograding sedimentary wedge and is associated with gravity-driven extension. This evidence points to the contemporary stress regime being $S_h<S_H<S_V$ representing an Andersonian extensional system (Anderson, 1905) or passive context (Grauls, 1994).

- **Sedimentation**

The sedimentation of the Offshore Louisiana region is characterised by rapidly deposited thick (up to 16 km) Tertiary successions of progradational deltaic (sands and shales) sediments. Depositional magnitudes varied across the region due to the style of the delta (a bird's foot delta) as sediment was transported into the depocentre along submarine canyons. In the Offshore Louisiana region the Pleistocene reaches 700 metres thick, the Pliocene 500 metres and the Middle and Upper Miocene is 1300 metres. These were all deposited under shelf conditions (Reymond & Stampfli, 1996).

- **Overpressure**

Undercompaction in the Gulf of Mexico has been used to infer that the large magnitudes of overpressure seen in the Offshore Louisiana region can be attributed to disequilibrium compaction (Dickinson, 1953; Yassir & Bell, 1994). The cause of the undercompaction was the rapid rate of sedimentation associated with the prograding Mississippi delta. Spatial variations in the magnitude of overpressure as a result of disequilibrium compaction are due to differences in the sand-shale ratio (Kan & Kilsdonk, 1998). Overpressures in rocks from greater than 3 km depth, while porosities show a component of undercompaction, have been attributed in part to the thermal generation of gas (Hunt *et al.*, 1998). Work by Kuo (1997) has shown that there is a compositional similarity between the original reservoir fluid and the combined compositions of the gas in the reservoirs and the "left-over" oil. This result has been quoted as evidence for the high fluid pressures resulting from a large amount of gas exsolution within a small depth interval.

5.4.2 Compiling the data

The Gulf of Mexico data come from the Mississippi Canyon, Green Canyon and Eugene Island. The data set was created from the *PI Erico* data (original records were unavailable). This lead to the compilation of 65 true leak-off (LOP-LOs) values and lost circulation (LOP-LCs) values. The LOP-LC data were corrected following the procedure described in **section 5.2.2** and using *equation 5.1*.

Out of the 65 S_h measurements in the data set only 11 had a P_p measurement taken within 100 metres of the pumping pressure test. These 11 data points are the Gulf of Mexico "*comparable depth*" data set (cf. **section 3.7.4**).

The lack of a density log for the study meant that once again the lithostat was calculated using the algorithm for S_V proposed by Traugott (1997). The algorithm was created based on data from the Gulf of Mexico (Traugott pers. comm., 2001). The method for calculating S_V is explained in **section 5.3.2**. An average water depth of 400 metres was assumed.

5.4.3 Stress-depth plots

Following the compilation of the data and the determination of the lithostat, S_h and P_p have been plotted on stress-depth plots. The objectives of this part of the Gulf of Mexico study are the same as those listed in **section 5.2.3**.

5.4.3.1 Relationships shown by stress-depth plots

All data from the Gulf of Mexico are plotted on a stress-depth plot in **Figure 5.24**. Also shown, for reference, are the lithostat, the hydrostat (10 MPa/km), 70% S_V, 80% S_V and 90% S_V gradients. The gradients show the changes in S_h relative to S_V with depth. The scatter in S_h is significant. Quantification of the scatter is given below (following the procedure described in **section 4.2**).

Depth (kilometres)	Variability in S_h (MPa)
0.5	2
0.75	1.5
1.0	4.5
1.25	6.5
1.5	8
1.75	12.5
2.0	9
2.25	3
2.5	12
2.75	17
3.0	16
3.25	5.5
3.5	2
3.75	11
4.0	10
4.25	17
4.5	2

Table 5.5: Variability in the magnitude of S_h at 250 metre intervals.

Table 5.5 and **Figure 5.24** show that the greatest scatter occurs between 2¾ and 3 km with a maximum of 17 MPa occurring at 2¾ km. The greatest S_h magnitude at this depth is 57 MPa so the scatter amounts to 30% of the maximum S_h. Depths where small amounts of scatter are seen are those depths with the fewest data points. Using the gradients to constrain S_h relative to the lithostat shows S_h magnitudes vary between 70% and 103% S_V throughout the section.

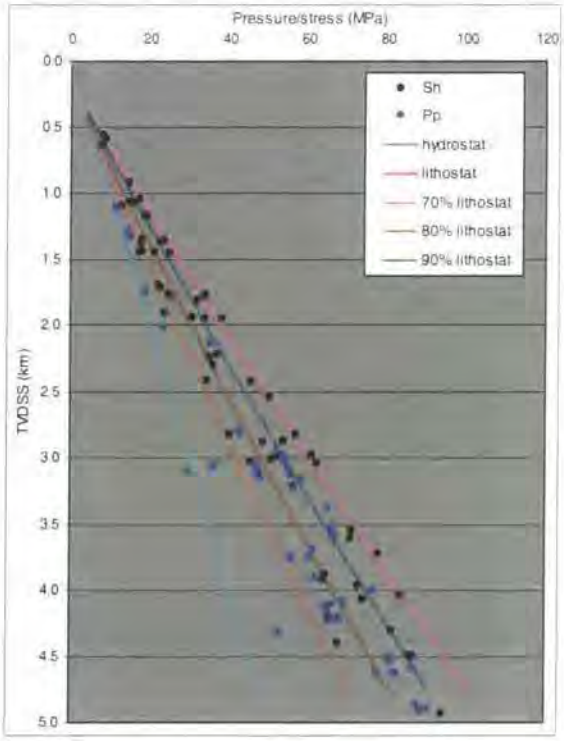

Figure 5.24: All S_h and P_p data for the Gulf of Mexico.

The variation in the magnitude of S_h relative to the S_V is illustrated by **Figure 5.25** which plots S_h:S_V versus depth. From 1 km depth down to 4½ km the S_h:S_V ratio is predominantly between 0.8 and 1.03. Below 2 km there is not a systematic increase in the S_h:S_V ratio with depth.

P_p data show more variation than the S_h data in **Figure 5.24**. Only 3 normal P_p occur within the data set used in this study. Small (<5 MPa) overpressures occur up to 1¾ km depth while larger (>20 MPa) overpressures are only seen below 3 km. With the exception of 4 measurements, P_p below 3 km ranges from 75% to 95% S_V. A pressure of 95% S_V at 4 km depth is 77 MPa or 37 MPa of overpressure. P_p show maximum levels of overpressure at the greatest depth. The deepest P_p measurements (at 4.9 km) have 42 MPa of overpressure.

At depths greater than 3 km, the magnitude of P_p is seen to be in excess of some S_h magnitudes at the same depth. Both P_p and S_h data plot between 70% and 95% S_V. This is clearly illustrated at 3 km depth (**Figure 5.24**) where P_p and S_h data overlap and have magnitudes of 70 - 80% S_V.

The 11 "*comparable depth*" data are shown in **Figure 5.26** to attempt to clarify the relationship between P_p and S_h. Only 3 "*comparable depth*" data are recorded from depths less than 3½ km. Fewer data mean the spread in S_h and P_p values seen in **Figure 5.24** is less evident. The S_h variation can be quantified as being 6 MPa at 3 km and 17 MPa over the 100

metres between 4.4 and 4.5 km. These data do not show a systematic increase in S_h relative to S_V with depth. P_p data show a variation of 53 - 87 MPa between 4.3 and 4.5 km depth.

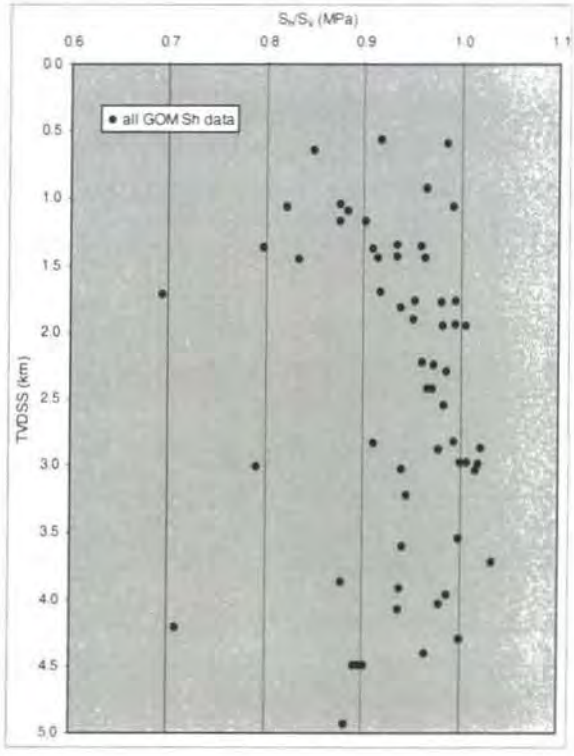

Figure 5.25: S_h normalised to S_V for the Gulf of Mexico.

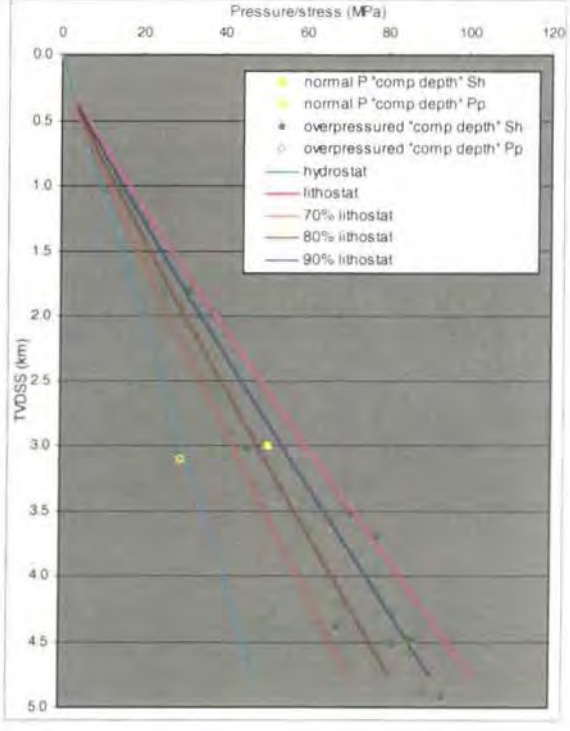

Figure 5.26: Normally pressured and overpressured "*comparable depth*" data.

Considering the data separated into normally pressured and overpressured groups shows there to be only one normally pressured data pair. No relationship can be drawn from one datum. Therefore the overpressured data are considered. These data show lower overpressures are associated with lower values of S_h while larger magnitudes of P_p are paired with greater S_h values. Examples come from 3 km and 3.6 km. At 3 km the P_p is 6 MPa overpressured and S_h is 46 MPa (75% S_V) where as at 3.6 km P_p is 30 MPa overpressured and S_h is 71.5 MPa (99% S_V). Such a relationship between P_p and S_h magnitude suggests overpressure may be exerting a control on S_h but from these data the relationship is non-quantifiable. P_p differences could therefore be interpreted as being a cause of S_h variability. Further investigations are described in **section 5.4.5**.

5.4.3.2 Understanding the patterns shown by stress-depth plots

Clearly shown in **Figure 5.24** is the large amount of variation in the magnitude of S_h at a given depth. In an attempt to interpret the variation, S_h data are plotted by lithology and wellbore diameter.

- **Lithology and S_h magnitude**

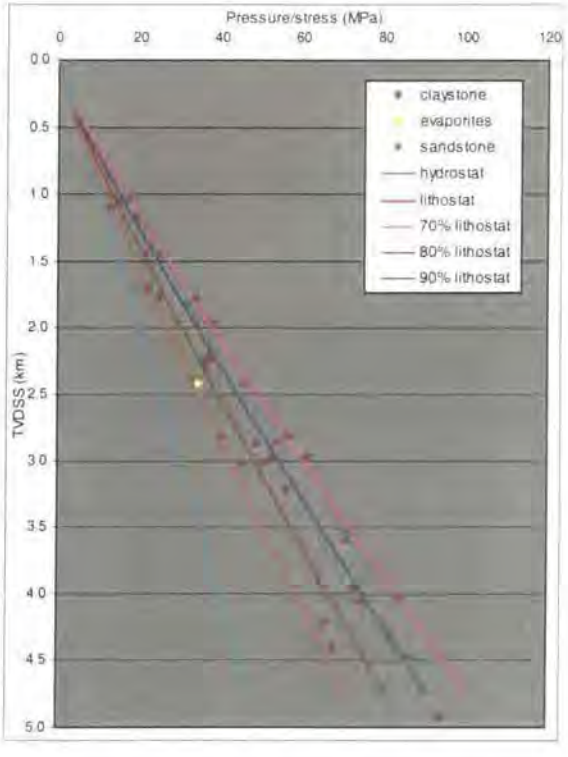

Figure 5.27: All S_h data plotted by the lithology that the test was conducted in.

Tests were performed in claystone (45 tests), sandstone (4 tests) and evaporites (1 test) in the Gulf of Mexico (**Figure 5.27**). The other 15 tests did not have a lithology recorded. Despite differing rheological properties, no one lithology records systematically higher S_h magnitudes than the others. 90% of the tests were conducted in claystone and the variability in S_h still occurs so differences in S_h cannot be attributed to lithological differences.

- **Wellbore diameter and S_h magnitude**

Those S_h measurements with a recorded wellbore diameter are plotted in **Figure 5.28**. Linear regression lines are fitted to the data series. The trends show a systematic increase in S_h magnitude relative to S_V for progressively smaller wellbores. The lowest S_h magnitudes recorded at a given depth are taken in the largest wellbore diameter (17½"). Larger S_h magnitudes are associated with smaller wellbores (8" and 6"). For example, at 1¾ km, the trends show S_h increases from the 17½" wellbore through the 13.375" to the 12¼" with maximum magnitudes associated with the 9.625" wellbore. Quantitatively, at 2 km, S_h increases from 23.7 MPa (17½") to 30.9 MPa (13.375") to 38.4 MPa (12¼"). From this evidence, some of the variability in S_h at a given depth can accounted for by wellbore diameter differences although they do not account for all variability.

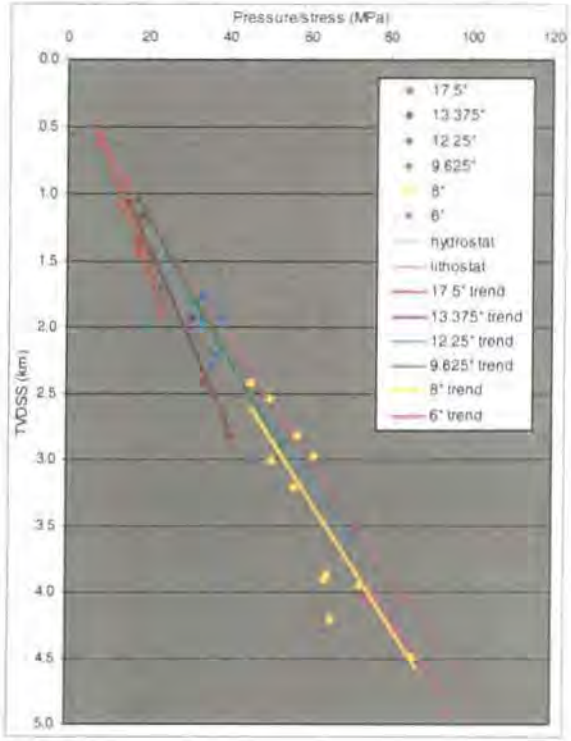

Figure 5.28: All S_h data plotted by the wellbore diameter that the test was conducted in.

5.4.3.3 Summarising what stress-depth plots reveal about S_h magnitude

There is a large amount of scatter in S_h magnitude in the Gulf of Mexico for all depths (**Figure 5.24**). Differences in P_p, especially at depths greater than 3 km, may explain some of the scatter. The "*comparable depth*" data show lower P_p pair with lower S_h magnitudes while high overpressures pair with higher S_h measurements. However, the relationship cannot be quantified.

The results of plotting the S_h data by lithology (**Figure 5.27**) do not explain the variability because 90% of tests are conducted in claystone. Plotting the S_h data by wellbore diameter (**Figure 5.28**) and fitting linear regression lines to the series suggests larger diameter wellbores are associated with lower S_h magnitudes. Where wellbores of different diameters overlap there is an increase in S_h with a decrease in wellbore diameter.

5.4.4 Using the data to estimate regional minimum *in-situ* stress

The regional S_h (the "*fracture gradient*") has been estimated using two approaches: the creation of a lower bound to LOPs and an upper limit to P_p data.

All 65 S_h measurements have been plotted on a stress-depth plot and a curve mathematically fitted so that the majority of the data fall either on or to the right of it. This created the lower bound to all LOPs (**Figure 5.29**). The same method was adopted to create a "*comparable depth*" lower bound (**Figure 5.30**). Independently plotting the P_p data and fitting a curve so that the majority of the data plotted either on or to the left of it produced an upper limit to P_p (**Figure 5.31**). The results are presented below:

The lower bound to LOPs for all Gulf of Mexico data (**Figure 5.29**) is curvi-linear in shape and follows the 70% S_V gradient down to 2½ km depth before "swinging" towards S_V. The magnitude increases from 70% S_V at 2½ km, to 80% S_V at 4 km and increases more rapidly to a maximum of 90% S_V at 4.9 km. The lower bound is a 2nd order polynomial:

$$y = -0.00025x^2 + 0.07356x + 0.1796 \qquad \textit{(equation 5.10)}$$

The creation of the "*comparable depth*" lower bound is hindered by the lack of data. The best attempt at fitting a curve to these data is shown by the green line in **Figure 5.30**. Despite this "*comparable depth*" lower bound being difficult to constrain it is described by:

$$y = -0.00055x^2 + 0.11503x - 1.01954 \qquad \textit{(equation 5.11)}$$

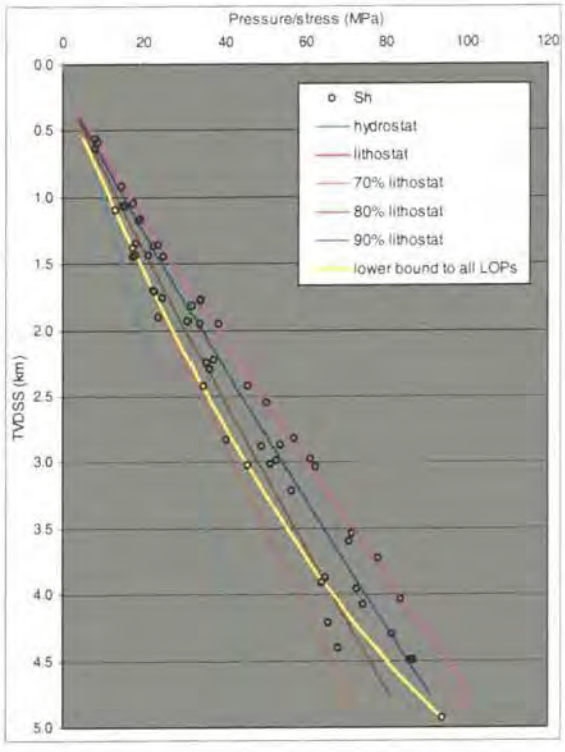

Figure 5.29: Lower bound to all LOPs from the Gulf of Mexico.

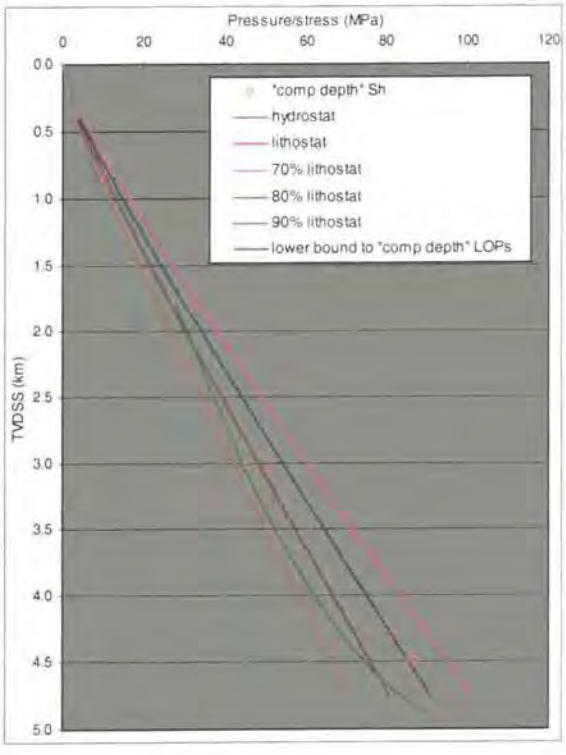

Figure 5.30: "*Comparable depth*" lower bound to LOPs for the Gulf of Mexico.

The "*comparable depth*" lower bound produces a lower bound to 90% of the data. Initial magnitudes are 85% S_V at 1¾ km before decreasing back to a minimum of 75% S_V between 2½ and 4 km. The curve subsequently increases in magnitude relative to S_V below 3½ km with the most rapid increase being from 80% S_V to 90% S_V in the 300 metres between 4.6 and 4.9 km. This rapid increase can be quantified as 33 MPa/km.

The upper limit to P_p (**Figure 5.31**) successfully estimates the maximum P_p in the Gulf of Mexico because 95% of the data fall on or to the left of the trend. The shallow occurrence of overpressures means the upper limit departs from the hydrostat at only 1 km depth. High P_p magnitudes account for the close proximity of the upper limit to S_V at all depths. At 3½ km the upper limit has a magnitude of 66 MPa; only 7 MPa below S_V at the same depth. The curve has the 3rd order polynomial:

$$y = (4.82E-06)x^3 - (6.96E-04)x^2 + 0.0748x + 0.215 \qquad \textit{(equation 5.12)}$$

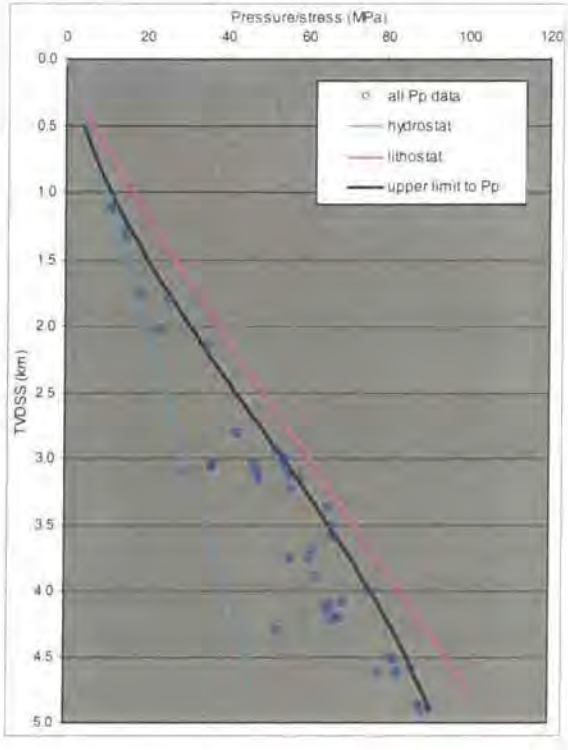

Figure 5.31: Upper limit to P_p for the Gulf of Mexico.

The two lower bounds show a significant difference in magnitude throughout the section and show how reducing the data set from 65 to 11 S_h measurements makes constraining the trend more difficult. While the lower bound to all LOPs can be determined from 500 metres depth, the scarcity in data in the upper 3 km means the "*comparable depth*" lower bound starts at 1¾ km. At initiation at 1¾ km, the "*comparable depth*" lower bound is 5

MPa in excess of the lower bound to all LOPs while this 5 MPa difference is reversed between 4 and 4½ km. The only depths of concurrence are where the two lower bounds cross at 2.8 km and where they converge at 4.9 km. To take into account the fewer data, the "*comparable depth*" lower bound has a greater curvature. This curvature is shown by the reduction in magnitude relative to S_V between initiation and 3½ km depth before it converges with the lower bound to all LOPs at 4.9 km.

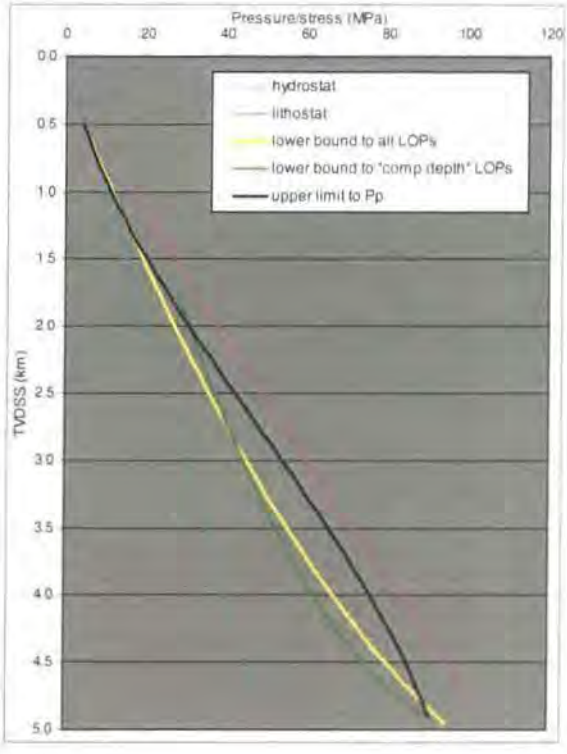

Figure 5.32: Comparative plot showing both lower bounds and the upper limit for the Gulf of Mexico.

Comparing both of the lower bounds and the upper limit (**Figure 5.32**) reveals a large difference between them – especially through the depth interval from 2½-4½ km. The mismatch is due to the overlap between S_h and P_p at these depths (see **Figure 5.24**). Quantitatively, the greatest mismatch occurs between the upper limit and the "*comparable depth*" lower bound at 3½ km where the difference is 13 MPa. The three curves having significantly different magnitudes at most depths has an important implication. It can be interpreted that using S_h data to constrain the maximum P_p and vice versa will lead to mis-estimates of up to 13 MPa.

5.4.5 Pore pressure *in-situ* stress coupling

This section describes the approaches used to examine the relationship between P_p and S_h. This took the form of an investigation into, and the quantification of, pore pressure *in-situ* stress coupling using the "*comparable depth*" data.

5.4.5.1 Looking for insights into coupling in the Gulf of Mexico

The "*comparable depth*" data are separated into the normally pressured datum and the 10 overpressured data in **Figure 5.33**. This figure cross-plots absolute magnitudes of P_p and S_h to show how they change relative to each other. The data were plotted wholesale normalised to a hypothetical unconstrained basin and depth and depth-normalised to determine the $\Delta S_h/\Delta P_p$ value. The data are plotted as normally pressured and overpressured groups by the same approaches (see explanation and reasoning in **section 4.5.1**) in **Figures 5.34** and **5.35**.

5.4.5.2 Results

The normally pressured (yellow) and overpressured (green) "*comparable depth*" data and the hypothetical unconstrained basin trend (see **section 5.2.5.2**) are shown in **Figure 5.33**. The single normally pressured datum plots 2 MPa above the "*unconstrained trend*". Overpressured data plot along a trend with a more shallow (0.9 versus 1.58) gradient than the "*unconstrained trend*". The result shows the rate of increase in P_p relative to S_h over a specific depth increment is greater than for the hypothetical unconstrained basin. Therefore the pressure-stress situation in the Gulf of Mexico does not follow that of an unconstrained basin. The pressure-stress situation is quantified below.

Fitting linear regression lines to all the "*comparable depth*" data normalised firstly to a hypothetical unconstrained basin and depth and then depth-normalised reveals the rate of increase in S_h with an increase in P_p ($\Delta S_h/\Delta P_p$) for all data. The data are separated into the normally pressured point and overpressured points in **Figures 5.34** and **5.35**. Regression lines are fitted to the overpressured data. All relationships are summarised below.

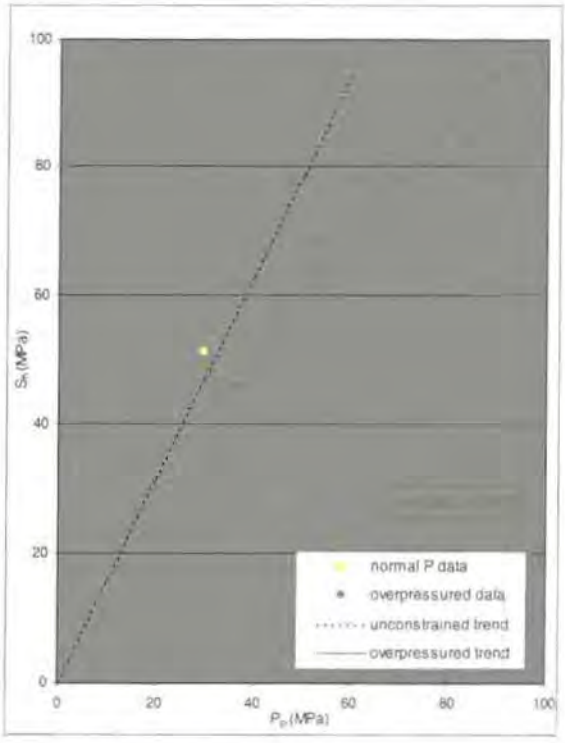

Figure 5.33: Absolute magnitudes of S_h versus P_p for the "*comparable depth*" data from the Gulf of Mexico.

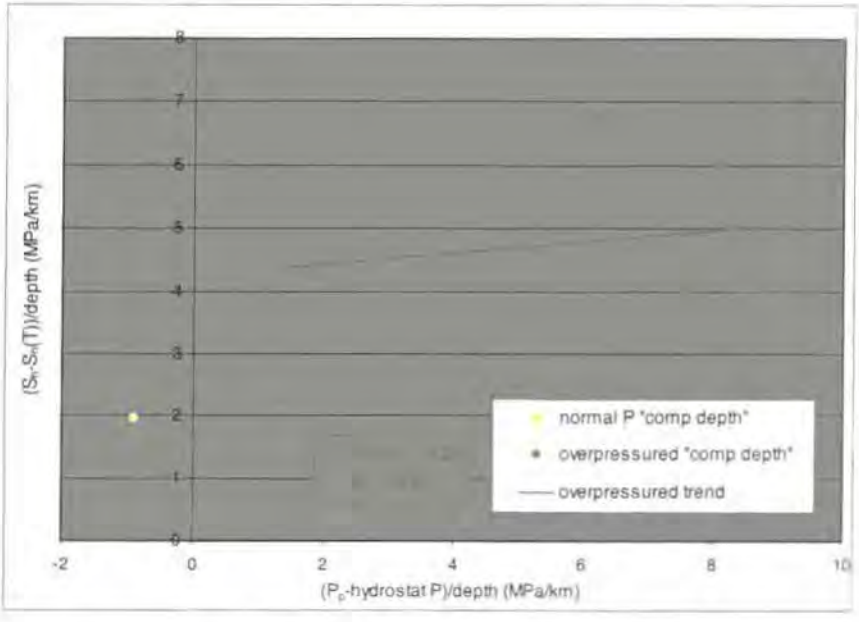

Figure 5.34: Normally and overpressured "*comparable depth*" data normalised to a hypothetical unconstrained basin and depth for the Gulf of Mexico.

Data statistics refer to	Data plotted as gradients (e.g. *[S_h-gradient]*)		Data normalised to an "unconstrained basin" & depth (e.g. *[(S_h-S_h(T))/depth]*)	
	$\Delta S_h/\Delta P_p$	r^2	$\Delta S_h/\Delta P_p$	r^2
All data	0.48	0.67	0.22	0.31
Overpressured	0.64	0.77	0.09	0.06

Table 5.6: Summary table showing the nature of pore pressure *in-situ* stress coupling ($\Delta S_h/\Delta P_p$) and correlation coefficients (r^2) for the Gulf of Mexico.

Table 5.6 shows varying results for the coupling analyses. Considering the "*comparable depth*" data plotted wholesale, linear regression lines show $\Delta S_h/\Delta P_p$ values of 0.22 (r^2 value = 0.31) and 0.48 (r^2 value = 0.67). The r^2 of 0.31 shows the first relationship to be weak but the second relationship (r^2 = 0.67) is strong. Looking at solely the overpressured data in **Figure 5.34** shows the relationship between overpressure and "excessive" S_h ($\Delta S_h/\Delta P_p$) is only 0.09. The r^2 value is only 0.06 indicating the relationship to be very poor (however a horizontal regression line will have a r^2 of zero regardless of how close to the line the data plot). Plotting the overpressured data as gradients (**Figure 5.35**) changes results. Here the $\Delta S_h/\Delta P_p$ is 0.64 with a r^2 value of 0.77 indicating a strong relationship.

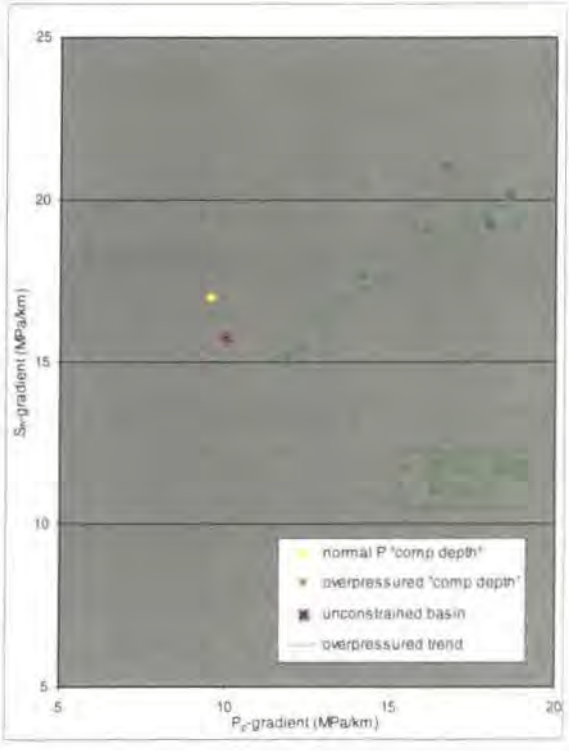

Figure 5.35: Normally and overpressured "*comparable depth*" data depth-normalised.

Plotting the "*comparable depth*" data as gradients as opposed to normalising to an unconstrained basin and depth increases the statistics. An explanation could be that the hypothetical unconstrained basin model is not applicable for the Gulf of Mexico. Depth-normalising the data does not rely on any assumptions so the approach is considered a more reliable means of testing for coupling.

To conclude, by depth-normalising the data, coupling can be inferred for the Gulf of Mexico. Considering the overpressured data shows that S_h increases at a rate of 64% of the P_p increase. Coupling can therefore explain some of the S_h variability seen on stress-depth plots (i.e. **Figure 5.24**) especially that seen for the "*comparable depth*" data.

5.4.6 Summarising the results for the Gulf of Mexico

The Gulf of Mexico data (compiled from *PressureView*,) have been plotted on stress-depth plots, normalised to a hypothetical unconstrained basin and/or depth-normalised. This was done to investigate the variation in the magnitude of S_h at a specific depth and look for insights into P_p-S_h coupling. A summary of the results is given below:

- Scatter in S_h magnitude on a stress-depth plot is large at all depths with a maximum of 17 MPa at 2¾ km. Smaller amounts of scatter occur where there are fewer data.
- There is not a systematic increase in the S_h:S_V ratio with depth.
- P_p data show greater scatter than the S_h data.
- Small (<5 MPa) overpressures occur to 1¾ km depth while larger (>20 MPa) overpressures are only seen below 3 km.
- P_p reach a maximum relative to S_V of 95% at 4 km depth.
- The overpressured "*comparable depth*" data show lower overpressures to be associated with lower values of S_h and larger overpressures are paired with greater S_h values.
- Plotting the S_h data by different parameters and fitting linear regression lines through the data show the strongest controls on S_h variability to be overpressure differences and wellbore diameter variations.
- The two lower bounds to LOPs show differences in their magnitudes (up to 5 MPa) at all depths and reveal that reducing the data set from 65 to only 11 makes constraining the lower bound more difficult.
- While successfully reflecting the maximum P_p seen, the upper limit to P_p shows up to a 13 MPa mismatch with the lower bounds at depths of greater than 2½ km. Using S_h data to constrain the maximum P_p (and vice versa) will lead to mis-estimates.

- Mismatches occur due to the "overlap" in S_h and P_p between 2½ and 4½ km depth.
- Investigating P_p-S_h coupling shows poor results when normalising to a hypothetical unconstrained basin and depth for all ($r^2 = 0.31$) and overpressured data ($r^2 = 0.06$).
- Plotting the data as "gradients" shows coupling can be inferred for the Gulf of Mexico.
- Overpressured data reveal S_h increases at 64% the increase in P_p.
- Coupling can therefore explain some of the S_h variability seen on stress-depth plots, especially that seen for the "*comparable depth*" data.

5.5 Onshore Nigeria

5.5.1 Introduction to Onshore Nigeria

This introduction gives the geographical location of Onshore Nigeria and summarises the contemporary stress situation. The burial history is reviewed followed by the overpressure in terms of occurrence and the likely causes of its generation.

- **Location**

The data used in this study come from the Onshore Nigeria (Niger Delta) region. The Niger Delta is situated in the coastal sedimentary basin of southern Nigeria and covers an area of >36000 km^2 (Abum & Omuso, 2000). Nigeria itself is a coastal country in western Africa in the region of the South Atlantic known as the Gulf of Guinea and sits between the countries of Benin to the west and Cameroon to the southeast.

- **The contemporary stress situation**

The Niger Delta is a classic passive margin setting and hence the tectonic regime is vertical stress dominated (Grauls, 1994). Geological and oceanographic surveys have shown that the upper section of the Niger Delta continental margin is an extensional zone characterised by growth faults beneath the continental shelf and upper slope. These growth faults are syn-sedimentary structures. Limited data from the *World Stress Map Project* (Mueller *et al.*, 2000) shows that the S_H direction is NW-SE implying that S_h is normal to the delta margin. More major, deeper-seated faults trend NE-SW and have strongly influenced sedimentation throughout the Tertiary (Onuoha, 1999).

- **Burial history**

Differential movement of faults controlled sedimentation rates across the region throughout the Tertiary due to the massive downwarping that occurred at sporadic rates. The primary influencing faults were those with a NE-SW orientation (Onuoha, 1999). The Niger Delta consists of a coarsening-upwards sequence of clastics which prograded over the passive continental margin (Coward *et al.*, 1999).

Sedimentation rates were generally low (an average of 36 m/Ma) in the Palaeocene for the entire margin. During the Eocene, due to the presence of the faults and fractures, sedimentation rates varied between <10 m/Ma to >300 m/Ma. During this period over 3 km of delta front and lower delta plain sands and interbedded shales were deposited. Sedimentation rates were also low in the Oligocene averaging about 27 m/Ma across the whole margin. Miocene sedimentation was once again extreme with rates up to 500 m/Ma although local variations occurred. The Oligocene to Recent Benin Formation consists of up to 2 km of poorly lithified sandstones and with minor mud rock interbeds deposited on a continental delta

plain (Jubril *et al.*, 1996). The greatest sedimentation rates are to be found in the central part of the delta (Onuoha, 1999).

Overpressure

The fluid pressure system can be broken down into three parts. Down to a depth of 1600 metres, through the predominantly sandstone interval is a hydrostatic system with circulating meteoric waters. Below 1600 metres is a "middle depth system" where P_p are hydrostatic or show small amounts of overpressure. The deepest section (below 3½ km) shows higher levels overpressures and high hydraulic heads (Onuoha & Ekine, 1999). In this deeper section are the more consistent shale horizons that produce seals for the hydrocarbon reservoirs (Jubril *et al.*, 1996; Onuoha, 1999).

Overpressures have been attributed mostly to disequilibrium compaction in the deeper sections, especially where greater sedimentation rates occurred. At the greater depths there is believed to have been a contribution from gas exsolution from oils (Kuo, 1997).

5.5.2 Compiling the data

TotalFinaElf also provided the Onshore Nigeria data set. Both P_p and S_h data were converted from grammes per cubic centimetre into Mega Pascals using *equation 5.5.* The result was a data set of 51 S_h and P_p measurements. These data are "*comparable depth*" data because S_h and P_p measurements were recorded at the same depth.

The lithostat reference line was also created using Traugott's (1997) method for calculating S_V based on assumed average densities for a sand-shale lithological succession. See **section 5.3.2** and *equations 5.6* and *5.7* for the methodology.

5.5.3 Stress-depth plots

Having converted the units of the data from g/cc to MPa and determined the lithostat for Onshore Nigeria the data have been plotted on stress-depth plots and S_h has been normalised to S_V and plotted versus depth. The objectives that apply to this section are listed in **section 5.2.3** and the results are given below.

5.5.3.1 Relationships shown by stress-depth plots

The Onshore Nigeria P_p and S_h measurements are plotted on a stress-depth plot in **Figure 5.36** together with the hydrostat (10 MPa/km), lithostat, 70% S_V, 80% S_V and 90% S_V gradients.

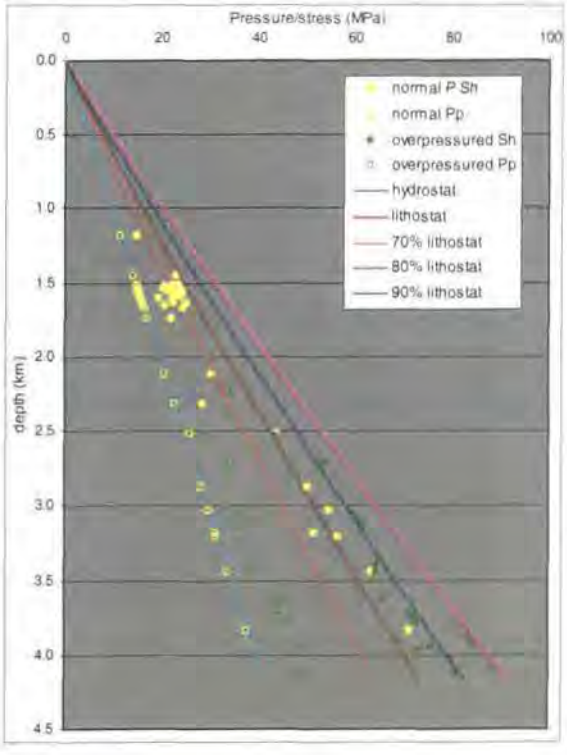

Figure 5.36: All S_h and P_p data separated into normally and overpressured groups for Onshore Nigeria.

Considering the S_h data shows a scatter in the magnitude at all depths (**Figure 5.36**). This scatter is quantified at 250 metre intervals in **Table 5.7** following the methodology described in **section 4.2**. Evident in **Figure 5.36** is the "clump" of S_h data occurring between 1½ km and 1¾ km. These data range between 19 and 25 MPa. At depths greater than 2½ km, despite S_h magnitudes increasing relative to S_V, scatter still occurs (the maximum amount of 12 MPa is at 4 km). Assessing the magnitude of S_h relative to S_V shows all bar 4 of the S_h data from below 2½ km to be 80 - 95% S_V in magnitude. Three of the deepest data (~4 km) are >80 MPa in magnitude which equates to 98% S_V.

Further quantification of the S_h:S_V ratio is given by **Figure 5.37**. The "clump" of data at 1½ km is clear where the ratios vary from 0.58 - 0.77. With an increase in depth, there is an increase in the S_h:S_V ratio. The ratio increases from an average of 0.68 at 1.6 km through to an average ratio of 0.92 at 4 km.

Depth (kilometres)	Variability in S_h (MPa)
1.25	1
1.5	4.5
1.75	5.5
2.0	-
2.25	6
2.5	2
2.75	4
3.0	5.5
3.25	9.5
3.5	3
3.75	4
4.0	12

Table 5.7: Variability in the magnitude of S_h at 250 metre intervals.

All P_p measurements bar one (**Figure 5.36**) in the upper 2½ km are hydrostatic. Overpressures are first seen at 2½ km and from 2½ to 4¼ km they are hydrostat sub-parallel and do not exceed 10 MPa. The average overpressure is 7 MPa in magnitude. At 4 km the highest P_p measurements show 31 MPa of overpressure (a pressure equivalent to 80% S_V).

Figure 5.36 shows the development of overpressure to be coincident with higher S_h magnitudes. Prior to the depth of overpressure development S_h is less than 80% S_V. The three greatest S_h magnitudes are paired with the greatest magnitudes of overpressure. These S_h measurements at 4 km are 84, 85 and 89 MPa and their comparable P_p measurements are 69, 70 and 73 MPa respectively.

Considering the normally pressured (yellow) data (**Figure 5.36**), P_p are paired with S_h measurements that are lower than those associated with overpressures at the same depth. A good illustration of this relationship is shown in the data below 3 km depth. Normally pressured S_h measurements range from 75% to 85% lithostatic below 3 km where as those S_h measurements associated with overpressured fluids are between 80 and 98% lithostatic. Therefore a "loose" relationship between P_p and S_h can be stated from these data. Where P_p are hydrostatic, S_h magnitudes are less than 85% S_V. Further approaches can quantify this relationship and these are given in **section 5.5.5**.

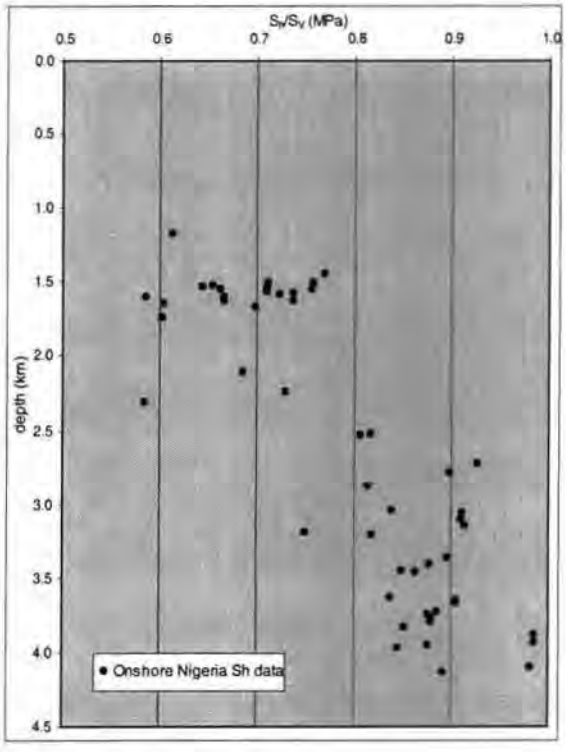

Figure 5.37: S_h normalised to S_v for Onshore Nigeria.

5.5.3.2 Understanding the patterns shown by stress-depth plots

The only parameter from Onshore Nigeria available to plot the S_h data by is the wellbore diameter. The results are shown in **Figure 5.38** and described below.

- **Wellbore diameter and S_h magnitude**

The S_h data (**Figure 5.38**) show wellbore diameter to correlate with the magnitude of S_h in the instances where overlap between different diameters occurs. At 2¼ km depth there is an overlap between the 12¼" and the 8½" wellbore, and the smaller wellbore supports the higher S_h measurement by 6 MPa. Three out of four stress measurements from 4 km depth recorded in 6" wellbores are 8 MPa greater than S_h measurements recorded in 8½" wellbores at the same depth.

Despite these links the scatter still occurs (between 1½ and 1¾ km the 6 MPa scatter in S_h occurs solely in the 12¼" wellbore). To conclude: analysing the S_h data by wellbore diameter partially explains S_h variation at certain depths (e.g. 2¼ and 4 km) but does not account for all the scatter.

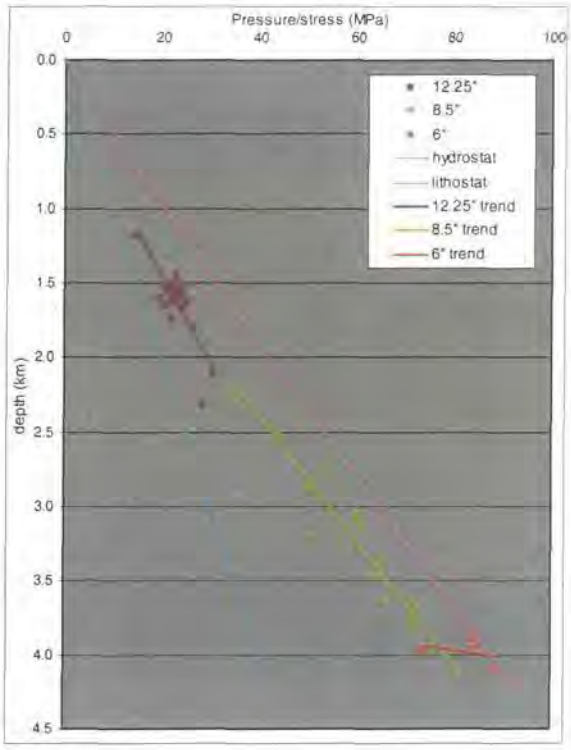

Figure 5.38: S_h plotted by the wellbore diameter that the test was conducted in.

5.5.3.3 Summarising what stress-depth plots reveal about S_h magnitude

The above sections show that there are two possibilities that explain the scatter in S_h magnitude. The link between overpressure and S_h is revealed by **Figure 5.36**. A "broad-based" conclusion is that lower P_p pair with lower S_h and overpressures are paired with higher S_h. P_p variations can therefore account for the scatter in the S_h data especially below 2½ km depth. Plotting the data by wellbore diameter (**Figure 5.38**) shows that smaller diameters support greater minimum stress measurements than are supported by larger diameters. However this relationship does not account for the scatter at all depths.

5.5.4 Using the data to estimate regional minimum *in-situ* stress

Two approaches have again been used to estimate the regional S_h. The first approach uses all Onshore Nigeria S_h data to create a lower bound to LOPs (**Figure 5.39**). The lower bound was created so that the majority of the data plotted to the right of the trend. The second approach independently uses the P_p data to constrain an upper limit to P_p (**Figure 5.40**). These trends are compared and contrasted below.

The result of creating a lower bound to LOPs for Onshore Nigeria (yellow curve) is shown in **Figure 5.39**. The curve produces a lower bound to 95% of the S_h measurements. The lower bound has a low magnitude relative to S_V of 60 - 65% throughout the upper 2½ km. It is not until 2.7 km that the magnitude reaches 70% S_V. Between 2.7 km and the deepest S_h measurements at 4.2 km the lower bound magnitude increases relative to S_V at a greater rate. The curve crosses the 80% S_V gradient at 3¾ km and has a maximum of 90% S_V at 4.2 km. The lower bound is described by the following quadratic:

$$y = -0.00035x^2 + 0.07699x + 0.1591 \qquad \textit{(equation 5.13)}$$

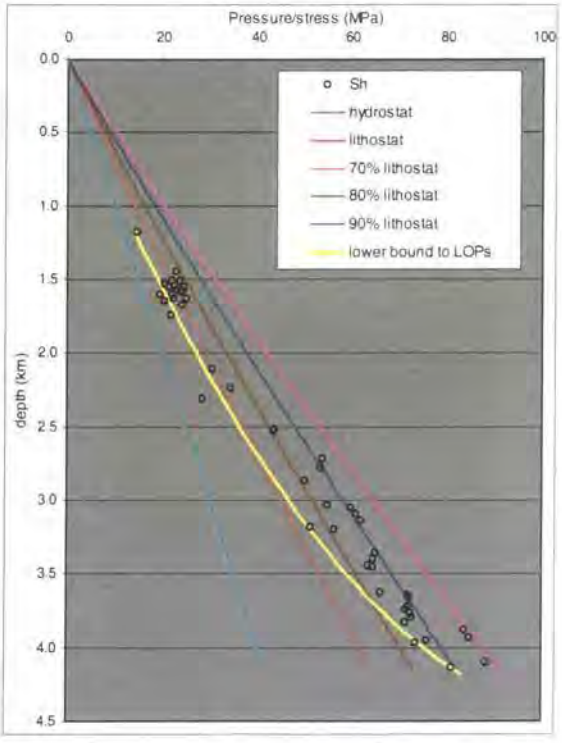

Figure 5.39: Lower bound to LOPs for Onshore Nigeria.

As **Figure 5.40** shows, the upper limit to pore pressures (black) produces a good estimate of the maximum P_p encountered in Onshore Nigeria. All of the data fall on the trend or plot to the left of it. The three measurements at 4 km strongly influence the shape of the trend and to take these data into account two inflexion points are used. The upper limit to P_p is described by the following cubic:

$$y = (1.349E-05)x^3 - (2.074E-03)x^2 + 0.138x - 0.1591 \qquad \textit{(equation 5.14)}$$

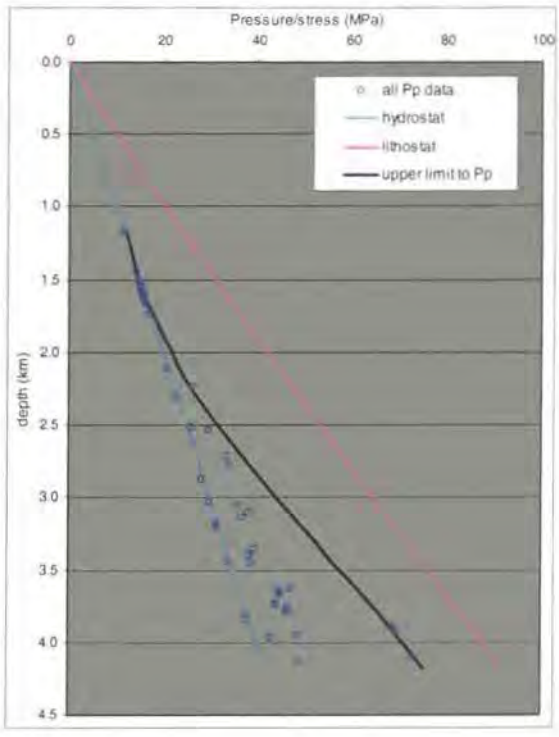

Figure 5.40: Upper limit to P_p for Onshore Nigeria.

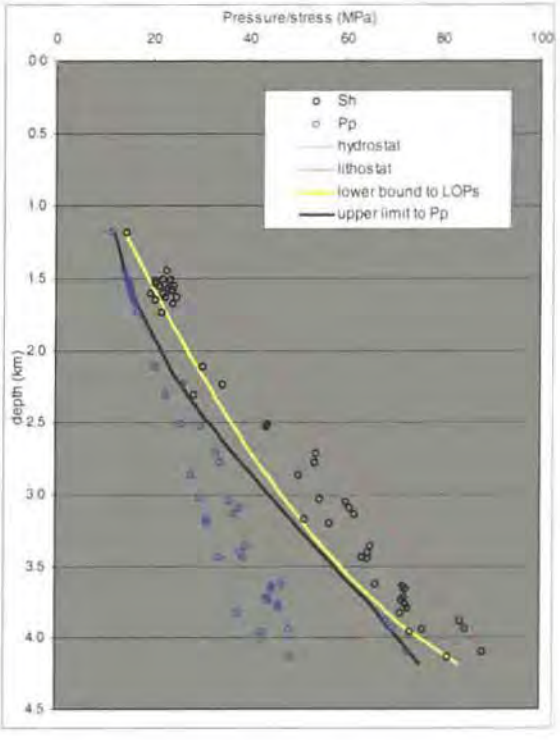

Figure 5.41: Comparative plot showing the lower bound and upper limit.

Comparing both the lower bound and the upper limit trends (**Figure 5.41**) shows a large mismatch at depths of less than 3 km. At less than 2¼ km the mismatch can be

attributed to all P_p being hydrostatic. The lower bound has a magnitude up to 6 MPa in excess of the upper limit to P_p at 2 km depth. Between 3¼ and 3¾ km the greatest concurrence between the curves occurs. The upper limit remains within 2 MPa of the lower bound throughout this interval but does not exceed it. At depths greater than 4 km the lower bound departs from the upper limit again.

Results show that the lower bound can produce a good estimate of the regional S_h and the upper limit can provide a good estimate of the maximum P_p. However, using the lower bound to LOPs to predict P_p and the upper limit to P_p to predict S_h (especially in the normally pressured zone) will lead to mis-estimates of up to 6 MPa. The lack of large overpressures in Onshore Nigeria (especially at deeper depths) is felt to contribute to the mismatch in the trends. Including the three P_p measurements at 4 km in the creation of the upper limit compensates for larger mismatches between the upper limit and lower bound that would otherwise occur at >2½ km depth.

5.5.5 Pore pressure *in-situ* stress coupling

This section describes the approaches used to examine the relationship between P_p and S_h in Onshore Nigeria. Quantification of the changes in S_h with changes in P_p is given through investigations into the presence of pore pressure *in-situ* stress coupling.

5.5.5.1 Looking for insights into coupling in Onshore Nigeria

Figure 5.42 shows the P_p:hydrostat and the S_h:S_V ratios plotted versus depth to examine if changes in each ratio are comparable at the same location. The hydrostat and S_V were chosen as normalisation parameters because of the accuracy of their calculation.

The 51 Onshore Nigeria data are separated into 28 normally and 23 overpressured pairs and cross-plotted with absolute magnitudes of P_p on the x-axis and absolute S_h magnitudes on the y-axis (**Figure 5.43**). This approach shows how both change relative to each other. All the Onshore Nigeria data are normalised to a hypothetical unconstrained basin and depth and depth-normalised to assess the $\Delta S_h/\Delta P_p$ value. **Figures 5.44** and **5.45** show the data separated into the normally pressured and overpressured pairs and plotted by these approaches.

5.5.5.2 Results

There is not an clear link between the S_h:S_V ratio and P_p:hydrostat ratio for the data from Onshore Nigeria (**Figure 5.42**). Above 2 km depth all P_p are hydrostatic yet the S_h:S_V ratio varies between 0.6 and 0.8. Below 2½ km depth, S_h:S_V ratios are between 0.8 and 0.9 and P_p:hydrostat ratios are 1 to 1.75. The greatest S_h:S_V ratios of 0.98 pair with P_p:hydrostat ratios of 1.75. Aside from the three cases at 4 km where there is strong positive link between high overpressure and high S_h, no conclusive relationship between P_p and S_h can be inferred from **Figure 5.42**.

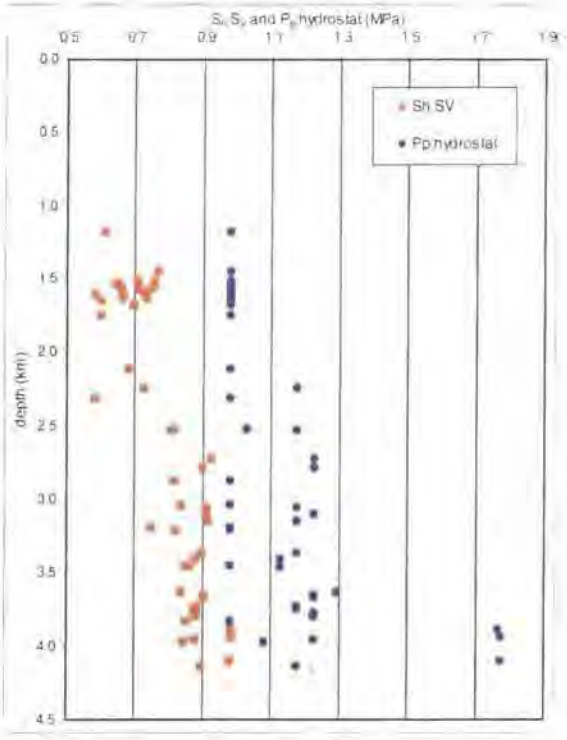

Figure 5.42: S_h:S_V and P_p:hydrostat versus depth for Onshore Nigeria.

S_h and P_p separated into normally pressured (yellow) and overpressured (green) pairs are cross-plotted in **Figure 5.43**. The dashed line represents a hypothetical unconstrained basin (cf. **section 5.2.5.2**). Normally pressured data plot along a trend with a steeper (2.11 versus 1.58) gradient than the "*unconstrained trend*". This steeper gradient shows S_h increases independently of changes in P_p and at a greater rate than would occur solely due to an increase in depth. Overpressured data show a less clear relationship. Those plotting to the left of the "*unconstrained trend*" show S_h to have increased at a greater rate than P_p (relative to the unconstrained situation) with depth. Those plotting to the right show P_p data have increased at a greater rate than S_h (relative to the unconstrained situation) with depth.

Figure 5.43 reveals whether the P_p and S_h relationship deviates from the hypothetical unconstrained basin but does not quantify a relationship. Normalising the data to a hypothetical unconstrained basin and depth and depth-normalising the data quantifies any increase in S_h with overpressure. Linear regression lines fitted through the data show the change in S_h with overpressure ($\Delta S_h/\Delta P_p$). Normally-pressured and overpressured groups are shown in both **Figures 5.44** and **5.45** and regression lines fitted to the overpressured data. Positive gradients to the regression lines show S_h increases at a greater rate than 70% S_v when overpressure occurs. The results are summarised in **Table 5.8**.

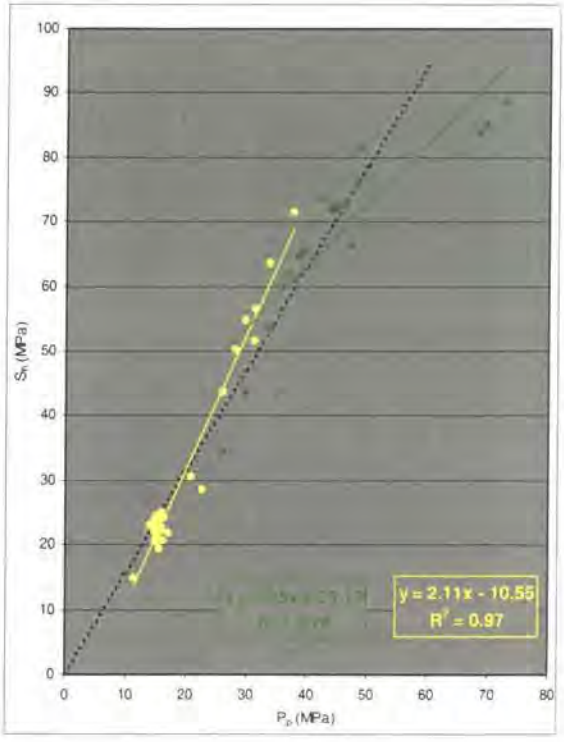

Figure 5.43: Absolute magnitudes of S_h versus P_p for Onshore Nigeria.

Data statistics refer to	**Data plotted as gradients (e.g. *[S_h-gradient]*)**		**Data normalised to an "unconstrained basin" & depth (e.g. *[(S_h-S_h(T))/depth]*)**	
	$\Delta S_h/\Delta P_p$	**r^2**	**$\Delta S_h/\Delta P_p$**	**r^2**
All data	1.01	0.54	0.90	0.54
Overpressured	0.44	0.47	0.41	0.48

Table 5.8: Summary table showing the nature of pore pressure *in-situ* stress coupling ($\Delta S_h/\Delta P_p$) and correlation coefficients (r^2) for Onshore Nigeria.

Figures 5.44 and **5.45** show normal P_p data have a large variation in S_h magnitude associated with them. S_h gradients in **Figure 5.45** vary between 12 and 18.5 MPa/km for normal P_p. The P_p gradients in **Figure 5.45** show large overpressures are not common in Onshore Nigeria. Gradients range between 9.8 and 13 MPa/km with the exception of three measurements with gradients of 17.8 MPa/km. Also shown by the overpressured data is that some P_p measurements (e.g. gradients of 11.8 MPa/km) have S_h measurements similar to the unconstrained basin magnitude associated with them.

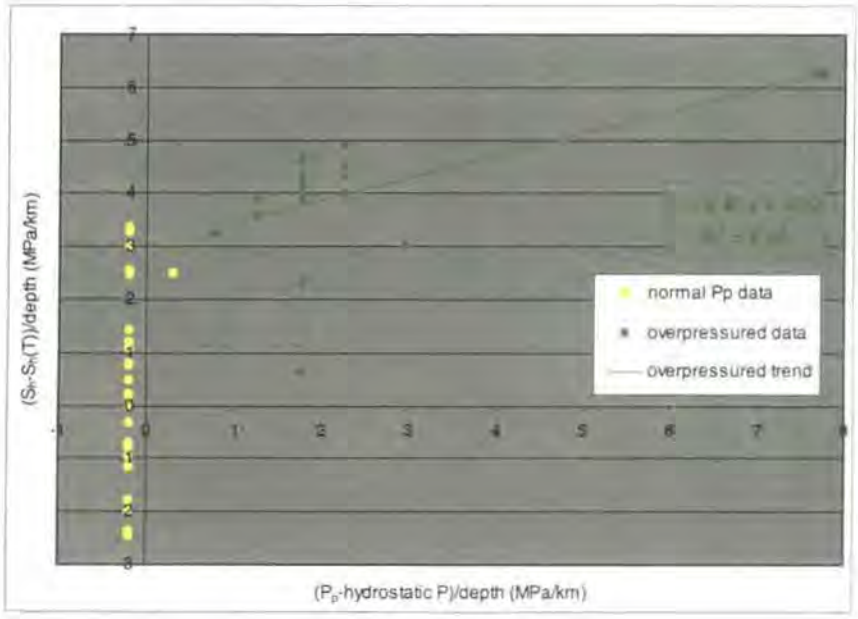

Figure 5.44: Normally and overpressured data normalised to a hypothetical unconstrained basin and depth.

Pore pressure *in-situ* stress coupling is not clear in Onshore Nigeria. The $\Delta S_h/\Delta P_p$ values for the overpressured data are ~0.4. Correlation coefficients (r^2 values) of 0.44-0.48 show relationships to be weak. These relationships are improved by the presence of the 17.8 MPa/km P_p gradients. Without these data the r^2 value would be lower. From the results shown in **Figures 5.44** and **5.45**, P_p-S_h coupling it not inferred for Onshore Nigeria. The variation in S_h showed by **Figure 5.36** cannot be attributed to coupling. For example, for a specific P_p gradient (11.8 MPa/km) the S_h gradient varies from 15.4 to 19.7 MPa/km. Coupling theory predicts that for this range of S_h gradients a range of P_p gradients should also be seen.

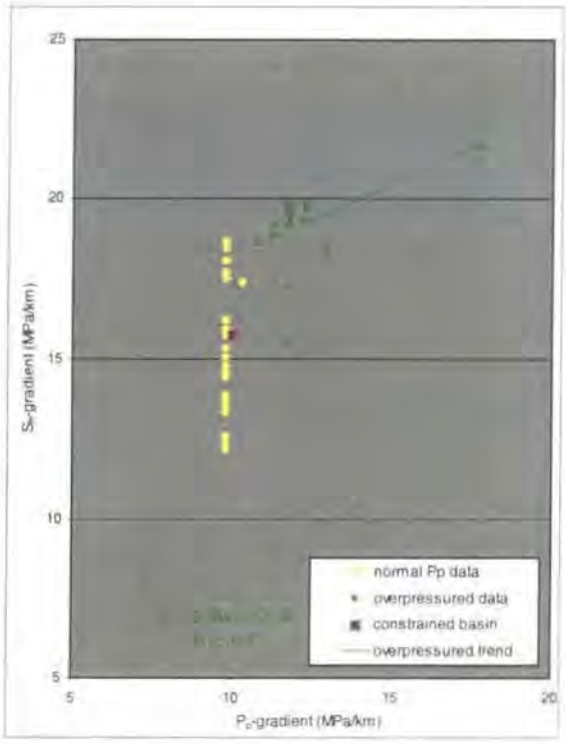

Figure 5.45: Normally and overpressured data depth-normalised for Onshore Nigeria.

5.5.6 Summarising the results for Onshore Nigeria

The Onshore Nigeria study plots S_h and P_p data on stress-depth plots. Analyses also involved normalising the data to an unconstrained basin and/or to depth. The aims were to examine and quantify the magnitude and scatter in S_h and assess the contribution other parameters had on S_h. Insights into P_p-S_h coupling were also sought. Results are summarised below:

- S_h data show a scatter of up to 12 MPa in magnitudes throughout the section.
- With an increase in depth there is an increase in the S_h:S_V ratio.
- A cluster of data between 1½ and 1¾ km (ranging from 58 to 77% S_V) occurs despite P_p being hydrostatic.
- Overpressures in Onshore Nigeria are low (with the exception of 3 measurements).
- Where overpressuring occurs most S_h magnitudes exceed 80% S_V.
- Where different wellbore diameters overlap, smaller wellbores support greater S_h magnitudes. However, wellbore diameter variations do not account for most of the scatter (i.e. at 1½ to 1¾ km) seen with depth.

- The lower bound to LOPs has a strongly curvi-linear shape and increases in magnitude from 60% S_V at 1½ km to a maximum magnitude of 90% S_V at 4.2 km.
- The lower bound to LOPs produces a good estimate of the regional S_h and the upper limit to P_p provides a good estimate of the maximum P_p.
- Lower bounds cannot be used to accurately estimate the maximum P_p and upper limits do not accurately constrain S_h. The lack of large overpressures is felt to contribute to the mismatch between the trends of up to 6 MPa.
- P_p-S_h coupling cannot be inferred for Onshore Nigeria. The overpressured $\Delta S_h/\Delta P_p$ value is only 0.4 and a r^2 value of ~0.45 shows the relationship to be weak. The lack of large overpressures in the region hinders the search for coupling.
- S_h gradients significantly vary for a constant P_p gradient and vice versa.

5.6 Offshore West Africa

5.6.1 Introduction to Offshore West Africa

This introduction provides background information on Offshore West Africa. The location of the region is given and the contemporary stress situation reviewed followed by a summary of the overpressure in terms of spatial location and the likely causes of generation.

- **Location**

The data come from the Gulf of Guinea region of Offshore Western Africa. The region is a Tertiary Basin setting and covers part of the South Atlantic Ocean seaboard of Africa that stretches for over 1200 km between The Democratic Republic of The Congo to the north and Namibia to the south.

- **The contemporary stress situation**

The eastern (continental) edge of the Offshore West Africa region is a gravity-driven passive margin tectonic regime (Grauls, 1997) and is considered to be a pull-apart basin associated with Early Cretaceous rifting (Burwood, 1999). A lack of constraint to the west means that the evolution of S_h occurs primarily as a function of the increase in depth (Grauls, 1994). The stress situation is confirmed by overcoring data from the *World Stress Map Project* (Mueller *et al.*, 2000) that show a N-S trend of S_H suggesting extension in an E-W direction, or normal to the coast. Seismic evidence shows a succession of half graben stepping to the west and a thrust duplex of seaward-displaced salt. This is quoted as further evidence for seaward extension (Cramez & Jackson, 2000).

- **Overpressure**

The overpressure present in the Gulf of Guinea is believed to have resulted from the thermal expansion of kerogen or the secondary cracking of oil to gas at higher temperatures (Grauls, 1998). Vitrinite reflectance ranging from 0.7 to 0.8% indicate that the source rocks are at peak generating levels at the present day. Hence, oil generation from the source rock is considered to be the cause of the high pressures (overpressures of 15 MPa) that occur at depths from 2500 metres. Porosity measurements, inferred from the sonic log, show the shales through the source rock interval are normally pressured which is believed to indicate a lack of disequilibrium compaction. In the Oligocene interval between 1200 metres and 2½ km lower overpressures are seen (Grauls, 1998). Below the oil-generating anomaly at 2½ km a range of P_p exist from near hydrostatic to high levels of overpressure.

5.6.2 Compiling the data

The data set for Offshore West Africa is the largest provided by *TotalFinaElf* and comprises of 68 P_p and S_h values. These were converted from g/cc into MPa using *equation 5.5.* As each S_h data point had a P_p measurement recorded at the same depth, these are "*comparable depth*" data (see explanation in **section 3.7.4**). The lack of a density log meant that the lithostat was again created using Traugott's (1997) method for calculating S_V for a sand-shale succession (see **section 5.3.2**).

5.6.3 Stress-depth plots

Following the creation of S_V and having converted the units of the data, the Offshore West Africa data have been plotted on stress-depth plots. S_h has also been normalised to S_V and plotted versus depth. The objectives are listed in **section 5.2.3** and the results given below.

5.6.3.1 Relationships shown by stress-depth plots

The 68 S_h and P_p data from Offshore West Africa are shown on a stress-depth plot (**Figure 5.46**) together with the hydrostat (10MPa/km), lithostat, 70% S_V, 80% S_V and 90% S_V gradients.

Immediately obvious is the large amount of variability in S_h at a specific depth. This variability has been quantified by 250 metre depth intervals in **Table 5.9** (cf. procedure explained in **section 4.2**). S_h measurements from depths of <1 km show a variation in magnitude of 4 MPa. Variation of up to 7½ MPa (at 2 km) is seen in data from between 1½ and 2¼ km. Data from 2½ km to the deepest measurement (3½ km) show a variation of up to 11 MPa (at 3 km).

Data from ½ km depth have magnitudes of 5 to 8½ MPa which correspond to 60 to 85% S_V. The data in **Figure 5.46** show that S_h increases at a greater rate than the lithostat with depth. While some S_h magnitudes are low at <1 km, high (relative to S_V) magnitudes exist at >3 km depth. Normalising S_h to S_V (**Figure 5.47**) quantifies the magnitude of S_h relative to the lithostat. An increase in S_h relative to S_V is shown by the average S_h:S_V ratio increasing from 0.7 at ½ km, to 0.85 at 1¾ km to 0.92 at 3 km depth.

Depth (kilometres)	Variability in S_h (MPa)
0.5	3.5
0.75	4
1.0	-
1.25	-
1.5	7
1.75	6.5
2.0	7.5
2.25	2
2.5	2
2.75	11
3	11
3.25	2
3.5	3

Table 5.9: Variability in the magnitude of S_h at 250 metre intervals.

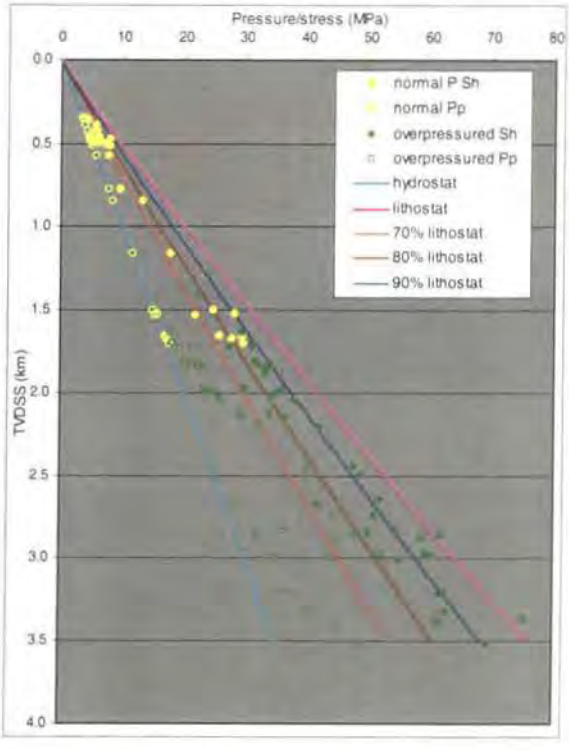

Figure 5.46: Normally and overpressured S_h and P_p data versus depth.

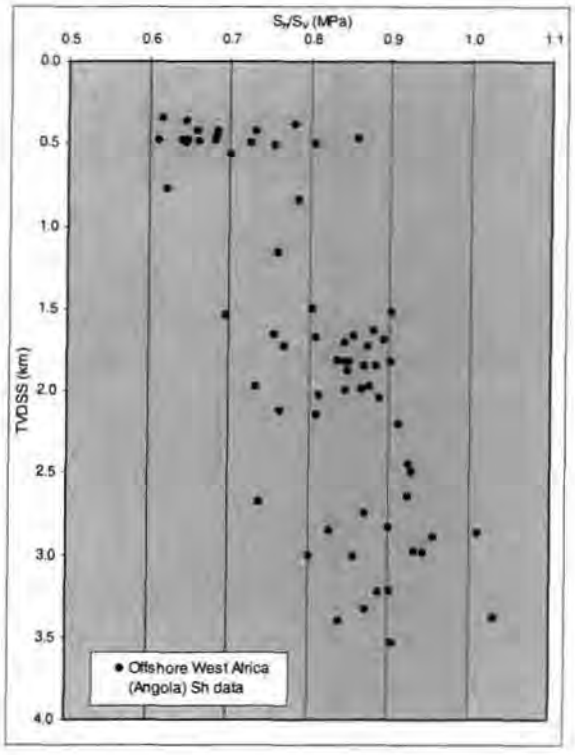

Figure 5.47: *S_h normalised to S_V for Offshore West Africa.*

Pore pressures show a greater range of magnitudes than the S_h data. From the surface to 1½ km P_p are hydrostatic (**Figure 5.46**). Below this depth all bar two of the available P_p data are overpressured. Overpressures develop in a transition zone between 1½ and 2¼ km and follow a trend that increases from the hydrostat to 70% S_V. A P_p of 70% S_V at 2¼ km corresponds to an overpressure of 10½ MPa. Overpressures below 2½ km show a large variation in magnitude. At 3 km overpressures range from 3 MPa to 23 MPa (over 80% S_V).

Considering the data as normally pressured (yellow) and overpressured (green) pairs (**Figure 5.46**) reveals normal P_p are paired with all S_h magnitudes less than 70% S_V. The greatest magnitude of S_h paired with a normal P_p is 90% S_V. All S_h magnitudes of 90% S_V and above are paired with overpressured fluids. Normally and overpressured data from the same depth (those from 1.6 km) show the majority of S_h measurements paired with normal P_p are lower than S_h associated with overpressures. This evidence suggests P_p magnitude variations may account for the scatter in S_h at a given depth. Specific evidence comes from the depth with the greatest range of overpressure (20 MPa at 3 km). Also at this depth is the greatest variation in S_h (11 MPa). Whilst stress-depth plots can only imply a relationship between P_p and S_h, the approaches described in **section 5.6.5** quantify how S_h changes with overpressure.

5.6.3.2 Understanding the patterns shown by stress-depth plots

There is clearly a large variation in the magnitude of S_h in Offshore West Africa at certain depths (**Figure 5.46**). Unfortunately, apart from the magnitude of the P_p at the location of the pumping pressure test, the only known parameter is the wellbore diameter. S_h magnitude has been plotted by wellbore diameter (**Figure 5.48**) to examine whether different diameters can explain S_h variation.

- **Wellbore diameter and S_h magnitude**

There are few instances where there is an overlap between different wellbore diameters (**Figure 5.48**). At 1½ km the two 12¼" wellbore S_h measurements exceed the 17½" wellbore measurement by 3½ and 8 MPa respectively. At 2.2 km the 8½" wellbore S_h measurement is in excess of the two 12¼" S_h measurements. The difference in S_h between the 6" and 8½" wellbore at 3.3 km is inconclusive.

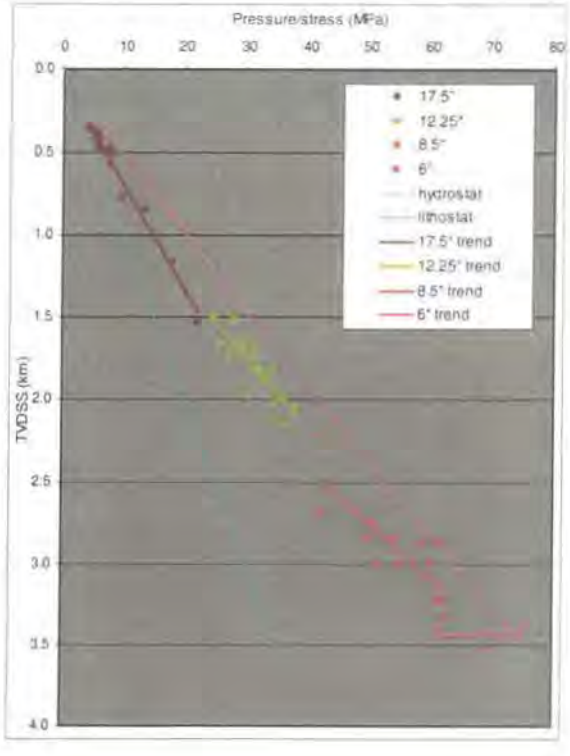

Figure 5.48: S_h data plotted by the wellbore diameter that the test was conducted in.

Fitting linear regression lines to the data series does not show a relationship between the swarms of data. Given the scarcity of overlap between S_h measured in different diameter wellbores and the large amount of scatter in the data, it cannot be said that different wellbore diameters sustain consistently different S_h magnitudes or explain the S_h variability.

5.6.3.3 Summarising what stress-depth plots reveal about S_h magnitude

Stress-depth plots reveal that S_h magnitudes increase from 60% S_V at ½ km to >90% S_V at 3½ km. There is significant scatter in S_h magnitude at all depths. Using a stress-depth plot to investigate if P_p variations explain S_h variation produces inconclusive results. In the upper 1½ km all P_p data are normally pressured yet the scatter in S_h still occurs. Overpressures do pair with higher S_h magnitudes in **Figure 5.46** but no quantifiable relationship between P_p and S_h can be deduced from this plot. Plotting the data by wellbore diameter (**Figure 5.48**) does not account for the differences in S_h magnitude at specific depths and does not explain the scatter in S_h.

5.6.4 Using the data to estimate regional minimum *in-situ* stress

All 68 S_h data from Offshore West Africa have been plotted on a stress-depth plot and a curve mathematically fitted so that the majority of the data fall either on the curve or to the right of it. This approach created a lower bound to LOPs (**Figure 5.49**): a means of estimating the regional minimum stress with depth. Plotting P_p separately on a stress-depth plot and fitting a curve so that the majority of the data plotted either on the curve or to the left of it produced an upper limit to P_p (**Figure 5.50**). The results are described below.

The lower bound to LOPs for Offshore West Africa (yellow curve) is shown in **Figure 5.49**. 95% of the S_h measurements plot either on the curve or to the right of it. Comparing the magnitude of the lower bound to S_V shows that in the upper 1½ km it remains a constant 65% S_V. Between 1½ and 3 km the lower bound increases from 70 to 80% S_V before curving abruptly towards S_V from 3 to 3½ km. The curve has a maximum of 90% S_V at 3½ km. The curvature towards S_V represents the increase in the S_h:S_V ratio shown by **Figure 5.47**. The quadratic equation of the lower bound is:

$$y = -0.00031x^2 + 0.07219x + 0.0811 \qquad \textit{(equation 5.15)}$$

As **Figure 5.50** shows, the upper limit to P_p (black) produces a good estimate of the maximum P_p given those data available. All of the data either sit on the trend or plot to the left of it. The upper limit to P_p can be described by the following 3rd order polynomial:

$$y = (2.05E-05)x^3 - (2.41E-03)x^2 + 0.1268x - 0.0637 \qquad \textit{(equation 5.16)}$$

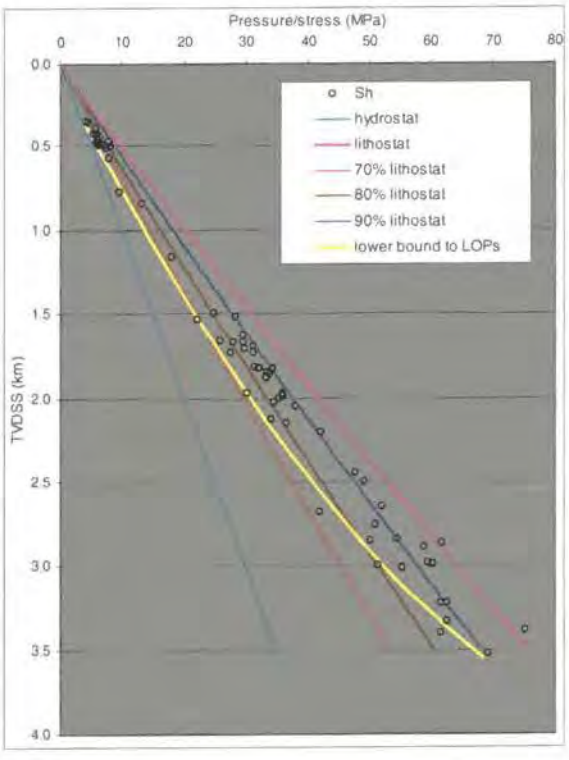

Figure 5.49: Lower bound to LOPs for Offshore West Africa.

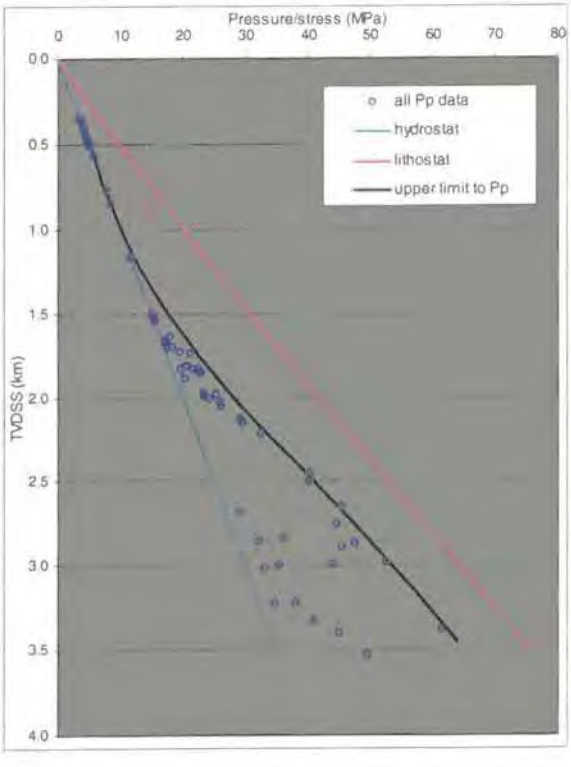

Figure 5.50: Upper limit to P_p for Offshore West Africa.

There is a mismatch of up to 4 MPa between the lower bound and upper limit trends (**Figure 5.51**) before convergence at 2¼ km. The data show P_p to be hydrostatic where the lower bound exceeds the upper limit by 4 MPa at 1¼ km. Below 2¼ km the two trends show a concurrence that exists down to the base of the section at 3½ km. In this depth interval the maximum pore pressures match the minimum S_h measurements. Between 2½ and 3¼ km the upper limit exceeds the lower bound by up to 1.2 MPa.

The results show that within the overpressured section (>2½ km depth) either the lower bound or the upper limit can be used to constrain both maximum P_p and minimum S_h (**Figure 5.51**). Hydrostatic pressures in the upper 1½ km mean the largest differences between S_h and P_p exist and using the upper limit to estimate S_h (or vice versa) will lead to mis-estimates of up to 4 MPa.

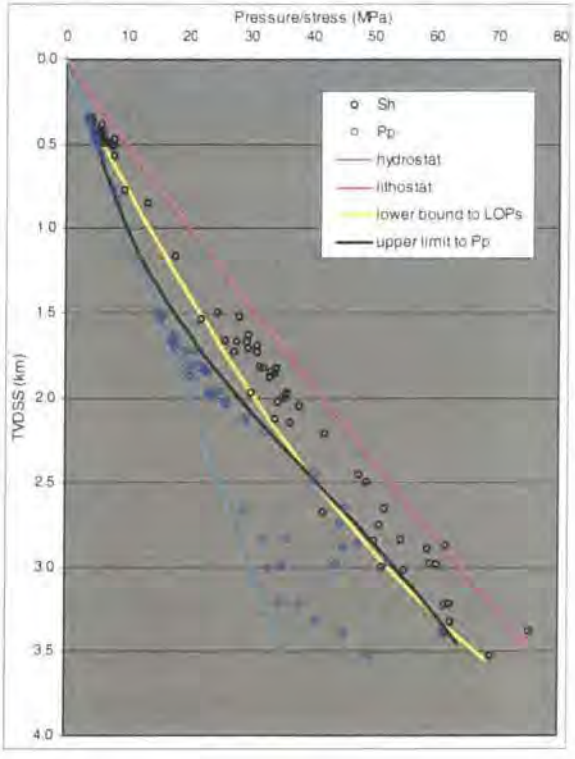

Figure 5.51: Comparative plot showing the lower bound and upper limit.

5.6.5 Pore pressure *in-situ* stress coupling

Described below are the techniques and the types of plots used to examine the relationship between P_p and S_h. Following this, the occurrence of and quantification of P_p-S_h coupling was investigated.

5.6.5.1 Looking for insights into coupling in Offshore West Africa

P_p and S_h data have been normalised to the hydrostat and S_V respectively (**Figure 5.52**) and plotted versus depth. This was to test whether changes in the P_p:hydrostat ratio are matched by changes in the S_h:S_V ratio at the same location.

The data are separated into 28 normally and 40 overpressured pairs and cross-plotted in **Figure 5.53**. Absolute magnitudes of P_p appear on the x-axis and absolute S_h magnitudes on the y-axis. Cross-plotting the data shows how both change relative to each other and relative to the P_p-S_h situation in a hypothetical unconstrained basin (cf. **section 5.2.5.2**). The data are then normalised by the methods described in **section 4.5.1** to investigate coupling. Normally pressured and overpressured pairs are plotted in **Figures 5.54** and **5.55**. Linear regression lines are fitted to the overpressured data.

5.6.5.2 Results

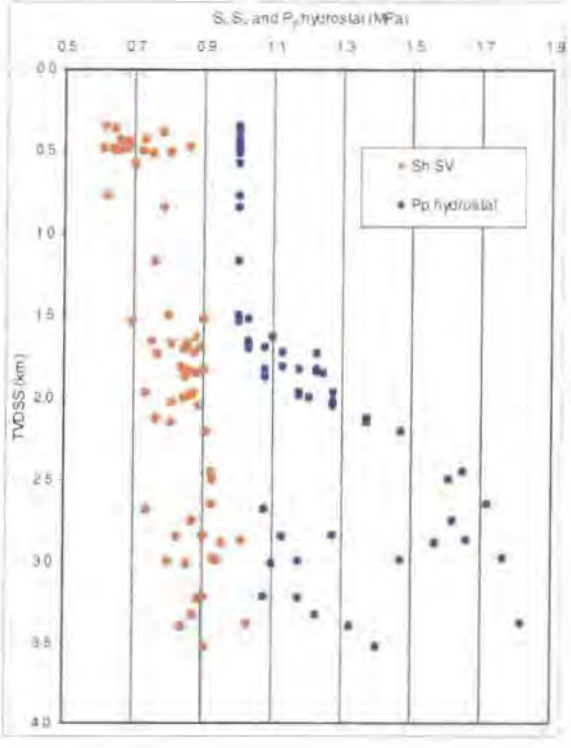

Figure 5.52: S_h:S_V and P_p:hydrostat versus depth for Offshore West Africa.

Figure 5.52 does not show a precise relationship between the S_h:S_V ratio and P_p:hydrostat ratio. P_p:hydrostat ratios of 1.0 in the upper 1½ km are paired with a range of S_h:S_V ratios from 0.6 to 0.85. Throughout the overpressure transition zone (between 1½ and 2¼ km) the P_p:hydrostat ratio increases from 1.0 to 1.6 while the S_h:S_V ratio is constrained

between 0.7 and 0.9. Between 2½ and 3½ km, P_p:hydrostat ratios range from 1.1 to 1.8 and S_h:S_V ratios vary from 0.8 to 1.0. Overall, it is not possible to quantify a relationship that defines the change in the S_h:S_V ratio with an increase in P_p using **Figure 5.52**.

Normally pressured (yellow) and overpressured (green) data are shown with P_p plotted versus S_h in **Figure 5.53**. Normally pressured data follow a trend that matches the "*unconstrained trend*". The relationship for the overpressured data shows a trend with a gradient that is more shallow (1.1 versus 1.58) than the "*unconstrained trend*". This shows that P_p increases at a rate greater than S_h (relative to the unconstrained situation) with depth.

All of the data were normalised to a hypothetical unconstrained basin and depth and depth-normalised to show the relationship between P_p and the increase in S_h. Linear regression lines were fitted through all the data. The data have been separated into normally pressured and overpressured pairs in both **Figures 5.54** and **5.55** and regression lines fitted to the overpressured data. **Table 5.10** summarises the relationships.

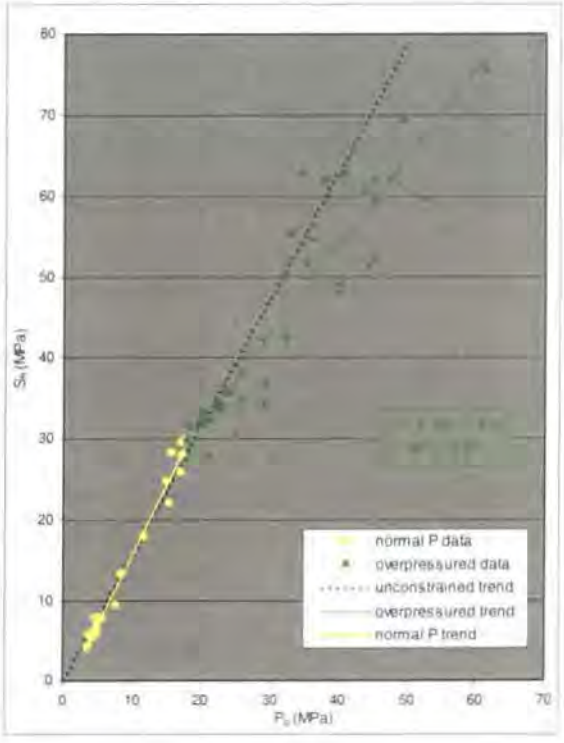

Figure 5.53: Absolute magnitudes of S_h versus absolute magnitudes of P_p for Offshore West Africa.

Data statistics refer to	Data plotted as gradients (e.g. *[S_h-gradient]*)		Data normalised to an "unconstrained basin" & depth (e.g. *[(S_h-S_h(T))/depth]*)	
	$\Delta S_h/\Delta P_p$	r^2	$\Delta S_h/\Delta P_p$	r^2
All data	0.85	0.53	0.68	0.51
Overpressured	0.43	0.39	0.38	0.36

Table 5.10: Summary table showing the nature of pore pressure *in-situ* stress coupling ($\Delta S_h/\Delta P_p$) and correlation coefficients (r^2) for Offshore West Africa.

Table 5.10 shows that depending which method of plotting the data is used and which data (all versus overpressured) are analysed, contrasting $\Delta S_h/\Delta P_p$ values appear. $\Delta S_h/\Delta P_p$ values ranging from 0.38 to 0.85 suggest S_h increases between 38% and 85% of P_p. However, correlation coefficients (r^2 values) of between 0.36 and 0.53 show the relationships to be weak (especially for the overpressured data). Given the low r^2 values, the relationships are poor and coupling cannot be inferred for Offshore West Africa.

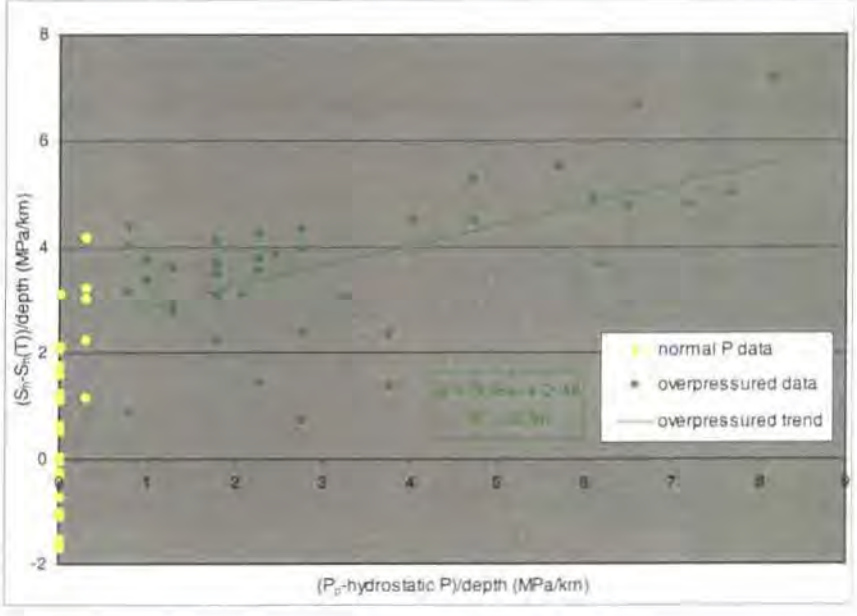

Figure 5.54: Normally and overpressured data normalised to a hypothetical unconstrained basin and depth.

The low r^2 values occur due to the variation in S_h for a specific P_p and vice versa. Normally pressured data in **Figures 5.54** and **5.55** show a large variation in S_h magnitude (gradients are between 11.75 and 18.5 MPa/km in **Figure 5.54**). S_h gradients paired with the

overpressured data also show large variations. Where the P_p gradient is 12.75 MPa/km, for example, the S_h gradient has a range of values between 15.3 and 19.2 MPa/km. For a S_h gradient of 18.5 MPa/km the P_p gradient ranges from 10.3 to 16.2 MPa/km. This scatter masks any linear coupling relationship.

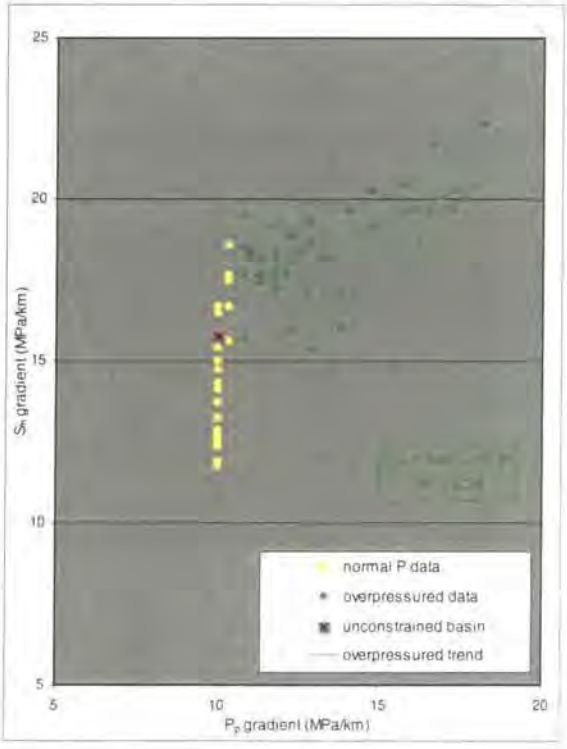

Figure 5.55: Normally and overpressured data depth-normalised for Offshore West Africa.

5.6.6 Summarising the results for Offshore West Africa

Following the conversion of units for the S_h and P_p data, these data were plotted on stress-depth plots and S_h was normalised to the lithostat. P_p and S_h were normalised to both a hypothetical unconstrained basin and depth, and depth-normalised before being cross-plotted. The reasons were to examine the magnitude of, and the variation in, S_h at specific depths and look for insights into P_p-S_h coupling. The results are summarised below.

- The S_h data show a variation in magnitude that is equivalent to 20% of the lithostat throughout the depth section. The maximum variation is 11 MPa at 3km.
- Despite the scatter, the average S_h:S_V ratio shows an increase with depth from 0.7 at ½ km to 0.85 at 1¾ km to 0.92 at 3 km.
- P_p show a greater amount of scatter than the S_h data.

- P_p are hydrostatic to 1½ km depth where a transition zone elevates overpressures up to 10.5 MPa at 2¼ km. Below 2½ km, variability is up to 20 MPa (at 3 km).
- Analysing P_p and S_h together shows normal P_p are paired with S_h magnitudes up to 90% S_V. All S_h measurements >90% S_V are paired with overpressures.
- The scatter in S_h at depths >2½ km may be explained by differences in P_p magnitude but stress-depth plots cannot quantify a relationship.
- Differences in the wellbore diameter that the test was performed in do not account for the scatter in S_h.
- The lower bound to LOPs has a curvi-linear form. The curvature towards S_V (especially below 3 km depth) reflects the increase in the S_h:S_V ratio with depth.
- The upper limit to P_p produces a good estimate of the maximum P_p but shows up to a 4 MPa mismatch with the lower bound before convergence at 2¼ km. Below 2¼ km the upper limit and lower bound are separated by <1.2 MPa.
- Plotting the S_h:S_V ratio and P_p:hydrostat ratio versus depth does not reveal a link between overpressure and S_h increase.
- Large variations in S_h for a specific P_p and vice versa contribute to the low r^2 values (< 0.53) and mask any linear coupling relationships. P_p-S_h coupling cannot account for the scatter in S_h at specific depths.
- Pore pressure *in-situ* stress coupling cannot be inferred for Offshore West Africa.

5.7 The Barents Sea

5.7.1 Introduction to the Barents Sea region

A brief introduction to the Barents Sea is given in this section. Firstly the location of the region is given and the contemporary stress situation reviewed. Since the rapid amounts of uplift and erosion relate more to the area than the burial history, this uplift is summarised. This region was chosen as a case study due to the lack of overpressure.

- **Location**

The Norwegian Barents Sea is part of the Arctic Ocean and lies between the northern coast of Norway and the islands of Svalbard. The entire Barents Sea region is north of the Arctic Circle.

- **The contemporary stress situation**

The stress situation is similar to that of Mid-Norway (see **section 3.5**). Borehole breakouts (18 in number) indicate a strong horizontal stress anisotropy and give a N-S direction for the maximum principal stress, S_H (Fejerskov *et al.*, 1995). The N-S orientation is confirmed by breakout data from the *World Stress Map Project* (Mueller *et al.*, 2000). Overcoring measurements in Northern Norway further confirm the stress direction (Fejerskov *et al.*, 1995). The region is characterised by a lack of seismic activity but small earthquakes on the Northern Norwegian mainland give a N-S S_H direction and show the stress field to have a compressive component. Like Mid-Norway, the stress generating mechanisms are believed to be the opening of the Atlantic and Fennoscandian uplift (Fejerskov *et al.*, 1995).

- **Burial and uplift history**

Reservoir rocks show the effects of deeper burial by having lower porosities and permeabilities than normal for their present depth of burial (Theis *et al.*, 1993). The high vitrinite reflectance levels indicate that there must have been up to 3 km of post-Cretaceous uplift and erosion especially in areas to the N and NW of the region. Porosities confirm that rocks were once at 500 - 2500 metres greater depth depending on geographical location. Porosities indicate normal compaction during burial (Theis *et al.*, 1993).

Considering the Hammerfest Basin in the south of the region, it has been suggested that 1000 metres of uplift occurred in the Late Tertiary. Prior to this time, subsidence is believed to have been ~100 m/Ma during the 6 Ma from the Late-Oligocene to the Early Miocene (23 Ma). Little or no subsidence occurred for the 20 Ma from the Mid-Miocene until the Late Pliocene. Rapid uplift and erosion (~300 m/Ma) took place in the Hammerfest Basin during the Pleistocene (Dahl & Augustson, 1993).

The erosion is believed to be associated with major glacial events during the time period. Greater erosional rates further north are related to "heavier" glacial activity at higher latitudes. The normal to sub-normal P_p found in the NW of the Hammerfest Basin and the reminder of the Barents Sea region have been attributed to the recent and rapid loss of sediment (Dahl & Augustson, 1993).

5.7.2 Compiling the data

The Barents Sea data was provided by *Enterprise Oil*. S_h and P_p measurements were selected from *PressureView* (see **section 1.2**) which led to the compilation of 108 S_h measurements.

Of the 108 S_h measurements only 9 had a P_p measurement recorded within 100 m of the pumping pressure test. These 9 data points are the Barents Sea "*comparable depth*" data set. The "*comparable depth*" data have also been separated into normally pressured and overpressured groups (see explanation in **section 4.2**).

The lack of a density log for this study meant that the lithostat was assumed to increase at a rate of 22.62 MPa/km or 1 psi/ft. An average water depth of 290 m was also assumed.

5.7.3 Stress-depth plots

Having compiled the data, both S_h and P_p have been plotted on stress-depth plots. The objectives of this section of the study are listed in **section 5.2.3**. The results of the Barents Sea investigations are given below.

5.7.3.1 Relationships shown by stress-depth plots

All S_h and P_p measurements have been plotted wholesale on a stress-depth plot (**Figure 5.56**). For reference are the lithostat and hydrostat (10 MPa/km). Gradients related to the lithostat (60%, 70%, 80% and 90% S_V) show how S_h changes relative to S_V with depth.

The S_h data (**Figure 5.56**) show notable amounts of scatter in their magnitudes at any given depth. Considering the gradients, S_h ranges between 60% and 100% S_V. This scatter is quantified at 250 metre depth intervals in **Table 5.11**. The shallow depth data (<1 km) show scatter of up to 6 MPa (at 1.1 km). The greatest scatter occurs between 1¼ and 2¾ km where

it is up to 15 MPa (at 2.4 km). There is a lack of data at depths greater than 3 km meaning the maximum variability is only 3 MPa (at 4 km).

Depth (kilometres)	Variability in S_h (MPa)
0.5	4
0.75	4.5
1.0	5.5
1.25	7
1.5	11.75
1.75	12
2.0	6
2.25	2.5
2.5	14.5
2.75	9.5
3.0	2
3.25	-
3.5	-
3.75	-
4.0	3
4.25	-
4.5	-
4.75	-
5.0	-

Table 5.11: Variability in the magnitude of S_h at 250 metre intervals.

The magnitude of S_h relative to the lithostat (S_h:S_V ratio) versus depth is shown in **Figure 5.57**. The shallow depth data (<1 km) show the largest range of S_h:S_V ratios. The range is between 0.58 and 1.12. However, 85% of the data plot between 0.7 and 1.0 for these depths. No systematic increase in the S_h:S_V ratio is seen with depth but there is a reduction in the amount of scatter, a consequence of there being fewer data at greater depths. Below 3 km depth the range of S_h:S_V ratios is between 0.8 and 1.0.

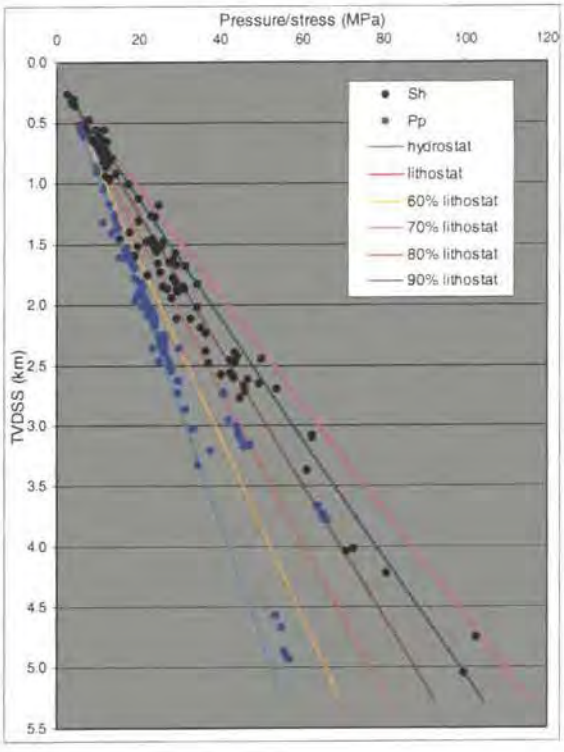

Figure 5.56: All S_h and P_p data versus depth for the Barents Sea.

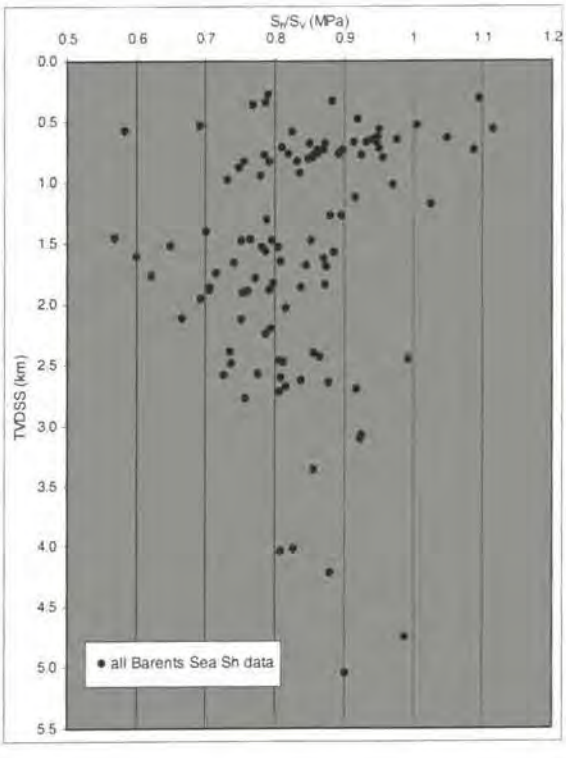

Figure 5.57: S_h normalised to S_V for the Barents Sea.

The majority of P_p in the Barents Sea are normally pressured or show small amounts of overpressure (**Figure 5.56**). No overpressures greater than 5 MPa occur at depths of less than 2¾ km. The only significant overpressures are between 2¾ and 3¼ km where they are 12 MPa above the hydrostat and at 3¾ km where P_p are 17 MPa overpressured.

The "*comparable depth*" data are shown in **Figure 5.58**. The variability in S_h seen in **Figure 5.56** is still present but on a reduced scale. The maximum scatter is 9 MPa at 2.4 km. The "*comparable depth*" data show an increase in S_h relative to S_v with depth. S_h increases from 65% S_v at 2.1 km through to 95% S_v at 3.1 km. Coincident with the increase in S_h relative to S_v is an increase in overpressure. Pore pressures increase from hydrostatic at 1.9 km to 70% S_v (15 MPa of overpressure) at 3.2 km.

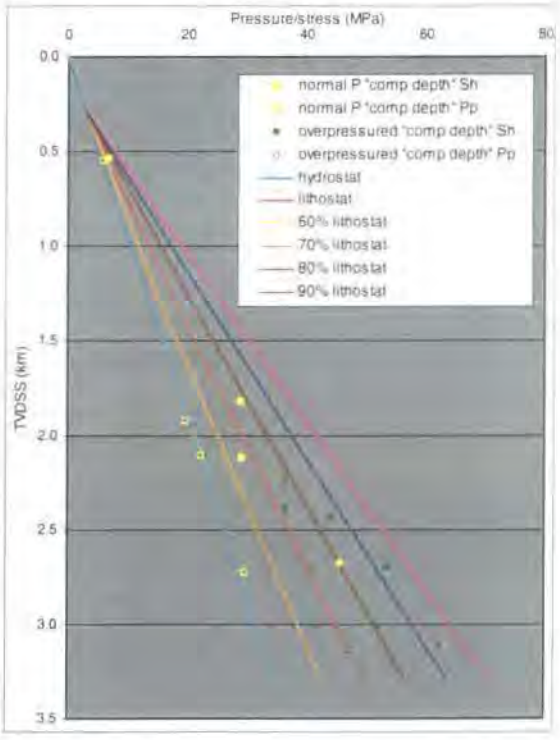

Figure 5.58: Normally and overpressured "*comparable depth*" S_h and P_p.

Considering the "*comparable depth*" data separated into normally pressured and overpressured subsets (**Figure 5.58**) shows a non-quantifiable link between the magnitude of overpressure and S_h. Most of the higher S_h measurements are associated with overpressured fluids. Other means of analysing the data are required to assess the relationship between P_p and S_h magnitude. From the results in **Figure 5.56**, P_p differences do not appear to be the cause of the S_h variability because hydrostatic pressures predominate in the Barents Sea.

5.7.3.2 Understanding the patterns shown by stress-depth plots

The S_h data are plotted by lithology (**Figure 5.59**) and wellbore diameter (**Figure 5.60**) in attempts explain the scatter in the S_h magnitude. Linear regression lines are fitted to the wellbore diameter data based on data series. The results are described below.

- **Lithology and S_h magnitude**

The results (**Figure 5.59**) show that 42 out the 48 tests with a lithology recorded were performed in claystone. Four tests were performed in limestone and only 2 in sandstone. All of the scatter in S_h manifests in the data for claystone. Considering the magnitude of S_h in each lithology, no single lithology supports consistently higher values of S_h. It is inferred that lithological differences do not exert a control on S_h and do not explain S_h variability.

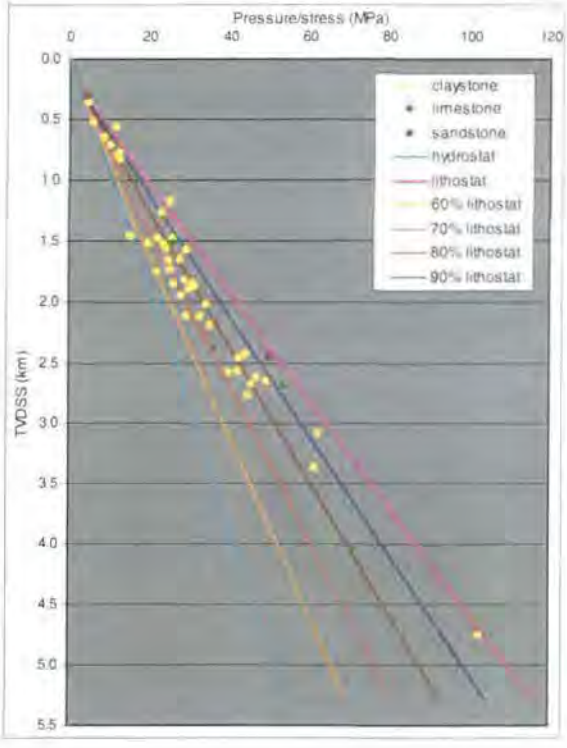

Figure 5.59: All S_h data plotted by the lithology the test was conducted in.

- **Wellbore diameter and S_h magnitude**

The Barents Sea data are plotted by wellbore diameter in **Figure 5.60** and linear regression lines fitted to the data series. From the results, wellbore diameter differences do not explain the scatter in S_h at a given depth and do not control the magnitude of S_h (see **section 4.3.2**). The regression lines show that S_h magnitude does not systematically increase or decrease from larger to smaller wellbores. For example, at 2½ km depth S_h is recorded in 12¼", 8½" and 6" diameter wellbores and the S_h magnitude does not scale with wellbore

diameter. The lack of relationship is further confirmed between 1½ and 2 km depth where data from 12¼" and 8½" diameter wellbores occur. The linear regression lines overlap indicating no difference in the average S_h from each wellbore.

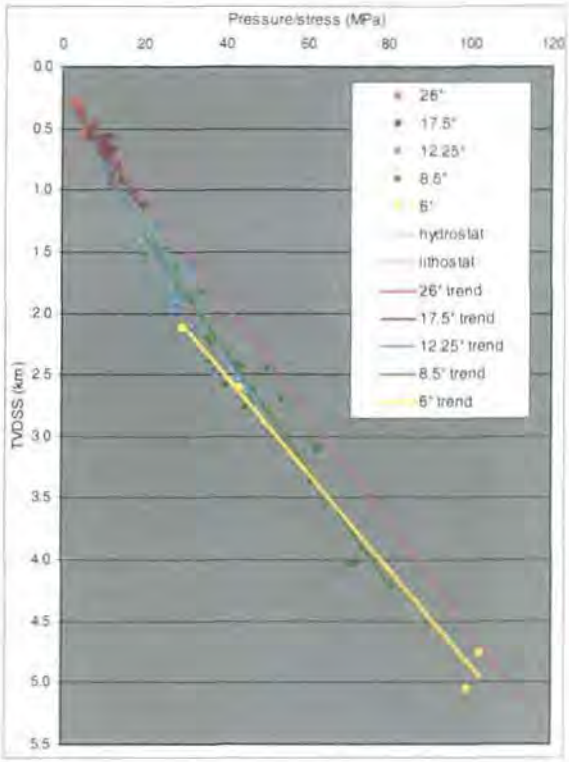

Figure 5.60: S_h data plotted by the wellbore diameter that the test was conducted in.

5.7.3.3 Summarising what stress-depth plots reveal about S_h magnitude

Because the majority of P_p in the Barents Sea are normally pressured, **Figure 5.56** does not reveal a link between P_p and S_h magnitude and variability. Of the 9 "*comparable depth*" data, 5 are overpressured and this data subset *does* indicate higher S_h measurements are associated with overpressured fluids.

Lithological differences do not explain S_h magnitude variations (**Figure 5.59**). 90% of the tests are performed in claystone meaning all the scatter manifests in this one lithology.

Plotting the data by wellbore diameter (**Figure 5.60**) does not show a link between the variation in S_h magnitude and differences in wellbore diameter. S_h magnitude does not scale with wellbore diameter.

5.7.4 Using the data to estimate regional minimum *in-situ* stress

Two approaches have been used to estimate the regional minimum *in-situ* stress: the creation of the lower bound to LOPs, and the upper limit to P_p. The methodology and results are given below.

The 108 S_h data have been plotted on a stress-depth plot (**Figure 5.61**) and a curve fitted to create a lower bound to LOPs (yellow line). The lower bound was created so that the majority of the data fell to the right of it. The same approach led to the creation of the "*comparable depth*" lower bound (green line in **Figure 5.62**). P_p data were plotted separately and a curve fitted so that the majority of the data plotted either on or to the left of it. This produced the upper limit to P_p (black line in **Figure 5.63**). The results are as follows:

Over 90% of the 108 S_h measurements plot on or to the right of the lower bound to all LOPs. The curve is a quadratic function and is described by:

$$y = -0.00021x^2 + 0.06955x + 0.17694 \qquad \textit{(equation 5.17)}$$

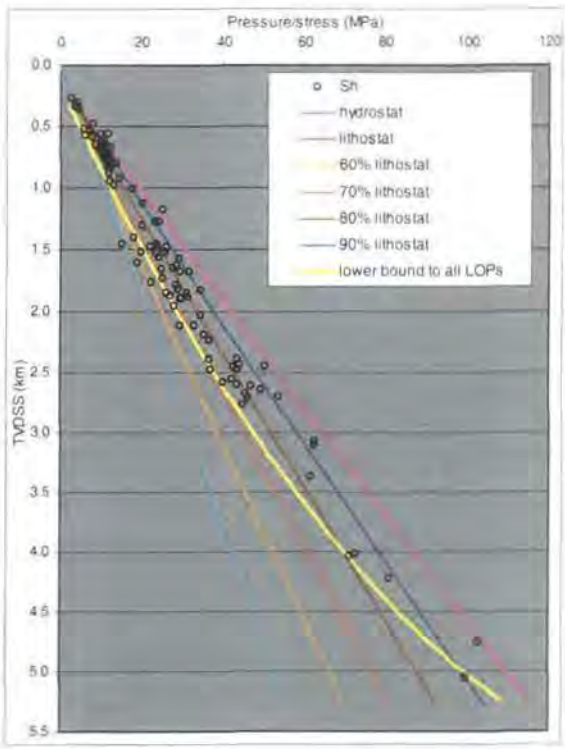

Figure 5.61: Lower bound to all LOPs for the Barents Sea.

The lower bound to all LOPs has a curvi-linear shape and curves towards S_v with depth. In the upper 1 km it has a magnitude relative to S_v of 50 - 60%. Between 1½ and 2½

km the magnitude increases and is 70% S_V. Below 2½ km there is a more noticeable increase with the lower bound crossing the 80% S_V gradient (magnitude = 70 MPa) at 4 km and the 90% S_V gradient at 5 km (magnitude = 100 MPa). However, a scarcity of data makes fitting an accurate curve at depths >3 km problematic.

Creating an accurate "*comparable depth*" lower bound is hindered by 8 out of 9 data falling between 1¾ and 3¼ km depth. The best attempt is shown by the green line (**Figure 5.62**) with the equation:

$$y = -0.00057x^2 + 0.0857x + 0.0063 \qquad \textit{(equation 5.18)}$$

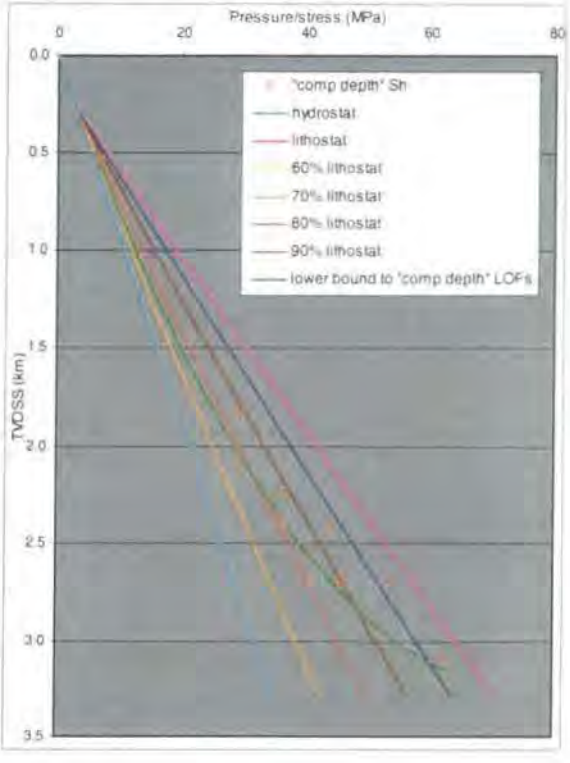

Figure 5.62: "*Comparable depth*" lower bound to LOPs for the Barents Sea.

The "*comparable depth*" lower bound has initial magnitudes that are low relative to S_V. The curve plots at 65% S_V until 1¾ km before increasing to 70% S_V at 2 km. A rapid increase in the magnitude of the lower bound towards S_V occurs between 2 and 3¼ km depth. At 2¾ km the curve has a magnitude of 80% S_V (48 MPa) and at 3¼ km the magnitude is 90% S_V (60 MPa).

The P_p data for the Barents Sea are plotted in **Figure 5.63** and an upper limit fitted. The upper limit provides a sound estimate of the maximum P_p encountered in the region

because all of the data fall on or to the left of it. Despite the majority of the P_p data being normally pressured or showing only slight amounts of overpressure, those overpressures at 3 - 3¾ km mean the upper limit is once again described by a cubic equation:

$$y = (1.52E-05)x^3 - (2.07E-03)x^2 + 0.13x - 0.251 \qquad \textit{(equation 5.19)}$$

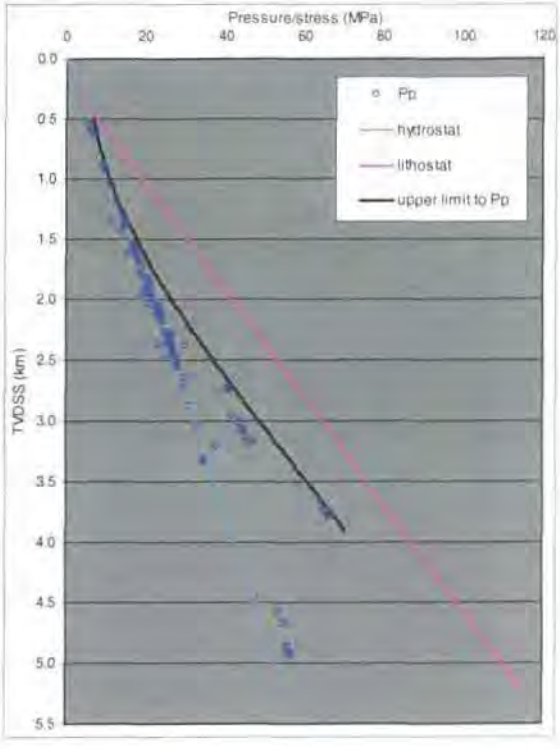

***Figure* 5.63:** *Upper limit to P_p for the Barents Sea.*

The maximum magnitude of the upper limit occurs at 3.9 km where it is 70 MPa or 82% S_V.

Comparing both lower bounds and the upper limit (**Figure 5.64**) shows a good match between the lower bound to all LOPs (yellow line) and the upper limit to P_p (black line). In the upper 2½ km, where P_p are mainly hydrostatic, the upper limit is <3 MPa lower than the lower bound. Below 2¾ km it is up to 2 MPa in excess of the lower bound to all LOPs. It can therefore be inferred that the upper limit to P_p can be used to estimate the minimum regional S_h in the upper 3 kilometres. Likewise, the lower bound to all LOPs provides a good estimate of the maximum P_p likely to be encountered at these depths (given the data in this study).

The "*comparable depth*" lower bound (green line) and the lower bound to all LOPs show a strong concordance as deep as 2½ km. The "*comparable depth*" lower bound is also within 2 MPa of the upper limit to P_p through this interval. Below 2½ km, the "*comparable*

depth" lower bound is well in excess of the lower bound to all LOPs and the upper limit. At 3.1 km the difference is 12 and 13 MPa respectively. Using the "*comparable depth*" lower bound to estimate P_p at depths >2½ km will produce errors of up to 13 MPa .

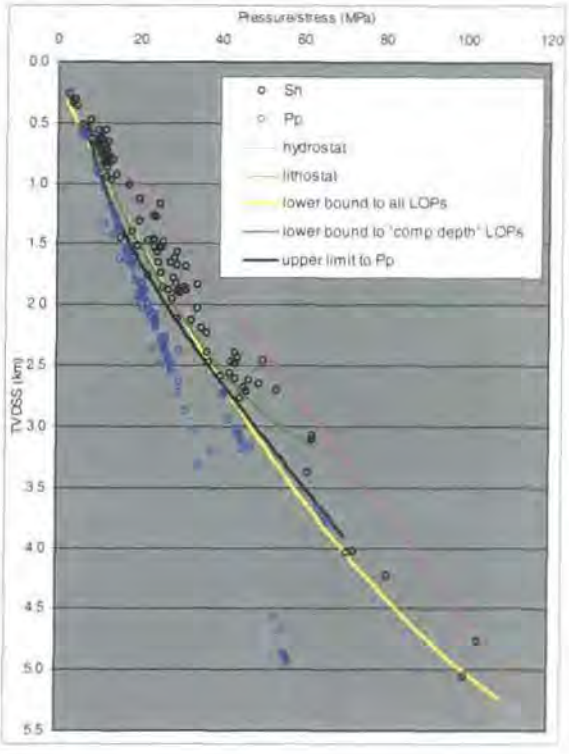

Figure 5.64: Comparative plot showing both lower bounds and the upper limit to P_p.

5.7.5 Pore pressure *in-situ* stress coupling

This section describes the methodology used to investigate the relationship between P_p and S_h using the 9 "*comparable depth*" data. The results of examinations into and quantification of P_p-S_h coupling are also given.

5.7.5.1 Looking for insights into coupling in the Barents Sea

The "*comparable depth*" data are separated into the 4 normally pressured and 5 overpressured points (**Figure 5.65**) and absolute magnitudes of P_p are cross-plotted with absolute S_h magnitudes. Following this, all of the "*comparable depth*" data were firstly normalised to a hypothetical unconstrained basin and depth and then depth normalised. The data are separated into normally pressured and overpressured subsets in **Figures 5.66** and

5.67. Fitting linear regression lines to all the data and then the overpressured data allowed the determination of $\Delta S_h/\Delta P_p$ values.

5.7.5.2 Results

The cross-plot of normally pressured (yellow) and overpressured (green) data is shown in **Figure 5.65**. Shown for reference is the hypothetical unconstrained basin trend. The normally pressured data plot in a trend closely matching the "*unconstrained trend*" indicating they follow this relationship. The green regression line through the overpressured data has a gradient that is more shallow (1.16 versus 1.58) than the "*unconstrained trend*" showing that the rate of increase in P_p relative to S_h over a given depth increment is greater than for the hypothetical unconstrained basin situation. The relationship is quantified below.

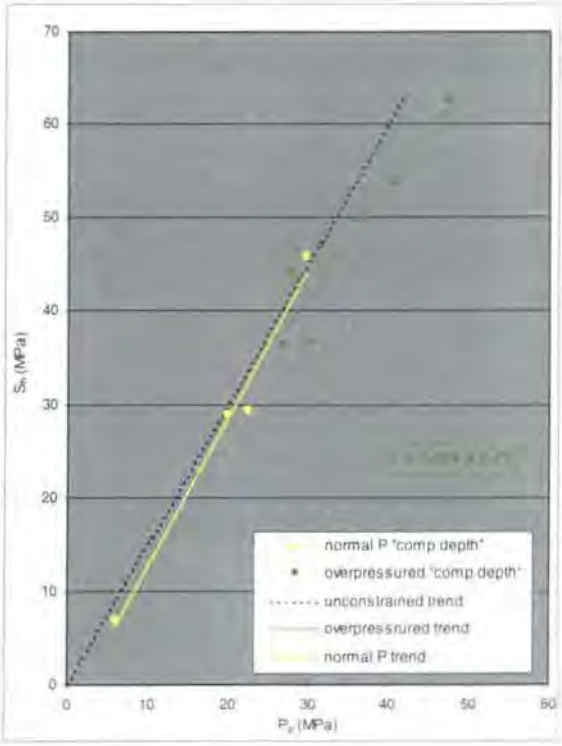

Figure 5.65: Absolute magnitudes of S_h versus absolute magnitudes of P_p.

The statistics of the regression lines ($\Delta S_h/\Delta P_p$ and r^2) fitted to all the data and solely the overpressured data are summarised in **Table 5.12**. The gradient of the linear regression lines shows numerically how S_h increases with an increase in P_p. This is the $\Delta S_h/\Delta P_p$ value.

Data statistics refer to	Data plotted as gradients (e.g. *[S_h-gradient]*)		Data normalised to an "unconstrained basin" & depth (e.g. *[(S_h-S_h(T))/depth]*)	
	$\Delta S_h/\Delta P_p$	r^2	$\Delta S_h/\Delta P_p$	r^2
All data	1.02	0.56	0.60	0.34
Overpressured	0.84	0.51	0.66	0.45

Table 5.12: Summary table showing the nature of pore pressure *in-situ* stress coupling ($\Delta S_h/\Delta P_p$) and correlation coefficients (r^2) for the Barents Sea.

Fitting linear regression lines to all of the "*comparable depth*" data produces contrasting results. Normalising the data to a hypothetical unconstrained basin and depth gives a $\Delta S_h/\Delta P_p$ value of 0.60 but the correlation coefficient ($r^2 = 0.34$) shows the relationship to be weak. Plotting the data as gradients improves the r^2 value to 0.56 but the $\Delta S_h/\Delta P_p$ value increases to 1.02. S_h increasing at 102% of the P_p increase is unrealistic if coupling is occurring. It is unlikely that P_p controls S_h magnitude within the overpressured zone.

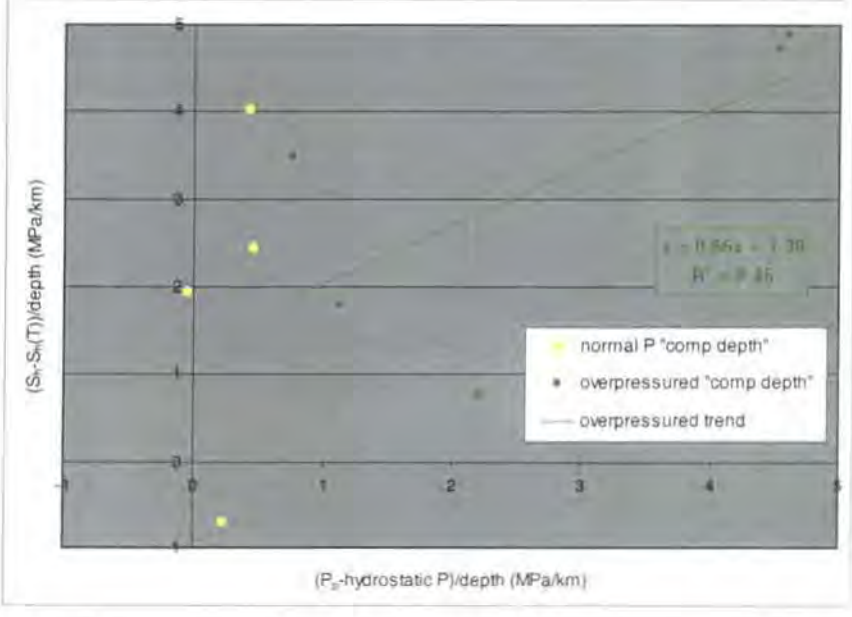

Figure 5.66: Normally and overpressured data normalised to a hypothetical unconstrained basin and depth for the Barents Sea.

Considering solely the overpressured data (**Figures 5.66** and **5.67**) shows a more consistent relationship between P_p and S_h. Normalising the data to a hypothetical unconstrained basin and depth reveals a $\Delta S_h/\Delta P_p$ value of 0.66 yet the r^2 value is low (0.45).

Plotting the overpressured data as gradients produces a $\Delta S_h/\Delta P_p$ value of 0.84 with a r^2 value of 0.51.

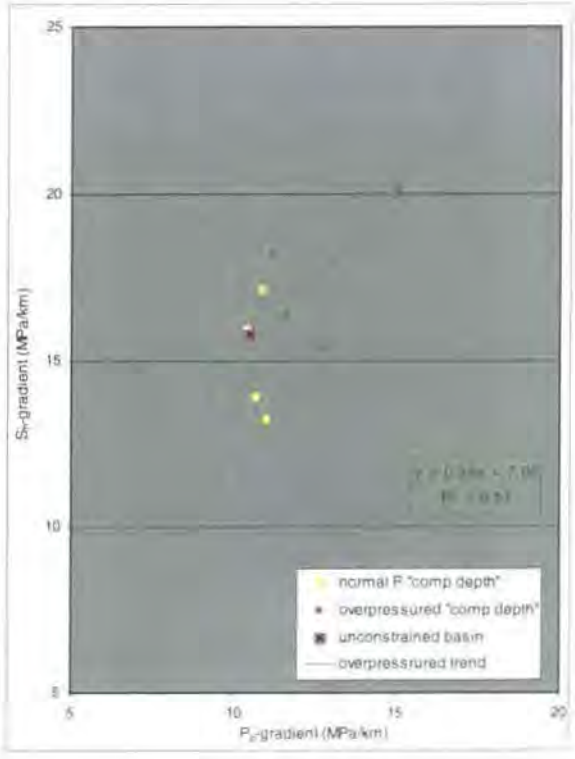

Figure 5.67: Normally and overpressured data depth-normalised for the Barents Sea.

The small number of data in the "*comparable depth*" data set hinders the results of the coupling analyses. The data used in the "*comparable depth*" set also misrepresent the data in the region. Over 90% of the P_p measurements in **Figure 5.56** are normally pressured yet 5-out-of-9 "*comparable depth*" data are overpressured. Hence it is inferred from these data that P_p-S_h coupling is not occurring in the Barents Sea.

5.7.6 Summarising the results for the Barents Sea

The Barents Sea S_h and P_p data have been plotted on stress-depth plots, normalised to a hypothetical unconstrained basin and/or depth. The aim was to investigate variations in and the controls on S_h with depth. Analyses were also performed that looked for insights into P_p-S_h coupling. The results are summarised below.

- The majority of P_p data are normally pressured yet there is still scatter in the S_h magnitude at all depths (up to 15 MPa at 2.4 km).
- The scatter reduces at depths >3 km as a consequence of there being fewer data.

- At depths of <1 km the S_h:S_V ratio ranges from 0.58 to 1.12. A reduction in the range of the ratio occurs at greater depths but there is not a systematic increase with depth.
- Overpressures are mostly <5 MPa except 3 km (12 MPa of overpressure) and 3¾ km (17 MPa of overpressure).
- The "*comparable depth*" data show a reduction in the scatter of S_h brought about by a reduction in the number of data. The maximum scatter is 9 MPa at 2.4 km.
- Higher S_h measurements are associated with overpressures but the link is non-quantifiable.
- Wellbore diameter variations and lithological differences do not explain the S_h magnitude differences at a given depth.
- The lower bound to all LOPs and the upper limit to P_p show a good match from ½ - 4 km. In the upper 2½ km (where P_p are hydrostatic) the upper limit is <3 MPa below the lower bound, yet it is up to 2 MPa in excess of the lower bound below 2¾ km (where larger overpressures occur).
- The "*comparable depth*" lower bound matches the lower bound to all LOPs to 2½ km before curving towards the lithostat. At 3.1 km it is 12 MPa in excess of the lower bound for all data.
- The upper limit to P_p can be used to estimate the regional S_h in the upper 3 km. Likewise, the lower bound to all LOPs provides a good estimate of the maximum P_p likely to be encountered at these depths.
- The small number of "*comparable depth*" data hinders the results of the coupling analyses.
- Low r^2 values (0.34 to 0.56) reveal coupling cannot be inferred.
- The "*comparable depth*" data misrepresent the Barents Sea data. Over 90% of P_p measurements in the Barents Sea are normally pressured yet 5-out-of-9 "*comparable depth*" data are overpressured.

5.8 Summary

This chapter shows the results for six case studies from differing areas throughout the world. The aim of the chapter was to present and describe the results for each case study individually. In **chapter 6** the results have been drawn together and compared to those found in **chapter 4** for Mid-Norway.

Chapter SIX: Summary, Discussions and Implications

6 Summary, Discussions and Implications

6.1 Introduction

Section 6.2 summarises the results from the seven case studies. Firstly, quantification of the variability in S_h with depth for each region is tabulated and observations made. The possible reasons for the variability are also tabulated. The equations and curves of the lower bounds to LOPs and upper limits to P_p are compared. Finally the results of the coupling analyses are shown and inferences into its presence summarised.

Section 6.3 discusses the data for all the regions. These discussions include a reason for why lithology does not account for the variations in S_h magnitude. The lower bounds to LOPs and upper limits to P_p are related to the tectonic regime of the region and observations are made. Finally, mechanisms that describe P_p-S_h coupling are proposed, their applicability is stated and results are explained.

Section 6.4 discusses the results found for Mid-Norway. The effect the quality control procedure had on the variability in S_h is explained and the implications that the magnitude of the lower bound has on the stress situation are discussed. A suggestion for why coupling does not manifest in Mid-Norway is given and the poro-elasticity and frictional limits equations are used to back-calculate ν and μ respectively. The section concludes with the implication the relationship between LOP and ISIP has on S_H for the region.

Section 6.5 summarises the key points that arise from this chapter.

6.2 Summarising the results

This section summarises the results of the case studies described in **chapters 4** and **5**. In **section 6.2.1** the quantification of the scatter in S_h is compared for specific depths and a summary of possible explanations given. The equations of the lower bounds to LOPs (all data and "*comparable depth*" data) and the upper limits to P_p are tabulated and graphs showing the relationships of these trends displayed (**section 6.2.2**). The regression lines for the approaches used to investigate P_p-S_h coupling are tabulated and shown graphically in **section 6.2.3** for all the data and the overpressured data.

6.2.1 Variability in the magnitude of S_h

Chapters 4 and **5** show investigations that quantify the variability in the magnitude of S_h at a given depth. The results are summarised at 250 metre intervals below:

	Regional variability in S_h (MPa)						
	Mid-Norway	**Central North Sea**	**Brunei**	**Gulf of Mexico**	**Onshore Nigeria**	**Offshore West Africa**	**Barents Sea**
Depth	**227 data**	**369 data**	**23 data**	**65 data**	**51 data**	**68 data**	**108 data**
0.5 km	2	4.5	1.5	2	-	3.5	4
0.75 km	3	5.5	-	1.5	-	4	4.5
1.0 km	3	6.25	3	4.5	-	-	5.5
1.25 km	4.5	9	-	6.5	1	-	7
1.5 km	5	8	2	8	4.5	7	11.25
1.75 km	4.5	6.25	2	12.5	5.5	6.5	12
2.0 km	5.5	8.5	-	9	-	7.5	6
2.25 km	9	12	2	3	6	2	2.5
2.5 km	7.75	4	9	12	2	2	14.5
2.75 km	8.5	17	-	17	4	11	9.5
3.0 km	6	11	-	16	5.5	11	2
3.25 km	6	2.5	-	5.5	9.5	2	-
3.5 km	10	15	-	2	3	3	-
3.75 km	13	14	-	11	4	-	-
4.0 km	13	13	-	10	12	-	3
4.25 km	12.75	6	-	17	-	-	-
4.5 km	-	4	-	2	-	-	-

Table 6.1: Summary of the variability in S_h at 250 metre intervals for each region.

The results in **Table 6.1** allow the following statements to be made:

- Variability in the magnitude of S_h at a specific depth is a phenomenon seen for all regions.

- Variability is still present for the Mid-Norway data despite the quality control procedure.
- Those regions with fewer data (Brunei) show smaller amounts of scatter.
- The Gulf of Mexico shows as much scatter as the Central North Sea – a data set nearly 6 times the size.
- Despite being a large data set, the scatter for Mid-Norway is less than that seen for smaller data sets such as the Gulf of Mexico and the Barents Sea.

Since variability is present in all regions, S_h data were plotted by different parameters (where available) in an attempt to explain its presence. The results are summarised below:

	Mid-Norway	Central North Sea	Brunei	Gulf of Mexico	Onshore Nigeria	Offshore West Africa	Barents Sea
Overpressure	Possibly	Yes	Yes	Yes	Yes	Yes	No
Lithology	No	No	-	No	-	-	No
Wellbore diameter	No	No	No	Yes	Yes	No	No
Pumping rate	No	-	-	-	-	-	-
Age (Formation)	Possibly	-	-	-	-	-	-
Position relative to structure	No	-	-	-	-	-	-

Table 6.2: Summary of possible explanations for the variability in S_h and their applicability ("-" indicates information not available for analysis).

6.2.2 Lower bounds to LOPs and upper limits to P_p

S_h and P_p data were used to create lower bounds to LOPs and upper limits to P_p as means of predicting the regional minimum *in-situ* stress. Lower bounds were created by fitting quadratic equations to the S_h data and upper limits created by fitting a cubic (3^{rd} order polynomial) envelope to P_p data. The results are tabulated and summarised in graphical form below.

6.2.2.1 Lower bounds to all LOPs

The lower bounds to LOPs for all the data are shown **Figure 6.1**. It is clear that all lower bounds are curvi-linear in shape. This feature is present regardless of the region. In the

upper 3 km little variation between the magnitudes of the lower bounds exists. The difference between the trend with the lowest magnitude at 3 km depth (the Gulf of Mexico) and the greatest magnitude (Offshore West Africa) is 7½ MPa. Below 3½ km a scarcity of data makes all lower bounds more difficult to constrain. The greatest mismatch through this depth interval is between the Gulf of Mexico and the Central North Sea of 14 MPa at 4½ km. The equations of the lower bounds to all LOPs are summarised in **Table 6.3**.

Region	Lower bound to all LOPs
Mid-Norway	$y = -0.00017x^2 + 0.06568x + 0.0415$
The Central North Sea	$y = -0.00023x^2 + 0.06855x + 0.0819$
Brunei	$y = -0.00055x^2 + 0.0819x + 0.04525$
The Gulf of Mexico	$y = -0.00025x^2 + 0.07356x + 0.1796$
Onshore Nigeria	$y = -0.00035x^2 + 0.07699x + 0.1591$
Offshore West Africa	$y = -0.00031x^2 + 0.07219x + 0.0811$
The Barents Sea	$y = -0.00021x^2 + 0.06955x + 0.1769$

Table 6.3: Summary of the equations for the lower bounds to all LOPs.

6.2.2.2 "*Comparable depth*" lower bounds to LOPs

The "*comparable depth*" lower bounds to LOPs are plotted in **Figure 6.2**. Since the data from Brunei, Onshore Nigeria and Offshore West Africa are also "*comparable depth*" data the same lower bounds as used in **section 6.2.2.1** are shown.

The "*comparable depth*" lower bounds are also curvi-linear in shape (**Figure 6.2**). The "tails" of the lower bounds for the Gulf of Mexico and the Barents Sea show a greater rate of increase in S_h with depth than the equivalent lower bounds to all data. The "tails" represent a scarcity of data at the greatest depths in each region. More variation occurs between "*comparable depth*" lower bounds than is seen for the lower bounds to all LOPs. At 3 km depth the Barents Sea lower bound exceeds the Gulf of Mexico lower bound by 10½ MPa. Between 3½ and 5 km the lower bounds are more difficult to constrain and larger mismatches occur. At 4 km the lower bound for the Gulf of Mexico is 17 MPa less than the Central North Sea lower bound. **Table 6.4** summarises the equations for the "*comparable depth*" lower bounds.

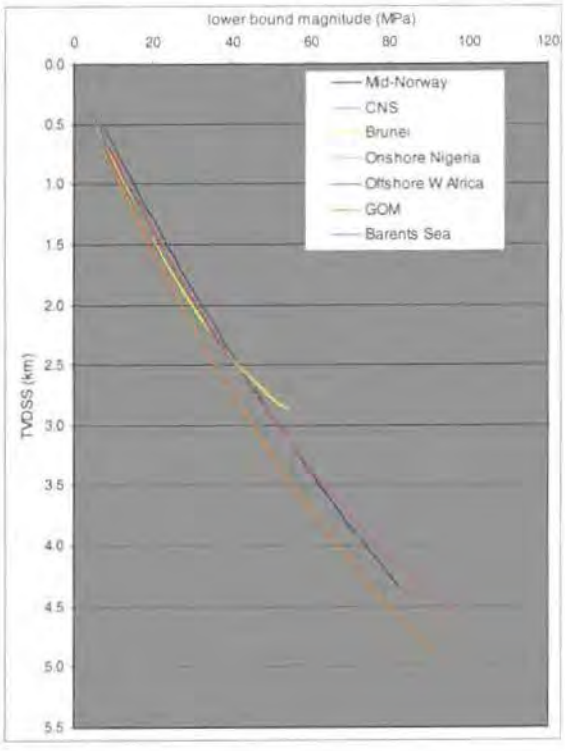

Figure 6.1: Comparative plot of the lower bounds to all LOPs from the seven regions.

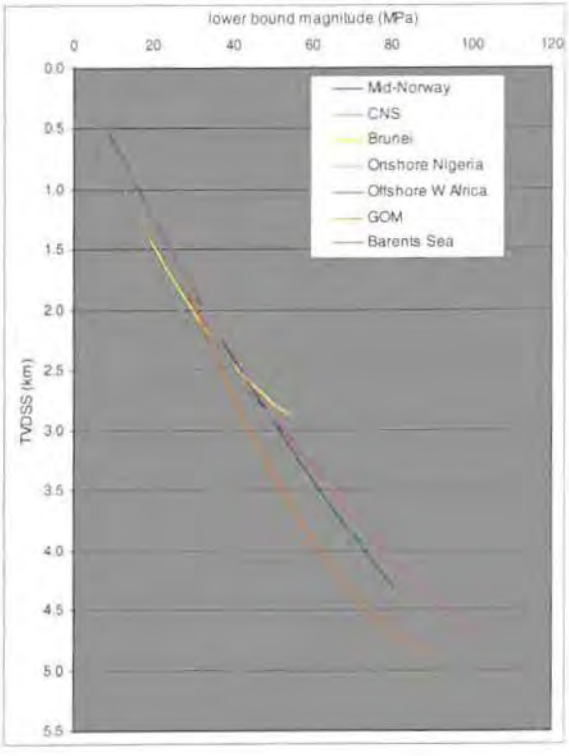

Figure 6.2: "*Comparable depth*" lower bounds to LOPs from the seven regions.

Region	*"Comparable depth"* lower bound to LOPs
Mid-Norway	$y = -0.00018x^2 + 0.06905x - 0.07954$
The Central North Sea	$y = -0.00022x^2 + 0.06884x - 0.04111$
Brunei	$y = -0.00055x^2 + 0.0819x + 0.04525$
The Gulf of Mexico	$y = -0.00055x^2 + 0.11503x - 1.01954$
Onshore Nigeria	$y = -0.00035x^2 + 0.07699x + 0.1591$
Offshore West Africa	$y = -0.00031x^2 + 0.07219x + 0.0811$
The Barents Sea	$y = -0.00057x^2 + 0.0857x + 0.0063$

Table 6.4: Summary of the equations for the *"comparable depth"* lower bounds to LOPs.

6.2.2.3 Upper limits to P_p

The comparative plot of all of the upper limits to P_p is shown in **Figure 6.3** and the equations that describe the upper limits are summarised below:

Region	Upper limit to pore pressure (P_p)
Mid-Norway	$y = (1.2E\text{-}5)x^3 - (1.9E\text{-}3)x^2 + 0.1314x - 0.1768$
The Central North Sea	$y = (5.34E\text{-}6)x^3 - (1.01E\text{-}3)x^2 + 0.096x - 0.039$
Brunei	$y = (1.54E\text{-}5)x^3 - (1.86E\text{-}3)x^2 + 0.107x - 0.0201$
The Gulf of Mexico	$y = (4.82E\text{-}6)x^3 - (6.96E\text{-}4)x^2 + 0.075x + 0.215$
Onshore Nigeria	$y = (1.35E\text{-}5)x^3 - (2.07E\text{-}3)x^2 + 0.138x - 0.159$
Offshore West Africa	$y = (2.05E\text{-}5)x^3 - (2.41E\text{-}3)x^2 + 0.127x - 0.0637$
The Barents Sea	$y = (1.52E\text{-}5)x^3 - (2.07E\text{-}3)x^2 + 0.13x - 0.251$

Table 6.5: Summary of the equations for the upper limits to P_p.

All curves depart from the hydrostat indicating there to be overpressures in each region (**Figure 6.3**). The magnitude of overpressure is also significantly different. Upper limits show Brunei to have the greatest magnitudes of overpressure at depths greater than 1 km whilst the lowest magnitudes occur in Onshore Nigeria. Each region shows hydrostatic P_p occur at depths of less than 1 km.

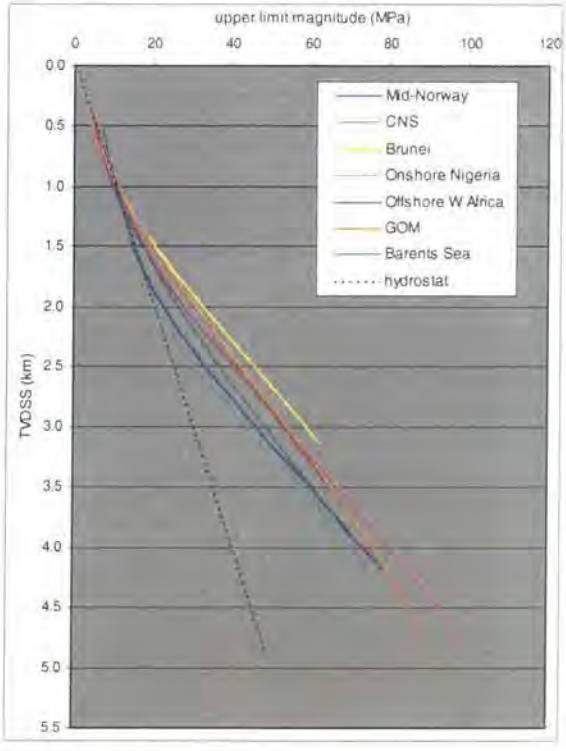

Figure 6.3: Comparative plot showing the upper limits to P_p from the seven regions.

Within the overpressured zone the upper limits for Brunei, the Central North Sea, Offshore West Africa, Mid-Norway and Onshore Nigeria trend sub-parallel to each other. There is also a degree of parallelism between the Gulf of Mexico and Barents Sea upper limits. A maximum difference between the upper limits of 16 MPa occurs between Onshore Nigeria and Brunei at 3.1 km depth. Onshore Nigeria P_p are 150% hydrostatic while Brunei P_p are 200% hydrostatic at this depth.

6.2.3 Pore pressure *in-situ* stress coupling

The relationships found for P_p-S_h coupling are summarised in **Figures 6.4** to **6.7**. Linear regression lines are fitted through all of the "*comparable depth*" data in **Figure 6.4** (data normalised to a hypothetical unconstrained basin and depth) and **Figure 6.5** (data depth-normalised). The linear regression lines for the overpressured "*comparable depth*" data

are shown in **Figure 6.6** (normalised to a hypothetical unconstrained basin and depth) and **Figure 6.7** (data depth-normalised). Summary tables show the equations of the regression lines and correlation coefficients (r^2 values) which reveal the statistical significance of the relationships. These r^2 values are discussed later.

6.2.3.1 Linear relationships for all "*comparable depth*" data

The linear regression lines for all the S_h and P_p data normalised to a hypothetical unconstrained basin and depth are shown in **Figure 6.4**. It is clear that there is a range of gradients to the lines from 0.22 for the Gulf of Mexico through to 0.9 for Onshore Nigeria. Gradients are the same for the Central North Sea and Offshore West Africa and very similar for Mid-Norway and the Gulf of Mexico.

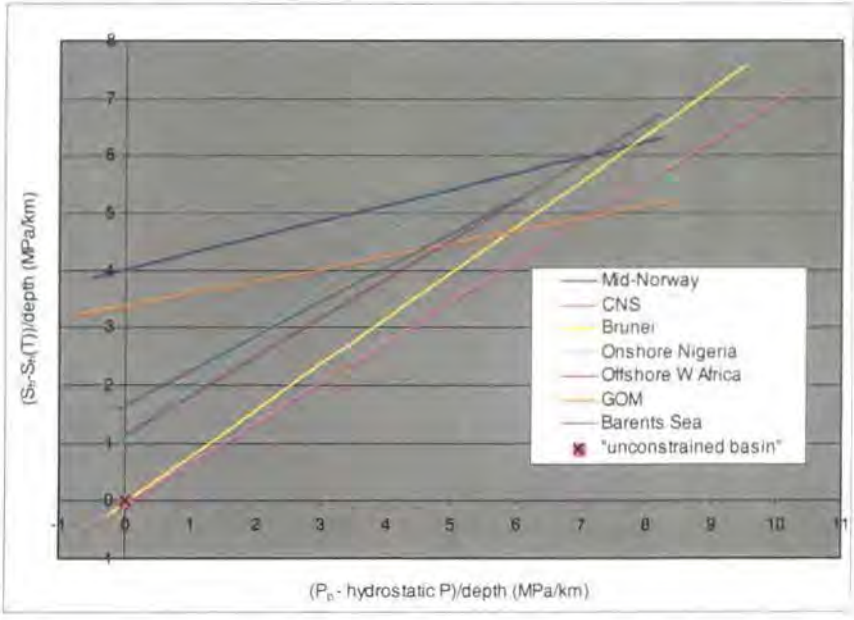

Figure 6.4: Linear regression lines for all data normalised to a hypothetical unconstrained basin and depth for the seven regions.

Y-axis intercepts for the Gulf of Mexico and Mid-Norway are also noticeably higher than the other regions (3½ and 4). The Central North Sea and Brunei lines both intercept the origin while the Barents Sea, Offshore West Africa and Onshore Nigeria intercept between 1 and 1½. **Figure 6.4** shows that lower y-axis intercepts are mainly associated with higher $\Delta S_h/\Delta P_p$ values (gradients). **Table 6.6** summarises the equations of the lines and shows correlation coefficients.

Region	Linear regression line in Figure 6.4	Correlation coefficient (r^2)
Mid-Norway	y = 0.28x + 4.01	0.43
The Central North Sea	y = 0.70x - 0.06	0.49
Brunei	y = 0.80x - 0.03	0.82
The Gulf of Mexico	y = 0.22x + 3.36	0.31
Onshore Nigeria	y = 0.90x + 1.04	0.54
Offshore West Africa	y = 0.68x + 1.14	0.51
The Barents Sea	y = 0.60x + 1.64	0.34

Table 6.6: Summary of the equations of the regression lines for all data.

The regression lines for all the data depth-normalised are summarised in **Figure 6.5**. Clearly more shallow gradients ($\Delta S_h/\Delta P_p$ value of <0.5) are seen for the Gulf of Mexico and Mid-Norway. Onshore Nigeria, Offshore West Africa, the Barents Sea and Brunei show a higher $\Delta S_h/\Delta P_p$ value where S_h increases at nearly 1:1 the rate of P_p increase (**Table 6.7**). Between these end members is the line for the Central North Sea with a gradient of 0.64.

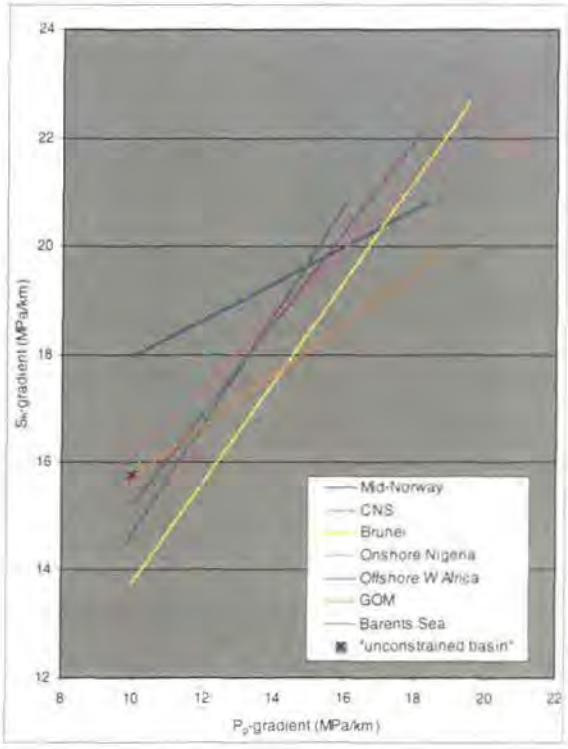

Figure 6.5: Regression lines for all data depth-normalised for the seven regions.

The Mid-Norway line shows S_h to be particularly high in the region (the y-axis intercept is 14.55 in **Table 6.7**) and shows only a small increase with the development of overpressure. Mid-Norway has the lowest $\Delta S_h/\Delta P_p$ value of any region at only 0.34. Brunei has much lower y-axis intercept (4.33) showing lower S_h gradients occur yet the $\Delta S_h/\Delta P_p$ is greater (0.94). **Figure 6.5** also shows lower $\Delta S_h/\Delta P_p$ values are again associated with higher y-axis intercepts. The equations for the lines are summarised below:

Region	Linear regression line in Figure 6.5	Correlation coefficient (r^2)
Mid-Norway	y = 0.34x + 14.55	0.41
The Central North Sea	y = 0.64x + 9.74	0.69
Brunei	y = 0.94x + 4.33	0.78
The Gulf of Mexico	y = 0.48x + 10.89	0.67
Onshore Nigeria	y = 1.01x + 5.70	0.54
Offshore West Africa	y = 0.85x + 6.69	0.53
The Barents Sea	y = 1.02x + 4.45	0.56

Table 6.7: Summary of the equations of the regression lines for all data.

6.2.3.2 Linear relationships for overpressured "*comparable depth*" data

Linear regression lines fitted to just the overpressured S_h and P_p data normalised to a hypothetical unconstrained basin and depth are displayed in **Figure 6.6**. This plot shows gradients (the $\Delta S_h/\Delta P_p$ value) are 0.29 to 0.66, a smaller range than for all the data normalised by the same method (cf. **Table 6.6**). The Central North Sea and Brunei lines have matching gradients (0.52 and 0.54) and similar y-axis intercepts (1.29 and 1.58). The gradient of the Onshore Nigeria line is similar to Offshore West Africa but the intercepts differ. The Gulf of Mexico has a sub-horizontal gradient (0.09) while the Barents Sea has a gradient that is steeper (0.66) than the other regions. Considering the y-axis intercepts, the range is smaller than for all the data (**Figure 6.4**). Intercepts vary between 1.3 and 4.2. Again there is a link between the magnitude of the y-axis intercept and the gradient of the line: higher y-axis intercepts are associated with lower gradients. **Table 6.8** summarises the equations of the lines in **Figure 6.6** and lists the correlation coefficients (r^2 values).

Region	Linear regression line in Figure 6.6	Correlation coefficient (r^2)
Mid-Norway	y = 0.29x + 3.93	0.48
The Central North Sea	y = 0.52x + 1.29	0.57
Brunei	y = 0.54x + 1.58	0.87
The Gulf of Mexico	y = 0.09x + 4.24	0.06
Onshore Nigeria	y = 0.41x + 3.02	0.48
Offshore West Africa	y = 0.38x + 2.48	0.36
The Barents Sea	y = 0.66x + 1.38	0.45

Table 6.8: Summary of the equations of the linear regression lines for the overpressured data (as shown in **Figure 6.6**).

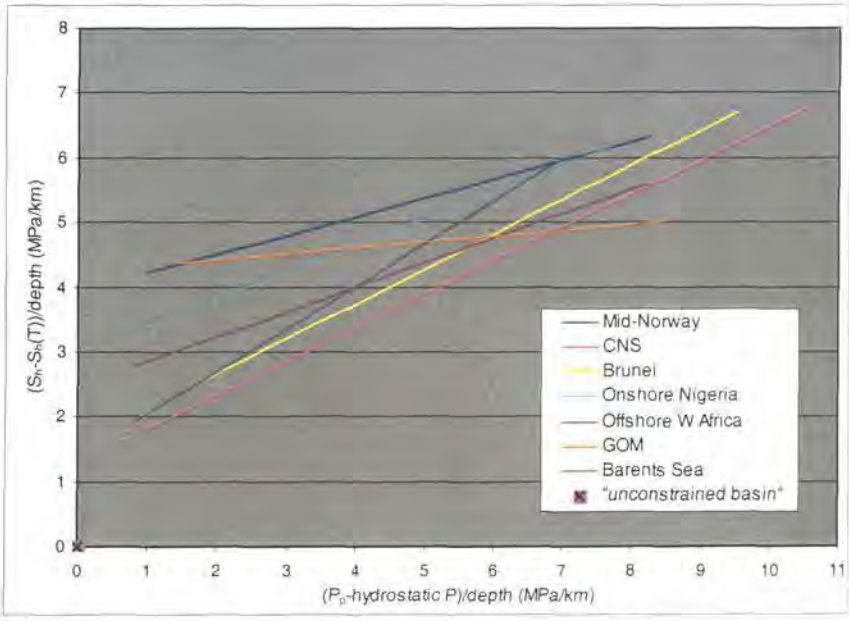

Figure 6.6: Linear regression lines fitted to the overpressured data normalised to a hypothetical unconstrained basin and depth for the seven regions.

The regression lines fitted to the overpressured S_h and P_p data (depth-normalised) are shown in **Figure 6.7**. The Central North Sea and Brunei both have gradients of ~0.55 and Offshore West Africa and Onshore Nigeria are both ~0.45. The Mid-Norway data have a more shallow gradient (hence a lower $\Delta S_h/\Delta P_p$ value) of 0.32 (see **Table 6.9**). The highest $\Delta S_h/\Delta P_p$ comes from the Barents Sea where S_h increases at a rate of 84% of P_p.

Intercepts on the y-axis vary. The lowest intercepts (7 and 8) occur for the Barents Sea and the Gulf of Mexico which have the highest gradients. The highest intercepts occur for Mid-Norway (15) and Onshore Nigeria (13.7). These regions also show the lowest gradients. Hence a relationship between higher gradients and lower y-axis also intercepts appears from **Figure 6.7**. The equations for the lines are summarised below:

Region	Linear regression line in Figure 6.7	Correlation coefficient (r^2)
Mid-Norway	y = 0.32x + 14.97	0.39
The Central North Sea	y = 0.54x + 11.41	0.59
Brunei	y = 0.59x + 10.08	0.87
The Gulf of Mexico	y = 0.64x + 8.03	0.77
Onshore Nigeria	y = 0.44x + 13.70	0.47
Offshore West Africa	y = 0.43x + 12.81	0.39
The Barents Sea	y = 0.84x + 7.06	0.51

Table 6.9: Summary of the equations of the linear regression lines for the overpressured data (as shown in **Figure 6.7**).

6.2.3.3 Observations

Based on the graphs and tables shown above, the following observations can be made concerning the linear regression lines fitted to the data:

- Steeper gradients (greater $\Delta S_h/\Delta P_p$ values) are paired with lower y-axis intercepts.
- More shallow gradients are paired with higher y-axis intercepts (lower gradients indicate the change in S_h with P_p to be smaller).
- Higher y-axis intercepts represent high S_h magnitudes occurring across the region for all pore pressures (especially for normally pressured data).
- A greater range of y-axis intercepts is associated with a greater range of $\Delta S_h/\Delta P_p$ values (cf. **Figures 6.4** and **6.6**).

The significance of these observations is linked to the significance of the relationships that the linear regression lines are describing. The following section shows the implication the correlation coefficients have on the presence of P_p-S_h coupling for each region.

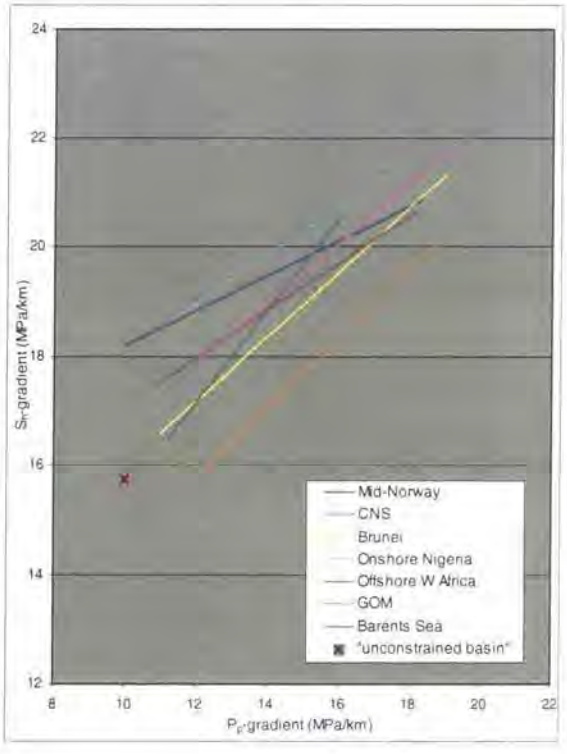

Figure 6.7: Linear regression lines fitted to the overpressured depth-normalised data for the seven regions.

6.2.3.4 Inference of P_p-S_h coupling

Coupling is inferred to be occurring based on the correlation coefficient (r^2 value) for the depth-normalised overpressured data. A correlation coefficient of greater than 0.5 is used as the basis for the inference. Such a value (r-value of 0.71) is felt to be statistically significant. The overpressured data are used, rather than all data, because the presence of overpressure is essential to develop a link between overpressure and stress. Normally pressured data, by definition, have no component of overpressure.

The best approach to test for the presence of coupling is depth-normalising. This approach is considered best because the absolute magnitudes of S_h and P_p are taken as opposed to relating the data to a modelled parameter (the "*hypothetical unconstrained basin*"). While the hypothetical unconstrained basin model is clearly applicable in most instances, results from the Gulf of Mexico show it not to be universally applicable. There are large difference in the $\Delta S_h/\Delta P_p$ values (**section 5.4.5**) and the subsequent r^2 values (see above) between the relationships for the hypothetical unconstrained basin and depth-normalised data and the data when plotted as "gradients". Coupling is not inferred to be occurring for the Barents Sea (despite the r^2 value being >0.5) because the "*comparable depth*" data misrepresent the whole data set. While over 90% of P_p in the region are normally

pressured the "*comparable depth*" data set contains 60% that are overpressured (see **section 5.7.5**). The r^2 values and the inference of coupling are tabulated below.

	All data		**Overpressured data**			
	Normalised to *hyp. uncon. basin* & depth	**Depth-normalised**	**Normalised to *hyp. uncon. basin* & depth**	**Depth-normalised**		
Region	**r^2**	**r^2**	**r^2**	**r^2**	**Coupling inferred?**	**Reason for inference**
Mid-Norway	0.43	0.41	0.48	0.39	**No**	Poor r^2 value
Central North Sea	0.49	0.69	0.57	0.59	**Yes**	Good r^2 value
Brunei	0.82	0.78	0.87	0.87	**Yes**	Good r^2 value
Gulf of Mexico	0.31	0.67	0.06	0.77	**Yes**	Good r^2 value
Onshore Nigeria	0.54	0.54	0.48	0.47	**No**	Poor r^2 value
Offshore West Africa	0.51	0.53	0.36	0.39	**No**	Poor r^2 value
Barents Sea	0.34	0.56	0.45	0.51	**No**	"*Comparable depth*" data misrepresent the region

Table 6.10: Summary of the correlation coefficients and whether coupling is inferred.

Results show that P_p-S_h coupling is inferred for the Central North Sea, Brunei and the Gulf of Mexico.

6.3 Discussions and implications arising from analyses of all regions

In this section the results of all of the case studies are collectively analysed and the following topics are addressed:

- A reason for the lack of effect that lithology has on the magnitude of S_h during pumping pressure tests.
- How the magnitudes of the lower bounds to LOPs relate to the tectonic setting of each region.

- The mechanisms that contribute to the presence of P_p-S_h coupling in some regions.
- The implications the pore pressure profile has on S_h magnitude and how this relates to the range of S_h gradients seen for hydrostatic P_p.
- Suggestions for why coupling may not always occur.

6.3.1 Variability in the magnitude of S_h

The following section discusses a reason for why lithology does not account for the variations in S_h magnitude. It explains that while rock mechanical testing in the laboratory reveals differences between S_h in sandstone and shale, data analyses in **chapters 4** and **5** reveal LOTs do not show equivalent differences.

- **Lithology variations and S_h magnitude**

The lack of relationships between S_h magnitude and lithology for the regions contradicts laboratory determined rock mechanical theory and the observations of previous workers. Breckels and van Eekelen (1982) state that shale displays up to a 5% increased S_h magnitude compared to sandstones in the North Sea. They also quote 400 to 1000 psi (2.8 to 7 MPa) lower S_h values for sandstone compared to shale for Onshore the Netherlands. These S_h data come from normally pressured sandstone and shale at the same depth. Payne *et al.* (2000) measured lateral *in-situ* stresses in sandstones and mudstones from the Upper Cretaceous (depths of 1.3 to 2.2 km) reservoirs of the Piceance Basin, Colorado. They found S_h in sandstone to be up to 10 MPa lower than S_h recorded in mudstones at 2 km depth.

A reason for differences in the magnitude of S_h due to lithology is revealed by laboratory testing of rock samples. Uniaxial testing has produced the following measurements of Poisson's Ratio:

Lithology	Poisson's Ratio
Sandstone	0.05 to 0.25
Limestone	0.17 to 0.31
Shale	0.12 to 0.48
Siltstone	0.15 to 0.30

Table 6.11: Various laboratory determined values for the Poisson's Ratio (from Daines, 1982; Alberty & McLean, 2001).

Testing shows the Poisson's Ratio for sand to be lower than that for shale (Daines, 1982). The results would be that given the assumptions of similar P_p and overburden conditions (see *equations 2.4* and *2.5*), shale will support a greater S_h than sandstone. The consequence would be that formations with a low Poisson's Ratio are at a greater risk of failure under high stress conditions. Because sandstones are unable to support as high stresses as shales, the "*fracture gradient*" would be reduced in sandstones (Alberty & McLean, 2001).

Lower leak-off pressure values are indeed sometimes seen to occur in sandstones relative to shales. The reason relates to the permeability of each lithology. Elevated permeabilities in sandstone can result in "pseudo" LOPs being chosen and recorded. The break from linearity on the LOT graph relates to injection of the fluid component of the drilling mud into the formation rather than the creation of an actual fracture (Grauls pers. comm., 2001).

In the regions studied there is not a difference between LOPs in sands and shales. Smith *et al.* (1987) and Alberty and McLean (2001) have proposed an explanation for why sandstones and shales reveal similar S_h magnitudes. During fracture propagation in a porous, permeable formation such as sand, drilling mud will migrate along the fracture face. As migration occurs, the filtrate of the mud invades the adjacent formation thus dehydrating the mud as it travels along the fracture. Loss of the filtrate results in the mud becoming too viscous to move down the fracture causing blockage that prevents further fracture growth. The existence of this dehydrated mud plug immediately behind the fracture tip has been documented in the DEA-13 experiments on Berea sandstone (Morita *et al.*, 1990). The result of the mud plug is that the near wellbore stress field is raised relative to the initial conditions due to the mud impinging a stress on the fracture walls. Such a process of propping a fracture open and therefore increasing the near wellbore stress field is called "*fracture screen-out*" (Smith *et al.*, 1987). Fracture screen-outs can increase the stress far enough to cause refracturing in a cyclic process (as mud pressure increases due to continuous pumping) with the consequence being that shale adjacent to sand becomes easier to fracture (Moschovides *et al.*, 1993). Fracturing in the shale leads to much larger mud losses as its low permeability will not allow the mud to dehydrate enough to cause screen-out and the fracture continues to propagate. Because fracture screen-out only effects the near wellbore stress, the far field minimum horizontal stress is still lower in the sand than adjacent shale. The effect of screen-out is to increase the near wellbore stress in the sand to such an extent that substantial mud losses do not occur in the sand (Alberty & McLean, 2001). A result of this would be that "*fracture gradients*" in sands appear similar to those in shales despite sand actually supporting lower magnitudes of S_h.

6.3.2 Lower bounds to LOPs and upper limits to P_p

The magnitudes of the lower bounds to all LOPs are shown in **Figure 6.1**. To draw conclusions from this part of the study, all the data from each region are considered rather than the "*comparable depth*" subset. Grauls (1994) shows that vertical stress dominated (passive) regimes are characterised by low magnitudes of the lower bound where as horizontal stress dominated regimes commonly show greater magnitudes of the lower bound. From the literature available and personal communication, the tectonic regime of the location of the data used in this study has been determined.

Passive margin settings are characterised by S_h increasing as a function of depth (Grauls, 1994). The passive margin settings in this study are believed to be the Gulf of Mexico (Breckels & van Eekelen, 1982), Offshore West Africa (Grauls, 1997) and Onshore Nigeria (Grauls, 1997). The Gulf of Mexico data come from the Mississippi Canyon, Green Canyon and Eugene Island regions located in a Tertiary delta setting (Dickinson, 1953; Yassir, 1997). Offshore West Africa is Tertiary basin analogous to the Gulf of Mexico (Grauls, 1994) and the Onshore Nigeria data come from the Niger Delta (Grauls pers. comm., 1999).

The regimes considered to be lateral stress dominated (strike-slip or compressive) are the Central North Sea at depths of 2½ km and greater (Aadnoy *et al.*, 1994), Mid-Norway (Lindholm *et al.*, 1995), the Barents Sea (Fejerskov *et al.*, 1995) and Brunei (Grauls, 1994 & 1997). Tabulated below is the orientation of the dominant stress (relates to tectonic regime) for each region and the magnitude of the lower bound to all LOPs taken at 2½ km depth. The table shows there is not a clear relationship between dominant stress and the lower bound.

	Gulf of Mexico	Onshore Nigeria	Barents Sea	Central North Sea	Offshore West Africa	Brunei	Mid-Norway
Dominant stress	Vertical	Vertical	Lateral	Lateral	Vertical	Lateral	Lateral
Magnitude of lower bound at 2½ km	35.7 MPa	36 MPa	38.2 MPa	40.8 MPa	41.1 MPa	41.8 MPa	42.3 MPa

Table 6.12: The relationship between the magnitude of lower bound to all LOPs and the orientation of the dominant stress at 2½ km depth.

The lower bounds for the Gulf of Mexico, Onshore Nigeria and the Barents Sea plot to the left of the other four lower bounds. The surprising result is the Barents Sea lower bound which plots with the passive margin (S_V dominated) lower bounds and substantially to the left of the lower bound for Mid-Norway despite being influenced by the same stress generating

mechanisms (Fejerskov *et al.*, 1995; Lindholm *et al.*, 1995). The *TotalFinaElf* data from Brunei are located in a lateral stress dominated regime yet it is felt that the high magnitude of lower bound at 2½ km reflects the curvature of the lower bound to higher magnitudes seen at depths where the number of data decrease. At <1½ km depth the Brunei lower bound is comparable to the Barents Sea and Onshore Nigeria lower bounds.

	Gulf of Mexico	Barents Sea	Mid-Norway	Onshore Nigeria	Central North Sea
Dominant stress	Vertical	Lateral	Lateral	Vertical	Lateral
Magnitude of lower bound at 4 km	68 MPa	70.6 MPa	74.7 MPa	75.4 MPa	77.3 MPa

Table 6.13: The relationship between the magnitude of lower bound to all LOPs and the orientation of the dominant stress at 4 km depth.

The result is further complicated by analysing the magnitude at 4 km. Mid-Norway shows a high magnitude of lower bound in the upper 2½ km yet intermediate magnitudes (compared to the other regions) in the deeper sections. Despite being a lateral stress dominated regime it shows 74.7 MPa at 4 km which is less than the passive Niger Delta (Onshore Nigeria) setting. The Barents Sea lower bound is second lowest at these depths despite being lateral stress dominated.

Upper limits to P_p are developed independently of the S_h magnitudes for the regions. Clearly a strong link between the magnitude of P_p and the magnitude of upper limit occurs. Regions with greater amounts of overpressure have upper limits that plot further to the right on **Figure 6.3**.

Considering **Figures 6.1** and **6.3**, regions with the greatest magnitude of lower bound do not show the greatest magnitude of upper limit. For example, the greatest magnitude of lower bound in the upper 2½ km is from Mid-Norway the while the upper limit from Mid-Norway is low relative to the other regions throughout this depth interval. Conversely the lower bound for Brunei plots in the middle of the data set (**Figure 6.1**) while the upper limit has the greatest magnitudes of all the regions. The Gulf of Mexico has the least magnitude of lower bound but some of the highest magnitudes of overpressure.

There is not a correlation between the magnitude of the lower bound (**Figure 6.1**), the magnitude of the upper limit (**Figure 6.3**) and the tectonic regime given the data and information available from these plots. From **Figures 6.1** and **6.3** nothing quantitative can be deduced about P_p-S_h coupling. It is also clear that the figures do not show a worldwide

relationship that links the magnitude of the lower bound magnitude to the magnitude of the upper limit.

The following conclusions can be drawn from the lower bounds to LOPs and the upper limits to P_p:

- In terms of using the lower bound to LOPs and the upper limit to P_p to constrain the magnitude of S_h, it can be said that lower bounds can be used accurately at any depth where as upper limits can be successfully used within the overpressured zone.
- From the data available, there is no link between tectonic regime and lower bound to LOP magnitude: passive regimes do not universally show lower magnitudes of lower bound.
- The relationship between lower bounds to LOPs for each region relative to each other is not consistent through the depth interval. Lower bounds cross at depths >2½ km.
- Higher magnitudes of upper limit to P_p are seen for regions with larger overpressures.
- There is not a systematic relationship between the magnitude of the lower bound to LOPs and the magnitude of the upper limit to P_p.
- Lower bounds to LOPs and upper limits to P_p cannot be used to determine (quantitatively or otherwise) P_p-S_h coupling relationships.

6.3.3 P_p-S_h coupling

From the data analyses presented in this study, coupling is a phenomenon that has been shown to be present in the Central North Sea, Brunei and the Gulf of Mexico. These analyses concentrated on "basin scale" coupling so that in order for coupling to be described as occurring, the relationship between overpressure and S_h has to be statistically significant for all overpressured data within the "*comparable depth*" data set.

Stress-depth plots can show that "*overpressures are generally associated with greater magnitudes of S_h*" but they cannot quantify the relationship. This was the case for Onshore Nigeria, Offshore West Africa, Mid-Norway and in some instances the Barents Sea. The data from Onshore Nigeria plotted on a stress-depth plot (**Figure 5.36**) show there to be a "loose" relationship between the presence of higher overpressures and higher S_h magnitudes (especially at greater depths). However correlation coefficients from **Figures 5.44** and **5.45** show the relationship to be statistically weak therefore basin scale coupling cannot be inferred.

In the following sections, a discussion on the likely mechanisms responsible for the coupling seen in the Central North Sea, Brunei and the Gulf of Mexico is given. Also suggested is an explanation for why there is a range of S_h gradients for hydrostatic P_p on a P_p

gradient versus S_h gradient plot and how the range of gradients relates to the P_p and S_h profiles shown on stress-depth plots. Finally, an explanation for why coupling may not always appear on a regional scale is proposed (**section 6.3.3.3**).

6.3.3.1 The mechanisms that describe P_p-S_h coupling

A change in tectonic regime with depth (as proposed by Grauls, 1997) can be used to explain why horizontal stresses and pore pressures in a basin are higher than expected at depth. Changing the tectonic regime changes the ratio between the vertical and horizontal stresses meaning S_3 evolves from being horizontal in extensional (or passive) and strike-slip regimes to vertical in compressive regimes (cf. **section 2.6.1**). A consequence of the increase in S_3 would be the supporting of greater overpressures before hydraulic fracturing (cf. **section 2.3.3.3**) occurs. **Section 6.3.2** shows that there is no systematic relationship between the magnitude of the lower bound, the magnitude of the upper limit to P_p and the tectonic regime. Also, given the information available in this study, the Central North Sea is the only region showing coupling where data have been used to propose a change in tectonic regime with depth (Aadnoy *et al.*, 1994; Grauls, 1997). It is therefore inferred that a change in tectonic regime with depth probably does not account the presence of coupling in all the data sets.

P_p-S_h coupling can be described in terms of two further schools of thought and it is felt that these best explain the coupling seen. These approaches are poro-elasticity (Engelder & Fischer, 1994) and frictional limits to stress (Zoback & Healy, 1984). Biot (1941) first proposed the variation of S_h as a function of changing P_p by explaining how a lithified, porous rock deforms when pore space is filled with fluid and pressurised. Engelder and Fischer (1994) followed Biot's work by proposing poro-elasticity as the mechanism that contributes to the excess S_h seen in Gaarenstroom *et al.*'s (1993) Central North Sea graben data. The effects of P_p on S_h (see **section 2.2.2.3**) can be modelled using a rigid container open at the top (i.e. the uniaxial strain model applies) containing porous sediment. Initially the sediment is dry and the grains press against the walls of the container (**Figure 2.3a**). Filling the container with water increases the pressure exerted on its walls by the magnitude of the pore pressure where the fluid is in contact with the walls. Where sediment grains touch the wall, the average stress increases by less than the magnitude of P_p because the grains and the contacts take up some of the force exerted by the pore fluid (**Figure 2.3b**). This partial rather than complete transfer of P_p to the walls of the container is known as the poro-elastic effect (Engelder & Fischer, 1994). Solving the elastic theory equations for porous rocks under uniaxial strain produces:

$$S_h = \frac{\nu}{1-\nu}\left(S_V - \alpha P_p\right) + \alpha P_p \qquad \textit{(equation 6.1)}$$

The Biot coefficient (α) is often considered to be unity and assuming the Poisson's Ratio factor can be considered as being k (see *equation 2.5*) then *equation 6.1* resolves to:

$$S_h = k\left(S_V - P_p\right) + P_p \qquad \textit{(equation 6.2)}$$

The above relationship predicts that S_h increases by a proportion of P_p ($\Delta S_h < \Delta P_p$). The poro-elastic effect does not effect the vertical stress because the surface of the Earth acts as a free surface and strain absorbs the P_p increase (Hillis, 2001a).

Engelder and Fischer (1994), when considering Gaarenstroom *et al.*'s (1993) data for the Central North Sea graben, stated the belief that S_h in normally pressured basins is kept within certain bounds of S_V by frictional slip on listric normal faults. Essentially the frictional limits model of Zoback and Healy (1984) restricts the magnitude of the differential stress. The idea is that in actively subsiding basins dominated by normal faulting, S_V increases by sedimentary loading until the differential stress equals the ultimate strength of the rock (see **section 2.3.1**) and frictional slip on normal faults occurs. Slip will act to laterally compress the sediments thereby increasing S_h and decreasing the differential stress (Engelder & Fischer, 1994).

However, Engelder and Fischer (1994) continue by stating that poro-elasticity is more likely to be responsible for the high S_h values in overpressured parts of the same basin. They suggest that perhaps friction sets the background stress at normally pressured, more shallow depths but increases in S_h in overpressured zones are due to poro-elasticity. However, as explained by Zoback *et al.* (1995), the results displayed by Gaarenstroom *et al.*'s (1993) data can also be explained by frictional limits to stress. The frictional limits to stress methodology is explained by *equation 2.12* (Zoback & Healy, 1984). Substituting realistic values for μ into *equation 2.12* can give values for the magnitude of S_h.

Hillis (2001a) states that there is some debate as to whether poro-elasticity or frictional limits type relationships should be separately used to describe P_p-S_h coupling. For example, in a normal fault regime, S_V is the maximum *in-situ* stress, S_1, and S_h is the minimum *in-situ* stress, S_3. Following Jaeger and Cook's (1979) relationship, the frictional limits equation for a normal fault regime (*equation 2.12*) can be simplified and expressed as a function of the coefficient of friction, μ:

$$\frac{S_V - P_p}{S_h - P_p} = f(\mu) = m \qquad \textit{(equation 6.3)}$$

It follows that *equation 6.3* can be solved to show that it is, in effect, the same as the poro-elastic equation (*equation 2.4*) for calculating fracture gradients:

$$S_V - P_p = m(S_h - P_p) \qquad \textit{(equation 6.4)}$$

$$S_h - P_p = \frac{1}{m}(S_V - P_p) \qquad \textit{(equation 6.5)}$$

$$S_h = \frac{1}{m}(S_V - P_p) + P_p \qquad \textit{(equation 6.6)}$$

The differences between *equation 6.6* and *equation 2.4* are expressed by the calibration constants. The similarity can be shown mathematically by considering *equations 2.3*, *2.5*, *2.6* and *6.3* from above. These equations show that:

$$k = \frac{S_h - P_p}{S_V - P_p} = \frac{\nu}{1-\nu} = \frac{1}{\left(\sqrt{(\mu^2+1)} + \mu\right)^2} = \frac{1}{m} \qquad \textit{(equation 6.7)}$$

Confirmation of the link between the frictional limits equation and the poro-elasticity equation is given by **Figure 6.8** (from Hillis, 2001a). The example shows calculated magnitudes of minimum stress for a step-wise increase in P_p using *equation 2.4* for poro-elasticity and *equation 2.12* for frictional limits. Using realistic values for μ and ν, two situations have been plotted to show that each equation gives the same result. These situations are a strong/stiff rock (μ = 0.9 and ν = 0.17) and a weak rock (μ = 0.6 and ν = 0.24).

In describing coupling, the key issue should really be the accurate constraint of the calibration constants in the poro-elastic and frictional limits models. How well these calibration constants (i.e. m and k) relate to their respective physical properties (i.e. the coefficient of friction, μ, and Poisson's Ratio, ν) depends on how well the assumptions made in the models are satisfied by the basin being tested. It is unlikely that in geology these assumptions are fully met and that sedimentary basins are in a state of stress, and behave in a way, that matches the conditions applied to a laboratory sample. For example, many basins are unlikely to fully comply with the conditions required for the frictional limits equation to produce

accurate results. It may be that the differential stress in a basin is below the magnitude of the ultimate strength of the rocks meaning the Mohr circle will not touch the envelope of shear failure described by the μ value used. Where this situation occurs, values of S_3 calculated will be incorrect.

It can therefore be stated that using laboratory derived values for μ and ν should be treated with caution (Hillis, 2001a) when deriving relationships for basin scale data. Since both frictional limits to stress and poro-elasticity can be used to generate the same results it is felt that accurate constraints on the calibration constants at the basin scale is of greater importance than which model "correctly shows the coupling mechanism".

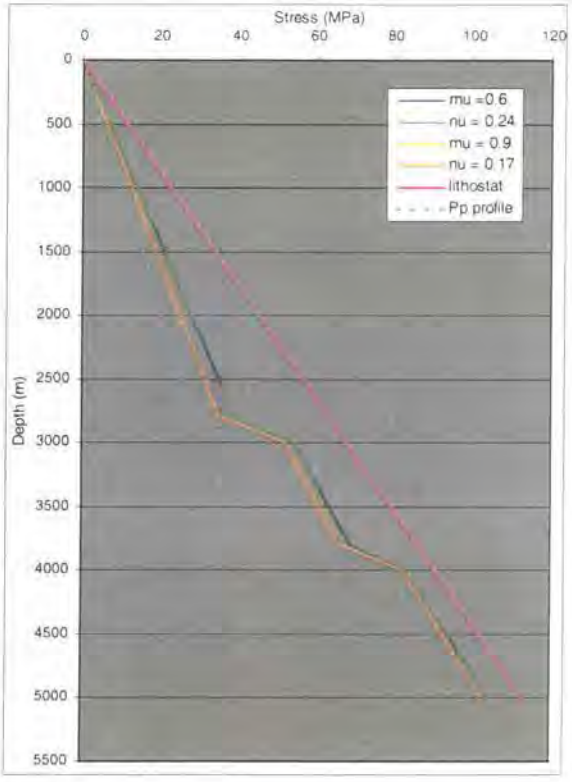

Figure 6.8: The similarity between the *poro-elastic* and *frictional limits to stress* equations when using realistic values of *nu* (ν) and *mu* (μ).

Using the poro-elastic (*equation 2.4*) and frictional limits to stress (*equation 2.12*) equations and S_v, S_h and P_p data from Mid-Norway, it has been possible to back-calculate values of the Poisson's Ratio, ν, and the coefficient of friction, μ. The aim was to test whether experimentally derived values of μ and ν match those calculated using actual basin scale data. The results are shown in **section 6.4.3**. Also described in **section 6.4.3** is the relationship between the level of compaction of the sediments in Mid-Norway and the lack of a presence of coupling.

6.3.3.2 Explaining the range of S_h gradients for a hydrostatic P_p gradient

When normalising the data for analyses into coupling, a range of S_h gradients is observed for a hydrostatic P_p gradient (10 MPa/km). Large ranges are seen for the Offshore West Africa and Mid-Norway regions. The normally pressured data mainly occur in the shallow depth sections above the development of overpressure. As the analyses in **chapters 4** and **5** show, different rock mechanical and pumping pressure test parameters (see **Table 6.2**) cannot fully explain the variability in S_h magnitude throughout these shallow depths. Given below is an interpretation of how the range of S_h gradients at hydrostatic P_p on P_p gradient versus S_h gradient plots could relate to different P_p and S_h profiles.

Figure 6.9a shows a schematic stress-depth plot showing an overpressure transition zone and the profile of S_h data typically associated with the P_p profile. An example of this type of P_p profile occurs in the Central North Sea (**Figure 5.1**) or the Scotian Shelf (**Figure 2.22**). Shown in **Figure 6.9b** is the range of S_h gradients expected for the normally pressured data. The range of S_h gradients for the normally pressured profile can be explained by an increase in S_h magnitude relative to S_V immediately above the transition zone. This relationship pairs a range of S_h gradients with the still normally pressured P_p data. The magnitude of the transition zone is also considered to effect the size of the range of S_h gradients (cf. blue and yellow P_p profiles). Where P_p data develop larger overpressures, i.e. the Central North Sea, a greater range in S_h gradient is seen for the normally pressured data above the transition zone.

A different situation occurs in **Figure 6.10a**. Here the P_p profile changes from a hydrostatic profile to a sub-lithostat parallel profile. This is the case for some wells from the Gulf of Mexico (cf. **Figure 2.24**). Because no transition zone exists (with a sudden change to very high P_p gradients) there is no large range of S_h gradients associated with the P_p data above the onset of overpressure. This manifests in the smaller spread in S_h gradients for hydrostatic P_p gradients **Figure 6.10b**.

The theory described above does not explain why the S_h data "respond" to the onset of overpressure before it is seen to occur. The range of S_h data between 1.2 and 1.5 km in **Figure 6.9** is not a result of pore pressure *in-situ* stress coupling as the pore pressures through these depths are hydrostatic. Investigations in this study based on the data available do not provide answers for why the S_h increase occurs and it is beyond the scope of this work to seek possible rock mechanical explanations.

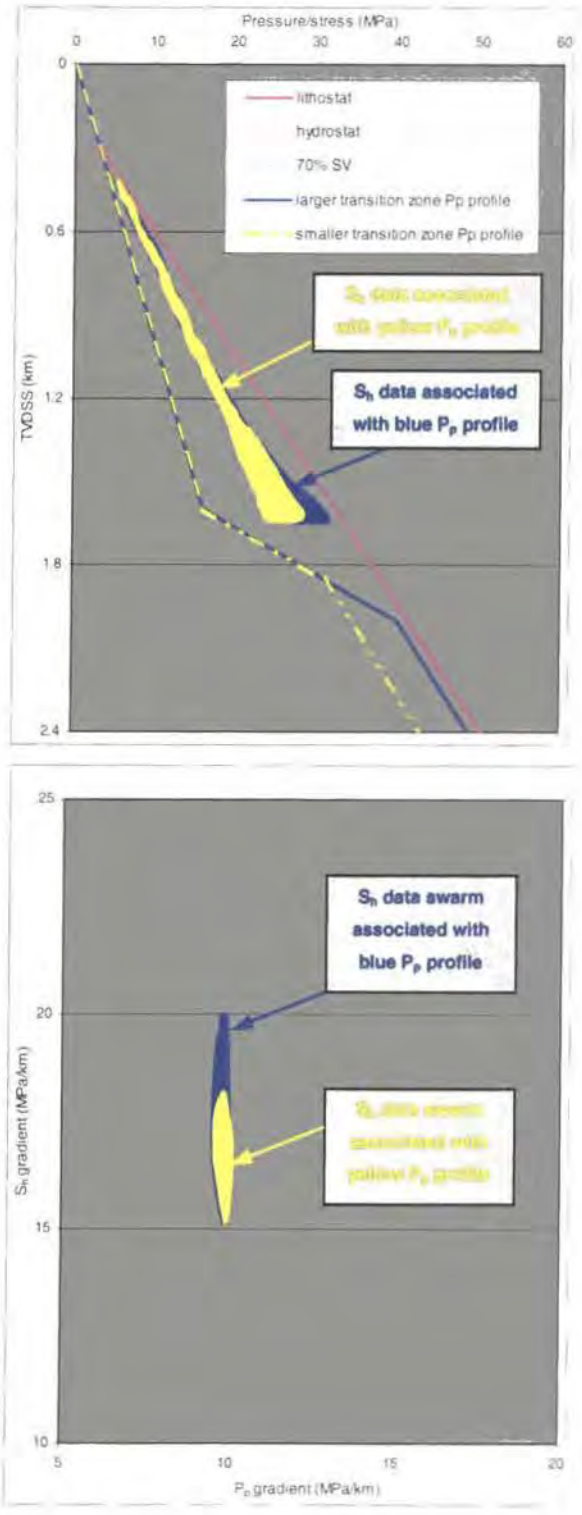

Figure 6.9: (a) Schematic diagram showing P_p profiles for larger and smaller overpressure transition zones and the associated S_h data swarms. **(b)** P_p gradient versus S_h gradient for the hydrostatic data in each P_p profile.

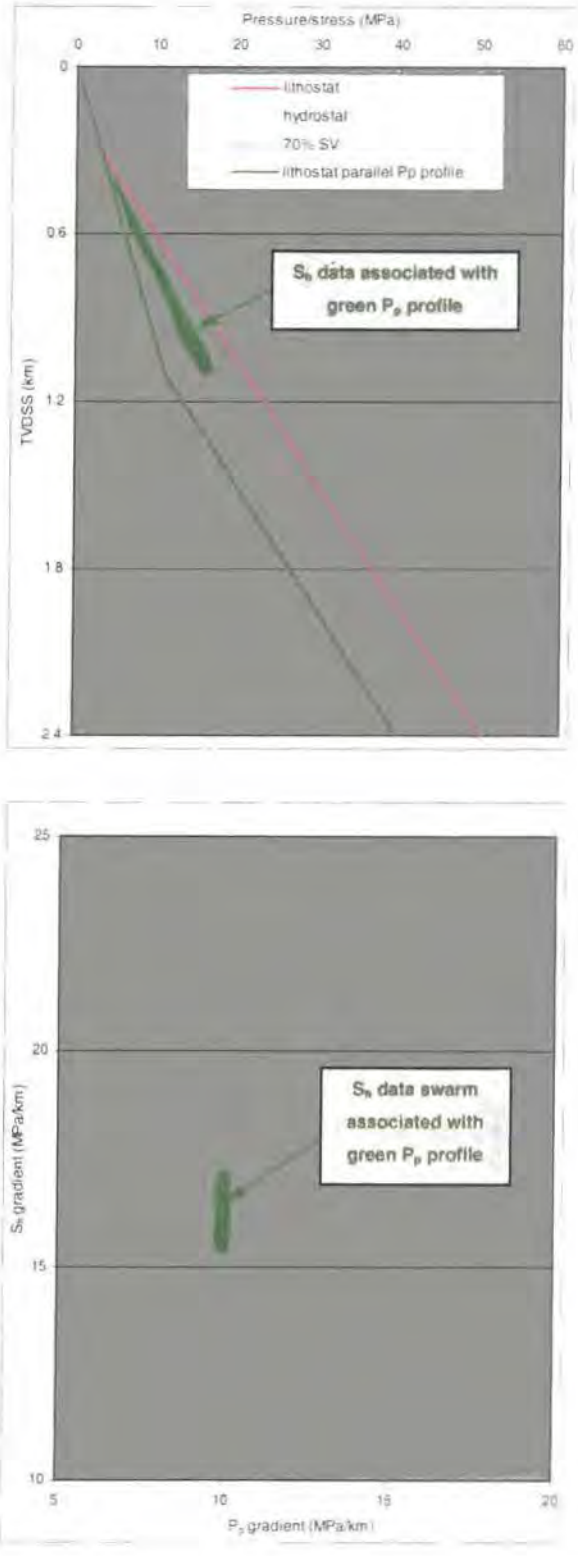

Figure 6.10: (a) Schematic diagram showing a P_p profile (without a transition zone) and the associated S_h swarm. P_p increase instantaneously from hydrostatic to a profile that is lithostat parallel. **(b)** P_p gradient versus S_h gradient for the hydrostat data in the upper 1 km.

6.3.3.3 Why coupling may not always appear

Coupling is inferred not to be present in Mid-Norway (see later discussions), Onshore Nigeria, Offshore West Africa and the Barents Sea based on the correlation coefficient for the overpressured data plotted as "gradients" (see **section 6.2.3**). This section suggests reasons why regional coupling may be obscured by scatter in the data on a P_p gradient versus S_h gradient plot.

A multiple well plot encompassing data from an entire region will have LOTs conducted in a range of rock types and at a succession of depths. Throughout the basin, it is also likely that P_p will vary both laterally and with depth (i.e. the pressure cells seen across the Central North Sea graben – Holm, 1998). This is the case in Mid-Norway for east and west of the Smørbukk Fault (**section 3.6.1**; Hermanrud *et al.*, 1998a). Different lithologies occur at different depths across the basin and these lithologies will have varying rheologies. Different rheologies will mean that the S_h response to P_p will also differ (Santarelli *et al.*, 1998; Engelder pers. comm., 1999). For example, Santarelli *et al.* (1998) propose that better (normally) compacted rocks adopt a more plastic rheology which has been shown to respond differently to overpressure than an elastic rheology (see further discussions in **section 6.4.3**).

The action of faults can effect the stresses independently of the pore pressures. Faults in the Central North Sea produce deviations in the magnitude of S_H (Mueller *et al.*, 2000) and modelling by Lewis *et al.* (2000) shows that the magnitude of S_h increases at the tip of a fault. The increase in magnitude is dependent on the amount of throw (Couples pers. comm., 2000). Even without taking into account the effects faults have on stress, they will still effect coupling relationships. The juxtaposing of different lithologies and rheologies next to each other at the same depth means overpressure at a given depth could produce different amounts of "excessive" stress in one tectonic block to an adjacent block.

The effects of P_p and rheological differences across the basin would be a range of P_p gradients for a given S_h gradient and vice versa. Laboratory testing shows that different lithologies have different Poisson's Ratios and will respond differently to P_p as revealed by varying $\Delta S_h/\Delta P_p$ values (Daines, 1982; Hillis pers. comm., 2001). Combining different $\Delta S_h/\Delta P_p$ profiles from a range of wells together on P_p gradient versus S_h gradient plot would likely produce a weak relationship for coupling for the *whole basin* resulting in a low r^2 value (representing the amount of scatter) for the data.

Ideally data would be analysed on a well-by-well basis to remove the effects of different P_p and rheological effects at the same depth brought about by combining data from a variety of spatial locations. This approach would generate $\Delta S_h/\Delta P_p$ values for individual wells. Plotting data from separate wells with known $\Delta S_h/\Delta P_p$ values on a multiple well plot would reveal how combining the data masks the coupling relationships possibly shown by the individual wells. Unfortunately insufficient data was available for this study to test the

hypothesis (especially since the "*comparable depth*" subset for each region was used for analyses which was, in most cases, a small subset of the entire data set). This type of investigation would make an interesting subject for future work in the field of pore pressures and their effect on *in-situ* stress.

6.4 Discussions and implications arising from Mid-Norway

Mid-Norway is the main case study area so it is felt that the discussions from this region and the implications that arise warrant a separate section. This section focuses on the following:

- The implications that the quality control procedure had on the scatter in S_h magnitude and what the scatter could really mean.
- The magnitude of the lower bound to all LOPs and the suggestion it makes about the stress situation.
- An explanation for the relationship between P_p and S_h seen when analysing for coupling.
- Use of the equations for poro-elasticity and frictional limits to stress to back-calculate values for μ and ν for basin scale data and a comparison between these values and laboratory derived ones.
- The implication that the amount of compaction has on coupling.
- The results of the investigation into the use of LOPs and ISIPs to calculate S_h and the insights into the magnitude of S_H provided by the Kirsch equations.
- The implication the magnitudes of the principal stresses has for the contemporary stress situation.

6.4.1 Quality controlling the data and S_h variability

Despite the quality control on the S_h data described in **section 3.7.2** there is still variability in S_h magnitude seen in Mid-Norway of up to 13 MPa at 3¾ km (as shown in **section 4.2**). The stringent quality control did not remove the scatter. Plotting the S_h data by a number of rock mechanical and pumping pressure test parameters (see **Table 6.2**) also cannot explain the variability.

Analysing the *Statoil* XLOT data (**Figure 4.28**) reveals there to be a +/- 2.5 MPa difference between the magnitude of LOP and ISIP in the first cycles (wellbore failure cycles) of extended leak-off tests. The majority of data used in the Mid-Norway case study originate from single cycle leak-off tests where fractures are inferred to be produced (analogous to first cycles). The analyses of XLOT data show that a consequence of using LOPs to calculate S_h is that the 5 MPa variability will be transferred into the S_h value. The 5 MPa variability occurs regardless of the depth of the LOT and can fully explain the variability shown in **Figure 4.1** in the upper 2 km and 50% or more of the variability from greater depths. **Figure 4.28** shows the difference between LOP and ISIP (analogous to S_h) reduces during later XLOT cycles. Therefore it is inferred that using LOPs from later cycles will reduce the variability in S_h. Unfortunately, as **section 4.6** shows, 3rd and 4th cycles are not commonly performed. XLOTs were not available for regions in this study other than Mid-Norway.

The variability in the magnitude of S_h is a presence that quality testing has showed cannot be removed. This suggests there to be two possibilities for the scatter seen at a given depth. Firstly, there is the chance that the scatter is a real feature and reflects the presence of heterogeneities in the structural style of a basin across a region. Examples of these heterogeneities are the faults and tectonic blocks shown in **Figure 3.3** from Mid-Norway. Heterogeneities in the basin structure will inevitably produce variations in stress magnitudes. Therefore a "basin scale" data set would be expected to contain differences in the S_h magnitude at a given depth.

Alternatively, the scatter in S_h could be explained by different rock mechanical properties (lithology, rheology etc.) and pumping pressure testing parameters (pump rate, wellbore diameter etc.) acting either in concordance or in opposition to each other. If several of these properties act together to reduce or increase the magnitude of the LOP, hence S_h, then plotting the data by individual parameters (as done in **chapters 4** and **5**) will not unravel or explain the true causes of the scatter.

6.4.2 The lower bound to LOPs and the contemporary stress situation

The lower bound to LOPs for *all* of the data is described in this section. This lower bound most closely represents the regional minimum stress as it was constrained from all the quality-controlled data. The magnitude of the lower bound with depth is greater than would be expected for a passive margin regime (Grauls, 1997). In the upper 1 km it is >80% of the lithostat and up to 90% at the base of the section. The consistently high magnitude of the lower bound implies the contemporary stress situation is more likely to be lateral stress dominated. Grauls (1997) states that the ratio between S_h and S_V within a "strike-slip" regime

is expected to be between 0.85 to 1.0. **Figure 4.15** shows the magnitude of the lower bound to all LOPs is greater than 80% S_V at all depths and between 85% and 90% S_V below 2 km.

A number of authors (Lindholm *et al.*, 1995; Fejerskov *et al.*, 1995) have used a collection of data from different depths (see **section 3.5**) to characterise the stress regime and have invoked a "strike-slip" setting. The *Statoil* XLOT data have been used in **section 6.4.4** to provide a quantification of S_H. Knowledge of the magnitude of S_H completes a quantification of the magnitudes of all three principal stresses. These data provide conclusive insights into the contemporary stress situation for Mid-Norway using different data to previous authors.

6.4.3 Coupling in Mid-Norway

This section addresses the inferred lack of a presence of coupling in Mid-Norway. Firstly, an explanation (**section 6.4.3.1**) is suggested for why the $\Delta S_h/\Delta P_p$ value for the region is so low. Following on from this explanation, in **section 6.4.3.2**, the equations for poro-elasticity (*equation 2.4*) and frictional limits to stress (*equation 2.12*) are used to back-calculate ν and μ. These calculated values are then compared with laboratory determined values for the calibration constants.

6.4.3.1 An explanation for the low $\Delta S_h/\Delta P_p$ value

Section 4.5 explains the relationship between P_p and S_h for a normally pressured passive margin setting where coupling is not occurring. In this passive margin setting, if overpressures do occur any horizontal stress components created by them are laterally dissipated. Mid-Norway does not display this relationship. Also shown by the analyses in **section 4.5** is the lack of coupling in Mid-Norway. The correlation coefficient for the overpressured data plotted as gradients (the best data to use for coupling analyses) is 0.39 while the $\Delta S_h/\Delta P_p$ value is 0.32.

One explanation for the lack of a coupling relationship in Mid-Norway is the late timing of overpressure development and the repercussions the timing has on rock mechanical properties. It is accepted that disequilibrium compaction can lead to overpressuring and this is believed to be the cause of most of the overpressures in the Central North Sea (Swarbrick *et al.*, 2000). The results of the analyses in **chapter 5** and the results of other authors (Engelder & Fischer, 1994; Hillis, 2000) show coupling to occur in the Central North Sea.

The timing and development of overpressure in Mid-Norway is discussed in **section 3.6**. Many authors (Skar *et al.*, 1998; Hermanrud *et al.*, 1998a & 1998b; Teige *et al.*, 1999)

use porosity measurements to draw inferences about the timing of overpressure. The porosities in Mid-Norway are similar to those associated with normally compacted rocks (Hermanrud *et al.*, 1998b). This implies they have arisen from high effective stress magnitudes. However, as the data in **Figures 4.5** and **4.13** show, effective stresses are presently low in the highly overpressured zones. A combination of low effective stresses and normally compacted rocks has been used to attribute the overpressure development in Mid-Norway to late stage "inflationary mechanisms" rather than a "mechanical process" (i.e. disequilibrium compaction) which occurs synchronous with deposition (Osborne & Swarbrick, 1997). The late stage development is thought to influence the lack of coupling in Mid-Norway for the reasons given below.

Teufel *et al.* (1991) and Santarelli *et al.* (1998) show that during reservoir (P_p) depletion rock compaction occurs and the porosity decreases. Field scale data from the Ekofisk field (Teufel *et al.*, 1991) also show that there is a decrease in the horizontal stresses. Santarelli *et al.* (1998) quote an example from a *Saga Petroleum* operated well in the Norwegian North Sea where injector wells were used to repressurise a previously depleted reservoir. They note that the reservoir stress path did not follow the same course during repressurisation as during depletion. Instead the repressurisation path was much flatter with very little stress increase compared to the P_p increase. Repressurisation showed a low $\Delta S_h/\Delta P_p$ value. Another example quoted by Santarelli *et al.* (1998) is the pumping of water back into the bedrock under Venice as a way of combating sinking. This repressurisation did not produce rebound but instead maintained the previous land surface level. The stress path shown by depletion and repressurisation is shown schematically in **Figure 6.11**.

Both observations suggest that "inflationary mechanism" generated overpressures do not produce the same stress response as overpressure due to "mechanical processes". A proposal by Santarelli *et al.* (1998) is that the irreversibility of the stress path (the inability to get the stresses back up to pre-depletion levels by injection of fluids) can be explained by rock behaviour following porosity loss during compaction.

Prior to depletion of the P_p in the reservoir, the rocks maintained a high porosity. The pressure depletion phase shows a linear decrease in stress magnitude that can be described as plastic behaviour by the rocks. Upon reloading (repressurisation), if there was no change in the stress magnitude with an increase in P_p then the reservoir rocks could be said to behave as a rigid plastic material that does not deform. However, there is a slight increase in stress with repressurisation that can be attributed to an elastic response of the rock to increasing P_p. Therefore the rocks can be said to have an elasto-plastic rheology where only a slight increase in stress is seen for an increase in P_p.

This rheological condition could explain why the $\Delta S_h/\Delta P_p$ value is low in Mid-Norway. Because the rocks were able to normally compact during burial (Teige *et al.*, 1999) and the porosity was reduced, when overpressuring occurred (assuming it was inflationary) the

development was akin to a repressurisation process. Santarelli *et al.*'s (1998) argument suggests that inflationary overpressures developing in compacted rocks only lead to slight increases in stress. The increase in stress can be attributed to the elastic component of their adopted elasto-plastic rheology following normal compaction. The plastic component of this rheology means the rock is incompressible and does not deform.

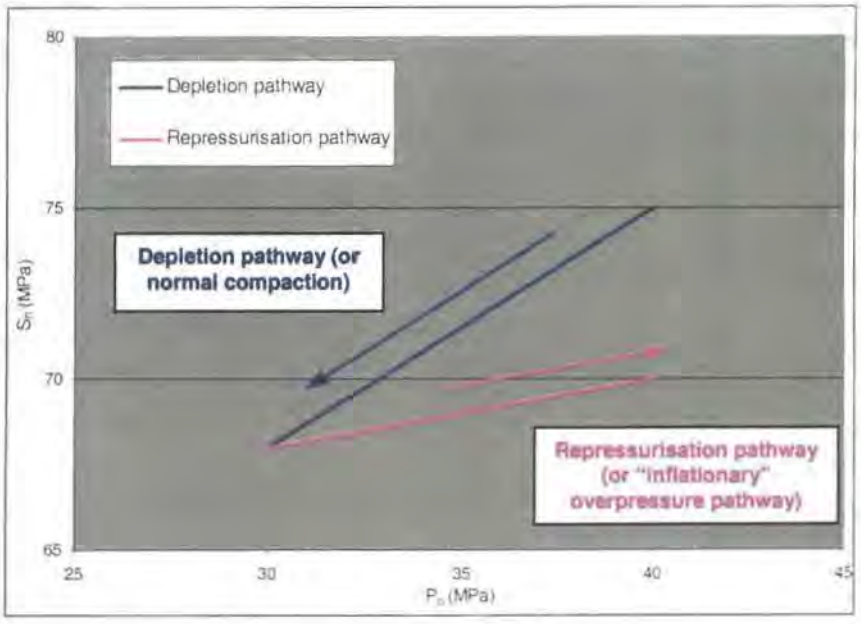

Figure 6.11: Schematic diagram showing the depletion pathway (compaction of the rock) and subsequent repressurisation pathway (akin to "inflationary" overpressure).

It is therefore possible that the burial history and amount of compaction, and overpressure generating mechanisms and history are the cause of the lack of coupling and the low $\Delta S_h/\Delta P_p$ value observed for Mid-Norway. Analyses in **section 4.3.6.2** show that the rocks west and east of the Smørbukk Fault have up to 30 MPa of P_p differences yet the dramatic overpressures in the west are not manifested in the S_h magnitudes. S_h paired with these high overpressures are <5 MPa greater than those paired with normal P_p in the east.

6.4.3.2 Calculating ν and μ

Using the equations for poro-elasticity (*equation 2.4*) and frictional limits to stress (*equation 2.12*) and the large number of S_V, S_h and P_p data from the Mid-Norway study it has been possible to back-calculate the magnitudes of the Poisson's Ratio, ν, and the coefficient of friction, μ. The results have important implications for the link between the level of compaction of the sediments in Mid-Norway and P_p-S_h coupling. Results can also be used to test the applicability of using measured pore pressures and lithostatic stresses combined with

laboratory determined values and ν and μ to calculate S_h. The results of calculating ν and μ are shown below in **Figures 6.12** and **6.13** respectively.

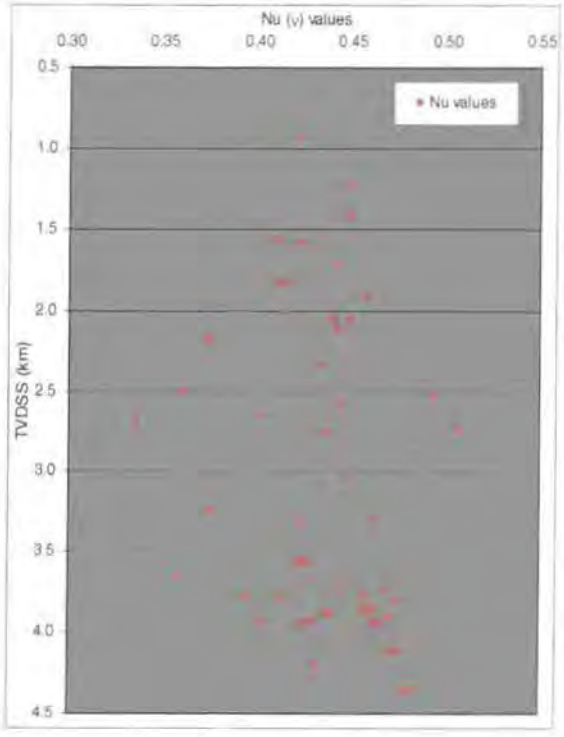

Figure 6.12: Nu (ν) values back-calculated using the poro-elastic equation for fracture gradient prediction (*equation 2.4*) and the Mid-Norway data.

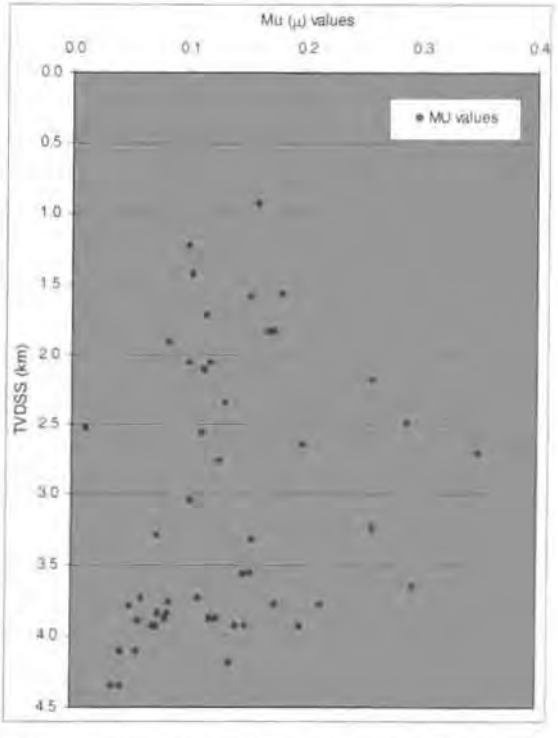

Figure 6.13: Mu (μ) values back-calculated using the frictional limits to stress equation (*equation 2.12*) and the Mid-Norway data.

Firstly, considering **Figure 6.12**, it can be stated that the values back-calculated for the Poisson's Ratio are higher than those listed in **Table 6.11** (Daines, 1982; Alberty & McLean, 2001) determined through laboratory experimentation. Since the Poisson's Ratio is a measure of horizontal expansion/vertical contraction (see *equation 2.2*) it would be expected that a more highly compacted rock would have a higher Poisson's Ratio. The reason being that vertical compression applied to a poorly compacted rock would lead to collapse of pore spaces with little horizontal expansion. Essentially compression would lead to a reduction in volume. Conversely, a well-compacted rock would suffer less dilation upon vertical compression but instead would horizontally expand.

The values for the coefficient of friction (μ) back-calculated using *equation 2.12* are shown in **Figure 6.13**. It is clear that the values for μ are low. All bar one of the values are below 0.3 where as values of μ for most rock types fall between 0.6 and 1.0 (Byerlee, 1978; Zoback & Healy, 1984). It is therefore probable that these values are unrealistic and an explanation for why the values are unrealistic comes from one of the assumptions made by the frictional limits equation. The frictional limits model assumes that S_3 can be accurately calculated when the differential stress is equal to the ultimate strength of the rock (i.e. when the Mohr circle touches the envelope of shear failure – see **section 2.3.1** and **Figure 6.14**). However there is no evidence to suggest that active faulting is currently occurring in Mid-Norway (Blystad *et al.*, 1995) so the differential stress seen is *not* equal the ultimate strength of the rocks in the region. For a fixed value of the lithostat (S_1 in **Figure 6.14**), using a differential stress than is smaller than the ultimate strength to calculate S_3 means that the frictional limits equation has to "compensate". It does so by using an unrealistically shallow gradient for the envelope of shear failure (see **Figure 6.14**) to invoke the required state of "dynamic equilibrium". In this case, the state of "dynamic equilibrium" means that shear failure, or slippage, will occur on "favourably orientated" fault planes (see **section 2.2.2.2**).

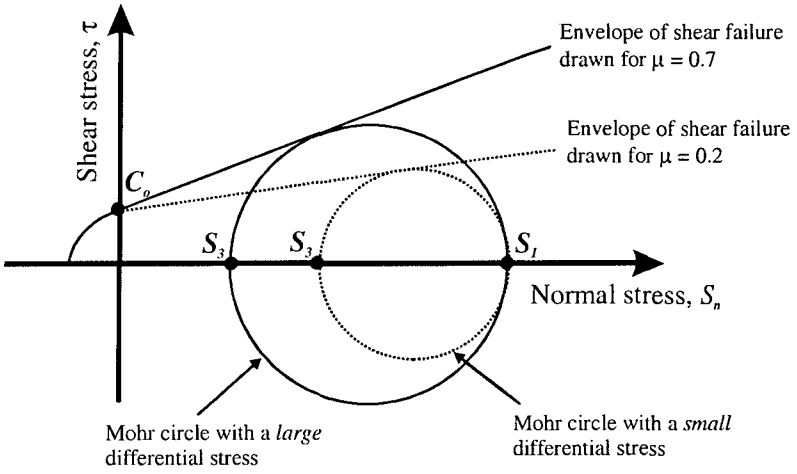

Figure 6.14: The relationship between the gradient of the envelope of shear failure and the magnitude of the differential stress (for a fixed magnitude of S_V or S_1).

6.4.3.3 Concluding remarks

Wireline log data have been used to show that the sediments in the Mid-Norway region are normally compacted (Hermanrud *et al.*, 1998a and 1998b). Normally compacted sediments are seen because dewatering has occurred during loading from above. The presence of the normally compacted sediments is used to infer that the overpressure seen in Mid-Norway occurred due to "inflationary mechanisms". A suggestion is made that normally compacted rocks overpressured by inflationary mechanisms due not show a strong coupling response – the $\Delta S_h/\Delta P_p$ value is low. The reason proposed is that normally compacted rocks adopt an elasto-plastic rheology meaning that with a subsequent increase in P_p they do not show much deformation (the magnitude of the horizontal stresses increases by only a small amount). The only increase in stress seen occurs as a consequence of the elastic component of the elasto-plastic rheology. It therefore appears that there is a strong link between the low $\Delta S_h/\Delta P_p$ value, the high level of compaction of the sediments and the late stage "inflationary" overpressure generating mechanism in Mid-Norway.

Using the poro-elastic equation for fracture gradient prediction and the Mid-Norway data, the Poisson's Ratios of the rocks in the region have been back-calculated. Poisson's Ratios have been found to be high. These values are consistent with well-compacted sediments. Using the same Mid-Norway data and the frictional limits to stress equation has shown that the values for the coefficient of friction back-calculated are unrealistically low. The reason is felt to be that the stress situation is such that the differential stress is less than the ultimate strength of the rocks. Essentially, active faulting is not occurring therefore using realistic values of μ and the frictional limits equation will lead to under-estimates of S_3 in Mid-Norway.

6.4.4 Using XLOT data to calculate S_H

The evidence displayed in **Figures 4.27** to **4.31** indicates that LOP and ISIP are almost identical in Mid-Norway. **Figure 4.28** shows the difference between LOP and ISIP is +/- 2.5 MPa. Because the majority of the magnitude of S_h comes from the static pressure of the mud column, the difference between the LOP and ISIP becomes proportionally smaller when calculating the total magnitude of S_h (**Figure 4.30** and **4.31**). The large influence of the static mud column suggests that for tests from greater depths an even larger percentage of the S_h estimation comes from the static mud column pressure. Therefore, the conclusion that adding either LOP or ISIP to the pressure exerted by the static mud column to create an estimate for S_h produces the same result, becomes more appropriate at greater depths.

For re-opening cycles of XLOTs, the LOP and ISIP values converge closer towards a 1:1 ratio (**Figure 4.28**). In re-opening cycles of XLOTs the LOP equals the fracture re-opening pressure (P_r). This has implications for the magnitude of S_H. By considering XLOT re-opening cycles (no tensile strength component), Bredehoeft *et al.* (1976) suggest that the magnitude of S_H may be determined from the Kirsch equation:

$$P_r = 3S_h - S_H - P_p \qquad \textit{(equation 6.8)}$$

If, as the results presented in **section 4.6** suggest, it can be assumed that for XLOT re-opening cycles LOP ≈ ISIP then because ISIP = S_h substituting $P_r = S_h$ into *equation 6.8* gives:

$$S_H = 2S_h - P_p \qquad \textit{(equation 6.9)}$$

Therefore using *equation 6.9* and the XLOT re-opening cycle data where LOP *equals* the ISIP, information on the magnitude of S_H in Mid-Norway can be deduced.

To test the validity of the assumptions that led to the creation of *equation 6.9*, LOPs and ISIPs were compiled from XLOT re-opening cycles. S_H has been calculated using both *equation 6.8* and *6.9*. Because "*comparable depth*" P_p data were not available for these XLOTs, mud weights had to be used as a proxy (Hillis pers. comm., 2001). S_H has been normalised to the lithostat (from well 6506/12-1 – see **section 3.8**) to provide insights into the tectonic regime of Mid-Norway.

- **Results**

The calculations of S_H using both *equation 6.8* and *equation 6.9* are shown in **Figure 6.15**. Also shown are the S_h magnitudes calculated using ISIP values. From **Figure 6.15** it can be seen that S_H is up to 13 MPa greater than S_h. In 9-out-of-12 instances the magnitude S_H is equal to or up to 7 MPa in excess of the lithostat. Results in **Figure 6.15** show that the difference between S_H calculated from *equation 6.8* and *equation 6.9* is <2 MPa.

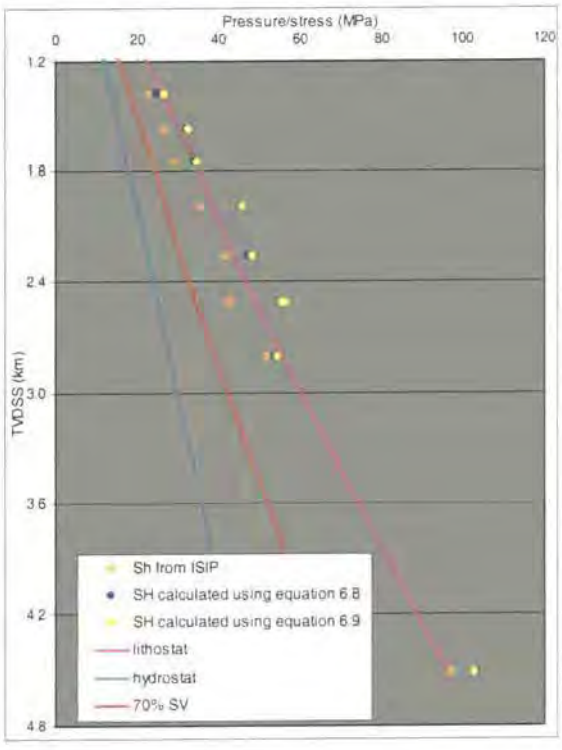

Figure 6.15: S_h and S_H calculated using *equations 6.8* and *6.9* for XLOTs from Mid-Norway.

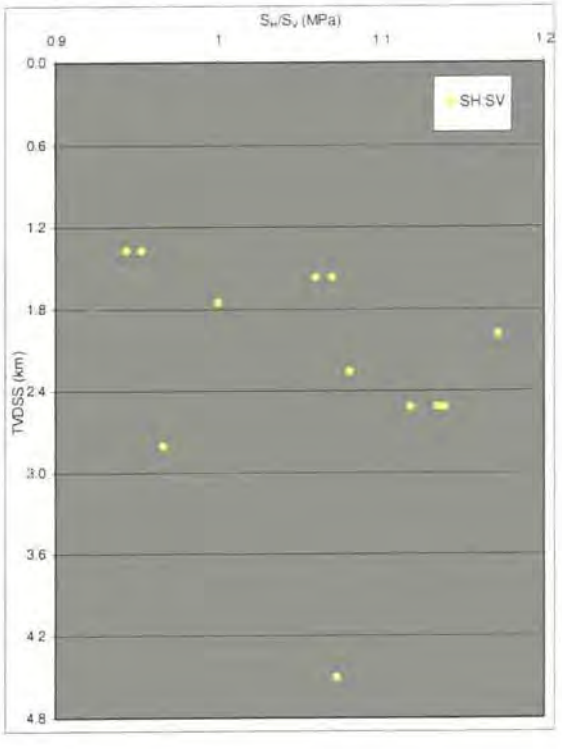

Figure 6.16: S_H calculated using *equation 6.8* normalised to S_V.

- **Implications**

A strong implication from the results shown by **Figure 6.15** is that S_H can be calculated using either *equation 6.8* or *6.9*. It can also be stated that accurate calculations of S_H can be made for Mid-Norway when only the LOP is known (assuming LOP comes from XLOT re-opening cycles).

The S_H:S_V ratio is plotted in **Figure 6.16**. Ratios of greater than 1.0 show that in Mid-Norway S_H is the maximum principal stress while S_V is the intermediate stress. These results, based on these data, show that the structural regime in Mid-Norway is "strike-slip" because S_h is the minimum principal stress. These results agree with Lindholm *et al.* (1995), Fejerskov *et al.* (1995) and Van Balen and Skar (2000) who used earthquake focal mechanisms and borehole breakout data to deduce that the contemporary stress situation is "strike-slip".

- **Concluding remarks**

From the analyses in **section 4.6** and the interpretations and discussions above the following conclusions can be drawn concerning Mid-Norway:

- XLOTs can be used to show that the fracture re-opening pressure (P_r) is equal to the minimum *in-situ* stress: $P_r = S_h = LOP$.
- Applying the Kirsch equations shows that S_H can be calculated when only the LOP and P_p are known (assuming XLOT re-opening cycles).
- S_H is shown to be the maximum principal stress and S_h the minimum principal stress in Mid-Norway meaning the contemporary stress situation is "strike-slip".

6.5 Summary

The aim of this chapter was to draw together and summarise the results of all of the analyses performed in **chapters 4** and **5**. From the results, specific issues have been addressed and the following statements can be made:

- Variability in the magnitude of S_h at a specific depth is a worldwide phenomenon and cannot be removed even by stringent quality control of the data (but can be reduced).
- The scatter may therefore be a real feature representing heterogeneities in the magnitude of stress across an individual basin.
- Alternatively, the scatter may result from a combination of rock properties and pumping pressure testing parameters either working in concordance or acting in opposition to create a range of stress magnitudes at a specific depth over the whole basin.

- Differences in the magnitude of S_h in different lithologies revealed by laboratory testing do not appear in LOT data. A suggestion for the lack of a difference in magnitude of S_h between shale and sandstone is "fracture screen-out".
- The Mid-Norway data show the difference between LOP and ISIP reduces from a maximum of +/- 2½ MPa with later runs of XLOTs. Since LOPs from first runs of leak-off tests make up the majority of the data, the 5 MPa variability can explain some of the S_h variability on stress-depth plots (especially at shallow depths).
- There is not a systematic relationship between the magnitude of the lower bound to LOPs and the tectonic regime of a region.
- Likewise, there is no systematic relationship between the magnitude of the lower bound to LOPs and the presence/occurrence of P_p-S_h coupling.
- Pore pressure *in-situ* stress coupling is inferred for the Central North Sea, Brunei and the Gulf of Mexico.
- The likely mechanisms for P_p-S_h coupling are poro-elasticity and frictional limits to stress. The Central North Sea is the only region where coupling is inferred with data to suggest a change in tectonic regime at depth.
- The lack of a coupling relationship in Mid-Norway could relate to the timing and generating mechanism of the overpressure.
- There is a good correlation between the high levels of compaction of the rocks, the high Poisson's Ratio values, and the low $\Delta S_h/\Delta P_p$ value in Mid-Norway.
- It is felt that "inflationary mechanism" generated overpressures in normally compacted rocks (as seen in Mid-Norway) result in a lower $\Delta S_h/\Delta P_p$ value.
- The shape and magnitude, and presence or lack of, the overpressure transition zone can be used to explain the size of the range of S_h gradients at hydrostatic P_p.
- Using XLOT data and the Kirsch equations, quantification of S_H has been achieved for Mid-Norway.
- Results show that S_H is the maximum principal stress and that the contemporary stress situation is lateral stress dominated in Mid-Norway.

Chapter SEVEN: Conclusions

7 Conclusions

7.1 Summary of conclusions

The main objective of this thesis has been to use leak-off test data to calculate the minimum horizontal stress (S_h) in a range of sedimentary basins. Following the quantification of S_h an assessment of the variability in S_h was undertaken and possible reasons for the variability investigated. Lower bounds to leak-off pressures and upper limits to pore pressures were created as alternative means of estimating the regional S_h. Finally a relationship between overpressure and "excessive" S_h was investigated and a quantification made. This took the form of analysing for pore pressure *in-situ* stress coupling. What follows is a list of the main conclusions for each topic.

7.1.1 Minimum horizontal stress

Pumping pressure values from leak-off tests (LOTs) were used to calculate the magnitude of S_h. The S_h data were plotted on stress-depth plots and the following conclusions arose:

- Variability in the magnitude of S_h at a specific depth is evident worldwide. Whilst this variability cannot be eliminated even by stringent quality control of the data, it can be reduced.
- Differences in the LOT technique (pumping rate) and differences in the wellbore where the test was performed (diameter differences) do not universally account for the variability in S_h.
- Rock mechanical properties (lithology, rheology) can explain why uniaxial testing of different lithologies in the laboratory yields different S_h measurements. However, the effects of these properties are not seen in the field. An explanation for the lack of a relationship between lithology and S_h during LOTs is "fracture screen-out".
- It appears that there are two explanations for the scatter in S_h magnitude. Firstly, the scatter could be a real feature and represent heterogeneities in basin structure. Secondly, the scatter could be accounted for by different rock mechanical properties and pumping pressure testing parameters acting in concordance with, or in opposition to, each other.
- Use of stress-depth plots reveals that overpressures exert a control on S_h but the relationship cannot be quantified.

- Multiple cycle extended leak-off test (XLOT) data from Mid-Norway show the difference between the leak-off pressure (LOP) and instantaneous shut-in pressure (the ISIP - considered to be the best estimate of S_h) reduces from +/- 2½ MPa with later runs of XLOTs. Since S_h is calculated from LOPs recorded during first runs of LOTs in the majority of the data used in this study, the 5 MPa variability can partially account for the S_h variability on stress-depth plots (especially at more shallow depths).

7.1.2 Lower bounds to LOPs and upper limits to P_p

Plotting S_h data on stress-depth plots and fitting a quadratic envelope to the left-hand edge of the data swarm created a lower bound to leak-off pressures (LOPs). Independently plotting pore pressure data and fitting a 3rd order polynomial to the right-hand edge of the data swarm created an upper limit to pore pressures. The following conclusions can be stated:

- The lower bound to leak-off pressures produces a good estimate of the minimum *in-situ* stress in a region.
- All lower bounds are curvi-linear in shape showing they increase their magnitude towards the lithostat with depth. While this represents an increase in the S_h:S_V ratio at greater depths, it also represents a reduction in data with depth (especially at the greatest depths).
- The lower bound to all LOPs and the "*comparable depth*" lower bound closely match in most regions indicating that the "*comparable depth*" S_h data are representative of the S_h data from the region as a whole.
- The upper limits can produce good estimates of the maximum pore pressure.
- There is not a systematic relationship between the magnitude of the lower bound to LOPs and the magnitude of the upper limit to P_p. Using lower bounds to LOPs to estimate the maximum P_p, or vice versa, can lead to mis-estimates (especially within normally pressured zones).
- However, the upper limit to P_p *can* be successfully used to estimate the minimum horizontal stress throughout the *overpressured* zone.
- Given the data and information available, there is not a systematic relationship between the magnitude of the lower bound and the tectonic regime of a region.

7.1.3 Pore pressure *in-situ* stress coupling

The "*comparable depth*" data were used to investigate the presence of pore pressure *in-situ* stress coupling. These data were normalised to an "*hypothetical unconstrained basin*" and/or depth. Linear regression lines were fitted to all the data and solely the overpressured data. Coupling was inferred to be occurring based on a r^2 value >0.5. The following conclusions arose:

- The "*comparable depth*" data are the best data to use for coupling analyses because the 100-metre vertical depth constraint on P_p and S_h means any effect overpressure has on S_h magnitude will most likely be revealed by these data.
- A general *rule-of-thumb* can be made from stress-depth plots: "greater S_h magnitudes are associated with greater magnitudes of overpressure".
- Normalising the data and fitting linear regression lines shows steeper gradients (higher $\Delta S_h/\Delta P_p$ values) are paired with lower y-axis intercepts of the regression lines.
- High y-axis intercepts represent high magnitudes of S_h occurring across a region for all pore pressures (especially the normally pressured data).
- Coupling can be inferred for the Central North Sea, Brunei and the Gulf of Mexico.
- Frictional limits to stress and poro-elasticity are felt to best describe the coupling mechanisms. The Central North Sea is the only region where coupling is inferred that has data to prove a change in tectonic regime occurs with depth.
- The timing and mechanism of overpressure generation may hinder the presence of coupling in Mid-Norway. Low porosities (indicative of high effective stresses) show normal compaction occurred during burial of the region. Low effective stresses at the present day are inferred to show overpressures are generated by "inflationary mechanisms".
- Compaction of the rock followed by "repressurisation" by late-stage overpressures produces a lower $\Delta S_h/\Delta P_p$ value than is shown for regions where the overpressures result from disequilibrium compaction.
- Using the poro-elastic equation for predicting fracture gradients shows that the Poisson's Ratio values for the rocks in Mid-Norway are high. These high values imply higher levels of compaction.
- There is thus a good correlation between the high levels of compaction of the rocks, the high Poisson's Ratio values, and the low $\Delta S_h/\Delta P_p$ value in Mid-Norway.
- Normal P_p data show a range of S_h magnitudes associated with them. The transition from normally pressured to overpressured P_p is thought to be the cause of the range of S_h gradients at hydrostatic P_p.

- Complex basin heterogeneity may also explain why coupling does not occur at the basin scale but can be seen at the individual well scale.

7.1.4 Additional conclusions arising from the Mid-Norway study

Following the quality control of the data from Mid-Norway, re-opening cycles of XLOTs were used to investigate the magnitude of S_H and draw inferences into the contemporary stress situation in the region. These are the conclusions:

- LOP ≈ ISIP in Mid-Norway.
- The Kirsch equations show that S_H is the maximum principal stress in Mid-Norway.
- From the quantification of the three principal stresses, the contemporary stress situation can be shown to be $S_h<S_V<S_H$. This is a transpressive relationship.

7.2 Future work

Researching for this thesis has revealed that there are a number of possibilities for future work in the field of *in-situ* stress and the relationship between pore pressure and stress. There is also a need for specific types of data. Listed below are some suggestions that have arisen:

- This study had only one data set (Mid-Norway) that included the original records of leak-off tests therefore allowing a stringent quality control of the data. Ideally, such a quality control would be applied to all data sets. More accurate results can be gained if good, original data sets are made available allowing workers to quality assess their own data.
- The analyses of pore pressure *in-situ* stress coupling were "hindered", for the most part, by the lack of data. Using the "*comparable depth*" data (comprising actual S_h and P_p measurements) meant in many cases the data set was substantially reduced. It is proposed that to determine meaningful relationships between P_p and S_h leak-off tests and RFT tests should be performed as close together as possible. Ideally, more RFT measurements should be performed to more accurately assess the P_p situation.
- Greater emphasis should be placed on field-scale analyses versus basin-scale analyses. Teufel *et al.* (1991) showed that coupling occurs on a field scale using data from Ekofisk. If other data sets of P_p and S_h measurements could be compiled at the field scale, further relationships between geological and *anthropomorphic* coupling could be deduced.

- More work assessing the relationship between P_p and S_h and different rock mechanical parameters is needed. Integration of field and laboratory analyses of the rocks where the tests were performed would lead to further understanding of the effects of rheological properties on coupling. An implication would be an increased understanding of the effects of basin history (the amount and nature of compaction, and the overpressure generating mechanisms) on coupling relationships.
- Ideally, data would be acquired with the specific objective of assessing P_p and S_h evolution with depth rather than the current state of relying on the generosity of the oil industry.

References

Aadnoy, B. S., Bratli, R. K. & Lindholm, C. D. 1994. *In-situ* stress modelling of the Snorre Field. *In: Eurock '94, Proceedings of the 1994 Eurock Conference*, Delft. August 1994. Balkema, Rotterdam. 871-78.

Abum, T. K. S. & Omuso, W. O. 2000. On river cross-sectional change in the Niger Delta. *Geomorphology,* **34**. 111-26.

Alberty, M. W. & McLean, M. R. 2001. Fracture gradients in depleted reservoirs: Drilling wells in late reservoir life. *SPE/IADC Drilling Conference.* Amsterdam, The Netherlands. 27th February - 1st March 2001.

Aleksandrowski, P., Inderhaug, O. H. & Knapstad, B. 1992. Tectonic structures and wellbore breakout orientation. *In:* Tillerson, J. R. & Wawerski, W. R. (eds.) *Rock Mechanics.* Balkema, Rotterdam. 19-37.

Anderson, E. M. 1905. Dynamics of Faulting. *Transactions of the Edinburgh Geol. Soc.,* **8**. 387-402.

Anderson, E. M. 1942. *The dynamics of faulting and dyke formation with applications to Britain.* Oliver & Boyd, London.

Arnesen, L., Dart, C., Telnes, N. & Larsen, B. T. 1997. Estimating fracture gradients and minimum horizontal stress in the Northern Viking Graben. E&P Research Division, Norsk Hydro Produksjon a.s. (Unpublished report). 57pp.

Artyushkov, E. V. 1973. Stresses in the lithosphere caused by crustal thickness inhomogeneities. *Journal of Geophysical Research*, **78**. 7675-7708.

Bell, J. S. 1990. Investigating stress regimes in sedimentary basins using information from oil industry wireline logs and drilling records. *In:* Hurst *et al.* (eds.) *Geological Applications of Wireline Logs.* Geological Society of London, Special Publication **48**, 305-25.

Biot, M. A. 1941. General theory of three-dimensional consolidation. *Journal of Applied Physics*, **12**. 155-64.

Bjørkum, P. A. 1996. How important is pressure in causing dissolution of quartz in sandstones? *Journal of Sedimentary Research*, **A66**. 147-54.

Blystad, P., Brekke, H., Færseth, R. B., Larsen, B. T., Skogseid, J. & Tørudbakken, B. 1995. *Structural elements of the Norwegian Continental shelf part 2: The Norwegian Sea region. NPD Bulletin*, **8**.

Borgerud, L. & Svare, E. 1995. *In-situ* stress field on the Norwegian margin, 62°-67° north. *In:* Fejerskov, M. & Myrvang, A. M. (eds.) *Proceedings of the Workshop on Rock Stresses in the North Sea.* Trondheim, Norway. 13th-14th February 1995. 165-78.

Bott, M. H. P. & Dean, D. S. 1972. Stress systems at young continental margins. *Nature (Physical Science)*, **235**. 23-5.

Breckels, I. M. & van Eekelen, H. A. M. 1982. Relationship between horizontal stress and depth in sedimentary basins. *Journal of Petroleum Technology,* **34**. 2191-9.

Bredehoeft, J. D., Wolff, R. G., Keys, W. S. & Schuter, E. 1976. Hydraulic fracturing to determine the regional *in-situ* stress field, Piceance Basin, Colorado. *Geological Society of America Bulletin,* **87**, 250-8.

Bredehoeft, J. D., Wesley, J. B. & Fouch, T. D. 1994. Simulations of the origins of fluid pressure, fracture generation and the movement of fluid in the Uinta Basin, Utah. *AAPG Bulletin,* **78 #11**. 1729-47.

Bukovics, C., Cartier, E. G., Shaw, N. D. & Ziegler, P. A. 1984. Structure and development of the Mid-Norway continental margin. *In:* Spencer, A. M. *et al.* (eds.) *Petroleum Geology of the North European Margin. Norwegian Petroleum Society.* Graham & Trotman Ltd., London. 407-23.

Burrus, J. 1998. Overpressure models for clastic rocks, their relationship to hydrocarbon expulsion: a critical re-evaluation. *In:* Law, B. E. *et al.* (eds.) *Abnormal pressures in hydrocarbon environments. AAPG Memoir,* **70**. 35-63.

Burwood, R. 1999. Angola: source-rock control for Lower Congo Coastal and Kwanza Basin petroleum systems. *In:* Cameron *et al.* (eds.) The Oil and Gas Habitats of the South Atlantic. Geological Society of London, *Special Publication,* **153**. 181-94.

Byerlee, J. D. 1978. Friction of rock. *Pure & Applied Geophysics,* **116**. 615-26.

Bøen, F., Eggen, S. & Vollset, J. 1984. Structures and basins of the margin from 62^{O} to 69^{O}N and their development. *In:* Spencer, A. M. *et al.* (eds.) *Petroleum Geology of the North European Margin. Norwegian Petroleum Society.* Graham & Trotman Ltd., London. 253-70.

Coward, M. P., Purdy, E. G., Ries, A. C. & Smith, D. G. 1999. The distribution of petroleum reserves in basins of the South Atlantic margins. *In:* Cameron *et al.* (eds.) The Oil and Gas Habitats of the South Atlantic. Geological Society of London, *Special Publication,* **153**. 101-33.

Cramez, C. & Jackson, M. P. A. 2000. Superposed deformation straggling the continental-oceanic transition in deep-water Angola. *Marine and Petroleum Geology,* **17 #10**. 1095-1109.

Curiale, J., Morelos, J., Lambiase, J. & Mueller, W. 2000. Brunei Darussalam – Characteristics of selected petroleums and source rocks. *Organic Chemistry,* **31**. 1475-93.

Dahl, B. & Augustson, J. H. 1993. The influence of Tertiary and Quaternary sedimentation and erosion on hydrocarbon generation in Norwegian offshore basins. *In:* Doré, A. G. *et al.* (eds.) *Basin Modelling: Advances and Applications. NPF Special Publication,* **3**. Elsevier Press, Amsterdam. 419-31.

Daines, S. R. 1982. Prediction of fracture pressures for wildcat wells. *Journal of Petroleum Technology,* **April 1982**. 863-72.

Davis, D. H. & Reynolds, S. J. 1996. *Structural Geology of Rocks and Regions.* 2nd Edition. John Wiley & Sons.

Dickinson, G. 1953. Geological aspects of abnormal reservoir pressures in Gulf Coast Louisiana. *AAPG Bulletin*, **37 #2**. 410-32.

Eaton, B. A. 1969. Fracture Gradient Prediction and its Application in Oilfield Operations. *Journal of Petroleum Technology*, **Oct. 1969**. 1353-60; *Transactions AIME*, **246**. *In: SPE Re-print Series,* **49***: Pore Pressure and Fracture Gradients.* Society of Petroleum Engineers.

Eaton, B. A. & Eaton, T. L. 1997. Fracture gradient prediction for the new generation. *World Oil*, **October 1997**. *In: SPE Re-print Series,* **49**: *Pore pressure and Fracture Gradients.* Society of Petroleum Engineers. 108-12.

Enever, J. R., Yassir, N., Willoughby, D. R. & Addis, M. A. 1996. Recent experience with extended leak-off tests for *in-situ* stress measurements in Australia. *Australian Petroleum Exploration & Production Association Journal*, **36**, 528-35.

Engelder, T. 1993. *Stress Regimes in the Lithosphere.* Princeton University Press.

Engelder, T. & Fischer, M. P. 1994. Influence of poro-elastic behaviour on the magnitude of minimum horizontal stress, S_h, in overpressured parts of sedimentary basins. *Geology,* **22**. 949-52.

England, P. 1992. Deformation of the Continental Crust. *In:* Brown, G. C. *et al.* (eds.) *Understanding the Earth: A new synthesis.* Cambridge University Press. 275-300.

Fejerskov, M., Bratli, R. K., Singelstad, A. & Jørgensen, T. 1996. How well do conventional leak-off tests predict *in-situ* rock stresses? Norwegian Rock Mechanics Symposium (Bergmekanikkdagan), 22nd Nov. 1996, Oslo, Norway. 20pp.

Fejerskov, M., Myrvang, A. M., Lindholm, C. D. & Bungum, H. 1995. *In-situ* rock stress pattern on the Norwegian continental shelf and mainland. *In:* Fejerskov, M. & Myrvang, A. M. (eds.) *Proceedings of the Workshop on Rock Stresses in the North Sea.* Trondheim, Norway. 13th-14th February 1995. 191-201.

Forsyth, D. W. & Uyeda, S. 1975. On the relative importance of the driving forces of plate motion. *Geophysical Journal of the Royal Astronomical Society*, **43**. 163-200.

Gaarenstroom, L., Tromp, R. A. J., de Jong, M. C. & Brandenburg, A. M. 1993. Overpressures in the Central North Sea: implications for trap integrity and drilling safety. *In:* Parker, J. R. (ed.) *Petroleum Geology of NW Europe: Proc. of the 4th Conference.* Geol. Soc. Lon. 1305-1313.

Goodman, R. E. 1980. *Introduction to Rock Mechanics.* John Wiley & Sons.

Grauls, D. 1994. Relation entre contrainte minimale actuelle et profondeur dans quelques bassins sedimentaires (Projet de Recherche HP-HT). *Elf Aquitaine Production* note technique (Unpublished report). 4pp.

Grauls, D. 1997. Minimum principal stress as a control of overpressures in sedimentary basins. *In*: Hendry, J. P. *et al.* (eds.) *Contributions to the Second International*

Conference on Fluid Migration and Interaction in Sedimentary Basins and Orogenic Belts. 219-222.

Grauls, D. 1998. Overpressure assessment using a minimum principal stress approach. *In: Overpressures in Petroleum Exploration.* Workshop proceedings 7-8th April 1998. 8pp.

Grauls, D. & Baleix, J. M. 1994. Role of overpressures and *in-situ* stresses in fault controlled hydrocarbon migration. *Marine & Petroleum Geology*, **11 #6**. 734-42.

Grauls, D. & Cassignol, C. 1993. Identification of a zone of fluid pressure-induced fractures from log and seismic data – a case history. *First Break,* **11 #2**. 59-68.

Grigo, D., Maragna, B., Arienti, M. T., Fiorani, M., Parisi, A., Marrone, M., Sguazzero, P. & Uberg, A. S. 1993. Issues in 3D sedimentary basin modelling and application to Haltenbanken, offshore Norway. *In:* Doré, A. G. *et al.* (eds.) *Basin Modelling: Advances and Applications. NPF Special Publication,* **3**. Elsevier Press, Amsterdam. 455-68.

Hancock, J. M. 1990. The Cretaceous. *In:* Glennie, K. W. (ed.) *Introduction to the Petroleum Geology of the North Sea.* Blackwell Scientific Publications. 255-72.

Harrold, T. W. D. 2000. *Porosity and effective stress relationships in mudrocks.* Ph.D. Thesis. University of Durham, United Kingdom.

Harrold, T. W. D., Swarbrick, R. E. & Goulty, N. R. 1999. Pore Pressure Estimation from Mudrock Porosities in Tertiary Basins, southeast Asia. *AAPG Bulletin*, **83 #7**. 1057-67.

Heppard, P. D., Cander, H. S. & Eggertson, E. B. 1998. Abnormal pressures and the occurrence of hydrocarbons in offshore eastern Trinidad, West Indies. *In:* Law, B. E. *et al.* (eds.) *Abnormal pressures in hydrocarbon environments. AAPG Memoir,* **70**. 215-46.

Hermanrud, C., Wensaas, L., Teige, G. M. G., Nordgård-Bolås, H. M., Hansen, S & Vik, E. 1998a. Shale Porosities from Well Logs on Haltenbanken (Offshore Mid-Norway) Show No Influence of Overpressuring. *In:* Law, B. E. *et al.* (eds.) *Abnormal pressures in hydrocarbon environments. AAPG Memoir,* **70**. 65-85.

Hermanrud, C., Teige, G. M. G., Vik, E., Paasch, B., Wensaas, L. & Nordgård-Bolås, H. M. 1998b. Overpressures in shales – do we know what they are and why they are there? *In:* Mitchell, A. & Grauls, D. (eds.) *Overpressures in Petroleum Exploration.* Proceedings of the Workshop, 7th-8th April 1998. Pau, France. 43-8.

Hillis, R. R. 1998a. Dilational and shear failure as mechanisms of generating fracture permeability and limiting overpressure in the North Sea and the significance of poro-elasticity. *In: GeoPOP 1: 7th Report, volume #2.* January 1998. 149-76.

Hillis, R. R. 1998b. The Australian Stress Map. *PESA News,* **Dec. 1998**. 40-3.

Hillis, R. R. 2000. Pore pressure-stress coupling and its implications for seismicity. *Exploration Geophysics,* **31**. 448-54.

Hillis, R. R. 2001a. Petroleum Geomechanics: *In-situ* Stress in Hydrocarbon Exploration and Development. *Course notes.* University of Durham, UK. 8th January 2001.

Hillis, R. R. 2001b. Coupled Changes in Pore Pressure and Stress in Oil Fields and Sedimentary Basins. *Petroleum Geoscience*, **7 #4**. 419-25.

Hillis, R. R., Meyer, J. J. & Reynolds, S. D. 1998. The Australian stress map. *Exploration Geophysics,* **29**. 420-27.

Hollander, N. B. 1984. Geohistory and hydrocarbon evaluation of the Haltenbank area. *In:* Spencer, A. M. *et al.* (eds.) *Petroleum Geology of the North European Margin. Norwegian Petroleum Society.* Graham & Trotman Ltd., London. 383-8.

Holm, G. M. 1998. Distribution and origin of overpressure in the Central Graben of the North Sea. *In:* Law, B. E. *et al.* (eds.) *Abnormal pressures in hydrocarbon environments. AAPG Memoir,* **70**. 123-44.

Hubbert, M. K. & Rubey, W. W. 1959. Role of fluid pressure in mechanics of overthrust faulting 1: Mechanisms of fluid-filled porous solids and its application to overthrusting. *Bull. Geol. Soc. of America,* **70**. 115-66.

Hubbert, M. K. & Willis, D. G. 1957. Mechanics of hydraulic fracturing. *Transactions AIME*, **210**. 153-68.

Hunt, J. M., Whelan, J. K., Buxton-Eglinton, L. & Cathles, L. M. 1998. Relation of shale porosities, gas generation and compaction to deep overpressures in the U.S. Gulf Coast. *In:* Law, B. E. *et al.* (eds.) *Abnormal pressures in hydrocarbon environments. AAPG Memoir,* **70**. 87-104.

Inglis, C. E. 1913. Stresses in a plate due to the presence of cracks and sharp corners. *Transactions of the Institute of Naval Architecture,* **55**. 219-41.

Jaeger, J. C. & Cook, N. G. W. 1979. *Fundamentals of Rock Mechanics.* Third Edition. Chapman & Hall, London.

Jensen, R. P. & Doré, A. G. 1993. A recent Norwegian Shelf heating event – fact of fantasy? *In:* Doré, A. G. *et al.* (eds.) *Basin Modelling: Advances and Applications. NPF Special Publication,* **3**. Elsevier Press, Amsterdam. 85-106.

Jubril, M. A., Shaw, H. F. & Fallick, A. E. 1996. Stable isotope and geochemical evidence of formation pore fluid evolution during diagenesis of Tertiary sandstones and mudrocks of the Niger Delta. *Journal of African Earth Sciences,* **27 #3-4**. 417-35.

Jørgensen, T. & Fejerskov, M. 1998. Leak-Off Tests: How to extract important *in-situ* stress information from a test originally designed for another purpose. *SPE/ISRM Eurock '98*, Trondheim, Norway, 8th-10th July 1998. 8pp.

Kan, T.-K. & Kilsdonk, B. 1998. Geopressure prediction from 3D seismic data: Case studies from the Gulf of Mexico. *Overpressures in Petroleum Exploration - Proceedings of the Workshop.* April 1998. Pau, France. *Bull. Centre Rech. Elf Explor. Prod., Memoir,* **22**. 157-65.

Katahara, K. W. 1996. Estimation of *in-situ* stress profiles from well logs. *Transactions of the Society of Professional Well Log Analysts.* 37th Annual Logging Symposium. 1-14.

Kirsch, G. 1898. Die Theorie der Elastizität und die Bedürfnisse der Festigheitslehre. *Zeitschrift des Vereines Deutscher Ingenieure,* **42**. 797-807.

Koch, J. O. & Heum, O. R. 1995. Exploration trends of the Halten Terrace. *In:* Hanslien, S. (ed.) *25 years of petroleum exploration in Norway. NPF Special Publication,* **4**. Elsevier Press, Amsterdam. 235-51.

Kuo, L.-C. 1997. Gas exsolution during fluid migration and its relationship to overpressure and petroleum accumulation. *Marine and Petroleum Geology,* **14 #3**. 221-9.

Kusznir, N. J. 1982. Lithosphere response to externally and internally derived stresses: A visco-elastic stress guide with amplification. *Geophysical Journal of the Royal Astronomical Society,* **70**. 399-414.

Laubach, S. E. 1988. Subsurface fractures and their relationship to stress history in east Texas basin sandstone. *Tectonophysics*, **156**. 37-49.

Leftwich, J. T. & Engelder, T. 199?. The Characteristics of Geopressure Profiles in the Gulf of Mexico Basin. Reference unknown.

Lewis, H., Olden, P. & Couples, G. D. 2000. Geomechanical modelling of seal integrity – Final report. *In: GeoPOP 2: 5th Report.* October 2000. 82-85.

Lindholm, C. D., Bungum, H., Villagran, M. & Hicks, E. 1995. Crustal stress and tectonics in Norwegian regions determined from earthquake focal mechanisms. *In:* Fejerskov, M. & Myrvang, A. M. (eds.) *Proceedings of the Workshop on Rock Stresses in the North Sea.* Trondheim, Norway. 13th-14th February 1995. 77-91.

Matthews, W. & Kelly, J. 1967. How to predict formation pressure and fracture gradient. *Oil & Gas Journal*, **65** (Feb. 1967). 92-106.

McNoleg, O. 1996. The integration of GIS, Remote Sensing, Expert Systems and Adaptive Co-Kriging for Environmental Habitat Modelling of the Highland Haggis using Object-Oriented, Fuzzy Logic and Neural Network Techniques. *Computers and Geosciences,* **22 #5**. 585-88.

Mjelde, R., Digranes, P., Shimamura, H., Shiobara, H., Kodaira, S., Brekke, H., Egebjerg, T., Sørenes, N. & Thorbjørnsen, S. 1998. Crustal structure of the northern margin of the Vøring Basin, Mid-Norway margin, from wide-angle seismic and gravity data. *Tectonophysics*, **293**. 175-205.

Miller, T. W. 1995. New insights on natural hydraulic fractures induced by abnormally high pore pressures. *AAPG Bulletin,* **79 #7**. 1005-18.

Miller, T. W., Luk, C. H. & Olgaard, D. L. 1998. The interrelationships between overpressure mechanisms and *in-situ* stress. *In: AADE Industrial Forum - Pressure regimes in sedimentary basins and their prediction.*

Milne, G. A., Davis, J. L., Mitrovica, J. X., Scherneck, H.-G., Johansson, J. M., Vermeer, M. & Koivula, H. 2001. Space-Geodetic Constraints on Glacial Isostatic Adjustment in Fennoscandia. *Science,* **291**. 2381-5.

Morita, N., Black, A. D. & Fuh, G.-F. 1990. Theory of lost circulation pressure. *SPE 20409.*

Moschovidis, Z. A., Gardner, D. C., Sund, G. & Veatch, R. W. 1993. Disposal of Oily Cuttings by Downhole Periodic Fracturing in Valhall, North Sea: A Case Study and Modelling Concepts. *SPE/IADC 25757.*

Mouchet, J. P. & Mitchell, A. 1989. *Abnormal pressures while drilling. Manuels techniques,* **2**. Elf Aquitaine.

Mueller, B., Reinecker, J., Heidbach, O. & Fuchs, K. 2000. The 2000 release of the World Stress Map (available online at www.world-stress-map.org).

Murrell, S. A. F. 1971. Micromechanical basis of the deformation and fracture of rocks. *In:* Te'eni, M. (ed.) *Structure, Solid Mechanics and Engineering Design.* Wiley, London. 239-48.

Nashaat, M. 1998. Abnormally High Formation Pressure and Seal Impacts on Hydrocarbon Accumulations in the Nile Delta and North Sinai Basins, Egypt. *In:* Law, B. E. *et al.* (eds.) *Abnormal pressures in hydrocarbon environments. AAPG Memoir,* **70**. 161-80.

Onuoha, K. M. 1999. Structural features of Nigeria's coastal margin: an assessment based on age data from wells. *Journal of African Earth Sciences,* **29 #3**. 485-99.

Onuoha, K. M. & Ekine, A. S. 1999. Subsurface temperature variations and heat flow in the Anambra Basin, Nigeria. *Journal of African Earth Sciences,* **28 #3**. 641-52.

Osborne, M. J. & Swarbrick, R. E. 1997. Mechanisms for generating overpressure in sedimentary basins: A re-evaluation. *AAPG Bulletin*, **81 #6**. 1023-41.

Payne, D. F., Tuncay, K., Park, A., Comer, J. B. & Ortoleva, P. 2000. A Reaction-Transport-Mechanical Approach to Modelling the Interrelationships Among Gas Generation, Overpressuring and Fracturing: Implications for the Upper Cretaceous Natural Gas Reservoirs of the Piceance Basin, Colorado. *AAPG Bulletin*, **84 #4**. 545-65.

Pennebaker, E. S. 1968. An Engineering Interpretation of Seismic Data. *SPE 1968 Annual Meeting.* Houston, TX. 29th September - 2nd October 1968. *SPE Paper 2165.*

***Philip's Atlas of the World*, 10th Edition.** 2000. George Philip Ltd.

Phillips, W. J. 1972. Hydraulic Fracturing and Mineralisation. *Journal of the Geological Society of London*, **128**. 337-59.

Pilkington, P. E. 1978. Fracture gradient estimates in Tertiary basins. *Petroleum Engineering International*, **May 1978**. 138-48.

Reymond, B. A. & Stampfli, G. M. 1996. Three-dimensional sequence stratigraphy and subtle stratigraphic traps associated with systems tracts: West Cameron region, offshore Louisiana. *Marine and Petroleum Geology*, **13**. 41-60.

Roberts, D. G., Thompson, M., Mitchener, B., Hossack, J., Carmichael, S. & Bjrnseth, H.-M. 1999. Palaeozoic to Tertiary rift and basin dynamics: Mid-Norway to the Bay of Biscay – a new context for hydrocarbon prospectivity in the deep water frontier. *In:* Fleet, A.

J. & Boldy, S. A. R. (eds.) *Petroleum Geology of NW Europe: Proceedings of the 5th Conference*. 7-40.

Sadler, A. J. & Thorning, D. W. S. 1987. *Understanding Pure Mathematics*. Second Edition. Oxford University Press.

Salz, L. B. 1977. Relationship between fracture propagation pressure and pore pressure. *SPE 52nd Annual Conference*. Denver, CO. 9th - 12th October 1977. *SPE Paper 6870*.

Santarelli, F. J., Tronvoll, J. T., Svennekjaer, M., Skele, H., Henriksen, R. and Bratli, R. K. 1998. Reservoir stress path: The depletion and rebound. *SPE/ISRM Eurock '98*, Trondheim, Norway, 8th-10th July 1998. 7pp.

Secor, D. T. 1965. Role of Fluid Pressure in Jointing. *American Journal of Science*, **263**. 635-46.

Sibson, R. H. 1981. Controls on low-stress, hydrofracture dilatancy in thrust, wrench and normal fault terrains. *Nature*, **289**. 665-7.

Sibson, R. H. 1985. A note on fault reactivation. *Journal of Structural Geology*, **7**. 751-4.

Sibson, R. H. 1996. Structural permeability of structure-driven fault-fracture meshes. *Journal of Structural Geology*, **18**. 1031-42.

Simpson, G. 1998. Evolution of rock strength and hydraulic connectivity during dehydration: results from microcrack model. *In: Abstracts - 1998 IFP Euroconference: Pore pressure, scale effect and the deformation of rocks.* November 1998.

Singh, B. & Emery, N. 1998. Fracture gradient predictions in depleted sands in the Gulf Coast sedimentary basin. *In: AADE Industrial Forum - Pressure regimes in sedimentary basins and their prediction.*

Skar, T., Van Balen, R. & Hansen, S. 1998. Overpressuring in Cretaceous shales on the Halten Terrace, Offshore Mid-Norway: Nature and causes. *In:* Mitchell, A. & Grauls, D. (eds.) *Overpressures in Petroleum Exploration.* Proceedings of the Workshop, 7th-8th April 1998. Pau, France. 69-75.

Skar, T., Van Balen, R. T., Arnesen, L. & Cloetingh, S. 1999. Origin of overpressures on the Halten Terrace, offshore Mid-Norway: the potential role of mechanical compaction, pressure transfer and stress. *In:* Aplin, A. C. *et al.* (eds.) *Muds and Mudstones: Physical and Fluid Flow Properties.* Geological Society of London, *Special Publication*, **158**. 137-56.

Smith, M. B., Miller, W. K. II & Haga, J. 1987. Tip screen-out fracturing: A techniques for soft unstable formations. *SPE Petroleum Engineering*, **May 1987**. 95-103.

Stein, S., Sleep, N. H., Geller, R. J., Wang, S. C. & Kroeger, G. C. 1979. Earthquakes along the passive margin in eastern Canada. *Geophysical Research Letters*, **6**. 537-40.

Swarbrick, R. E., Osborne, M. J., Grunberger, D., Yardley, G. S., Macleod, G., Aplin, A. C., Larter, S. R., Knight, I. & Auld, H. A. 2000. Integrated study of the Judy Field (Block 30/7a) – an overpressured Central North Sea oil/gas field. *Marine and Petroleum Geology*, **17**. 993-1010.

Swiecicki, T., Gibbs, P. B., Farrow, G. E. & Coward, M. P. 1998. A tectonostratigraphic framework for the Mid-Norway region. *Marine and Petroleum Geology*, **15 #3**. 245-76.

Teige, G. M. G., Hermanrud, C., Wensaas, L. & Nordgård-Bolås, H. M. 1999. The lack of relationship between overpressure and porosity in North Sea and Haltenbanken shales. *Marine and Petroleum Geology*, **16 #4**. 321-35.

Teufel, L. W., Rhett, D. W. & Farrell, H. E. 1991. Effect of reservoir depletion and pore pressure drawdown on *in-situ* stress and deformation in the Ekofisk Field, North Sea. *Proceedings of 32nd U.S. Symposium on Rock Mechanics*. Balkema, Rotterdam. 63-72.

Theis, N. J., Nielsen, H. H., Sales, J. K. & Gail, G. J. 1993. Impact of data integration on basin modelling in the Barents Sea. *In:* Doré, A. G. *et al.* (eds.) *Basin Modelling: Advances and Applications. NPF Special Publication,* **3**. Elsevier Press, Amsterdam. 433-44.

Traugott, M. O. 1997. Pore/fracture pressure determinations in deep water: basic concepts for predicting pore/fracture pressures in deep water, including the Centroid Concept for pore pressures in shales and reservoir. *Deepwater Technology*, **Aug. 1997**. 67-70.

Twiss, R. J. & Moores, E. M. 1992. *Structural Geology*. W. H. Freeman & Co.

Van Balen, R. T. & Skar, T. 2000. The influence of faults and intraplate stresses on the overpressure evolution of the Halten Terrace, Mid-Norwegian margin. *Tectonophysics*, **320 #3-4**. 331-45.

Van Rensbergen, P. & Morley, C. K. 2000. 3D Seismic study of a shale expulsion syncline at the base of the Champion delta, offshore Brunei and its implications for the early structural evolution of large delta systems. *Marine and Petroleum Geology*, **17**. 861-72.

Vik, E. & Hermanrud. C. 1993. Transient thermal effects of rapid subsidence in the Haltenbanken area. *In:* Doré, A. G. *et al.* (eds.) *Basin Modelling: Advances and Applications. NPF Special Publication,* **3**. Elsevier Press, Amsterdam. 107-17.

Wang, C-y. & Xie, X. 1998. Hydrofracturing and Episodic Fluid Flow in Shale-Rich Basins – A Numerical Study. *AAPG Bulletin,* **82 #10**. 1857-69.

White, A. J., Traugott, M. O. & Swarbrick, R. E. 2001. The use of leak-off tests as means of predicting minimum *in-situ* stress. *Petroleum Geoscience* (in press).

Yale, D. P., Rodriguez, J. M., Mercer, T. B. & Blaisdell, D. W. 1994. *In-situ* stress orientation and the effects of local structure - Scott Field, North Sea. *In: Eurock '94, Proceedings of the 1994 Eurock Conference*, Delft. August 1994. Balkema, Rotterdam. 945-51.

Yassir, N. A. 1997. Geomechanical controls on overpressuring: implications for pore pressure prediction in compressional basins. *In*: Hendry, J. P. *et al.* (eds.) *Contributions to the Second International Conference on Fluid Migration and Interaction in Sedimentary Basins and Orogenic Belts.* 235-8.

Yassir, N. A., Addis, M. A. & Hennig, A. 1998. Relationships between pore pressure and stress in different tectonic settings. *In: AADE Industrial Forum - Pressure regimes in sedimentary basins and their prediction.*

Yassir, N. A. & Bell, J. S. 1994. Relationships between pore pressure, stresses, and present day geodynamics in the Scotian Shelf, offshore eastern Canada. *AAPG Bulletin,* **78 #12**. 1863-80.

Yassir, N. A. & Zerwer, A. 1997. Stress Regimes in the Gulf Coast, Offshore Louisiana: Data from Well-Bore Breakout Analysis. *AAPG Bulletin,* **81 #2**. 293-307.

Zoback, M. D. & Healy, J. 1984. Friction, faulting and *in-situ* stress. *Annales Geophysicae*, **2**. pp. 689-98.

Zoback, M. D., Barton, C., Brudy, M., Chang, C., Moos, D., Peska, P. & Vernik, L. 1995. A review of some new methods for determining the *in-situ* stress state from observations of borehole failure with applications to borehole stability and enhanced production in the North Sea. *In:* Fejerskov, M. & Myrvang, A. M. (eds.) *Proceedings of the Workshop on Rock Stresses in the North Sea.* Trondheim, Norway. 13th-14th February 1995. 6-21.

Zoback, M. L. 1992. First- and second-order patterns of stress in the lithosphere: The world stress map project. *Journal of Geophysical Research*, **97**. 11703-28.

Appendix ONE

Appendix 1: World map showing the location of the six regional case studies described in **Chapter 5**.


The Barents Sea
The Central North Sea
Onshore Nigeria
Offshore West Africa
Brunei
The Gulf of Mexico